A Constitutive Model for Lead Free Solder Including Aging Effects and Its Application to Microelectronic Packaging

by

Mohammad Motalab

A dissertation submitted to the Graduate Faculty of
Auburn University
in partial fulfillment of the
requirements for the Degree of
Doctor of Philosophy

Auburn, Alabama
August 3, 2013

Keywords: lead-free solder, aging, constitutive models, mechanical properties, finite element model, and reliability

Approved by

Jeffrey C. Suhling, Chair, Quina Distinguished Professor of Mechanical Engineering
Hareesh V. Tippur, McWane Professor of Mechanical Engineering
Richard C. Jaeger, Distinguished University Professor Emeritus of Electrical and Computer Engineering
Michael J. Bozack, Professor of Physics

Abstract

The microstructure, mechanical response, and failure behavior of lead free solder joints in electronic assemblies are constantly evolving when exposed to isothermal aging and/or thermal cycling environments. Traditional finite element based predictions for solder joint reliability during thermal cycling accelerated life testing are based on solder constitutive equations (e.g. Anand viscoplastic model) and failure models (e.g. energy dissipation per cycle model) that do not evolve with material aging. Thus, there will be significant errors in the calculations with lead free SAC alloys that illustrate dramatic aging phenomena. In this research, a new reliability prediction procedure has been developed that utilizes constitutive relations and failure criteria that incorporate aging effects, and then validated the new approach through correlation with thermal cycling accelerated life testing experimental data.

In this study, a revised set of Anand viscoplastic stress-strain relations for solder that include material parameters that evolve with the thermal history of the solder material has been developed. The effects of aging on the nine Anand model parameters have been examined by performing stress-strain tests on SAC305 samples that have been aged for various durations (0-12 months) at a temperature of 100 C. For each aging time, stress-strain data have been measured at three strain rates (0.001, 0.0001, and 0.00001 1/sec) and five temperatures (25, 50, 75, 100, and 125 C). Using the measured stress-strain data, the Anand model material parameters have been determined for various aging

conditions. Mathematical expressions were then developed to model the evolution of the Anand model parameter with aging time. The results show that 2 of the 9 constants remain essentially constant during aging, while the other 6 show large changes (30-70%) with up to 12 months of aging at 100 C. Also the theoretical equations for the creep response of solder have been derived from the Anand viscoplastic model.

Procedures for extracting the Anand model constants from experimental stress-strain and creep data have also been established. The two developed methods have been then applied to find the Anand constants for SAC305 (Sn-3.0Ag-0.5Cu) lead free solder using two completely different sets of experimental test data. The first set of Anand parameters were extracted from uniaxial stress strain data measured over a wide range of strain rates ($\dot{\varepsilon}$ = 0.001, 0.0001, and 0.00001 sec^{-1}) and temperatures (T = 25, 50, 75, 100, and 125 ^{o}C). The second set of Anand parameters were calculated from creep test data measured at several stress levels (σ = 6, 8, 10, 12 and 15 MPa and temperatures (T = 25, 50, 75, 100, and 125 ^{o}C).

New aging aware failure criteria have also been developed based on fatigue data from a parallel study for lead free solder uniaxial specimens aged at elevated temperature for various durations prior to mechanical cycling. Using the measured fatigue data, mathematical expressions have been developed for the evolution of the solder fatigue failure criterion constants with aging for Morrow-Darveaux (dissipated energy based) type fatigue criteria.

After development of the tools needed to include aging effects in solder joint reliability models, these approaches have been applied to predict reliability of PBGA components attached to FR-406 glass epoxy laminated printed circuit boards that were

subjected to thermal cycling. Finite element modeling has been performed to predict the stress-strain histories during thermal cycling of both non-aged and aged PBGA assemblies, where the aging at constant temperature occurred before the assemblies were subjected to thermal cycling. The results from the finite element calculations have been combined with the aging aware fatigue models to estimate the reliability (cycles to failure) for the non-aged and aged assemblies. As expected, the predictions show significant degradations in the solder joint life for assemblies that had been pre-aged before thermal cycling. To validate the new reliability models, the finite element results have been compared with the experimental reliability data for fine pitch PBGA daisy chain components. Before thermal cycling began, the assembled test boards were divided up into groups and were subjected to several sets of aging conditions (preconditioning) including different aging temperatures (T = 25, 55, 85 and 125 C) and different aging times (no aging, and 6 and 12 months). After aging, the assemblies were subjected to thermal cycling (-40 to +125 C) until failure occurred. As with the finite element predictions, the Weibull data failure plots have demonstrated that the thermal cycling reliabilities of pre-aged assemblies were significantly less than those of non-aged assemblies. Good correlation was obtained between the new reliability modeling procedure that includes aging and the measured solder joint reliability data.

Acknowledgments

I would like to heartily express my gratitude to my major advisor Dr. Jeffrey C. Suhling for the support, guidance and mentorship throughout this research. Sincere appreciation is sent to my advisory committee members including Dr. Hareesh V. Tippur, Dr. Richard C. Jaeger and Dr. Michael J. Bozack for their insightful instruction and discussion regarding this research. Special thanks are also extended to all my co-workers and friends, Dr. Chang Lin, Dr. Yifei Zhang, Dr. Zijie Cai, Jordan Roberts, Safina Hussain, Muhannad Mustafa, Nusratjahan Chhanda, Munshi Basit, Md Hasnine, Kun-yen Wang, Jing Zou, Michael Palmer, John Marcell and Charles Ellis for their help, encouragement and friendship.

I am also grateful to my family specially to my father Asad Ullah and mother Marzia Asad for their endless love and support to my life and study in the United States. I am truly in debt to my wife Badrun Nessa for her extraordinary endurance, perseverance, and heartfelt consideration.

Table of Contents

List of Tables

List of Figures

CHAPTER 1

INTRODUCTION

1.1 Lead Free Solders in Microelectronics

With the emergence of the modern electronic packaging technology over the last few decades, solder alloys have been the primary interconnect material used in electronic packaging. In the past, eutectic 63Sn-37Pb has been the most extensively used soldering alloy in the packaging industries. The eutectic Sn-Pb solders were very attractive due to their relatively low melting temperature (183 °C) and excellent ductility and good reliability and for their superior wettability and compatibility with most substrates and devices [1].

There is a general trend towards products that minimize harmful effects on the environment and human health. This trend is further reinforced by the RoHS ban on harmful substances and WEEE regulations on recycling and minimizing of electronic wastes. In June 2000, the EU adopted two directives, the Waste of Electrical and Electronic Equipment (WEEE) and the Directive of the Restriction of the Use of Certain Hazardous Substances (RoHS) [2]. The WEEE directive requires that lead has to be removed from any end-of-life electrical or electronic components. The RoHS specifically bans lead from electrical and electronic components manufactured after July 1, 2006. As a result of the enforcement of the directives, all electrical or electronic equipment and devices produced in or imported to E.U. member states must comply with these lead-free

standards except those items that are exempted from the bans. In addition to legislation enforcement there are emerging detection technologies to enforce compliance. So due to the general push towards the eco-efficiency and green electronics, manufacturers are motivated for the adoption of lead free electronics. Therefore, the conversion to lead free solders in the global electronic market appears imminent [3].

In the United States, as soon as lead-free solder legislation was proposed, the lead-free solder project headed by the NCMS initiated research and development of lead-free solder in a program lasting 4 years [4]. The results of the project have been made available in a database and offer information on such matters as modifying equipment and processes for selecting alternative materials. The project initially selected for study 79 types of alloys considered at the time to be potential candidates for use in lead-free solder. Basic attributes considered included toxicity, resource availability, economic feasibility, and wetting characteristics. The selection process narrowed the field down to the final seven alloys, and these received secondary evaluation for reliability and ease of mounting manufacturing. Evaluation of the individual alloys did not result in the final selection of a single candidate, but three alloys, Sn–58Bi, Sn–3.5Ag–4.8Bi, and Sn–3.5Ag, were recommended as candidates. Screening comments indicated that the Sn–58Bi eutectic alloy was not suitable for use as standard solder due to the scarcity of Bi resources. However, since this material can be used for mounting at less than 200 C, and has chalked up a 20-year plus record of use in mainframe computers, this solder was deemed suitable for special applications. These results were used to construct a database on lead-free solder that includes the information in these tables along with other items such as (1) recommended applications for lead-free solder, (2) alloy composition

guidelines reflecting price and availability, (3) database of the 7 selected alloys and comparison with Sn–Pb eutectic alloy, (4) data on the characteristics of the other 70 eliminated alloys, (5) optimal process conditions using various test PWBs, (6) strength evaluation and metallurgical reaction analysis for the selected alloys and various surface mounting process reactions, (7) predicted life (using NCMS Project proprietary life prediction software) and thermal fatigue evaluation for 4 of the selected alloys, and (8) assessment of nontoxicity and alloy composition.

In selecting suitable alternative of Sn-Pb soldering materials, it is important to take into consideration that the properties of the alternative solders are comparable or superior to Sn-Pb solders. Compatible candidates of the Sn-Pb solders must have the following behaviors [5]:

- melting temperature similar to eutectic Sn-Pb for a similar reflow profile
- sufficient wettability for good metallization process
- good electrical properties for transmitting electrical signals
- strong mechanical properties for good fatigue resistance and reliability
- inexpensive and easier manufacturability

1.2 Lead Free Solder Choices

Among various alloy systems that are considered as lead-free solder candidates, Sn-Ag-Cu alloys have been recognized as the most promising because of their relatively low melting temperature (compared with the Sn-Ag binary eutectic lead free solder), superior mechanical properties, and good compatibility with other components [6-8]. Sn-Ag-Cu alloys are widely used as lead-free solutions for ball-grid-array (BGA) interconnection in the microelectronic packaging industry as solder balls and pastes.

Although no “drop in” replacement has been identified that is suitable for all applications, Sn-Ag, Sn-Ag-Cu (SAC), and other alloys involving elements such as Sn, Ag, Cu, Bi, In, and Zn have been identified as promising replacements for standard 63Sn-37Pb eutectic solder. Industries have proposed several SAC alloys which include 96.5Sn-3.0Ag-0.5Cu (SAC 305) in Japan, 95.5Sn-3.8Ag-0.7Cu (SAC 387) in the EU, and 95.5Sn-3.9Ag-0.6Cu (SAC 396) in the USA. The International Printed Circuit Association has suggested that 96.5Sn-3.0Ag-0.5Cu (SAC305) and Sn-3.9Ag- 0.6Cu (two near-eutectic alloys) will be the most widely used alloys in the future [9]. This prediction is attributed to their good mechanical properties, acceptable wetting properties, and suitable melting points [10-12].

A relatively large number of lead free solder alloys have been proposed so far, including binary, ternary and even quaternary alloys. More than 70 alloys have been identified in the literature. Among them, the majority of the alloys are Sn-based alloys, that is, Sn is the preferred major constituent. In fact, Sn-rich lead free alloys have occupied more than 80% in the wave solder market share and more than 90% in the reflow solder (http://www.ameslab.gov/files/LeadFreeSolder_Foundation.pdf) market share (Figure 1.1). The main benefits of the various SAC alloy systems are their relatively low melting temperatures compared with the 96.5Sn–3.5Ag binary eutectic alloy, as well as their superior mechanical and solderability properties when compared to other lead-free solders. There are some major challenges for the current series of lead-free solders. SAC series alloys have a higher melting temperature, around 217 °C, compared to 183 °C for the eutectic Sn-Pb solders. They thus require higher reflow temperature during the manufacturing process, which can lead to reliability problems.

The excessive buildup of intermetallic formed at the interface between the solder joints and the copper pad can also cause reliability problems. High costs are another issue for lead-free solders.

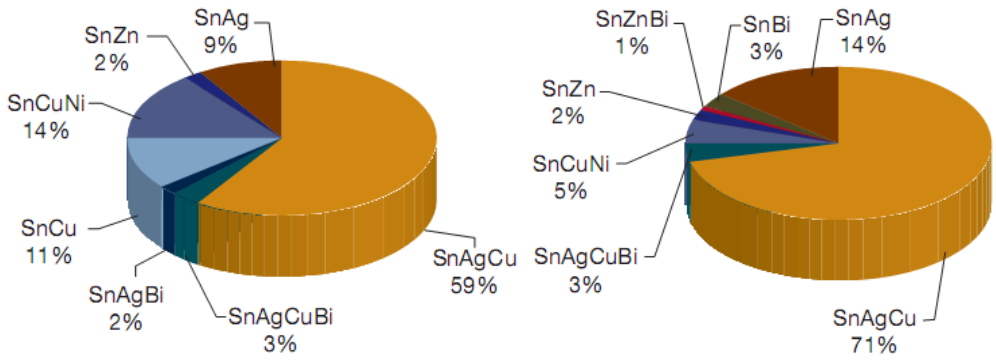

(a) Wave Solders (b) Reflow Solders

Figure 1.1 Lead Free Solder Market Share

1.3 Pb-free Candidates

There are several Pb-free solder candidates that have been considered for replacing Sn-Pb solders. The candidates primarily originate from a group of adequate binary alloy systems, which are further developed by adding small quantity of third or fourth elements in order to (1) lower the solder melting temperature and (2) increase its wettability and reliability [13].

As illustrated in Figure 1.1, Sn-based lead free solders are widely used and have been regarded as the best option for replacing eutectic Sn-Pb solder thus far. Actually, most of these lead free candidates originate from binary alloy systems and some are further optimized by adding small amount of third chemical elements in order to lower the melting point and/or increase the wettability and reliability [14]. Figure 1.2

summarizes popular lead free choices available on the market and their current applications.

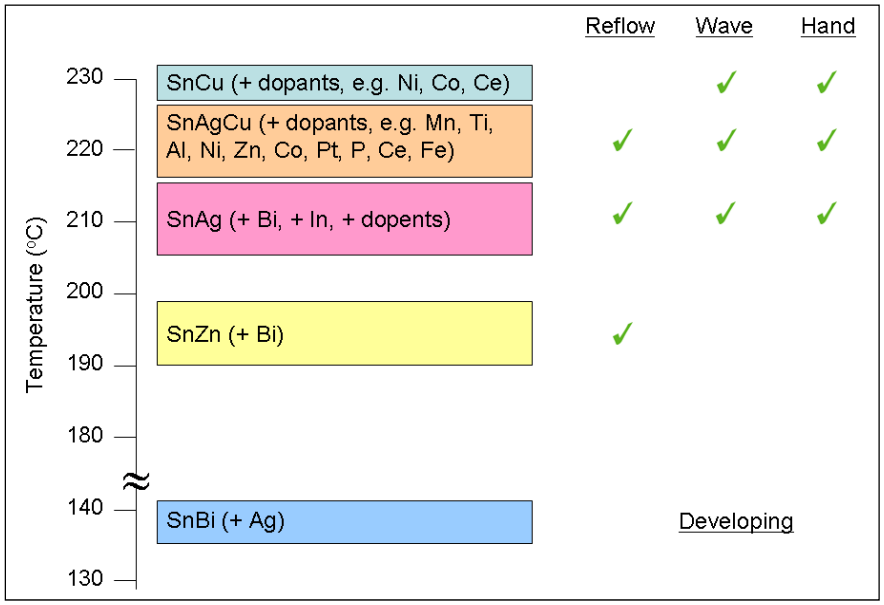

(Lee, C. N., Professional Development Course, ECTC 2011)

Figure 1.2 Prevailing Lead Free Choices and Their Applications

1.3.1 Sn-Cu System

The Sn-Cu binary system has a eutectic composition of 99.3Sn-0.7Cu and a melting temperature of 227 °C. This alloy is preferably used in wave soldering and might be suitable for high temperature applications required by the automotive industry. But it has unsatisfactory wettability and low thermal resistance. Furthermore, Sn-Cu alloys have relatively poor mechanical properties [15].

1.3.2 Sn-Ag System

The Sn-Ag binary system has a eutectic composition of 96.5Sn-3.5Ag in weight percentage and a melting temperature of 221 °C. The solidified microstructure of the

eutectic alloy features β-tin phase with dendritic globules and inter-dendritic regions with a eutectic dispersion of Ag_3Sn precipitates within β-tin matrix [15]. Although this alloy does not have excellent wettability, its joint strength is very good. But the diffusion rate for Cu from the Cu base into the solder is accelerated by high reflow temperatures and Sn concentration gradient between solder and base metal. For this reason, a layer of brittle Cu_6Sn_5 intermetallic is often observed near the interface between Cu pads and bulk solder balls, which is known to be detrimental to the reliability of the electronic assembly.

1.3.3 Sn-Zn System

The eutectic composition of the Sn-Zn binary system is 91Sn-9Zn with a eutectic temperature of 199 °C which is near that of eutectic Sn-Pb (183 °C). The lamellar microstructure consists of alternating Sn-rich and Zn-rich phases, which is similar to the eutectic Sn-Pb system. However, Zn-Cu phases are known to decrease the reliability of Sn-Zn/Cu assemblies. The presence of Zn in solder alloys easily leads to oxidation and corrosion due to the high oxidation potential of Zn. Zn reacts with flux to form hard paste and it also causes oxidation and corrosion problems due to the high oxidation potential of Zn.

1.3.4 Sn-Bi System

The eutectic Sn-Bi alloy has an eutectic composition of 42Sn-58Bi and a relatively low melting temperature of 139 ^{o}C. It has been recommended as a promising replacement for Sn-Pb solders. This alloy has equivalent, even better properties than 63Sn-37Pb and is suitable for low temperature applications. Additionally, eutectic Sn-Bi solder has proven to have better manufacturability than Pb-Sn. However, Bi has a

tendency to precipitate from the solder matrix aggregate along grain boundaries through which cracks can occur resulting in early failures of solder joints due to the embrittlement of the interface between and bulk Sn-Bi solder joint and the Cu trace [16, 17].

1.3.5 Sn-In System

The eutectic point of Sn-In binary system is 50.9Sn-49.1In and the melting temperature is 117 °C. There are two phases in the eutectic microstructure: an In-rich, psudo-body-centered tetragonal phase, β, which has 44.8% Sn, and a hexagonal Sn-rich phase, γ, with 77.6% Sn. Despite its low melting temperature and limited tendency to scavenge gold compared to Sn-Pb solders, the high material cost and low availability greatly handicaps its application in the electronics packaging industry.

1.3.6 Sn-Ag-Cu System

As shown in Figure 1.1, SnAgCu (SAC) has been the most popular, widely used lead free solder in today's market. Although they are still not identified as the "drop in" replacement for all applications, a variety of SAC alloys with different chemical compositions have been the proposed by various user groups and industry experts. These include: SAC105 (98.5Sn-1.0Ag-0.5Cu), SAC205 (97.5Sn-2.0Ag-0.5Cu), SAC305 (96.5Sn-3.0Ag-0.5Cu), and SAC405 (95.5Sn-4.0Ag-0.5Cu), known as the SACN05 series; SAC387 (95.5Sn-3.8Ag-0.7Cu), SAC396 (95.5Sn-3.9Ag-0.6Cu), and SAC357 (95.2Sn-3.5Ag-0.7Cu), identified as near eutectic SAC choices; SAC3810 (95.2Sn-3.8Ag-1.0Cu), SAC3595 (95.55Sn-3.5Ag-0.95Cu), SAC0307 (9Sn-0.3Ag-0.7Cu), and SAC107 (98.3Sn-1.0Ag-0.7Cu), designed for special needs such as high temperature application, drop and shock optimization, etc. The main benefits of the various SAC

alloy systems are their relatively low melting temperatures compared with the 96.5Sn-3.5Ag binary eutectic alloy, as well as their superior mechanical and manufacturability properties when compared to other lead free solders [18].

Figure 1.3 shows a typical 3-D ternary phase diagram. The contours on the top surfaces of the figure represent the isothermal lines. Each of the 3 sectors represents the binary phase diagram of two of the three elements. The center of the diagram, where the isothermal lines reach the common, lowest point, is the eutectic point of the ternary system. Figure 1.4 is the top view (2-D) of the ternary phase diagram of Sn-Ag-Cu.

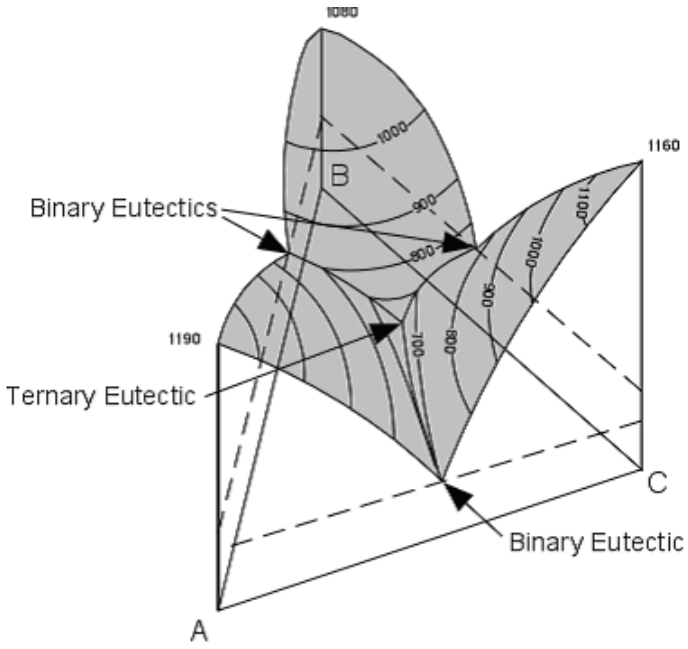

Figure 1.3 Typical 3-D Ternary Phase Diagram

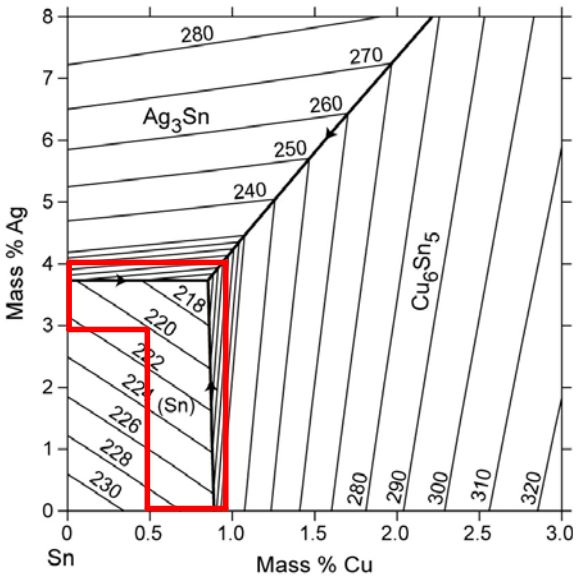

Figure 1.4 Sn-Ag-Cu Ternary Phase Diagram

The area indicated in the red box is the near eutectic region. Most of the SAC alloy compositions currently on the market are within this region. The eutectic and near eutectic melting temperature has been determined to be 217 °C, although the precise eutectic point is not known [19].

In SAC alloys, the formation of intermetallic compounds between the primary elements Sn and Ag, and Cu affect all the properties of the alloys. There are three possible intermetallic compounds that may be formed: Ag_3Sn forms due to the reaction between Sn and Ag (Figure 1.5) and Cu_6Sn_5 forms due to the Sn and Cu reaction. The compound Cu_3Sn will not form at the eutectic point unless the Cu content is high enough for the formation of Cu_3Sn at higher temperatures, so in bulk specimens Cu_3Sn is not presented. There is no reaction between Ag and Cu to form any kind of intermetallic compounds. The particles of intermetallic compounds possess much higher strength than the bulk material. Fine intermetallic particles in the Sn matrix can therefore strengthen the alloys. The intermetallic compounds can also improve the fatigue life of the solders,

as SAC alloys are reported to be 3-4 times better fatigue properties than the Sn-Pb eutectic solders. The higher fatigue resistance is believed to be contributed by the interspersed Ag_3Sn and Cu_6Sn_5 particles, which pin and block the movement of dislocations. The many patents that have been granted for SAC systems have limited their use and hindered research on several of the SAC alloys. However, many familiar alloy such as SAC305 and SAC405 are not patented to avoid excessive licensing and fees [18].

Despite the benefits mentioned above, SAC family solders sometimes are still questionable as complete substitutes for eutectic Sn-Pb because of costs, some patent issues (particularly outside Europe), aesthetic consideration (dross problem of SAC solders), and relatively high melting temperature (217 ^{o}C vs. 183 ^{o}C).

1.3.7 Sn-Ag-Cu + X System

SnAgCu alloys have shown potential to be successful substitutes for eutectic Sn-Pb, however, the industry is still looking for a "perfect" solution. According to the results of many recent studies, performance characteristics of solder alloys are able to be optimized by doping, that is, by adding a small amount of other alloying elements into the SAC solder alloys.

The proposed doping element candidates include Bi, Ni, Co, Ge, Zn, La, Mg, Mn, Ce, Ti, Fe, In, B, etc. For example, adding 0.05% (wt.) Ni can successfully stabilize the microstructure, inhibit the excessive consumption of metal base and thus increase the reliability of the solder joints [20-22]. In addition, doping rear earth (RE) elements can significantly enhance wettability, refine microstructure and improve ductility of SAC alloys [23-26].

Even though dopants can greatly alter the mechanical, electrical and physical behavior of SAC solders, the effect on melting temperature, however, is found to be negligible. This is another advantage for doped solder alloys because manufacturers can still use the same processing conditions as conventional SAC alloys.

Meanwhile, the known issues for SAC-X solders are also apparent. For instance, the material properties and interfacial behavior of solder alloys have been demonstrated to be very sensitive to the quantity of the X-additive. As a result, it takes much more time and cost to figure out the optimal composition levels for the dopants.

1.4 Characteristics and Applications of Sn-Ag-Cu Solder Material

The advantages of SAC series over other Pb-free systems include relatively low melting temperatures, superior mechanical and solderability properties, and good tolerance for Pb contamination. These characteristics give SAC alloys good compatibility with existing electronics packaging infrastructure. In fact, there is a long history of using 95.5Sn–4.0Ag–0.5Cu (SAC405) to form solder joints for BGA packages. The high market share (≈ 70%) by SAC series alloys on a global scale provides strong evidence of its world-wide acceptance. Also, nanoscale lead-free solders ("nano-solders") have been proposed and investigated in the development of nano-soldering technique for nanoscale assembly and integration. Tin (Sn)-based and indium (In)-based lead-free nano-solders have been synthesized directly onto multisegmented nanowires using electro deposition method in nanoporous templates. Furthermore, high temperature lead free solders are being used in medical industries today where a variety of intrusive procedures used requiring tools, instruments, sensors and components in materials that are inert with respect to reactions with the body [27]. Also, new surgical techniques have been

developed to improve the quality of operations, reduce the risk to patients and reduce the pain experienced by patients. Environmental concerns and the concern about toxicity and health hazards indicate that there is a drive to develop and use lead-free solders.

1.5 Mechanical Properties of Lead Free Solders

Electronics equipment is somewhat unusual as all categories of engineering materials may exist in close proximity. For example, a printed circuit board is often a fiber-reinforced polymer (it is a composite); a chip may be located on a ceramic and the tracking and solder will be metallic materials. Solder joints are used to mount chips and components onto printed circuit boards (PCB) and thus create an electrical circuit. Therefore, an ideal solder material needs both excellent conductivity to transmit signals and adequate strength to provide mechanical support and connection. The mechanical properties of solder alloys are therefore critically important in producing reliable products. Among the all mechanical properties of solders, tensile properties and creep are of particular concern. Also most failures of solder joints in electronic assembly are caused by fatigue/fracture [28], special focus has also been given to understand and analyze this behavior.

1.5.1 Tensile Properties (Stress-Strain Behavior)

Under the action of an increasing stress, metals usually exhibit elasticity, plasticity, and a maximum in stress is followed by necking and fracture. The slope of the linear elastic portion of the stress vs. strain plot is the modulus, and the stress at termination of elastic behavior is the yield stress. The extent of deformation prior to fracture is known as ductility. Ceramics display only elastic behavior until fracture, which is associated with cracking and very limited deformation (brittleness). Polymers

may exhibit both characteristics above according to the temperature. Above the glass transition temperature, T_g, extensive deformation due to mechanisms quite unlike those in metals may follow a small degree of elasticity. Below this temperature, polymers exhibit ceramic-like behavior. In all material categories, the maximum stress attained is the tensile/compressive/shear strength according to the mode of stressing employed. Composites are physical mixtures and exhibit the average properties of their components, taking into account the proportions of each. These characteristic features of monotonic behavior are summarized in Figure 1.5. The fracture strains of brittle materials and the yield strains of metals are generally less than 1% (the yield strain of solders is around 0.1–0.2%). The amount of deformation prior to the attainment of maximum strength is between about 3% and 7% for common solder alloys.

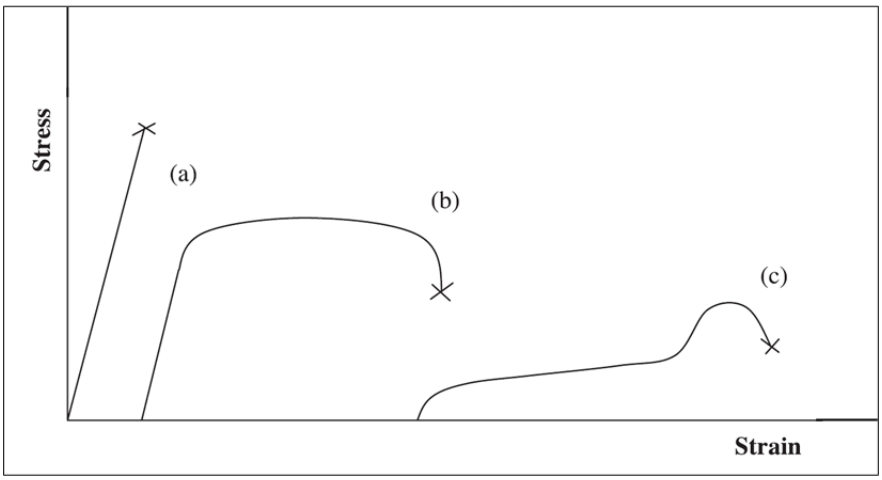

Figure 1.5 Schematic Overview of Mechanical Behavior of a) Ceramics, Polymers below their Glass Transition Temperature and Non Ductile Material b) Ductile Materials c) Polymers above Tg

Tensile properties indicate how the material will react to forces being applied in tension. Although solder joints are rarely under pure tensile/compressive loading, tensile properties are still crucial indicators for design purposes. Through tensile tests, several material properties can be determined, such as effective modulus, yield strength (YS), ultimate tensile strength (UTS), elongation, etc. In most of the cases that engineering stress-strain curves are employed by neglecting the change in cross sectional area.

Figure 1.6 shows a typical engineering stress strain curve. Tensile properties are generally described by stress-strain curves. A typical engineering stress-strain curve for solder alloys consists of an elastic region and a plastic region. In the elastic region, when the stress is reduced, the material will return to its original shape. In this linear region, the material obeys the relationship defined by Hooke's Law. However, since the effective modulus includes small inelastic deformations or time-dependent deformations such as creep, it is usually smaller than the dynamic modulus measured by the acoustic or ultrasonic wave method, which largely eliminates the inelastic deformation due to rapid wave propagation [29-31]. Also, Ralls, et al. showed that the elastic modulus of metal will decrease with increasing temperature [32]. The underlying reason for this is because the distance between adjacent atoms increases at higher temperatures which in turns decrease the elastic modulus.

When the load is high enough to exceed the elastic limits the material will experience plastic deformation, which is permanent. At this stage the material is undergoing a rearrangement of its internal molecular or microscopic structure, in which atoms are being moved to new equilibrium positions. Specimens subject to plastic deformation will simultaneously elongate and decrease in diameter. The Yield Stress (YS)

is defined as just enough stress to cause the onset of plastic deformation. However, YS is difficult to determine. In engineering practice, a specified small amount of plastic deformation is used, with 0.2% being the widely accepted value [28]. This is determined by a parallel line drawn at 0.2% of the strain to the elastic slope (Figure 1.6). When the load is removed at a point above the yield stress, the stress-strain curve will be approximately parallel to the initial modulus.

The ultimate tensile strength (UTS) is the maximum engineering stress level reached in a stress-strain test. In ductile materials similar to solders, the UTS are usually well outside of the elastic portion and the elastic strain is very small comparing to the plastic strain. When necking occurs, the engineering stress decreases and the specimen eventually fail.

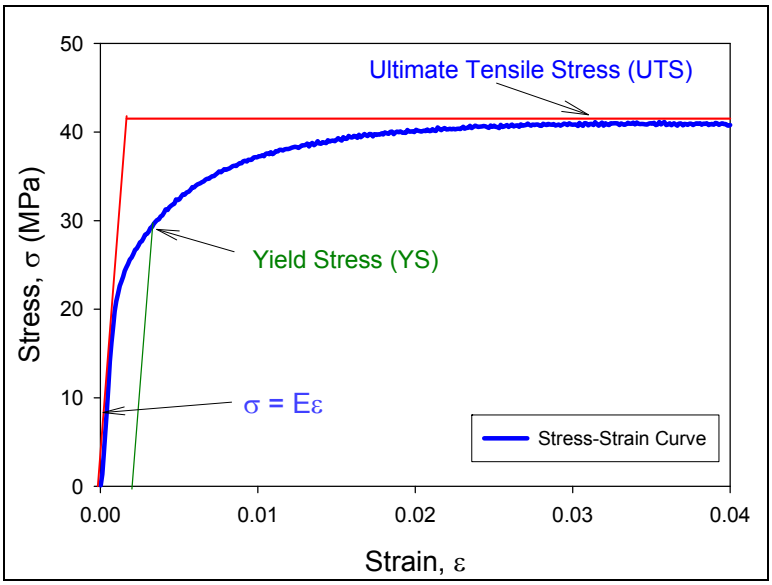

Figure 1.6 Typical Stress-Strain Curve.

1.5.2 Creep

Elevated temperature, time-dependent deformation, or *creep,* is a critical parameter that affects the performance of solder interconnections. This significant contribution is a result of the low solidus temperature of solder alloys. Even room temperature (T = 25 C) represents an elevated temperature for the Pb-free alloys, as indicated by a high homologous temperature, $T_h = T/T_m$, (T is the use/process temperature and T_m is the melting temperature of solder) for these and nearly all electronic solders. Therefore, there is a significant likelihood for creep to occur in interconnections, even under modest stresses.

Due to the CTE mismatches in the packaging materials, electronic assemblies are subjected to stresses. Creep deformation is one of the major failure modes of solder joints due to its high homologous temperature [33]. When T_h is greater than $0.5T_m$, the creep deformation will be the dominate deformation mode in metallic materials [34]. Solders have extremely high homologous temperatures even at room temperature due to their low melting temperature. For the Sn-Pb eutectic solder, T_m is 183 °C and the T_h is $0.65T_m$ at room temperature. For the lead free solders T_h is $0.61T_m$ at room temperature (T_m = 217 °C). So, both of these homologous temperatures are greater than $0.5T_m$, and thus, creep is not negligible for most solder materials even at room temperature. Consequently, solder alloys will undergo significant creep in normal use conditions. For example, if the normal operating temperature is considered as -40 °C to +125 °C in the actual assemblies, then the lead free solder T_h is between 0.48 - 0.81 and this is in the range of rapid creep deformation.

1.5.3 Creep Curve

Creep is a time-dependent permanent deformation that occurs when a material supports a constant load for a very long period of time at a constant temperature. Creep deformation tends to be rapid when the homologous temperature is above $0.5T_m$. The level of load/stress and the temperature are dominant factors in creep. Figure 1.7 shows a typical creep curve, which generally consists of three stages after the initial instantaneous elastic strain when a constant load is applied [35]. In every creep tests there is an initial strain which is due to the elastic jump and/or plastic deformation for application of the load. The strain rate starts with a very high magnitude and decreases rapidly over time in the first stage of creep test. This is caused by work hardening, which restricts the deformation. The second stage is called as the *Secondary Creep*, or *Steady-State Creep* Stage, in which the strain rate becomes approximately constant. The steady state creep rate is due to the dynamic balance of strain hardening and recrystallization [31] and mostly the region of plastic deformation. It is very important because so many researchers use the steady state creep rate for the finite element simulation to predict the solder stress, strain, and life. The tertiary creep region occurs when rupture is imminent, and typically features an abrupt change to a nearly constant but significantly increased creep rate.

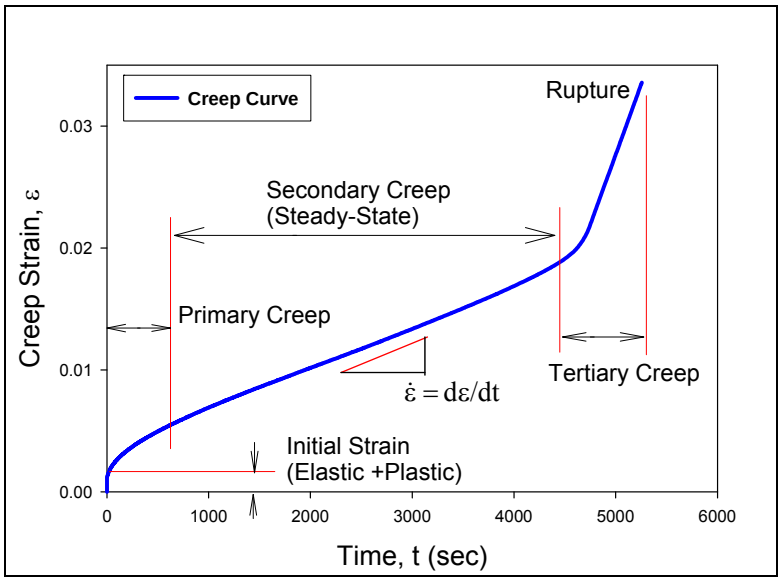

Figure 1.7 Typical Creep Curve.

1.5.4 Mechanisms of Creep Deformation

Several creep mechanisms have been proposed such as dislocation glide, dislocation creep, grain boundary diffusion, and lattice diffusion which can be summarized in a creep deformation map, as shown in Figure 1.8 [35, 36]. The deformation diagram was first introduced by Ashby in 1972 [36], and has been widely accepted and studied by other researchers in the area. In the deformation map show in Figure 1.8, the abscissa is the homologous temperature and the ordinate is normalized tensile or shear stress. The top of the map is bounded to the theoretical or ideal stress, below which is the onset of dislocation glide. *Dislocation glide* occurs at high stress levels over the entire homologous temperature range. In this case, the dislocation moves along the slip planes [37]. Dislocation creep is characterized by a high-temperature deformation mechanism with homologous temperatures greater than $0.5T_m$ and requiring intermediate high stress. The deformation results from diffusion controlled dislocation movement, with dislocations climbing away from barriers.

Coble proposed a *grain boundary based diffusion* mechanism, which involves the atomic or ionic diffusion along the grain boundaries [38]. The deformation occurs at intermediate low stress levels over an intermediate to low temperature range. Nabarro-Herring Creep or *lattice or bulk diffusion* occurs at low stress level and high temperature. In this case, interstitial atoms and lattice vacancies along the gradient of a grain boundary migrate in reversed directions in the presence of tension or compression pressure. Lattice or bulk diffusion becomes the primary deformation mechanism under this circumstance [39]. If there is no pressure, interstitial atoms and lattice vacancies will migrate in proportion to the gradient of their concentrations. Under pressure, the lattice defects tend to move in directions to relieve the imbalance of pressure. The movement will eventually cause creep deformation.

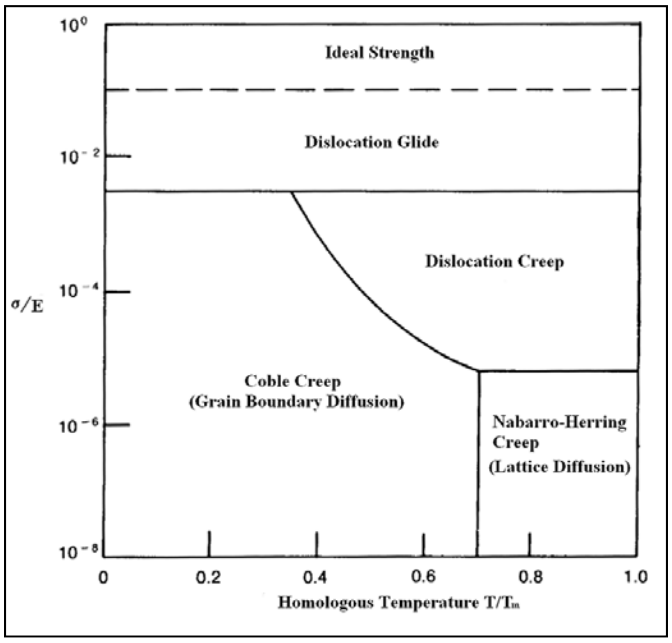

Figure 1.8 A Typical Creep Deformation Map

Grain-boundary sliding may also be involved in the creep deformation at high temperatures [31] where the displacement of grains can be induced by stress at high temperatures. However, this is not an independent deformation mechanism, but may accompany one or more of the above deformation mechanisms.

Due to the high homologous temperature ($> 0.5T_m$) of most solder alloys under normal operating conditions, the stress level determines the creep deformation mechanism. At low stress levels, the controlling mechanism is lattice diffusion and grain-boundary diffusion. As the stress rises to intermediate levels, dislocation creep takes over, and at high stress level, dislocation gliding becomes dominant. Additionally, the contribution of grain boundary gliding to creep deformation should be taken in account at all stress levels.

1.5.5 Shear

Solder joints in microelectronics systems are subjected to shear loading due to the thermal cycling conditions and CTE mismatch of the materials in an assembly. A typical shear stress-strain diagram is shown in Figure 1.9. Similar to tension (Figure 1.10), when a material is subjected to shear loading, it will have a linear region and a proportional limit τ_{pl}. As shown in Figure 1.9, a typical engineering shear stress-strain curve for solder alloys consists of an elastic region and a plastic region. In the elastic region, when the stress is reduced, the material will return to its original shape.

Strain hardening takes place from proportional limit to the ultimate share stress τ_u. Then, the stress starts to decrease until failure. Hooke's Law also holds for shear stress-strain responses at small shear strains, as shown in Figure 1.9. Quantity *G* is called the shear modulus of rigidity. It is measured as the slope of the linear portion on the shear

stress-strain diagram. In isotropic materials, the shear modulus can also be expressed in terms of the elastic modulus and Poisson's ratio.

Electronic assemblies often are subjected to combined shear deformation, warpage, and distortion under the action of thermal or power cycling and due to the CTE mismatch of different material in the assembly. Combined tension and shear loading can act on solder joints in these operating conditions.

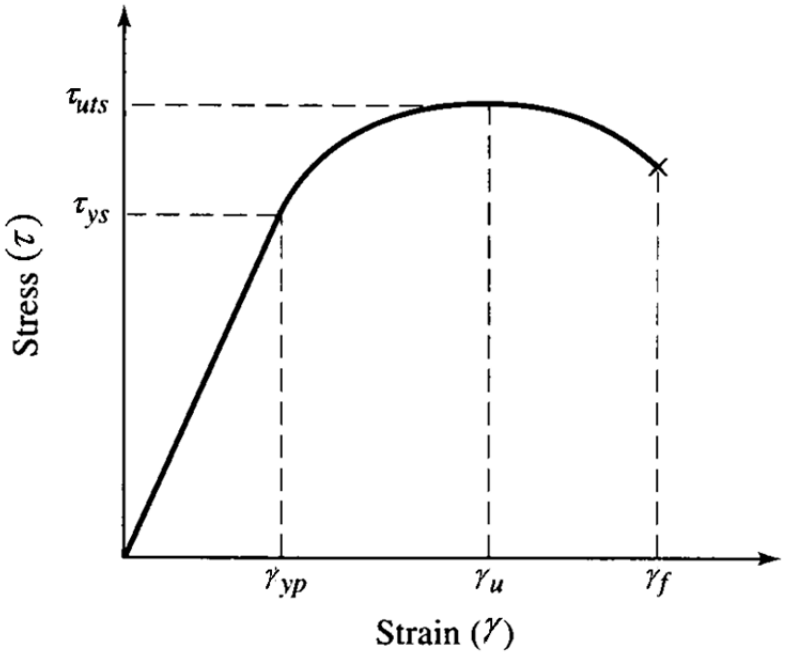

Figure 1.9 Typical Shear Stress-Strain Response for Ductile Materials

1.5.6 Fatigue

Electronics equipment rarely experiences a single constant or a continuously increasing stress. More common are stress or strain fluctuations induced by the service conditions, and these give rise to fatigue failure (failure due to a number of cycles, the magnitude of which is insufficient to cause failure in a single application). The key design parameters are the stress, or strain, amplitude, and the number of cycles, N_f,

necessary for failure. The process involves the initiation and gradual growth of cracks until the remaining section of the material can no longer support the applied load. It is by far the most common mode of failure in engineering applications.

When subjected to temperature changes, stresses or strains in electronic assemblies are typically developed due to the mismatches in the coefficients of thermal expansion (CTE) of the soldered components and the PCB. Cyclic temperature changes, either due to external environment or power switching, can therefore lead to substantial alternating stresses and strains within the solder joints. During cyclic loading, micro cracks form within the solder material followed by macro cracks which leads to damage and ultimately to fatigue failure. The total strain ε_t is made up of the elastic and plastic strain. For solder, the extent of elastic strain is small so that in most cases, $\Delta\varepsilon_p \gg \Delta\varepsilon_e$.

A hysteresis loop is a convenient means of depicting stress–strain relationships during fatigue as shown in Figure 1.10. The width of the loop is equal to the plastic strain range, $\Delta\varepsilon_p$, and the elastic strain range is given by the difference between the total strain range and the plastic strain range. The area enclosed by the loop is a measure of the plastic strain energy required to produce the observed deformation. This type of representation is very convenient when considering more complex and real cycles. During strain controlled fatigue, the stress range necessary to maintain the strain limits may increase (cycling hardening) or decrease (cycling softening). These changes may be due to the deformation process or cracking. Similarly, for stress-controlled fatigue the strain range necessary to maintain the stress level may increase or decrease.

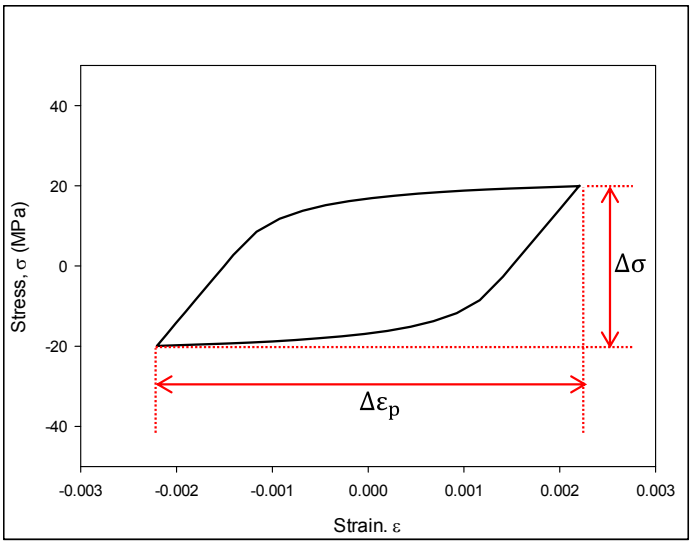

Figure 1.10 A Typical Hysteresis Loop

It has been observed that for a strain-controlled fatigue test, the peak stress drops continuously during cyclic loading due to damage accumulation. Plastic strain also increases due to material softening. During the test, cyclic tension-compression loading causes damage accumulation eventually resulting in crack initiation. Different stages of peak stress drop during a fatigue test are shown in Figure 1.11. It is seen that the stress drops rapidly during the initial cycles due to damage accumulation and material softening. A steady state stage is then attained where grain growth progresses, re-crystallization occurs in the microstructure, and micro-voids forms as shown in Figure 1.12. In the tertiary region, the stress drops rapidly when macro cracks initiate and crack growth progress to final rupture of the material. The number of cycles until fracture is commonly defined as the fatigue life of for material. Generally the number of cycles at 50% drop of the tensile load is taken to be the fatigue life as recommended by ASTM [40, 41]. Typically, the 50% load drop is considered to be the point of crack initiation, and the crack growth rate depends on the dissipation of plastic strain energy per cycle in the solder joint. If the fatigue data obeys a linear relationship when plotted on a log-log

plot of plastic strain range vs. number of cycles, it generally obeys the Coffin-Manson law [42]. Also, if the fatigue data obeys a linear relationship when plotted on a log-log plot of dissipated strain energy density vs. number of cycles, it generally obeys a Morrow type low cycle fatigue law.

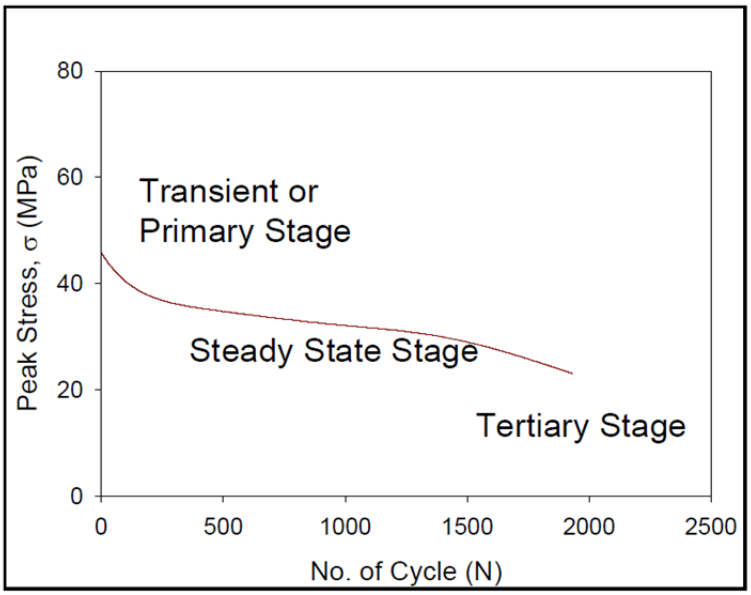

Figure 1.11 Different Stages of Stress Drop During Fatigue Test [41]

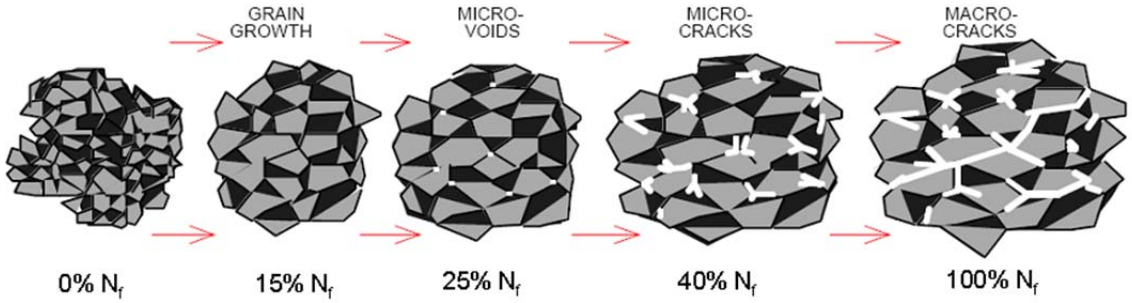

Figure 1.12 Depiction of the Effects of the Accumulating Fatigue Damage [41]

1.6 Objectives of This Research

The motivation of this research is to systematically study the effects of aging on mechanical behavior of lead free solder alloys and to develop new constitutive equations and reliability models that include aging effects to predict solder joint reliability in microelectronic packaging. The following objectives will be achieved in this research:

(1) Develop specimen preparation procedures that produce uniaxial testing coupons with consistent microstructures comparable to actual lead free solder joints in commercial electronic packages;

(2) Perform uniaxial tensile tests for lead free solders over a wide range of temperatures, strain rates, and aging conditions;

(3) Perform creep tests for lead free solders over a wide range of temperatures, stress levels, and aging conditions;

(4) Examine mechanical properties of lead free solders of interest and explore the effects of aging on them;

(5) Develop viscoplastic constitutive models including aging effects (modification of the Anand model) for predicting uniaxial tensile and creep behaviors;

(6) Develop reliability models including aging effects for lead free solder;

(7) Predict the life of microelectronic components using finite element analysis of BGA assemblies and aging included reliability models. Also, correlate the predicted life with the experimental results;

(8) Perform finite element analysis of CLGA and CBGA assemblies to determine the die stresses due to the assembly processes, thermal and power cycling

operations, and heat sink clamping using the Anand viscoplastic constitutive model for solder;

1.7 Organization of the Dissertation

This dissertation mainly focuses on studying the procedures for reliability prediction with aging effects for lead free solder materials, and the application of aging aware constitutive models for solders. The study is presented in the following chapters:

Chapter 1: Introduction to lead free solders alloys and mechanical properties of solder materials.

Chapter 2: Literature review on isothermal aging effects, mechanical properties, constitutive models, life prediction and reliability models, and finite element analysis of electronic packages that consist of lead free solder materials.

Chapter 3: Description of experimental procedure, uniaxial tensile and creep tests and data processing, investigation of aging effects on mechanical properties of lead free solder alloys.

Chapter 4: Study on the Anand viscoplastic constitutive model and the effects of aging on the model parameters, development of a modified Anand model with aging effects for lead free solder materials.

Chapter 5: Investigation on the effects of aging on the reliability model parameters for lead free solder materials.

Chapter 6: Prediction of life for lead free solder joints in PBGA assemblies, with and without prior aging effects, subjected to thermal cycling using finite element analysis.

Chapter 7: Application of the modified Anand constitutive model with aging effects in finite element analysis of microprocessor packages and prediction of life for lead free solder joint in CBGA assemblies, with and without prior aging effects, subjected to thermal cycling.

Chapter 8: Summary and conclusions of the dissertation.

CHAPTER 2

LITERATURE REVIEW

2.1 Introduction

As the electronic industries transition to lead free soldering by the motivation of environmental concerns, legislative mandates, and market differentiation, great efforts have been undertaken to develop desirable lead free solders and establish a corresponding database of material properties. Many researchers have attempted to measure the key mechanical properties of lead free solders. However, large discrepancies have been found in the published data from various groups. There are several reasons for these discrepancies. Firstly, the differences in specimen preparation methods among the researchers cause different microstructures in the specimens that directly affect the experimental results significantly. Secondly, the testing methods and the test conditions may also be different which will again affect the results. Thirdly, mechanical properties obtained from the bulk solders might be different from the measured properties of solder joints. Finally, the lack of standardization in the data acquisition and processing of mechanical properties makes it difficult to obtain good laboratory-to-laboratory comparisons.

Apart from the above mentioned reasons for the discrepancies in solder material properties, another critical factor is aging effects. Aging is mostly neglected in the majority of prior studies, which will further exacerbate these problems. It has been

observed from recent studies that isothermal aging leads to large reductions (up to 50%) in several key material properties for lead free solders including stiffness (modulus), yield stress, ultimate strength, and strain to failure [43]. Even more dramatic evolution has been observed in the creep response of aged lead free solders, where up to 100X increases were found in the steady state (secondary) creep strain rate (creep compliance) of SAC solders that were simply aged at room temperature [44, 45]. For elevated temperature aging at 125 C [46], the creep strain rate was observed to change even more dramatically (up to 10,000X increase for SAC105).

In real applications, solder joints are continuously exposed to aging/thermal cycling during service. It has been well documented that the microstructure, mechanical response, and failure behavior of solder materials are constantly evolving under such circumstances [47-82]. It has also been demonstrated that aging effects are universally detrimental to reliability and cause reductions in stiffness, yield stress, ultimate strength, and strain to failure, as well as highly accelerated creep. Solder joints with highly degraded microstructure and material properties are so vulnerable that the service life of the package is often severely shortened.

The components of electronic packages undergo complex stress-strain conditions during the assembly process as well as when subjected to thermal or power cycling. This happens due to the CTE mismatch of different parts of the components so for a reliable product design, it is very important to have well-established and reliable constitutive models for lead free solder alloys to perform accurate solder joint stress-strain analysis or creep analysis. Among all the widely used constitutive models, however, none of them take aging effects into account. In addition, current finite element prediction methods for

solder joint reliability do not take into account aging effects which are very critical for lead free solders. Thus, it is necessary to study constitutive models for solders that include aging effects and to also incorporate the aging included constitutive models in FEA analysis for the better predictions of solder joint reliability.

2.2 Aging Effects on Tensile Properties

Studies on the effects of aging on solder material properties are primarily divided into two groups, which are aging effects on bulk solders and aging effects on solder joints. These are described in subsequent sub-sections.

2.2.1 Aging Effects on Bulk Solders

Evolution of mechanical properties with aging in both Sn-Pb and lead free solders has been reported in recent years. Researchers have done numerous studies on the effects of aging on bulk solder properties as well as some studies on solder joints in actual components. Most studies show aging has significant effects on the mechanical properties of solder materials. In 1956, Medvedev [47] reported a 30% loss of tensile strength for bulk Sn-Pb solder after 450 days of room temperature (RT) aging, and a 23% loss in tensile strength for solder joints under a similar exposure. Room temperature aging effects on solder alloys has been presented by Lampe [48]. He showed that after 30 days of room temperature aging, the shear strength and the hardness of Sn-Pb and Sn-Pb-Sb solders reduced by approximately 20%. Miyazawa [74] reported reduction of hardness and microstructural coarsening for Sn-Pb solders aged at 25 and 100 ^{o}C for 1000 hours.

Xiao, et al. [63] investigated the stress-strain behavior of SAC396 solder alloy which were subjected to aging at 25 and 180 ^{o}C for various amount of time. They have shown that the strength reduces by 25% for aging at room temperature for 35 days and a

33% reduction for aging at 180 C for 9 days. Ding, et al. [62] investigated the influence of aging on fracture behavior of Sn-Ag solder in tensile tests. They have shown that the solder samples tensile strength reduce very quickly for isothermal aging at 180 ^{o}C for 120 hours. Ma, et al. [45] studied the evolution of Young's modulus, yield strength, and ultimate tensile strength of SAC305 and SAC405 solder alloys under various aging conditions. A linear-exponential model was developed to describe the material property evolution. They have shown that the material properties decreased dramatically in the first 20 days for both room temperature aging as well as elevated temperature aging. After 20 days of aging, the properties change slowly and linearly and it continues for longer aging time.

Zhang, et al. [46] also studied the aging effects on tensile properties of SACN05 (N = 1%, 2%, 3% and 4% silver) series solders for different amount of aging at temperatures 25-125 ^{o}C. They have demonstrated that the mechanical properties degraded more dramatically when the aging temperature was increased. The data also shows that the degradation becomes linear with longer aging time. Cai, et al. [59] have also shown that the aging effects are significant for lead free solders (SAC105, SAC205, SAC305 and SAC405) for room temperature aging as well as elevated temperature aging. They have also shown that the aging effects can be reduced by using certain dopants to (e.g. Bi, In, Ni, La, Mg, Mn, Ce, Co, Ti, Zn, etc.) SAC solder alloys to enhance the reliability of lead free solders. Finally, Mustafa, et al. [70] have demonstrated that the hysteresis loop area in cyclic (tension/compression) loading of various SAC solder alloys changes significantly with aging. For strain controlled tests, the hysteresis loop area deceases and for the stress controlled tests, the loop area increases with aging time.

2.2.2 Aging Effects on Solders Joints

Isothermal aging effects have also been reported to lower the strength and to reduce reliability of solder joints. The mechanical response of solder joints to external loading can be different from the bulk solders due to fine microstructure, grain orientation (single grain/ multigrain), and the presence of intermetallic compounds at joint boundaries.

Coyle, et al. [83] reported 20% shearing strength reduction of BGA solder joints after 240 hours of aging at room temperature. A 10% shearing strength reduction has been reported by Lee, et al. [84] for the BGA packages just after 3 days room temperature aging. Chilton, et al. [85] reported a 15% fatigue strength reduction of Sn-Pb solder joints of a SMD test package which were aged for 60 days at room temperature. Li, et al. [86] studied the elevated temperature aging effects on flip-chip packages with SAC solders. They have shown that the shear strength of solder bumps subjected to aging at 80 ^{o}C decreased gradually with aging. Also for the aging temperatures 150 and 175 ^{o}C, the degradation of shear strength of the bumps were much faster. They also reported that the fracture of the solder bumps occurred at the bulk solder. Koo, et al. [87] found that 63Sn-37Pb solder joint strength on electroplated Ni/Au BGA substrate was significantly affected by aging at 170 °C for up to 21 days, while the deterioration of shear properties of Sn-3.5Ag was much smaller. Darveaux [56] indicated that after 24 hours of aging at 125 °C, all alloys showed a 10% to 30% reduction in solder joint strength. All of the solder joints failed within the bulk solder and exhibited high ductility. In addition, the ductility of all of the Pb-free solder joints decreased with increased aging [63]. Oliver et al. [88] reported that the joint strength of Sn-3.5Ag and SAC325 solder on both Ni/Au

and Sn/Pb pad metallizations were unchanged after aging at room temperature as well as elevated temperature for 1000 hours. However they found reduction in shear strength of solder joint in Sn-Pb solders.

Pang, et al. [89] studied the aging effects on the mechanical properties and fatigue life of Sn-Pb solder joint specimens that were subjected to thermal cycling conditions from -40 to 125 ^{o}C. They have shown that the shear strength reduces significantly for specimens that were subjected to 1000 thermal cycles. They have also shown that the fatigue life of the specimens dropped by 6 times compared to non-cycled specimens. Zhou, et al. compared the joint strengths of SAC387 on both Cu and Ag substrates at an aging temperature of 170 °C, and concluded that aging had little effect on the SAC/Ag interface, but dramatically softened the SAC/Cu joint. The softening difference was said to be due to lower residual stresses at the SAC/Ag joint interface. Chen, et al. [72] studied the effects of aging on the solder bump shear strength for both Sn-Pb and Sn-3.5Ag solders. They reported that shear strength for both solder materials decreases after aging at 150 ^{o}C for 1500 hours, 8.9% for Sn-Pb solder bumps and 5.3% for Sn-3.5Ag. Kim, et al. [65] also reported similar results in which they reported an average 5% decrease in joint strength in stud bump samples for aging at 150 ^{o}C for 300 hours.

The degradations of the stiffness, strength, and creep compliance with aging are expected to be universally detrimental to reliability of solder joints in lead free assemblies. This has been demonstrated explicitly in the recent investigation of Lee and coworkers [84], where aging has been shown to degrade the Thermal Cycling Reliability (TCR) of lead free Plastic Ball Grid Array (PBGA) assemblies subjected to Accelerated Life Testing (ALT). They have shown dramatic degradation in fatigue life of BGA

components with SAC 305 solders, which were subjected to thermal cycling from 0 to 100 ^{o}C with prior aging at either 100 or 150 ^{o}C. The amount of life degradation was found to be dependent on the surface finish of the PCB substrates, with 44% degradation observed for ENIG surface finish and 20% degradation observed for OSP surface finish under the most severe aging conditions (1000 hours at 150 C) prior to thermal cycling accelerated life testing.

In a similar study, Lee, et al. [90] showed that the lifetime of wafer-level chip scale packages with SAC305 solder interconnects was reduced by 29% for 500 hours of aging at 150 C. Zhang, et al. [80] have investigated the correlation between the effects of isothermal aging on the reliability of PBGA components. They have shown that for 6 months aging at 125 C that the reliability of SAC105 components dropped by 53%. Smetana, et al. [91] have performed an extensive study on the effects of prior isothermal preconditioning (aging) on the thermal cycling lifetime for a variety of components. Similar to the investigations discussed above, it was observed that prior aging reduced the thermal cycling characteristic life of SAC BGA assemblies subjected to 0 to 100 C cycling. It was also found that changes occurred in the Weibull slope, suggesting other failure modes were created by aging. They also found that prior aging increased the thermal cycling reliability of certain components (e.g. 2512 chip resistors and certain QFNs). Similar results of improved reliability with aging were found for components subjected to a smaller thermal cycling range of 20 to 80 C. This led them to conclude that aging does not universally reduce solder joint fatigue life.

The effects of aging on the degradation of the thermal cycling reliability of lead free BGA assemblies have been studied recently by Zhang, et al. [80]. In their studies,

PBGA daisy chain test assemblies were subjected to up to 2 years of aging (25, 55, 85, and 125 C), followed by thermal cycling from -40 to 125 C or -40 to 85 C to failure. They have shown that for all component sizes and lead free solder alloys, the solder joint thermal cycling reliabilities of the BGA components were severely reduced by prior aging. For up to 12 months prior aging for the components with Im-Ag PCB surface finish and thermal cycling from -40 to 125 ^{o}C, they have observed clear degradation in life for aged components relative to non-aged components and the amount of degradation was exacerbated with higher aging temperatures. Using the 63.2% Weibull characteristic life (η) as a failure metric, the reliability was observed to decrease by 37% (6 months aging) and 53% (12 months aging) for the 19 mm BGA components subjected to aging at 125 C prior to thermal cycling.

Gradual aging also occurs during thermal cycling tests due to the high temperature dwells at the top of each thermal cycle. Several recent studies [102-106] have demonstrated that there is a strong dwell time effect on thermal cycling reliability for lead free electronics; with longer dwell times leading to reductions in the thermal cycling life.

2.3 Aging Effects on Creep Properties

It has been found in the literature that aging at room temperature as well as elevated temperatures have significant effects on creep deformation of lead free solder alloys. Darveaux, et al. [56] reported a faster creep rate for aged solder specimens than non-aged specimens. For both SAC305 and SAC405 solders and for aging at 125 C for 1 day, they found 20 times increase in the creep rate for aged specimens. Xiao, et al. [63] found that SAC396 showed much lower absolute creep rates compared with eutectic Sn-

Pb and ascribed this increase in creep resistance to the finely dispersed intermetallic compound (IMC) precipitates in the Sn matrix. Wiese, et al. [57, 92] investigated the creep behavior of SAC 387 solder with short (1 day at 125 C) and long (49 days at 125 C) thermal storage times. They found that the creep rate of solder increase significantly for short time aging at 125 C but relatively smaller changes occurred for longer aging times.

Ma, et al. [44] studied the evolution of secondary creep rate with aging for SAC305 and SAC405 solders. They showed that the secondary creep rates for SAC solders increase with aging at either room temperature or elevated temperature. Also, for both SAC solders exposed to elevated temperature aging, the effects were much higher than those for room temperature aging. A more detailed investigation was conducted by Zhang, et al. [46] on aging effects on the creep behavior of lead free solders. They reported that for 6 months aging at 125 ^{o}C, the secondary or steady state creep rate of SAC105 solder increased by about 10000 times. Also, for other aging temperatures (25 to 125 C), they found that the both the primary and secondary creep rates increase with 6 months aging. Finally, Cai, et al. [59] demonstrated that by using certain types of dopants in SAC solders, the aging effects on steady state creep rate can be reduced. They showed that for no aging the creep rates of doped solders were higher than SAC105 and SAC205 due to lower silver contents of the doped solders compared to SAC105. However, with 6 months aging at temperatures 25 to 125 C, the secondary creep rates of the doped solders were smaller than the creep rates of SAC105.

2.4 Constitutive Modeling for Solder Materials

In microelectronics packaging, complex stresses and strains are usually generated in the components due to the CTE mismatch of different materials. Solder interconnects are usually subjected to deformations that lead to three-dimensional stress and strain states. The solder material constitutive law plays an important role in the development of thermo-mechanical models for microelectronic assemblies. Under thermo-mechanical loading, the solder material undergoes elastic and in-elastic deformations. Elastic deformations are recoverable, while inelastic deformations consist of time-independent plastic deformations and time-dependent creep deformations, which are not recoverable. Solder constitutive behavior can be represented by a combination of elastic, plastic (isotropic or kinetic hardening), and viscoplastic/creep models.

2.4.1 Constitutive Modeling for Stress-Strain Tests

The linear elastic region in a uniaxial stress-strain curve can be modeled by Hooke's law where stress and strain are related by an elastic modulus (E). The plastic strain hardening region can be modeled by a time-independent non-linear stress-strain relationship based on either isotropic or kinematic strain hardening. Isotropic hardening assumes that the origin of the von Mises yield surface remains stationary in the stress space and the size of its yield surface expands resulting from strain hardening. In kinematic hardening, the von Mises yield surface does not change in size, but the origin of the yield surface is allowed to translate in the stress space to model strain hardening

effects of increasing plastic flow stress. For solder materials, the tensile stress and strain curves are dependent on the test temperature and strain rate. The elastic modulus (E), yield stress (YS) and the tensile strength (UTS) properties vary with temperature and strain rate.

For a typical thermal cycling temperature range from -40 to 125 ^{o}C, these mechanical properties reduce with the increase in temperature. The solder material has a homologous temperature from 0.5 to 0.8 for this temperature range. Also, the creep deformation in a solder material is highly dependent on the stress and temperature state. Thus, a time-dependent elastic-plastic-creep constitutive model, or viscoplastic constitutive model, is needed to facilitate finite element modeling for simulation of solder joint reliability during thermal cycling tests. High temperatures induce transitions in macroscopic fracture, and these transitions parallel the changes in the strength and ductility of materials [31]. Materials lose strength at higher temperatures. Hertzberg stated that the material strength increases with the testing strain rate, following a form similar to Holloman's Equation [31], where stress is related to strain rate through some strain hardening exponent.

Solder alloys possess very high homologous temperatures. The properties of solder alloys are strongly dependent on both the temperature and strain rate. Jones, et al. [93, 94] have observed an approximately linear relationship between the strength and temperature. Pang, Shi and co-workers [95] have observed similar experimental results, with a near linear relationship with temperature and a power law relation with the strain rate. Several other studies have also observed similar material behavior for both Sn-Pb eutectic and lead-free solder alloys [96-99].

The Ramberg-Osgood model describes the elastic-plastic behavior of materials, and can be used to describe to describe the stress-strain curve of solder materials [100]. In prior work, the Ramberg-Osgood model hardening exponent n and the stress coefficient σ_o were modified to be temperature and strain rate dependent. The temperature and strain-rate dependent modified Ramberg-Osgood model was also applied by Pang, et al. [100].

2.4.2 Constitutive Modeling for Creep

In general, the creep behavior of materials consists of three different stages: primary creep, secondary creep, and tertiary creep. In the primary creep regime, the material undergoes strain hardening, resulting in a decreasing strain rate with time. In the secondary stage, also known as steady-state creep regime, the creep strain rate is essentially constant, showing a very slow decrease. In tertiary stage, strain rate increases with time and ultimately results in failure of the material. Solder alloys are often subjected to steady-state creep regime under typical thermo-mechanical loading conditions. Constitutive modeling of creep deformation is needed to predict the end-of-life of electronic components by using finite element analysis. A constitutive creep model is established by conducting creep tests at different temperatures and stress levels. The materials constants are important in determining the accuracy of end-of–life predictions for solder joints using finite element analysis. Large discrepancies between the creep model and experimental data would degrade the accuracy of these predictions.

The minimum creep rate may be linked with the applied stress, σ, by a series of equations according to the dominant creep mode. There are mainly three types of creep modes, namely, power law creep, exponential creep, and combination creep. Creep is

highly sensitive to both applied stress level and to test temperature. As a thermally activated process, the creep rates increase exponentially with temperature. The effect of stress is dependent upon the controlling creep mechanism. The two widely used creep models are the Dorn power law model [101], and the Garofalo hyperbolic sine model [34]. In logarithmic coordinates, the Dorn power law model yields a linear relationship between the creep strain rate and applied stress for a specified temperature. Nonlinear experimental curves for creep, however, have been found over the entire stress range. The high stress regime exhibits the largest stress exponent n, and the low stress regime exhibits the smallest n value for any given temperature. This phenomenon is referred to as "power law break down" and indicates that the Dorn model is not suitable for fitting data obtained over large stress ranges.

The Garofalo model was established for matching creep behavior at both low and high stresses. At low and medium stresses, the creep strain rate depends on stress to the power n. At high stresses, the creep strain rate is an exponential function of stress. The model is able to predict the creep deformation over intermediate temperature regimes for the entire stress range, but it underestimates the creep deformation at both low (-40 °C) and high (125 and 150 °C) temperatures.

Ma and Suhling [43] have evaluated the creep parameters in the two models for various Pb-containing and Pb-free solder alloys and found large discrepancies in the creep data for solder alloys of the same chemical composition. There are several reasons that could explain the differences, including the specimen design, variations in testing method and test conditions used by different researchers, and storage time and temperature before the creep test. Moreover, it is important to recognize that the creep

behavior of bulk solder significantly differs from solder in a joint due to the effects of microstructure evolution, intermetallic compound formation, and constraint due to different methods of assembly. Since creep modeling is often to be incorporated in finite element analysis to predict the end-of-life of electronic package, the discrepancies in material constants will directly affect the accuracy of prediction.

A third widely used creep constitutive model was proposed by Weise, et al [92], and is often referred to as the double power law. They identified two mechanisms for steady state creep deformation for the bulk and PCB samples. They attributed them to climb controlled (low stress process) and combined gliding/climbing (high stress process) behavior and represented steady state creep behavior using two power law terms. In electronic packages, thermal mismatch induced stresses can result in extensive plastic deformation at solder joints, which is responsible for the low cycle thermal fatigue failure of solder materials. An expression for the strain was proposed by Yang, et al. [102] where total strain was divided into elastic, plastic, and creep strains.

Apart from these models, several other creep constitutive models have been proposed by researchers. Shi, et al. [103] established a unified dislocation-controlled creep constitutive model that described the creep deformation of solder alloy over a wide temperature range (-40 to 150 °C) and explained the temperature dependencies of the stress exponent n and activation energy Q. For creep strain rates at very low stress levels, they further developed a unified diffusion-controlled creep constitutive model to describe low temperature Coble creep and high temperature Nabarro-Herring creep. Clech [104] established obstacle-controlled creep models for both Pb-containing and Pb-free solder alloys. Creep deformation is impeded by discrete obstacles (phases, precipitates, grain

boundaries, and other defects) distributed throughout the Sn-matrix in Sn-based solders. By taking these impeding elements into consideration, the rate-dependent obstacle-controlled creep models are able to resolve the anomalies observed in the classical analysis of creep data including stress and/or temperature dependences of activation energies and stress exponents in the Power Law or Hyperbolic Sine models.

2.4.3 Anand Viscoplastic Constitutive Model

Since solder alloys are used at high homologous temperatures, creep deformations are significant. The Garofalo Hyperbolic Sine model and Dorn Power-Law model focus on steady-state creep data, which only involves a portion of the total creep deformation. Constitutive models for solders are principally divided into two groups. One is rate-independent plasticity (stress-strain response) and the other is rate-dependent steady state creep (creep deformation developed as a function of strain rate or time). However, it is very difficult to separate the plastic strain from the creep strain based on the mechanical tests of solder alloys. Therefore, a unified plastic/creep constitutive relation is highly desirable. The Anand model was initially proposed by Anand [105, 106], and is considered to be a unified model that does not require explicit yield conditions or loading/unloading criteria. The instantaneous response of the material is dependent on its current state. The Anand model also employs a single scalar internal variable "*s*" to represent the isotropic resistance to inelastic flow of the material. This scalar variable is believed to be related to the dynamic process of strain hardening and dynamic recovery. The Anand model is implemented in both the ANSYS and ABAQUS commercial finite element packages.

There are a total of nine parameters in the Anand model: A, Q, m, n, a, h_0, ξ , $\hat{s}$, and s_0. One method to obtain the values of these parameters for a specific material is to perform a series of stress-strain tests over a wide range of temperatures and strain rates [122-123]. Using the measured UTS and the stress-strain data for each temperature and strain rate and using the non-linear least squared fit options, the values of the 9 Anand parameters can be determined. However, there are big discrepancies among the literature values of the Anand parameters for lead free solders [107]. The Anand model will be discussed in more detail in Chapter 3.

A large number of researchers have used the Anand model for electronic packaging applications. For example, Che, et al. [108] have demonstrated four different constitutive models for the Sn-3.8Ag-0.7Cu solder alloy including elastic-plastic, elastic-creep, elastic plastic with creep, and the viscoplastic Anand model. They showed that the Anand model was consistent with fatigue life predictions for lead free solders. Pei, et al. [109] performed monotonic tensile tests at a wide range of different temperatures and strain rates with two types of lead free solders (Sn3.5Ag and Sn3.8Ag0.7Cu) to get the material parameters of the Anand constitutive model. They showed that using temperature dependent values of the nine constants in the model gave better matching with the experimental results. Mysore and coworkers [110] conducted double lap shear tests on Sn3.0Ag0.5Cu solder alloy and used the results to fit the materials constants in the Anand model. They reported there were significant differences in results obtained with bulk samples and those found with solder joint specimens. A modified Anand Constitutive model was proposed by Chen, et al. [111] that involved using temperature dependent values of one of the model parameters (h_o). Amagai, et al. [112] have

established values for the Anand model constants for Sn3.5Ag0.75Cu and SAC105 (Snl.0Ag0.5Cu) lead free solders. In their work, one of the nine required constants was ignored (s_o), and only 8 were specified. Kim, et al. [113] presented values for all 9 constants for SAC105 lead free solder. A modified Anand model was presented by Bai, et al. [114] for SAC305 (Sn3.0Ag0.5Cu) and Sn3.5Ag0.7Cu lead free solders. Their approach employed temperature and strain rate dependent values of for one of the model parameters (h_o).

The Anand model has also been widely used in the finite element simulation of solder interconnection in electronic components [115-118]. There are various sets of Anand model parameters available in literature for a specific solder alloy composition. Unfortunately the predictions (stress-strain or creep) using the different sets of constants differ significantly, which is very alarming. For example, Figure 2.1 shows the predicted stress-strain curves for SAC305 solder using various sets of Anand constants From the literature. The solid black curve is the predicted stress-strain curve using the constants found in this study (see Chapter 4). The predicted UTS, elastic modulus, and yield stress from all of these sets of parameters at the same temperature and strain rate were significantly different. Thus, a reliable method of determining the best set of Anand parameters is necessary to accurately predict the mechanical behavior of the solder material using this constitutive model.

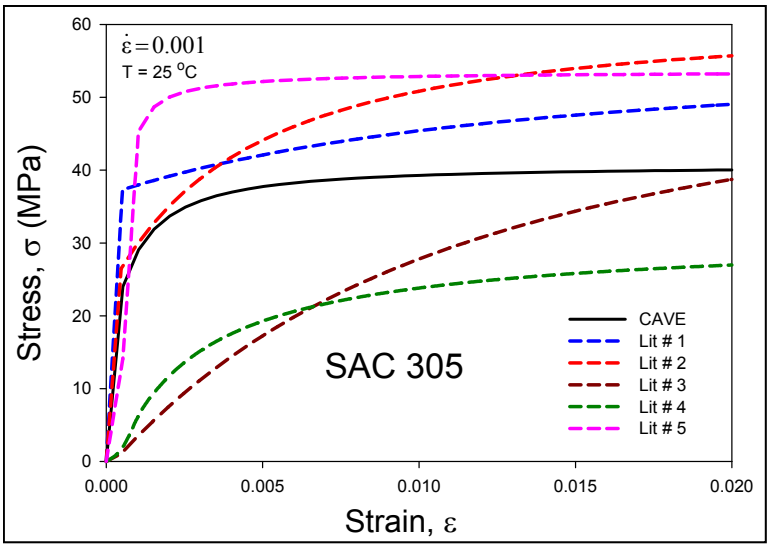

Figure 2.1 Differences in Stress-Strain Curve Predictions Using Several Anand Parameters for SAC305 in Literature

2.5 Modeling of Solder Joint Reliability

In order to make faster, cheaper, and more reliable electronic products, it is very important for the packages to be evaluated at early design stages by simulation tools. Solder joint reliability models based on actual test data, accurate constitutive modeling, dominant damage mechanisms, and appropriate simulation, are needed to perform this task. Electronic packages often undergo thermal and/or power cycling conditions throughout their service life. CTE mismatch induced stresses/strains are the root cause of most solder joint failures. Solder joints fail mostly due to the fatigue caused by the thermal or power cycling operations. The procedure of reliability modeling can be divided in two major steps:

(1) Finite element modeling to predict stresses, strains, and deformations of the solder joints during thermal cycling. The required output parameters (e.g. plastic strain or energy density per cycle) are extracted by post-processing the finite element analysis results.

(2) Application of a solder life prediction model to the output parameters of the finite element analysis to calculate the number of cycles until failure of the solder joint. The material constants in the life prediction model for the solder need to be evaluated from the experimental crack growth data for components having similar geometric form factors.

Syed [119] has used double power law and hyperbolic sine creep equations to predict the reliability of solder joints in BGA assemblies. He showed that failure criteria based on accumulated strains and dissipated energy density per cycle can provide good predictions of the measured mean life of solder joints. In addition, it was demonstrated that the energy density approach better captures low temperatures and high stress effects than the accumulated creep strain approach. Schubert, et al. [120] have presented thermo-mechanical analyses that predicted the life of solder joints in flip chip on board (FCOB) and PBGA assemblies for both SnPb and SnAgCu solders. They have also used double power law and hyperbolic sine creep constitutive equations, as well as accumulated creep strain and strain energy density methods for the fatigue life models. Both fatigue models were found to fit their experimental failure data reasonably well. Also, SAC solders were shown to perform poorer for stiffer components and higher strain levels.

An energy-partitioning approach has been used by Zhang, et al. [121] for SAC396 solder alloy. The model constants for creep and plasticity were obtained from correlating partitioned creep and plastic work to mechanical cycling testing results. In addition, lead free SAC solders were found to have better low-stress creep resistance than SnAg solders. Zahn [122] used a volume average energy density method to predict the life of 63Sn37Pb

and SAC405 solder joints. He also explored model simplifications based on symmetry, and found that one-eighth models are the smallest that can yield correct results, and that diagonal slice symmetry models yield different accumulated energy per cycle values than the true three-dimensional case.

Lee and coworkers [123] have classified solder fatigue models into five categories: stress based, plastic strain based, creep strain based, energy based, and damage based. Other methods have been classified as empirical models. They have shown a general procedure to choose an appropriate fatigue model based on the package conditions and limited finite element analysis times. They identified 14 models in the literature, which were developed based upon various assumptions, including the manner in which the physical and metallurgical aspects of fatigue are taken into account. The characteristics of the 14 identified fatigue models are presented in Table 2.1.

Ridout, et al [124] have classified the methods of calculating solder cycles to failure into three categories, analytical methods, combined constitutive law and fatigue methods, and damage mechanics methods (Figure 2.2). They have reported that the constitutive law and fatigue law class of methods (encompassing FEA and other alternatives) are very popular, providing more accurate predictions with fewer restrictions than analytical methods. However, they have with increased set up time and computational cost. The damage mechanics based methods require considerably more effort both in implementation and computational cost and their predictive capability is unproven.

Fatigue Model	Model Class	Parameters	Coverage	Applicability
Coffin-Manson	Plastic strain	Plastic strain	Low cycle fatigue	All
Total Strain	Plastic + elastic strain	Strain range	High and low cycle fatigue	All
Solomon	Plastic shear strain	Plastic shear strain	Low cycle fatigue	All
Engelmaier	Total shear strain	Total shear strain	Low cycle fatigue	Leaded & leadless, TSOP
Miner	Superposition (plastic and creep)	Plastic failure & creep failure	Plastic shear and matrix creep	PQFP, FCOB
Knecht & Fox	Matrix creep	Matrix creep shear strain	Matrix creep only	All
Syed	Accumulation of creep strain energy	gbs energy and mc energy	Implies all coverage	PBGA, SMD, NSMD
Dasgupta	Total strain energy	Energy	Joint geometry accounted for	LLCC, TSOP
Liang	Stress/strain energy density based	Energy	Constants from isothermal low cycle fatigue tests	BGA and leadless joints
Heinrich	Energy density based	Energy	Hysteresis curve	BGA
Darveaux	Energy density based	Damage + energy	Hysteresis curve	PBGA, leadless
Pan	Strain energy density	Strain energy density and plastic energy density	Hysteresis curve	LCCC
Stolkarts	Damage accumulation	Damage	Hysteresis curve & damage evolution	All
Norris & Landzberg	Temperature and frequency	Temperature frequency	Test condition vs. use conditions	All

Table 2.1 Summary of Solder Joint Fatigue Models [123]

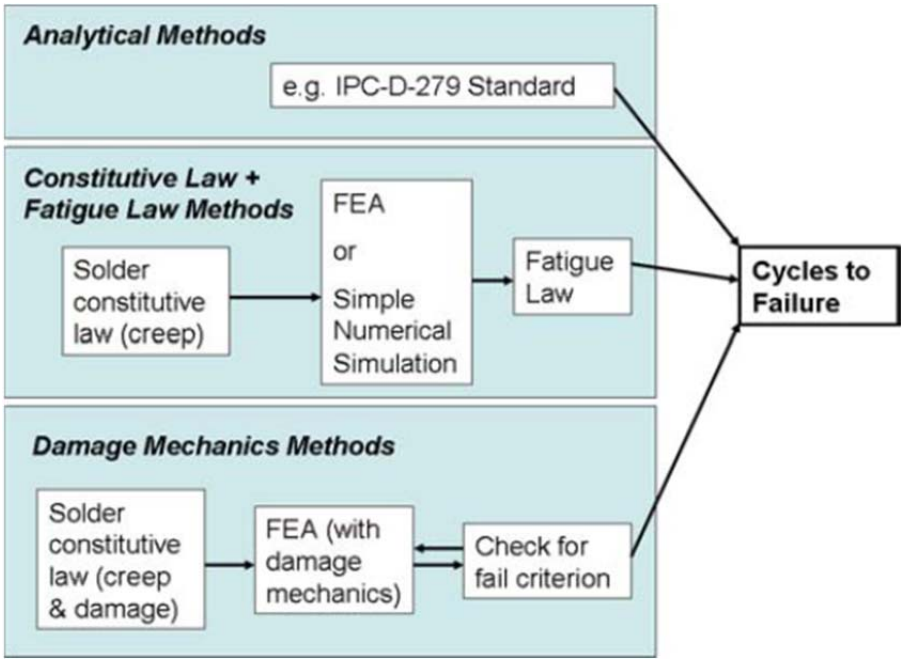

Figure 2.2 Modeling Methods to Calculate the Cycles to Failure in Thermo-mechanical Cycling [124]

A damage mechanics based fatigue life model has been presented by Tang and Basaran [125]. They have coupled an internal damage variable with a unified viscoplastic model to characterize the response of solder alloys. Gustafsson, et al. [126] have used the volume average energy method to predict the life of BGA solder joints and have shown that a linear global model with a nonlinear submodel drastically overestimates the life in comparison with the nonlinear global models.

Pang, et al. [127] have predicted flip chip solder joint reliability by using dwell creep (creep during dwell times) and full creep (creep during the whole analysis) methods. They have shown that the dwell creep method predicts much longer fatigue life of the solder joints than the full creep method. Shnawah, et al. [128] have studied the thermal cycling and drop impact reliability of SAC solder joints. A significant thermal cycling performance improvement was found for assemblies made from SAC305/SAC405 solders relative to those assembled with lower silver content SAC105 solder. Liu, et al.

[129] have used finite element analysis to examine pad design and found that the fatigue lifetime of BGA solder joints with dent pad OSP surface finish is 25% lower than that for flat pad Ni/Au surface finish. Thermal cycling reliability of a BGA SiP has been investigated by Yu, et al. [130]. They have found that the failure position changed relative to conventional BGA packages. Vasudevan and Fan [131] have incorporated acceleration terms into conventional fatigue models to examine the effects of thermal cycling range and frequency.

Darveaux [132] has presented energy dissipation based models for crack initiation and crack growth rate in solder joints. These types of models have been subsequently used by many researchers for life prediction of the SnPb and SAC solders. The four constants in the failure models are determined by curve fitting using the experimental failure data, where the energy dissipation per cycle is found from FEA simulations.

2.6 Summary and Discussion

Isothermal aging has been found detrimental to the mechanical properties and the reliability of lead free solder materials. The dramatic changes in the material properties, constitutive and failure behavior of bulk solder materials as well as solder joints have been reported in the literature. However, traditional finite element based predictions for solder joint reliability during thermal cycling accelerated life testing are based on solder constitutive equations (e.g. Anand viscoplastic model) and failure models (e.g. energy dissipation per cycle model) that do not evolve with material aging. Thus, there will be significant errors in the calculations with lead free SAC alloys that illustrate dramatic aging phenomena.

Large discrepancies in measured solder mechanical properties from one study to another have been found and widely acknowledged due to the differences in the microstructures of the tested samples. This problem is exacerbated by the aging issue, as it is clear that the microstructure and material behavior of the samples change rapidly even at room temperature. For elevated temperature aging, this effect has been found to cause more dramatic change in the microstructure, material behavior and the reliability of lead free solder. Thus, the effects of aging on solder behavior must be better understood so that more accurate viscoplastic constitutive equations can be developed for SnPb and SAC solders. Without such well-defined relationship, it is doubtful that finite element reliability predictions can ever reach their full potential.

In the current study, effects of aging on the lead free solder material have been investigated by performing stress-strain tests for a wide range of temperature, strain rate and aging conditions. Also, creep tests for wide range of temperature and stress level have been performed for specimens that were aged for different duration of time. Using the tensile test or creep data for different aging condition, the Anand viscoplastic constitutive model has been modified to include the aging effects. The modified Anand model with aging effects has been implemented in the finite element software ANSYS for accurate prediction of the thermal cycling reliability of lead free solder joints.

The discussion on life prediction or reliability models for lead free solders includes the model parameters that do not evolve with material aging. The energy based Darveaux model has four parameters (K_1, K_2, K_3 and K_4) and has been used in this study to calculate the thermal cycling reliability of solder joints. The effects of aging on these four parameters have been determined through the results of experimental investigations

(fatigue tests and reliability tests). Empirical models for these parameters have been developed to include the aging effects, and by combining the finite element results with the reliability model, cycles to failure of the solder joint in a PBGA assembly have been determined for different aging conditions. Finally, good correlations have been found between the predictions of the constitutive and reliability models that include aging effects, and the experimental thermal cycling reliability data.

CHAPTER 3

EXPERIMENTAL CHARACTERIZATION OF AGING EFFECTS ON THE MECHANICAL PROPERTIES OF LEAD FREE SOLDERS

3.1 Introduction

In this chapter, a novel specimen preparation technique is presented. This unique approach is able to fabricate micro-scale uniaxial tensile specimens without further modification and machining. The test specimens are formed in glass tubes with rectangular cross-section by using a vacuum suction system. The specimens are then cooled by either a water quenched cooling profile or a specifically designated reflow profile. For the current work, uniaxial samples with nominal dimensions of 80 (length) × 3 (width) × 0.5 (height) mm were utilized. Uniaxial tensile and creep tests were then carried out by using a micro tension torsion testing system. Several empirical constitutive models were adopted to represent the collected raw data and to extract the desired mechanical properties of the solder materials of interest.

3.2 Uniaxial Test Specimen Preparation Procedure

Solder uniaxial samples have been fabricated by machining of bulk solder material, or by melting of solder paste in a mold. Use of a bulk solder bars is undesirable, because they will have significantly different microstructures than those present in the small solder joints used in microelectronics assembly. In addition, machining can develop internal/residual stresses in the specimen, and heat generated

during turning operations can cause localized microstructural changes on the exterior of the specimens. Reflow of solder paste in a mold causes challenges with flux removal, minimization of voids, microstructure control, and extraction of the sample from the mold. In addition, many of the developed specimens have shapes that significantly deviate from being long slender rods. Thus, undesired non-uniaxial stress states will be produced during loading.

Other investigators have attempted to extract constitutive properties of solders by direct shear or tensile loading, or indenting, of actual solder joints (e.g. flip chip solder bumps or BGA solder balls). While such approaches are attractive because the true solder microstructure is involved, the unavoidable non-uniform stress and strain states in the joint make the extraction of the correct mechanical properties and stress-strain curves from the recorded load-displacement data very challenging. Also it can be difficult to separate the various contributions to the observed behavior from the solder material and other materials in the assembly (bond pads, silicon die, PCB/substrate, etc.).

In an attempt to avoid many of the specimen preparation pitfalls identified above, a novel specimen preparation procedure was developed. Compared with other specimen fabrication approaches, this unique technique is able to make micro-scale uniaxial tensile specimens with no requirement of further machining/cutting. The solder specimens in this study were formed in high precision rectangular cross-section glass tubes using a vacuum suction process [44-46, 59, 70]. The tubes were then cooled by water quenching and sent through a SMT reflow to re-melt the solder in the tubes and subject them to any desired temperature profile (i.e. same as actual solder joints). The solder is first melted in a quartz crucible using a pair of circular heating elements (Figure 3.1). A thermocouple

attached on the crucible and a temperature control module is used to direct the melting process. One end of the glass tube is inserted into the molten solder, and suction is applied to the other end via a rubber tube connected to the house vacuum system. The suction forces are controlled through a regulator on the vacuum line so that only a desired amount of solder is drawn into the tube. The specimens are then cooled to room temperature using a user-selected cooling profile.

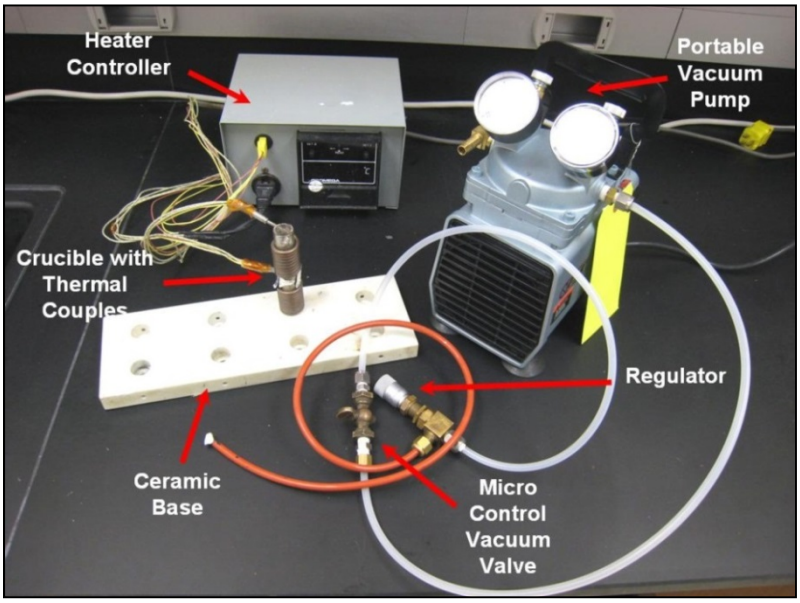

Figure 3.1 Specimen Preparation Hardware

In this work, the glass tube solder samples were first water quenched. They were then sent through a reflow oven (9 zone Heller 1800EXL) to re-melt the solder in the tube and subject it to the desired temperature profile. A typical temperature versus time plot for water quenching is shown in Figure 3.2(a). In the reflow oven, thermo-couples were attached to the glass tubes and monitored continuously using a radio-frequency KIC temperature profiling system to ensure that the samples are formed using the desired temperature profile (same as actual solder joints). Figure 3.2(b) illustrates the reflow

temperature profile used in this work for lead free solder specimens, and Figure 3.3 shows the reflow oven.

Typical glass tube assemblies filled with solder and final extracted specimens are shown in Figure 3.4. For some cooling rates and solder alloys, the final solidified solder samples can be easily pulled from the tubes due to the differential expansions that occur when cooling the low CTE glass tube and higher CTE solder alloy. Other options for more destructive sample removal involve breaking the glass or chemical etching of the glass. The final test specimen dimensions are governed by the useable length of the tube that can be filled with solder, and the cross-sectional dimensions of the hole running the length of the tube. In the current work, uniaxial samples were formed with nominal dimensions of 80 x 3 x 0.5 mm. A thickness of 0.5 mm was chosen because it matches the height of typical BGA solder balls. The specimens were stored in the aging oven immediately after the reflow process to eliminate possible room temperature aging effects.

The described sample preparation procedure yielded repeatable samples with controlled cooling profile (i.e. microstructure), oxide free surface, and uniform dimensions. By extensively cross-sectioned on several specimens, the microstructure of any given sample is proven to be very consistent throughout the volume of the sample. In addition, the specimen preparation method has been demonstrated to yield repeatable sample microstructures for a given solidification temperature profile. Samples were inspected using a micro-focus x-ray system to detect flaws (e.g. notches and external indentations) and/or internal voids (non-visible). Figure 3.5 illustrates results for good

and poor specimens. With proper experimental techniques, samples with no flaws and voids were generated.

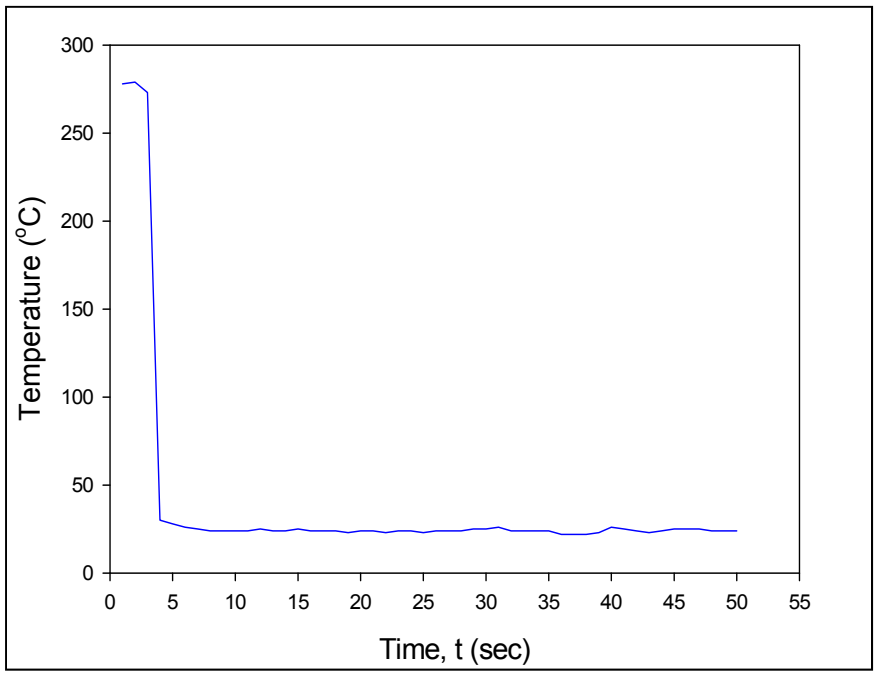

(a) Water Quenching Profile, W.Q.

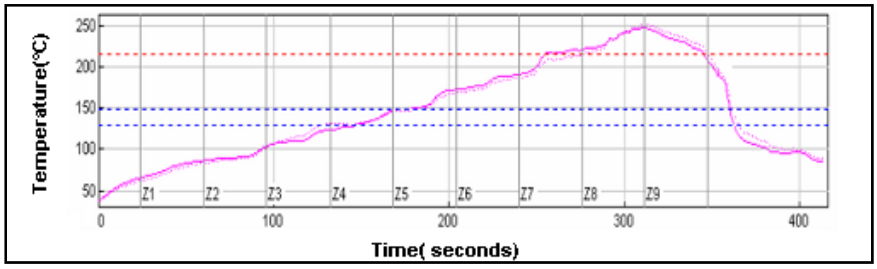

(b) Reflow Profile, R.F.

Figure 3.2 Specimen Cooling/Reflow Profiles

Figure 3.3 Heller 1800EXL Reflow Oven

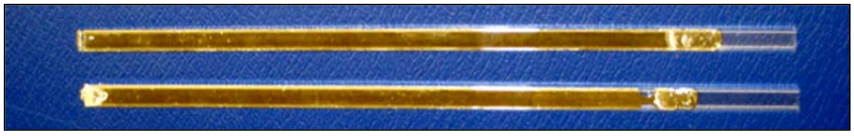

(a) Within Glass Tubes

(b) After Extraction

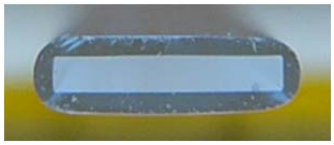

(c) Cross-Section

Figure 3.4 Solder Uniaxial Test Specimens

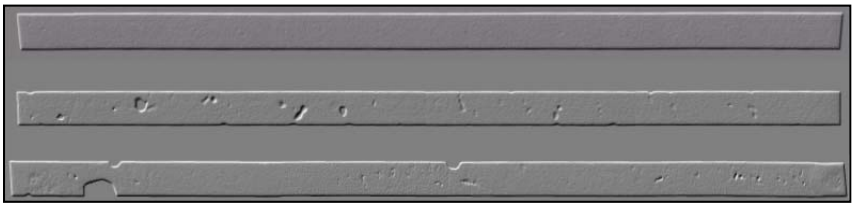

Figure 3.5 X-Ray Inspection of Solder Test Specimens (Good and Bad Samples)

3.3 Mechanical Testing System

A MT-200 tension/torsion thermo-mechanical test system from Wisdom Technology, Inc., as shown in Figure 3.6, has been used to test the samples in this study. The system provides an axial displacement resolution of 0.1 micron and a rotation resolution of 0.001°. Testing can be performed in tension, shear, torsion, bending, and in combinations of these loadings, on small specimens such as thin films, solder joints, gold wire, fibers, etc. Cyclic (fatigue) testing can also be performed at frequencies up to 5 Hz. In addition, a universal 6-axis load cell was utilized to simultaneously monitor three forces and three moments/torques during sample mounting and testing. Environmental chambers added to the system allow samples to be tested over a temperature range of -185 to +300 °C.

During uniaxial testing, forces and displacements were measured. The axial stress and axial strain were calculated from the applied force and measured cross-head displacement using:

$$\sigma = \frac{F}{A} \qquad \varepsilon = \frac{\Delta L}{L} = \frac{\delta}{L} \tag{3.1}$$

where σ is the uniaxial stress, ε is the uniaxial strain, F is the measured uniaxial force, A is the original cross-sectional area, δ is the measured crosshead displacement, and L is the specimen gage length (initial length between the grips). The gage length of the specimens in this study was 60 mm, so that the specimen length to width aspect ratio was 20 to 1 (insuring true uniaxial stress states).

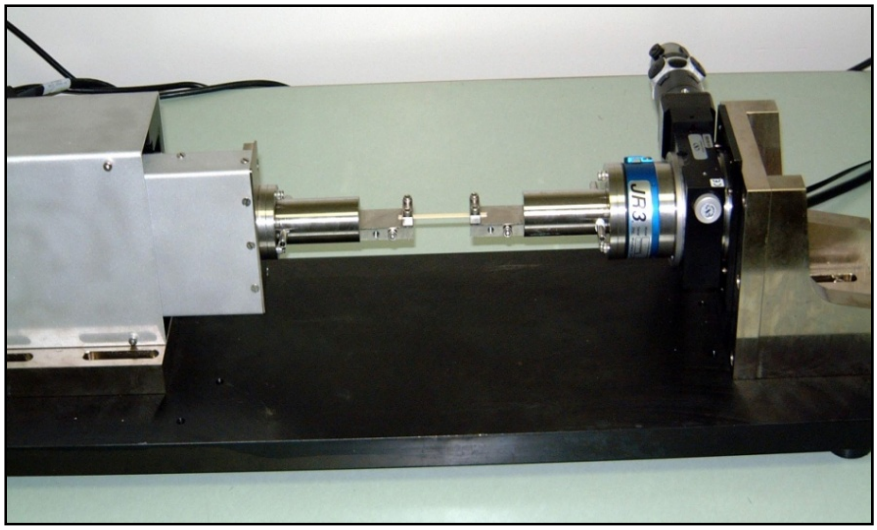

Figure 3.6 MT-200 Testing System with Solder Sample

3.4 Typical Testing Data and Data Processing

A typical recorded tensile stress strain curve for solder with labeled standard material properties is shown in Figure 3.7. The notation "E" is taken to be the effective elastic modulus, which is the initial slope of the stress-strain curve. Since solder is viscoplastic, this effective modulus will be rate dependent, and will approach the true elastic modulus as the testing strain rate approaches infinity. The yield stress σ_Y (YS) is taken to be the standard .2% yield stress (upon unloading, the permanent strain is equal to $\varepsilon = .002$). Finally, the ultimate tensile strength σ_u (UTS) is taken to be the maximum (saturation) stress realized in the stress-strain data. As shown in Figure 3.7a, the solders tested in this work illustrated nearly perfect elastic-plastic behavior (with the exception of a small transition region connecting the elastic and plastic regions). As the strain level becomes extremely high and failure is imminent, extensive localized necking takes place. These visible reductions in cross-sectional area lead to non-uniform stress-states in the specimen and drops in the applied loading near the end of the stress-strain curve.

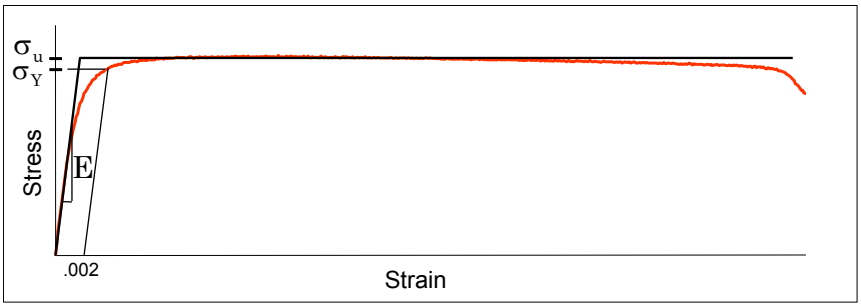

(a) Typical Solder Stress-Strain Curve (Whole Curve)

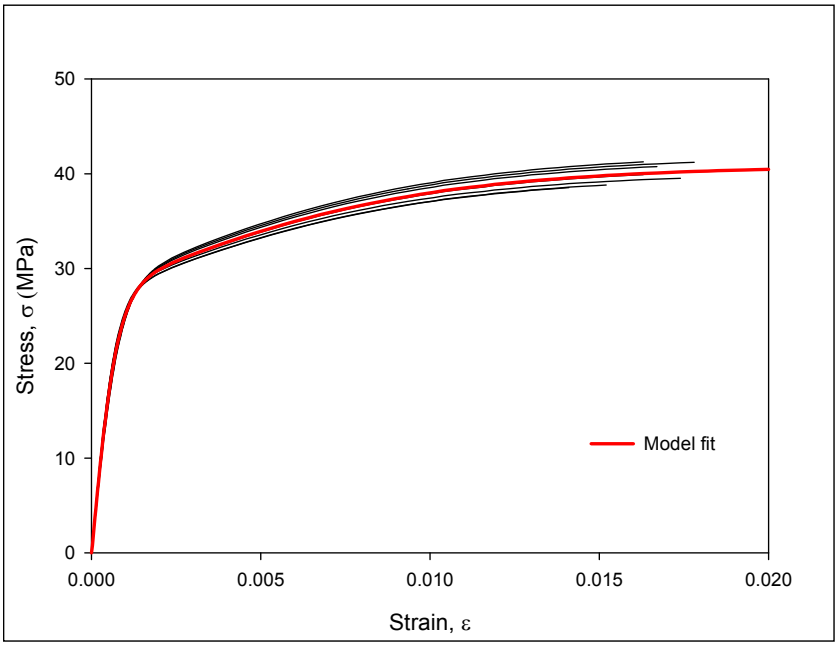

(b) Typical Solder Stress-Strain Curves and Empirical Model

Figure 3.7 Typical Solder Stress-Strain Curve and Material Properties

Creep response under constant uniaxial stress begins with a quick transition to the initial "elastic" strain level, followed by regions of primary, secondary, and tertiary creep. Depending on the applied stress level, the primary creep region can be more extensive for the SAC alloys. The secondary creep region is typically characterized by a very long duration of nearly constant slope. This slope is referred to as the "steady state" secondary creep rate, and it is often used by practicing engineers as one of the key material parameters for solder in finite element simulations used to predict solder joint reliability.

In this work, the measured creep rates were taken to be the minimum slope values in the secondary creep regions of the observed $\dot{\varepsilon}$ versus t responses. The tertiary creep region occurs when rupture is imminent, and typically features an abrupt change to a nearly constant but significantly increased creep rate. Figure 3.8 illustrates a typical solder creep curve (strain vs. time response for a constant applied stress). The stress level applied in a creep test was calculated as:

$$\sigma = \frac{F \times g}{w \times t \times 10^3} \tag{3.2}$$

where σ is the chosen stress level for the creep test in MPa, F is the input holding force in grams, w is the specimen width in mm, t is the specimen thickness in mm, and g is the acceleration of gravity (9.8 N/kg).

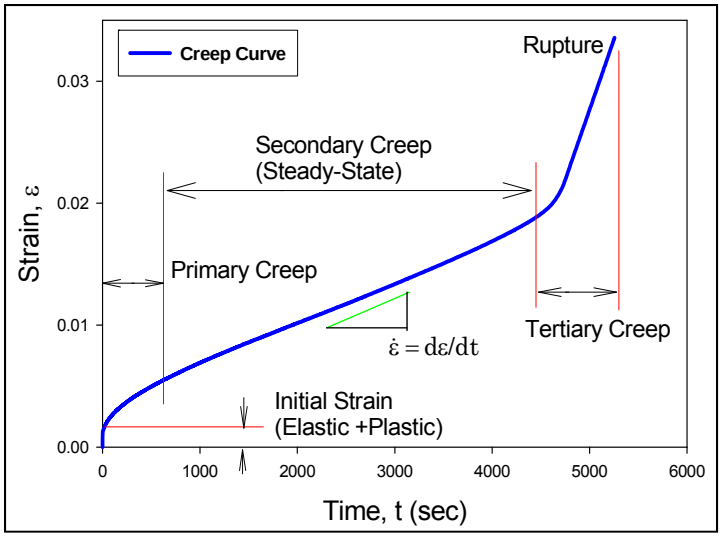

Figure 3.8 Typical Solder Creep Curve and Material Properties

3.4.1 Stress-Strain Data Processing

For the uniaxial stress-strain tests, a total of 10 specimens have been tested at a specific aging/testing condition. From the recorded stress-strain data, a set of averaged material properties were extracted. Variations of the average mechanical properties (effective modulus, yield stress, ultimate strength, creep compliance, etc.) with aging were observed and then modeled as a function of aging time. In this work, a single "average" curve was generated to represent a set of 10 recorded stress-strain curves for a certain testing configuration. Although, several different empirical models can be used to represent the observed stress-strain data for solder, we have chosen to use a four parameter hyperbolic tangent model

$$\sigma = C_1 \tanh(C_2\varepsilon) + C_3 \tanh(C_4\varepsilon) \tag{3.3}$$

where C_1, C_2, C_3, C_4 are material constants to be determined through regression fitting of the model to experimental data. The initial (zero strain) effective elastic modulus E can be calculated from the model constants as

$$\lim_{\varepsilon\to 0}\frac{d\sigma(\varepsilon)}{d\varepsilon} = \lim_{\varepsilon\to 0} C_1C_2\left\{\left(1-\tanh^2(C_2\varepsilon)\right)+C_3C_4\left(1-\tanh^2(C_4\varepsilon)\right)\right\}$$

$$E = \sigma'(0) = C_1C_2 + C_3C_4 \tag{3.4}$$

When consider extreme large strain situation ($\varepsilon \to \infty$), the ultimate tensile strength (UTS) can be obtained by:

$$\lim_{\varepsilon\to 0}\sigma(\varepsilon) = C_1 + C_3 \tag{3.5}$$

Figure 3.7b illustrates a typical set of 10 solder stress strain curves measured under similar environmental and aging conditions, and the corresponding fit of Eq. 3.3 to the data. The excellent representation provided by the empirical model suggests that it

indeed provides a mathematical description of a suitable "average" stress-strain curve for a set of experimental curves measured under fixed test conditions.

3.4.2 Creep Data Processing

In the solder creep experiments, constant stress levels on the order of 25-50% of the observed UTS were applied, resulting in a range of applied stresses of σ = 6 to 15 MPa. Due to the long testing time involved, only 5 specimens were tested for each alloy and set of aging/testing conditions. The curves in each set were fitted with an empirical strain-time model to generate an "average" representation of the creep response for those conditions. It was observed that creep data has more variability than the stress-strain data. For the range of test conditions considered in this work, the raw strain versus time data in the primary and secondary creep regions were found to be well fitted by creep response of the four parameter Burger's (spring-dashpot) model (see Figure 3.9):

$$\varepsilon = \varepsilon(t) = k_0 + k_1 t + k_2\left(1 - e^{-k_3 t}\right) \tag{3.6}$$

From the recorded strain vs. time curves under constant stress, the "steady state" creep strain rates (k_1) have been extracted. In practice, the measured creep rate for each curve was also compared to numerical evaluation of the minimum slope value in the secondary creep region for the observed $\dot{\varepsilon}$ versus t response. Variations of the average creep rates with aging were determined and then modeled as a function of aging time.

3.5 Tensile Testing Results for SAC305 Solder

SAC305 uniaxial specimens for tensile testing were prepared by using the casting method and controlled reflow cooling profile described in the preceding sections, followed by up to one year of aging at T = 100 °C. Specimens were grouped in sets of 10, which

were each exposed to a specific set of aging conditions (aging temperature and aging time), and then tested at a selected temperature and strain rate. Using the measured stress-strain data, material constants were extracted and the nine Anand model material parameters have been determined (see Chapter 4) for each of the aging times. k

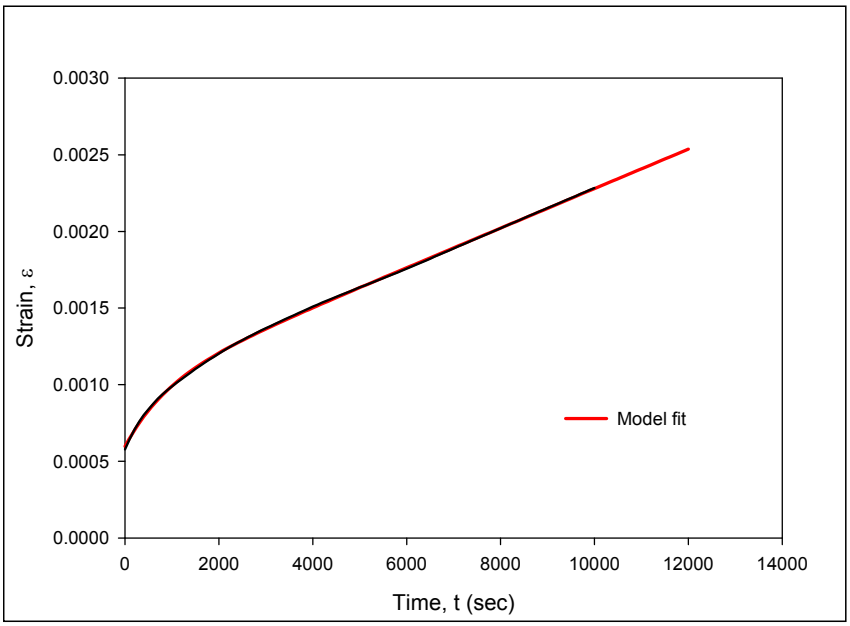

Figure 3.9 Solder Creep Curve and Burger's Model Fit

3.5.1 Stress-Strain Data for Various Temperature, Strain Rates, and Aging Conditions

The effects of aging on the tensile behavior of lead free solder have been examined by performing uniaxial stress-strain tests on SAC305 (96.5Sn-3.0Ag-0.5Cu) samples that were aged for various durations (0-12 months) at a temperature of 100 C. The aging conditions included the baseline/reference state of no aging, as well as 8 different aging times including 1, 5, 20, 60, 120, 180, 270, and 360 days at 100 C. For each aging time, stress-strain data were measured at three strain rates (.001, .0001, and

.00001 1/sec) and five temperatures (25, 50, 75, 100, and 125 C). For example, Figure 3.10 illustrates typical stress-strain curves for SAC305 with no aging (0 days aging) prior to testing (samples were tested immediately after reflow and cooling) for strain rates of 0.001, 0.0001, and 0.00001, respectively. In each plot, the 5 colored curves are the stress-strain results for temperatures of T = 25, 50, 75, 100, and 125 C. Each curve is the "average" stress-strain curve representing the fit of Eq. (3.3) to the 10 recorded raw stress-strain curves for a given set of temperature, strain rate, and aging conditions. For example, the top (black) curve in each plot is the average stress-strain curve at room temperature (25 ^{o}C), and the bottom (red) curve in each plot is the average stress-strain curve at 125 ^{o}C. Analogous results for the other 8 aging conditions are shown in Figures 3.11-3.18. It is observed in each graph in Figures 3.10-3.18 that the effective elastic modulus, yield stress (YS), and ultimate tensile strength (UTS) all decrease monotonically with temperature as expected.

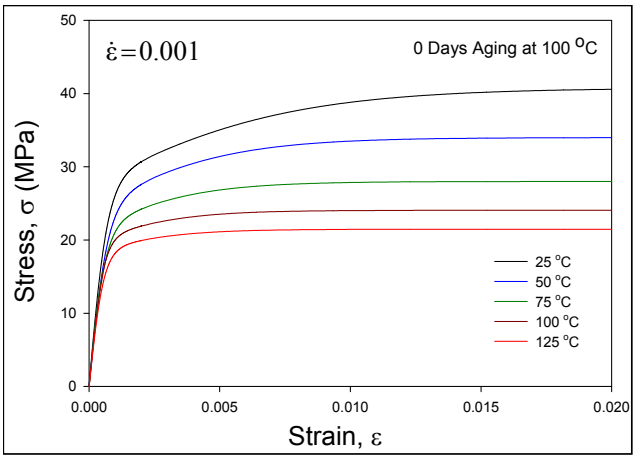

(a) $\dot{\varepsilon} = 0.001$

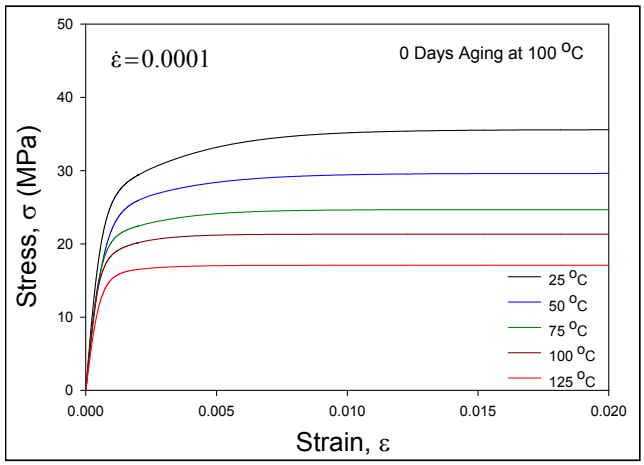

(b) $\dot{\varepsilon} = 0.0001$

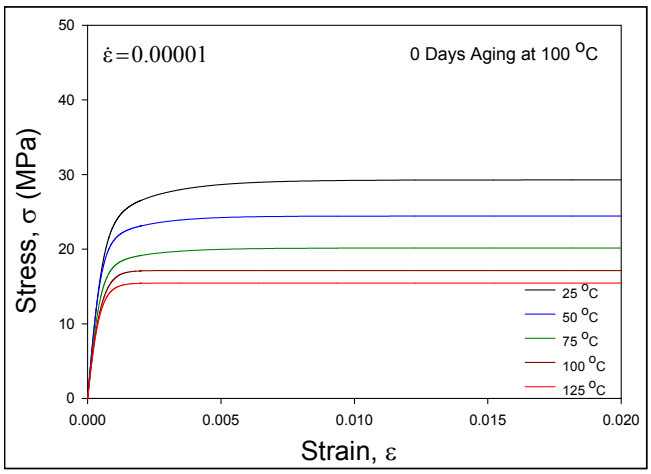

(c) $\dot{\varepsilon} = 0.00001$

Figure 3.10 Stress-Strain Curves for SAC305 for No Aging

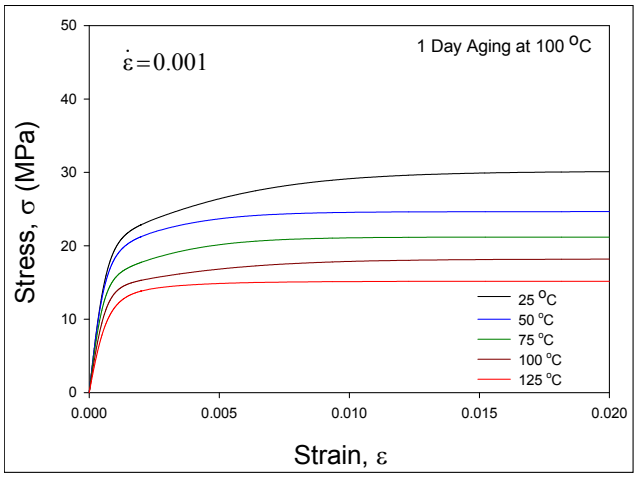

(a) $\dot{\varepsilon} = 0.001$

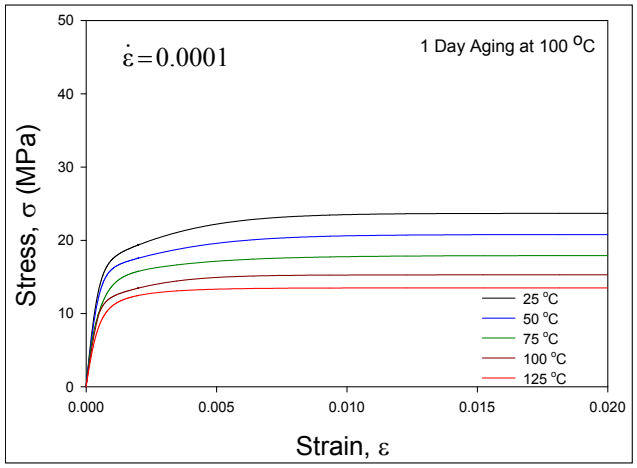

(b) $\dot{\varepsilon} = 0.0001$

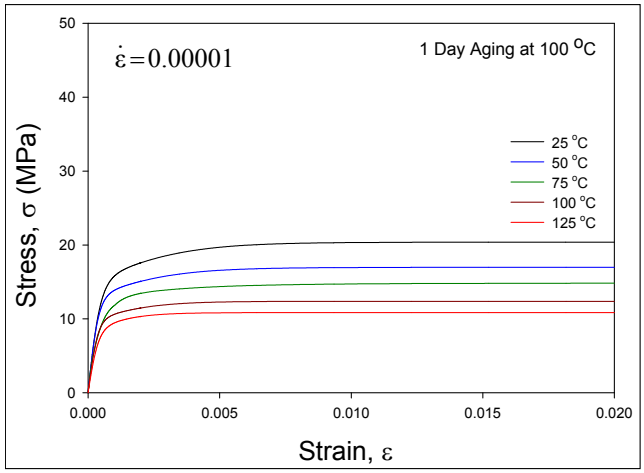

(c) $\dot{\varepsilon} = 0.00001$

Figure 3.11 Stress-Strain Curves for SAC305 for 1 Day Aging at 100 °C

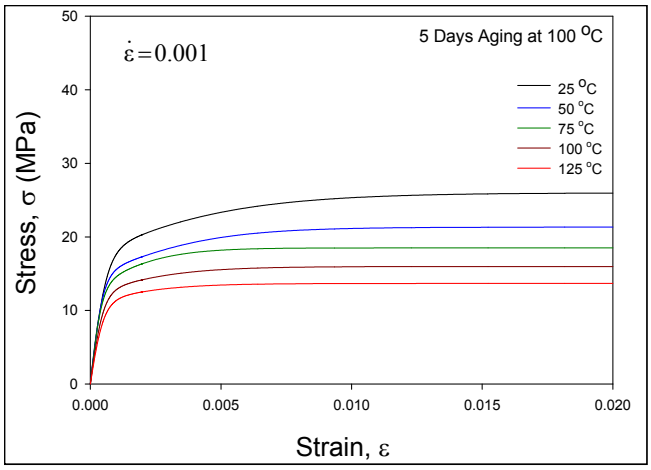

(a) $\dot{\varepsilon} = 0.001$

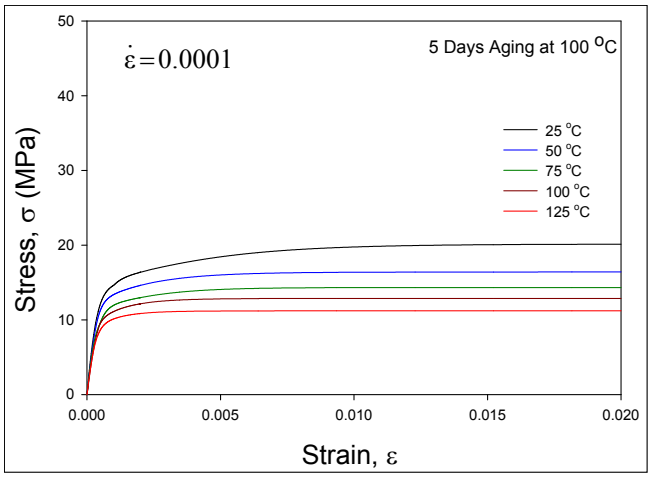

(b) $\dot{\varepsilon} = 0.0001$

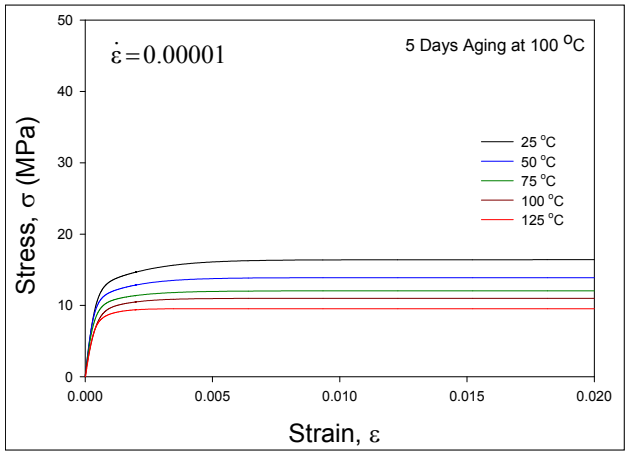

(c) $\dot{\varepsilon} = 0.00001$

Figure 3.12 Stress-Strain Curves for SAC305 for 5 Days Aging at 100 °C

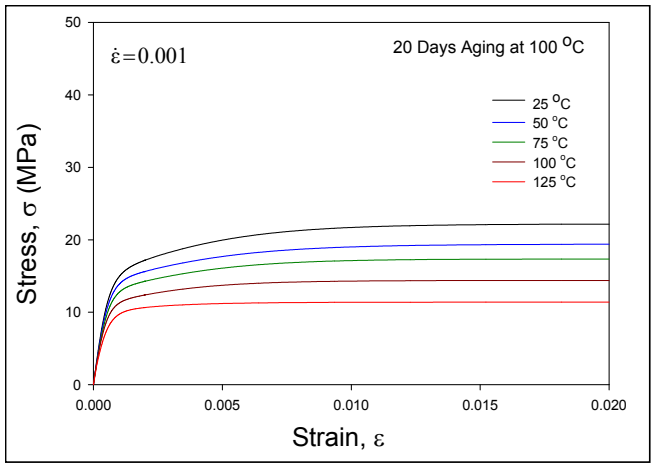

(a) $\dot{\varepsilon} = 0.001$

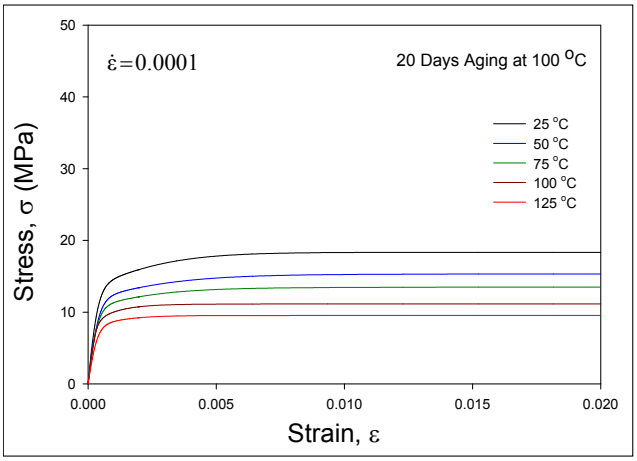

(b) $\dot{\varepsilon} = 0.0001$

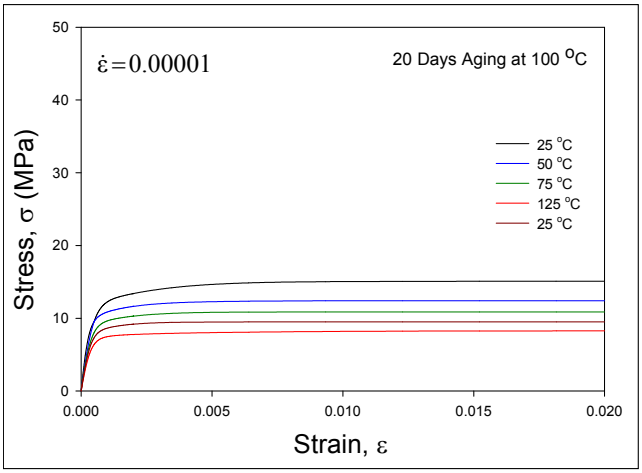

(c) $\dot{\varepsilon} = 0.00001$

Figure 3.13 Stress-Strain Curves for SAC305 for 20 Days Aging at 100 °C

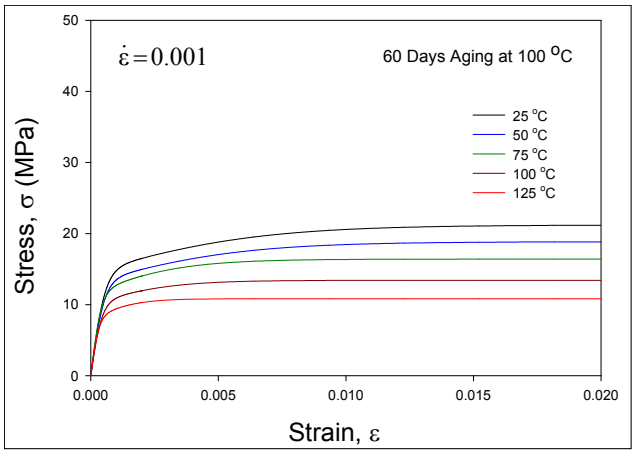

(a) $\dot{\varepsilon} = 0.001$

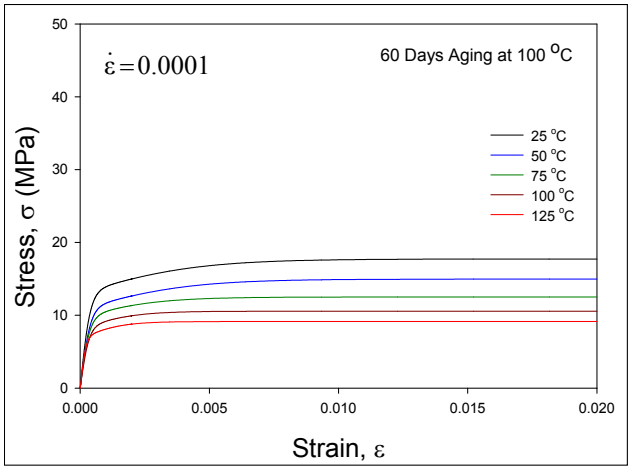

(b) $\dot{\varepsilon} = 0.0001$

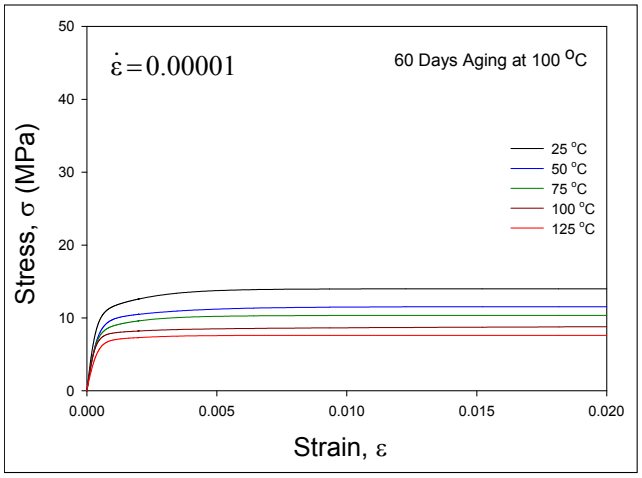

(c) $\dot{\varepsilon} = 0.00001$

Figure 3.14 Stress-Strain Curves for SAC305 for 60 Days Aging at 100 °C

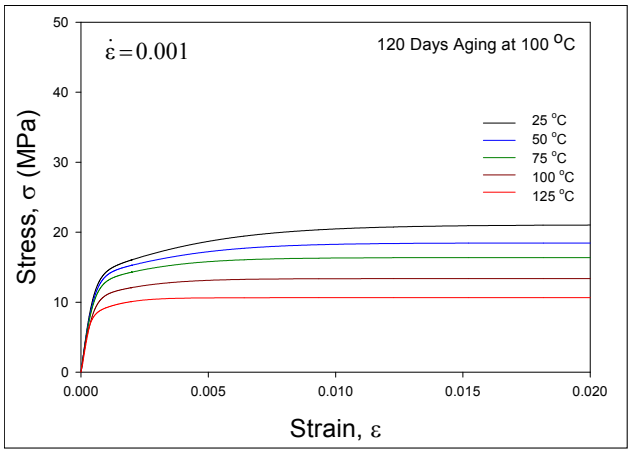

(a) $\dot{\varepsilon} = 0.001$

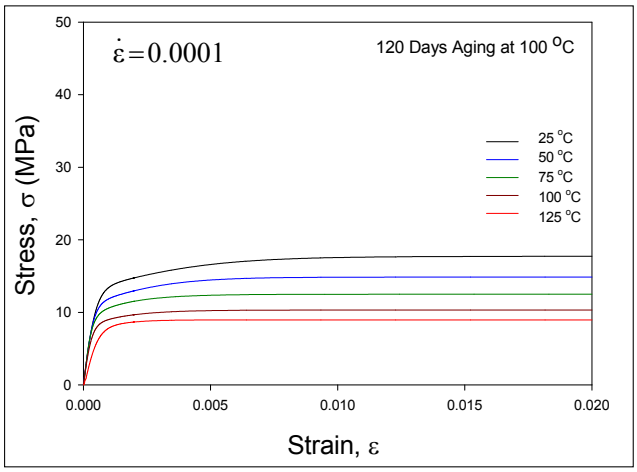

(b) $\dot{\varepsilon} = 0.0001$

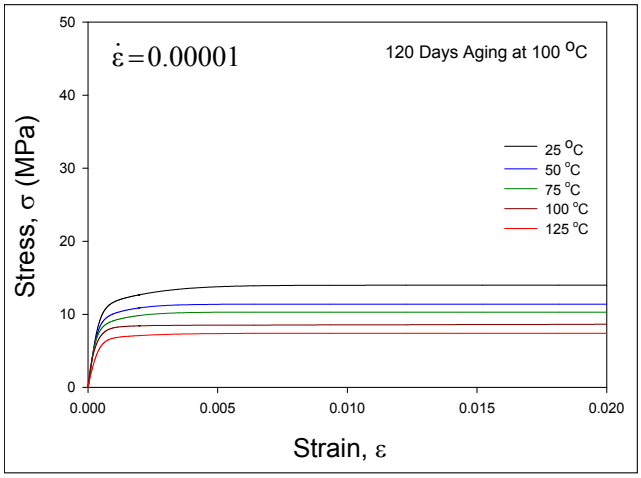

(c) $\dot{\varepsilon} = 0.00001$

Figure 3.15 Stress-Strain Curves for SAC305 for 120 Days Aging at 100 °C

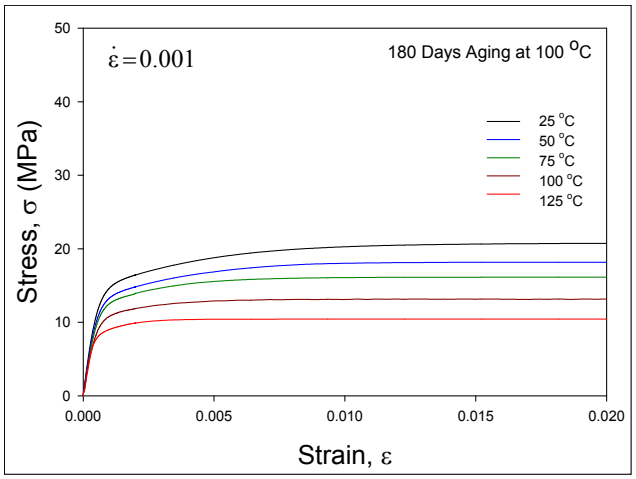

(a) $\dot{\varepsilon} = 0.001$

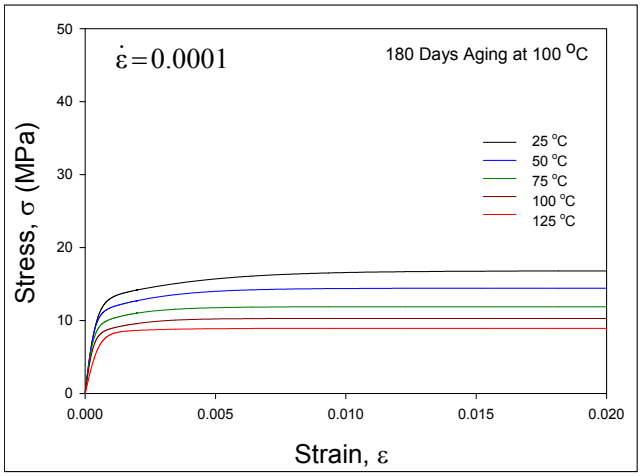

(b) $\dot{\varepsilon} = 0.0001$

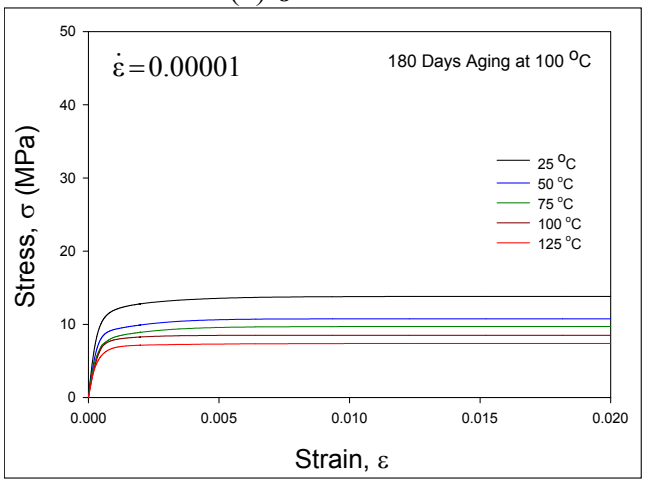

(c) $\dot{\varepsilon} = 0.00001$

Figure 3.16 Stress-Strain Curves for SAC305 for 180 Days Aging at 100 C

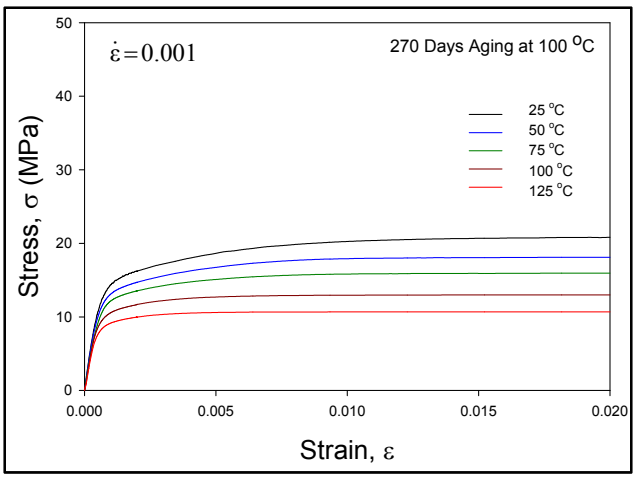

(a) $\dot{\varepsilon} = 0.001$

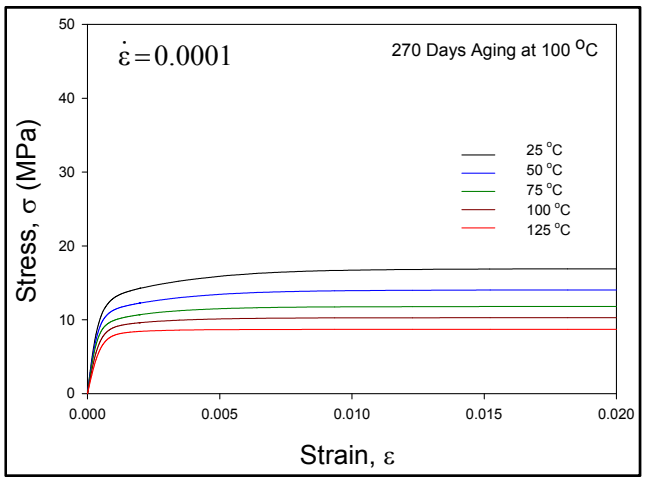

(b) $\dot{\varepsilon} = 0.0001$

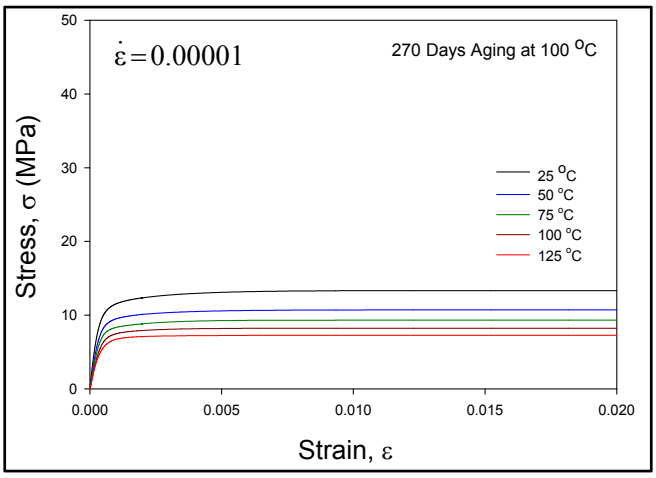

(c) $\dot{\varepsilon} = 0.00001$

Figure 3.17 Stress-Strain Curves for SAC305 for 270 Days Aging at 100 C

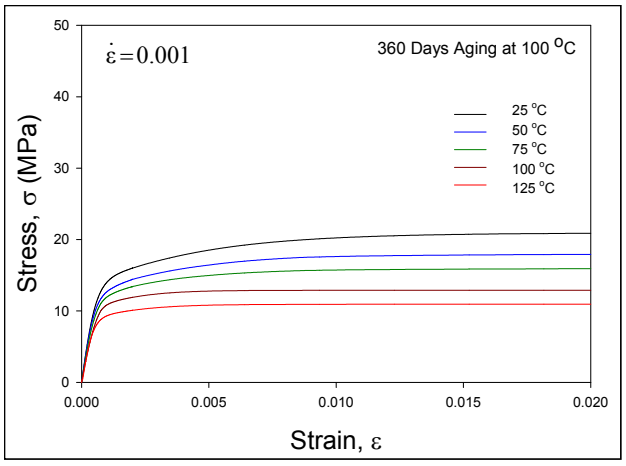

(a) $\dot{\varepsilon} = 0.001$

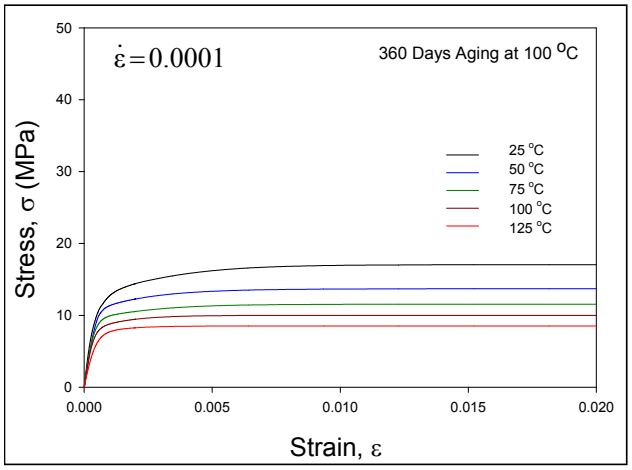

(b) $\dot{\varepsilon} = 0.0001$

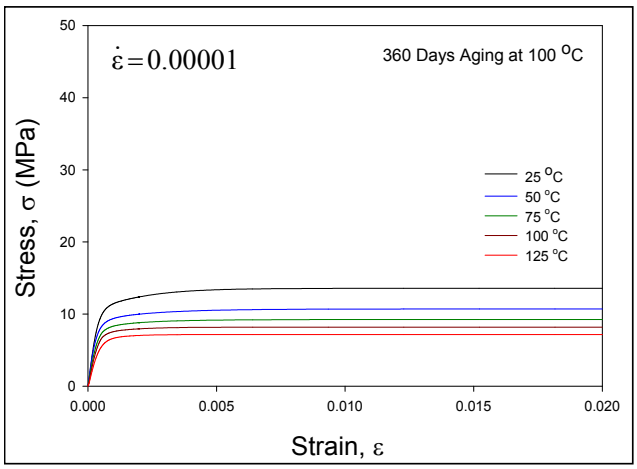

(c) $\dot{\varepsilon} = 0.00001$

Figure 3.18 Stress-Strain Curves for SAC305 for 360 Days Aging at 100 C

3.6 Effects of Aging on Tensile Behavior

3.6.1 Aging Effects on Stress-Strain Response

The effects of aging on the stress-strain response of SAC305 can be directly observed by regrouping of the various curves in Figures 3.10-3.18, so that each graph is at a constant testing temperature instead of a constant aging time. For example, Figure 3.19 illustrates the effects of aging for the 5 different testing temperatures (T = 25, 50, 75, 100, and 125 C) and a strain rate of 0.001. Similar results were obtained for the other two strain rates. The various colored curves in each graph represent the data for different aging times. In particular, the black top curve in each graph is for no aging (0 days aging) prior to tensile testing, and the purple bottom curve in each graph is for 360 days aging at 100 C prior to testing. The results in Figure 3.19(a) for testing at T = 25 (room temperature) are similar to those published previously for SAC alloys tested at room temperature [44, 46, 59]. The results in Figures 3.19(b), 3.19(c), 3.19 (d), and 3.19 (e) for testing at T = 50, 75, 100, and 125 C, respectively, represent the first extensive set of newly measured data [133] on the effects of aging on the elevated temperature stress-strain response of lead-free solders.

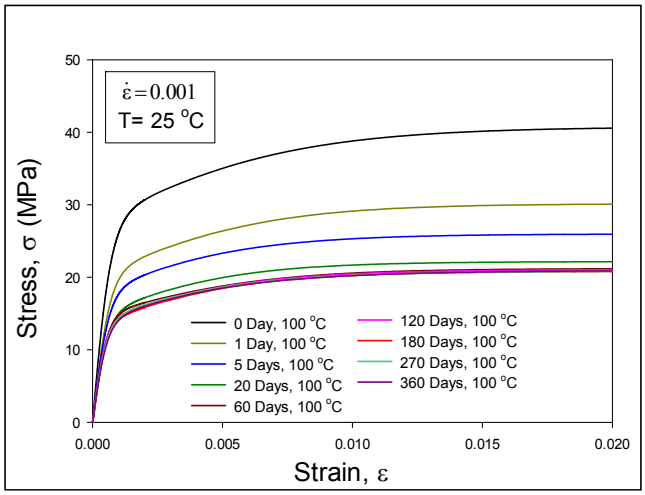

(a) T = 25 °C

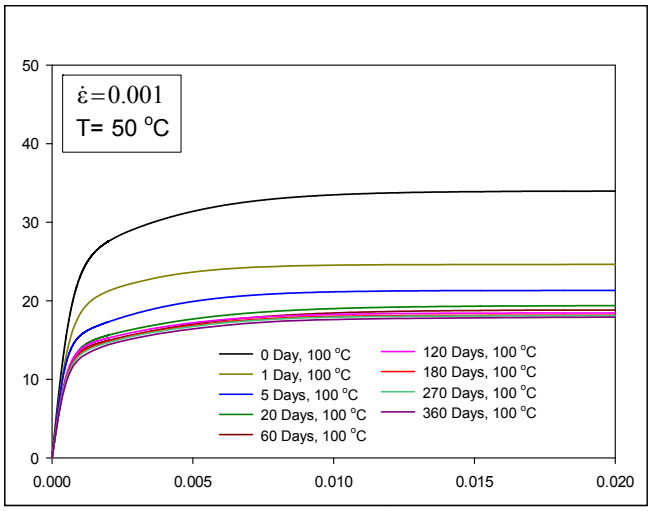

(b) T = 50 °C

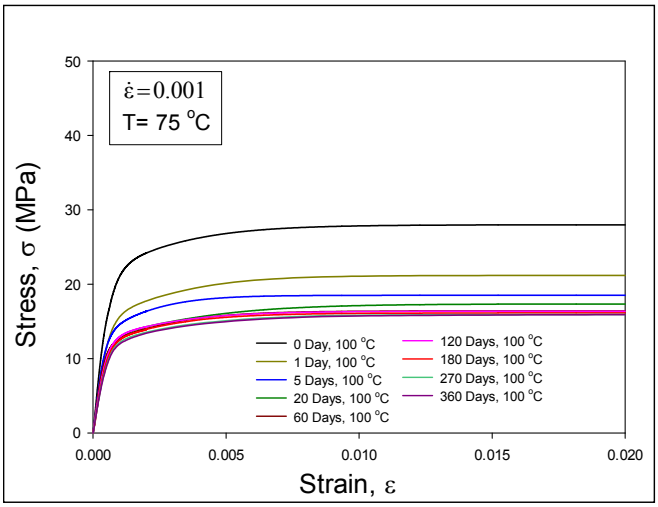

(c) T = 75 °C

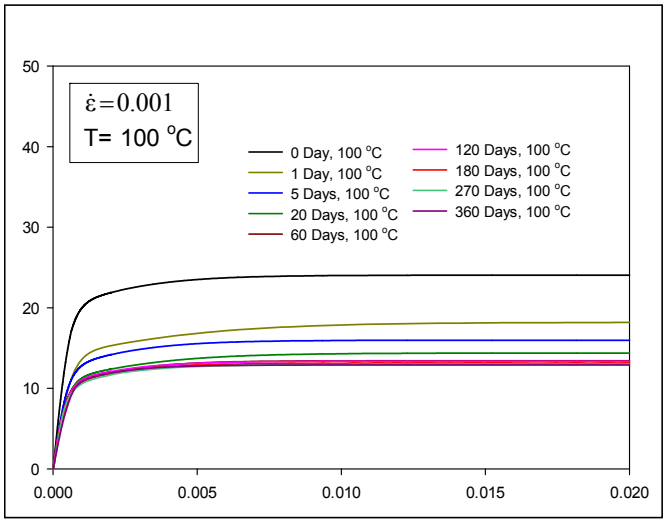

(d) T = 100 °C

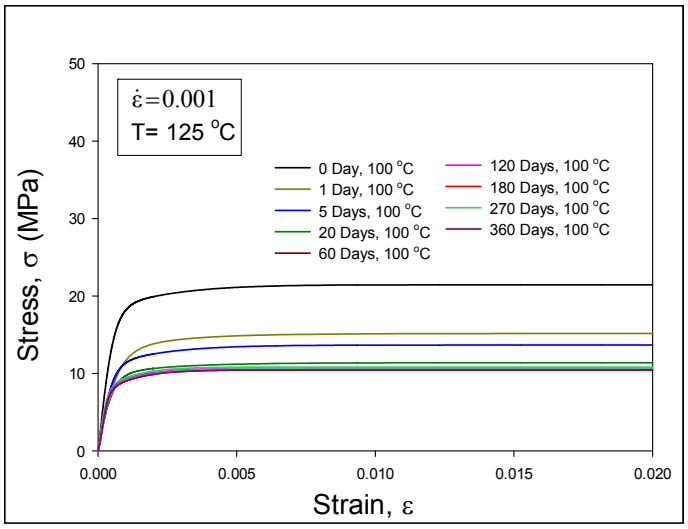

(e) T = 125 °C

Figure 3.19 Effects of Aging on the Stress-Strain Curves for SAC305 Solder ($\dot{\varepsilon}$ = .001)

3.6.2 Aging Effects on Tensile Properties

As expected, aging causes large degradations in the elevated temperature mechanical behavior of SAC solders, with large degradations in the material properties (elastic modulus, yield stress, and UTS). The elastic modulus for each alloy and set of aging conditions was extracted from the model-fitted stress-strain curves as discussed in the preceding section. Variations of the modulus as a function of testing temperature are illustrated in Figure 3.20 for the various aging time (0-360 days) and three different strain rates. For the SAC305 solder alloy, the elastic modulus decreased with increasing testing temperatures at all aging conditions. For example in Figure 3.20(a), the top red curve is the variation of elastic modulus with temperature for no aging, and the other colored curves are for samples that were aged at 100 C for different durations of time. It was observed that the degradation is quite large during first few days of aging and then it slows down and degrades linearly for long aging times. It was also observed from the

previous work that for SAC alloys, the elastic modulus decreased as the aging temperature increased.

The ultimate tensile strength (UTS) is the maximum stress level that a material can withstand before failure under uniaxial loading. Similar to earlier sections, variations of the UTS as a function of testing temperature are illustrated in Figures 3.21 for the various aging time (0-360 days) and three different strain rates. The changes in UTS (maximum/saturation stress) with aging are especially evident from each of the 3 plots in Figure 3.21. It can be seen that the majority of the changes in the material strength at each strain rate occurs during the first 20 days of aging, with slower degradations occurring from 20 to 180 days of aging.

The yield stress (YS) is the maximum stress level up to which the material shows elastic behavior. Similar to earlier sections, variations of the YS as a function of testing temperature are illustrated in Figures 3.22 for the various aging time (0-360 days) and three different strain rates. The changes in YS (maximum/saturation stress) with aging are especially evident from each of the 3 plots in Figure 3.22. Similar to the UTS variation, it can be seen that the majority of the changes in the yield stress at each strain rate occurs during the first 20 days of aging, with slower degradations occurring from 20 to 180 days of aging.

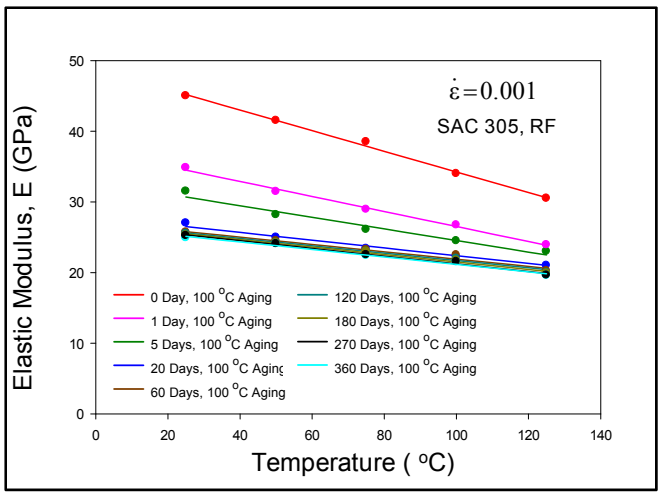

(a) $\dot{\varepsilon}$ = .001

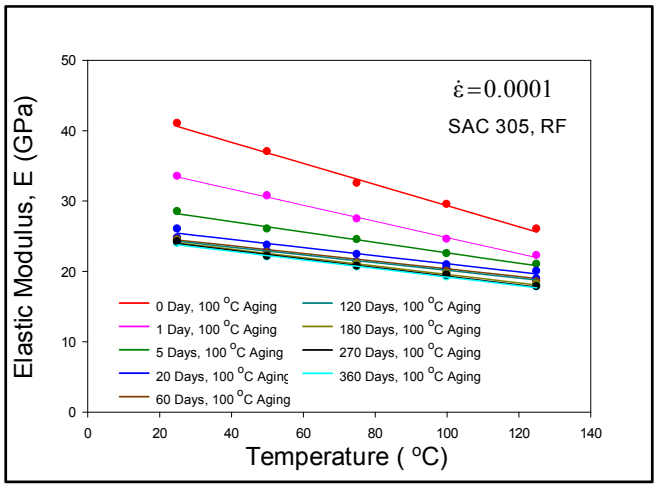

(b) $\dot{\varepsilon}$ = .0001

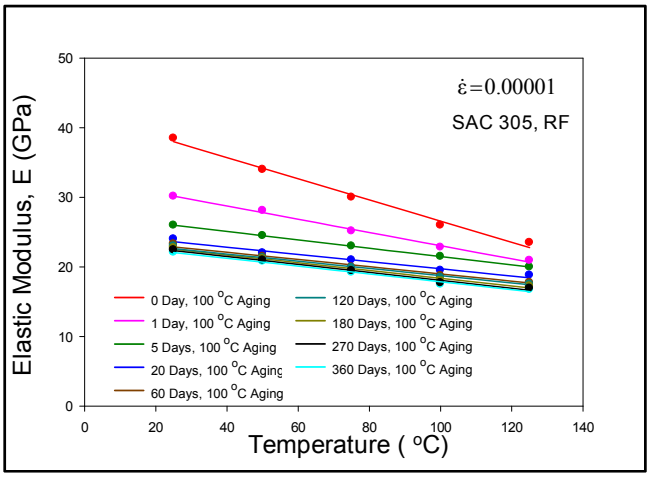

(c) $\dot{\varepsilon}$ = .00001

Figure 3.20 Effects of Aging on Elastic Modulus of SAC305 Solder

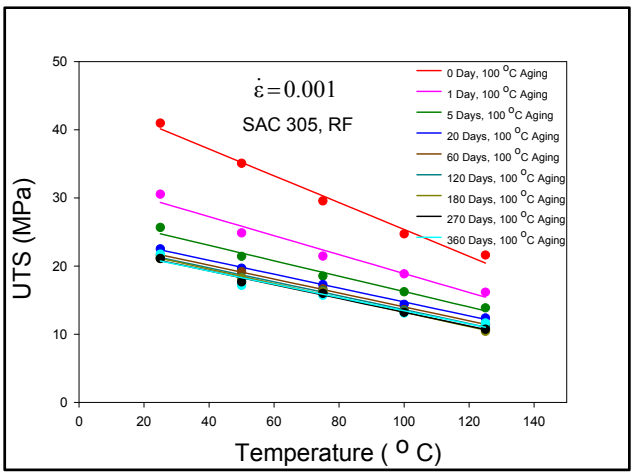

(a) $\dot{\varepsilon}$= .001

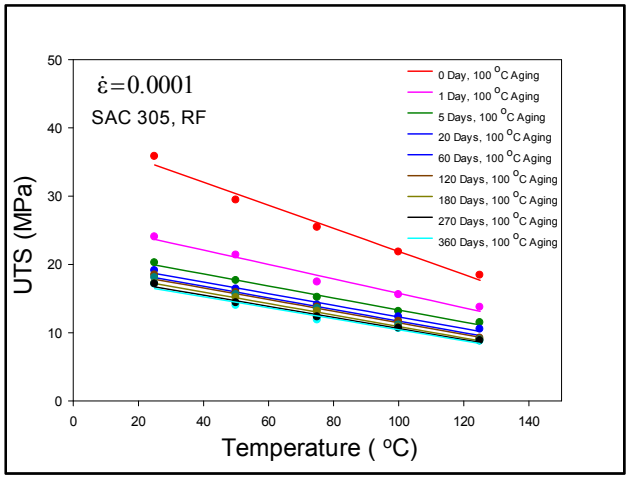

(b) $\dot{\varepsilon}$= .0001

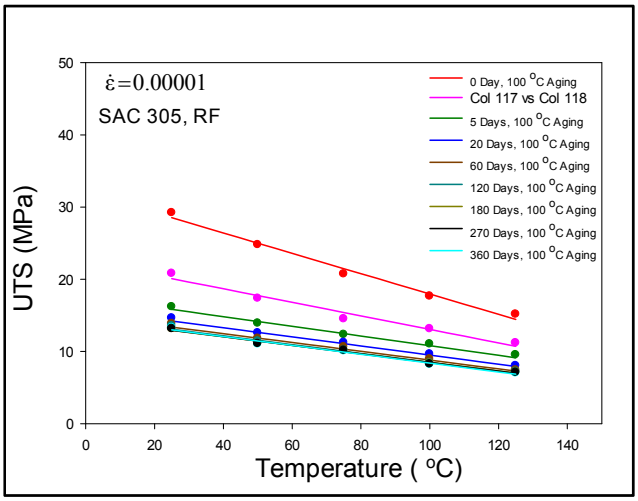

(c) $\dot{\varepsilon}$= .00001

Figure 3.21 Effects of Aging on UTS of SAC305 Solder

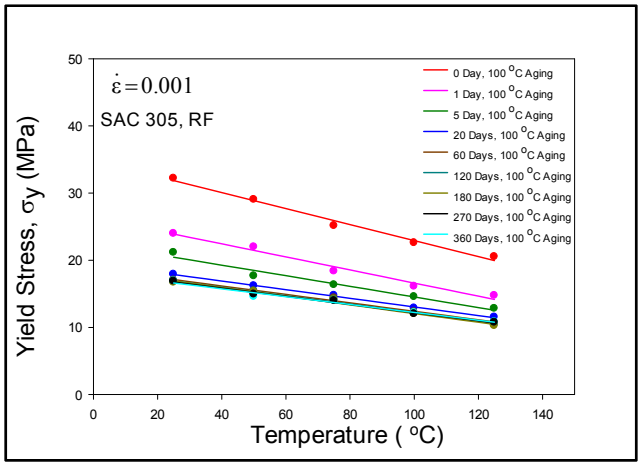

(a) $\dot{\varepsilon}$ = .001

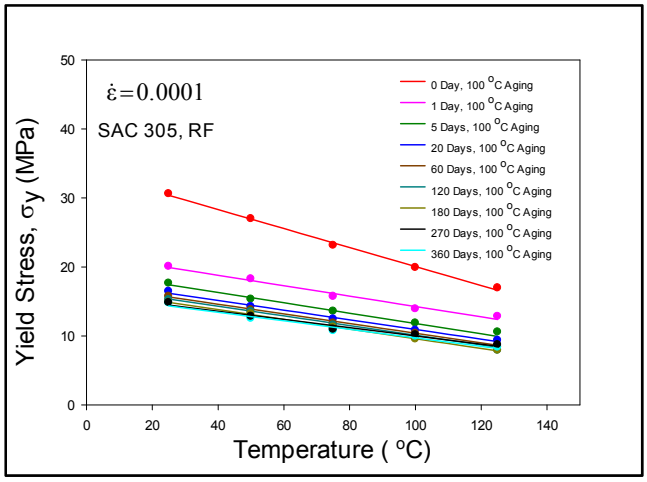

(b) $\dot{\varepsilon}$ = .0001

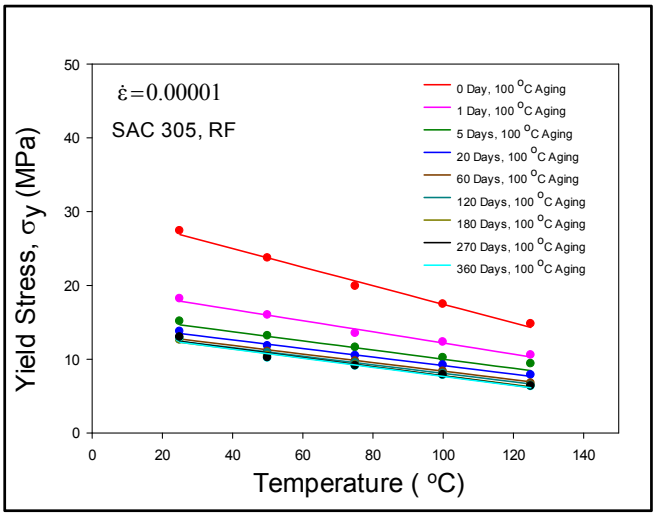

(c) $\dot{\varepsilon}$ = .00001

Figure 3.22 Effects of Aging on Yield Stress of SAC305 Solder

3.7 Creep Testing Results for SAC305 Solder

Aging effects on SAC solder creep behavior were examined by performing creep tests with a test matrix of different stress levels, testing temperatures, and aging times. Uniaxial specimens were formed for SAC305 solder alloy using the casting method and controlled reflow cooling profile described in earlier sections. After solidification, the samples were subjected to up to six months of aging at temperature 100 °C which was similar to the aging studies for the stress-strain specimens. The creep tests were conducted at room temperature as well as elevated temperatures. Specimens were tested in groups of 5, with each group being subjected to a unique set of aging conditions, testing temperature, and applied stress level.

The stress levels for the creep tests were determined according to the UTS of the SAC solders. As the UTS decreased for the aged specimens when compared with the non-aged specimens, the applied stress levels were also made smaller for the aged specimens in the creep tests. For each specific aging condition, creep tests were performed under three stress levels and at five temperatures (T = 25, 50, 75, 100, and 125 C). For specimens with no aging, the stress levels were 10, 12, and 15 MPa. For specimens with 5 days of aging, the stress levels were 8, 10, and 12 MPa. For specimens aged for more than 5 days of aging, stress levels of 6, 8, and 10 MPa were used.

Figures 3.23-3.28 illustrate the recorded creep curves for the SAC305 solder specimens. In each figure, there are three graphs for the three different stress levels for that aging condition. In each graph, the various creep curves are for different testing temperatures, illustrating the variation of the creep response with testing temperature. For example, in Figure 3.23(a), the bottom black curve is the creep response for non-aged

specimens at a testing temperature of 25 C, and the top red curve in the same figure shows the creep response at a testing temperature of 125 C. As expected, it is observed from the figures that creep rates are much higher at elevated temperatures than at room temperature. For the brevity and clarity of representation, only one of the five available creep curves is shown in each plot for each set of aging conditions.

3.7.1 Aging Effects on Creep Behavior for a Fixed Stress Level

The effect of aging on creep behavior can be studied by comparing the creep curves for different aging time that were measured under the same stress level (σ = 10 MPa). For example, Figure 3.29 illustrates typical recorded creep curves for the five different testing temperatures (T = 25, 50, 75, 100, and 125 ^{o}C) at the fixed stress level of 10 MPa. Each plot is for a given testing temperature, and the various creep curves in a particular plot are for different aging times 0-6 months), illustrating the evolution of the creep response with duration of aging. The lowest (black) curve in each plot represents the creep response for the non-aged SAC305 solder (tested immediately after solidification and cool down) and the top (green) curve represents the creep response for specimens aged for 6 months. The plots in Figure 3.29 clearly indicate a dramatic evolution of the creep response at all aging temperatures. The slope of the secondary creep region changes by several orders of magnitude as aging progresses.

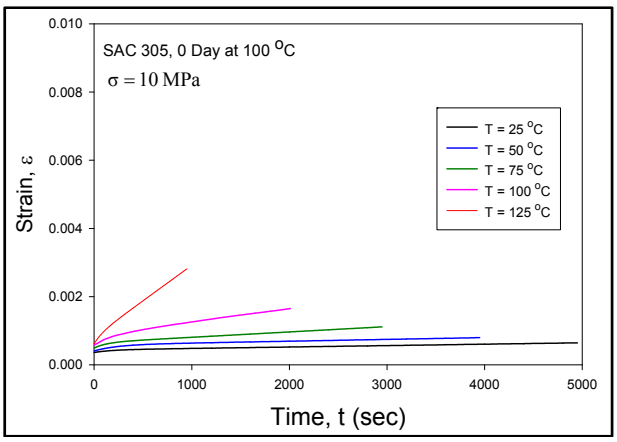

(a) σ = 10 MPa

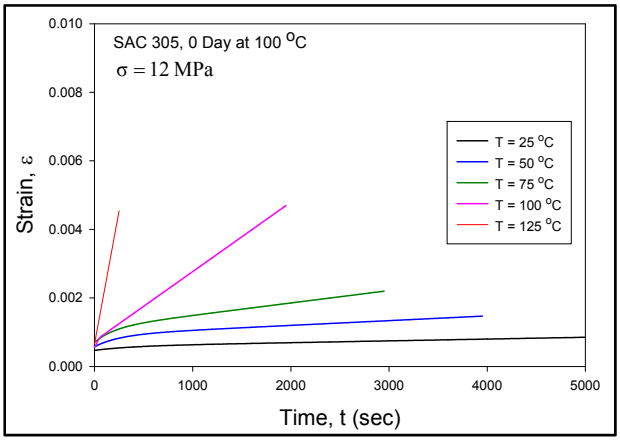

(b) σ = 12 MPa

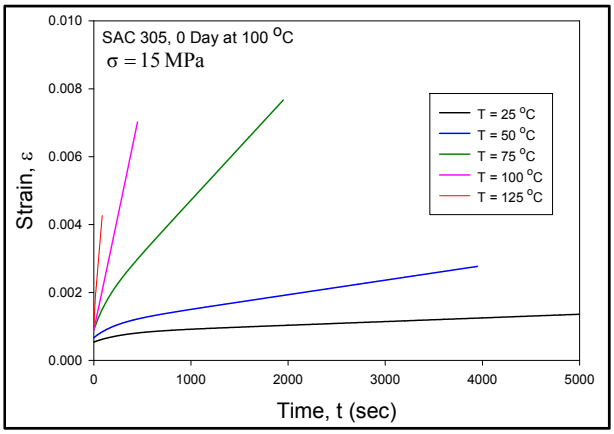

(c) σ = 15 MPa

Figure 3.23 Creep Curves for No Aging

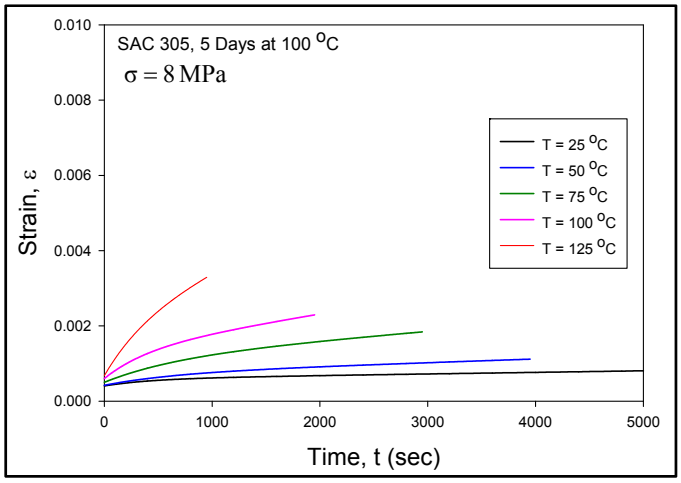

(a) σ = 8 MPa

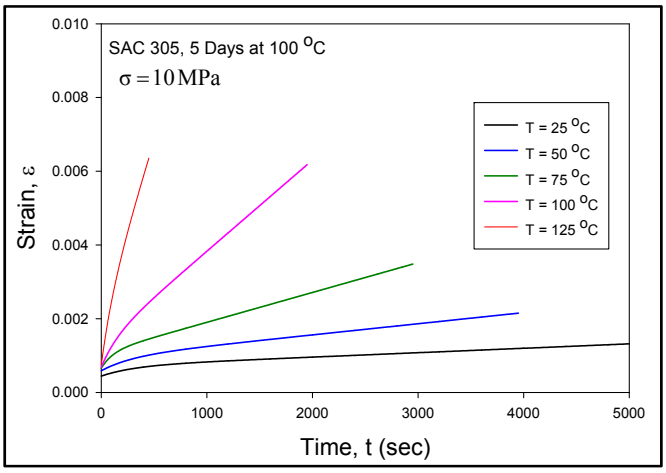

(b) σ = 10 MPa

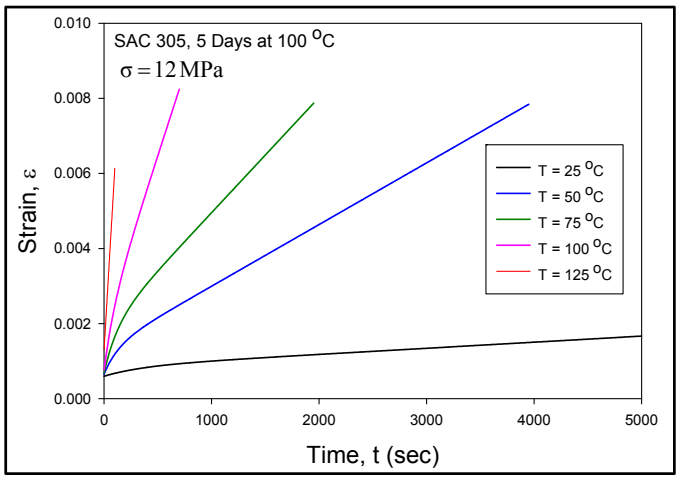

(c) σ = 12 MPa

Figure 3.24 Creep Curves for 5 Days Aging at 100 °C

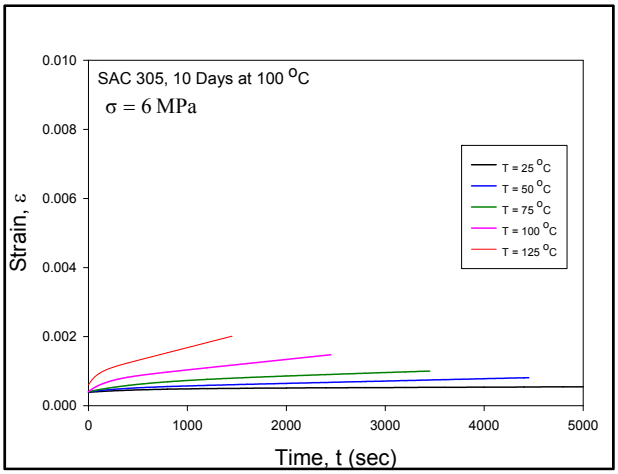

(a) σ = 6 MPa

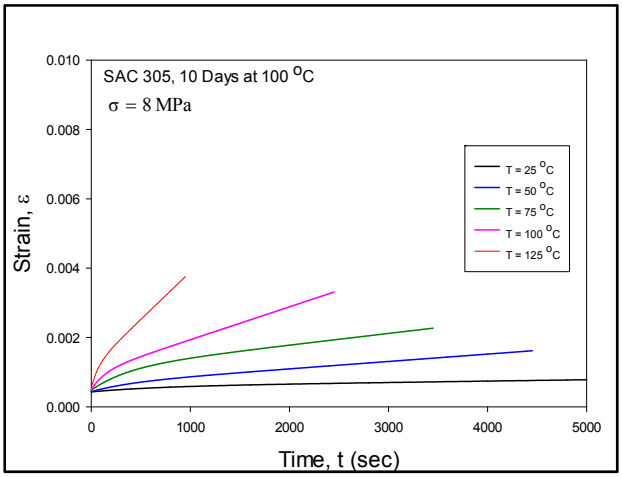

(b) σ = 8 MPa

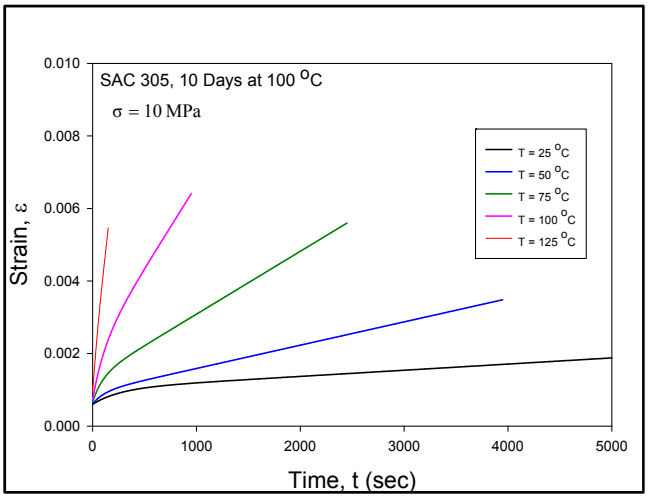

(c) σ = 10MPa

Figure 3.25 Creep Curves for 10 Days Aging at 100 °C

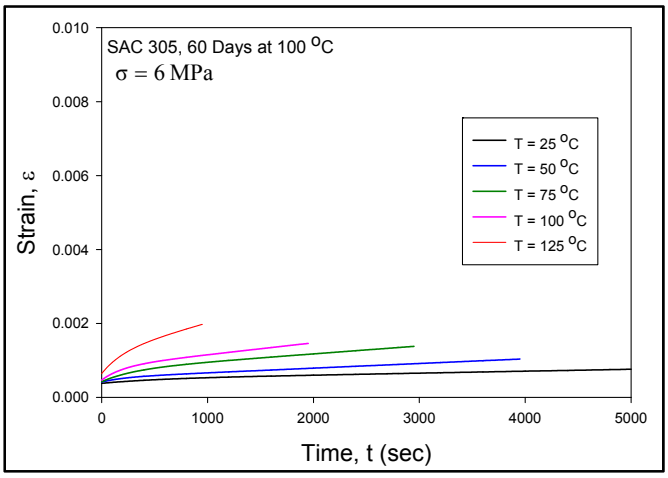

(a) σ = 6 MPa

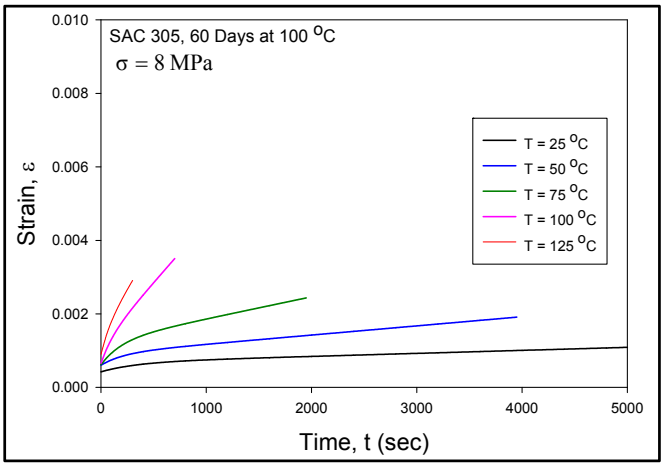

(b) σ = 8 MPa

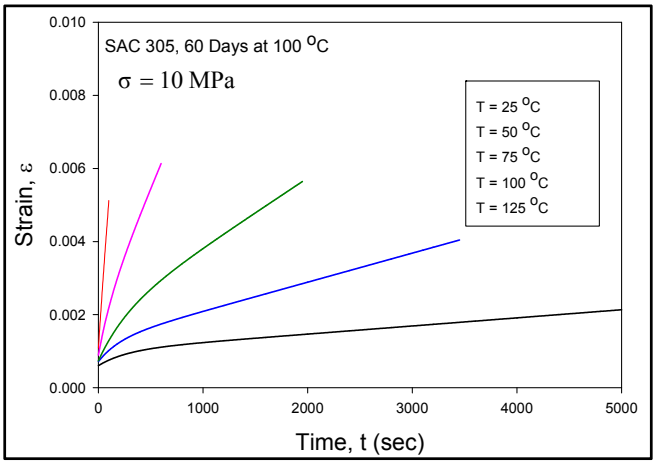

(c) σ = 10 MPa

Figure 3.26 Creep Curves for 60 Days Aging at 100 °C

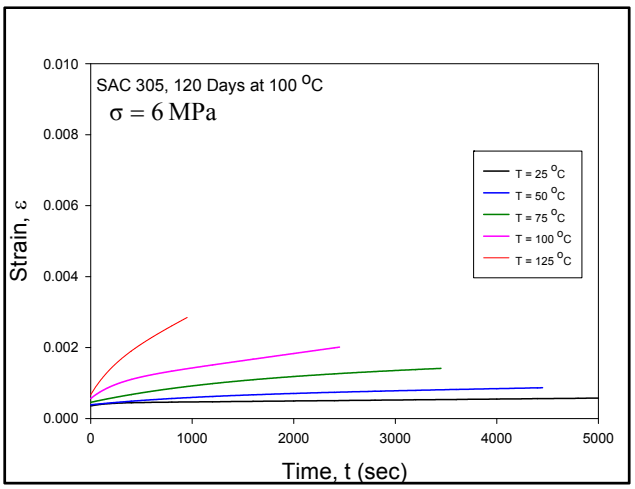

(a) σ = 6 MPa

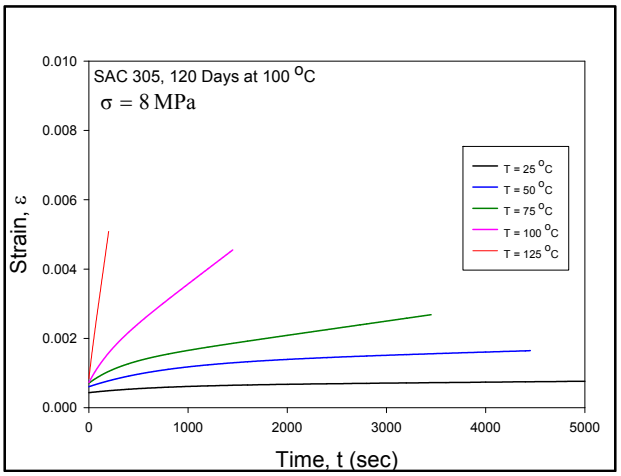

(b) σ = 8 MPa

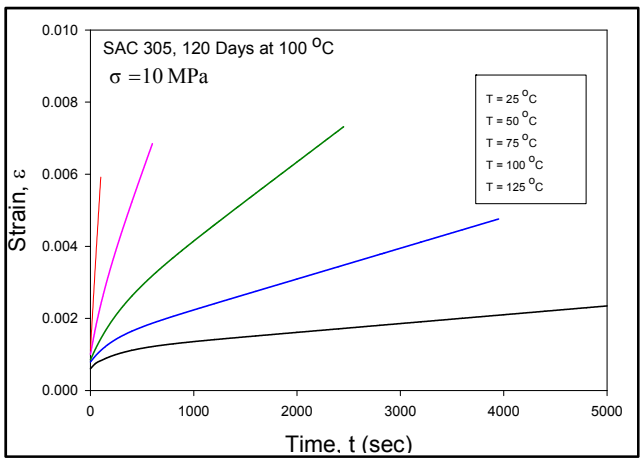

(c) σ = 10 MPa

Figure 3.27 Creep Curves for 120 Days Aging at 100 °C

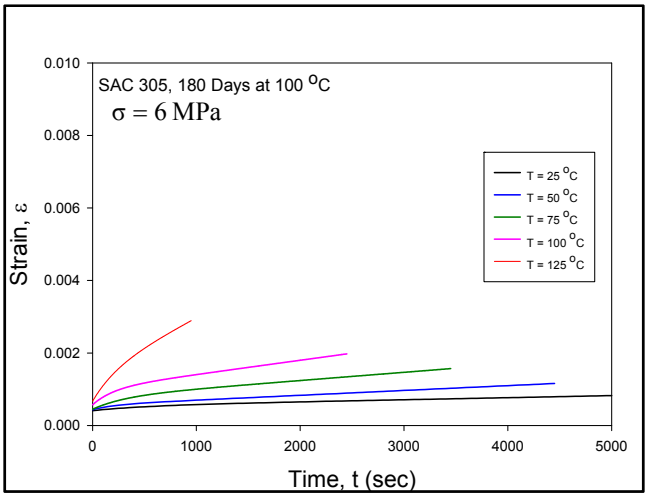

(a) σ = 6 MPa

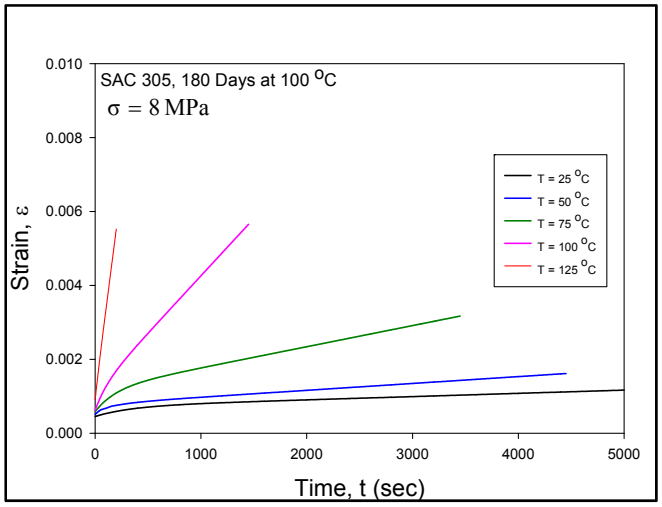

(b) σ = 8 MPa

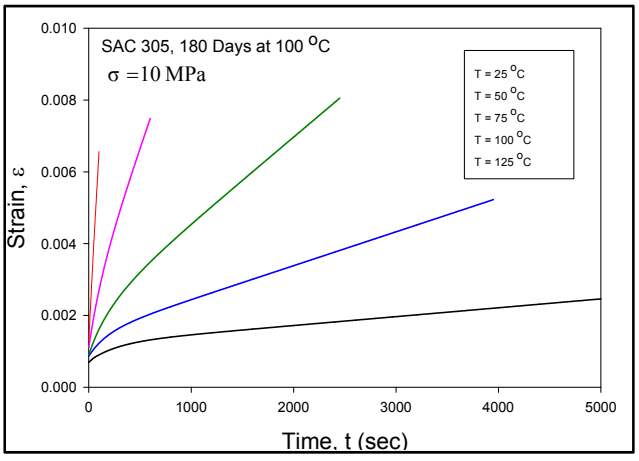

(c) σ = 10 MPa

Figure 3.28 Creep Curves for 180 Days Aging 100 °C

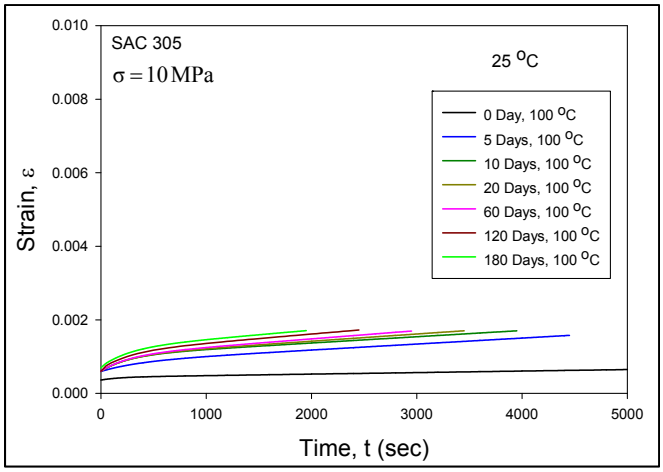

(a) T = 25 °C

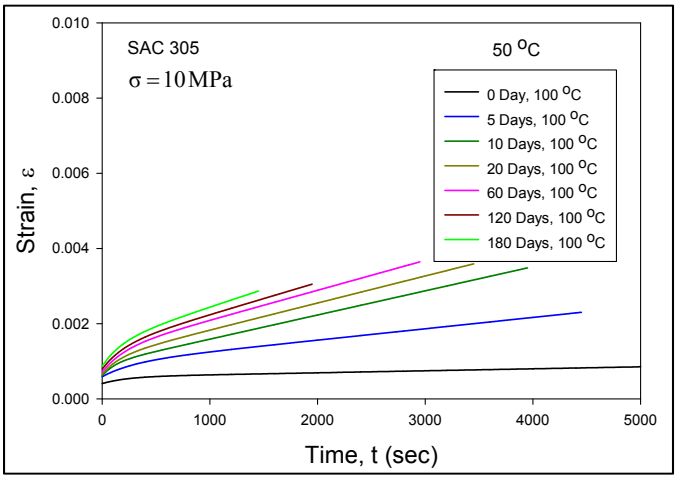

(b) T = 50 °C

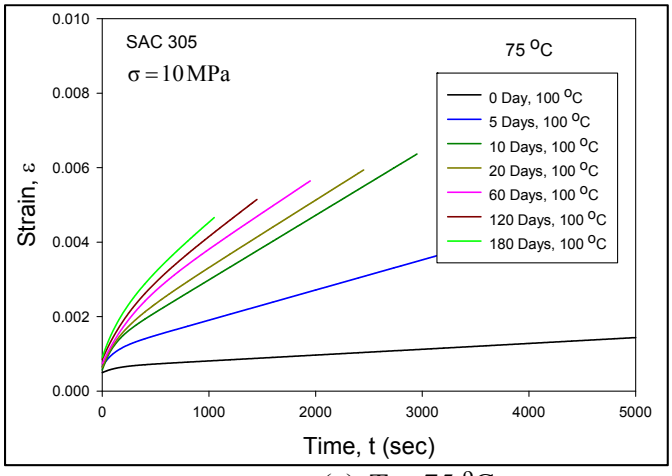

(c) T = 75 °C

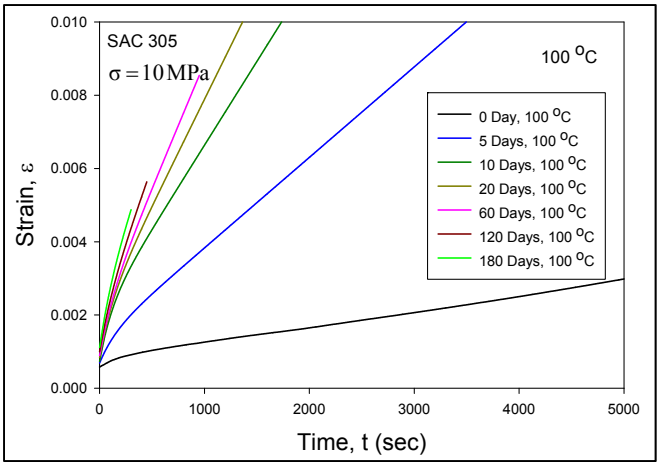

(d) T = 100 °C

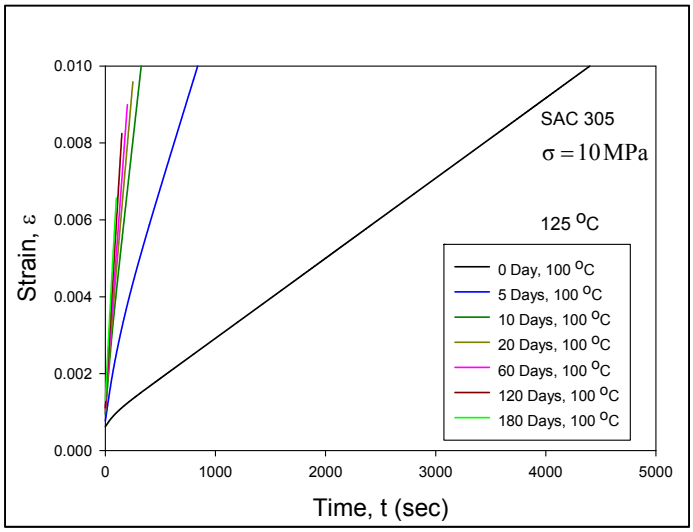

(e) Aging at T = 125 °C

Figure 3.29 Effects of Aging on Creep Curves at Different Temperatures

3.7.2 Aging Effects on Creep Strain Rates

The effects of aging on solder creep behavior were explored by extracting the secondary creep rates from the raw experimental creep data. The evolution of the creep strain rate with aging was then studied and modeled. An empirical mathematical model was established to perform this function:

$$\dot{\varepsilon} = e^{C_0 + C_1 t + C_2 (1 - e^{-C_3 t})} \tag{3.7}$$

or

$$\log \dot{\varepsilon} = C_0 + C_1 t + C_2(1 - e^{-C_3 t}) \tag{3.8}$$

where $\dot{\varepsilon}$ is the averaged secondary creep strain rate; t is aging time; and C_0, C_1, C_2 and C_3 are temperature dependent fitting constants.

Figure 3.30 shows an example of the application of the model in Eq. (3.8) to a set of solder aging data. Using this illustration, the significance of the four constants in Eq. (3.8) can be visualized. In this graph, each green dot represents the averaged secondary creep strain rate at one specific aging time. Totally, there are 8 data points and they were fitted using the empirical model in Eq. 3.8. Constant C_0 is the intercept of the curve with the vertical log-scale axis on the graph, and therefore is the secondary creep strain rate for no aging. Constant C_1 is the slope of the linear portion on the curve for long aging times. The last two constants C_2 and C_3 jointly govern the position and shape of the transitional region on the curve. Constant C_2 determines the rise of the creep rate during the initial period of aging, before it enters the constant slope region.

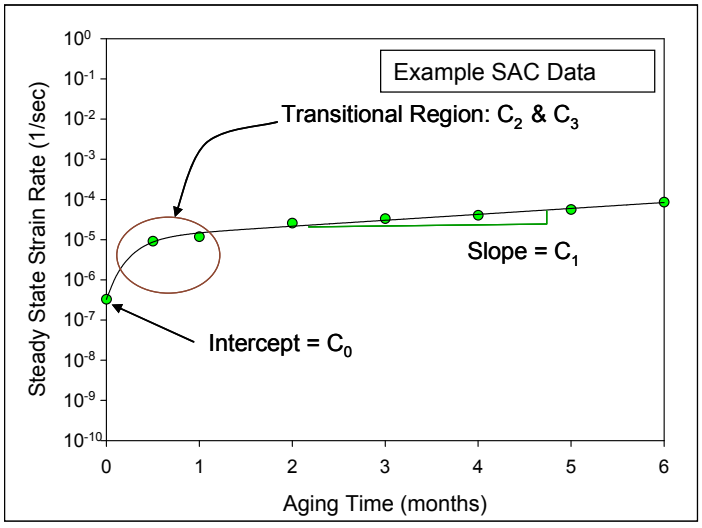

Figure 3.30 Empirical Model for the Creep Strain Rate Evolution

The creep rates for SAC305 under σ = 10 MPa and various aging times were obtained from each creep curve in Figure 3.23-3.28 and then plotted in Figure 3.31 for the 5 testing temperatures. Each data point represents the average creep rate measured for the five samples tested at a given set of aging and testing conditions. According to Figure 3.31, it is apparent that SAC305 experiences dramatic aging induced changes in its creep rate at all testing temperatures. It is also evident from these curves that the largest changes occur during the first 20 days of aging. The variation of the creep rate (log scale) for all testing temperatures then becomes nearly linear for longer aging times (1-6 months).

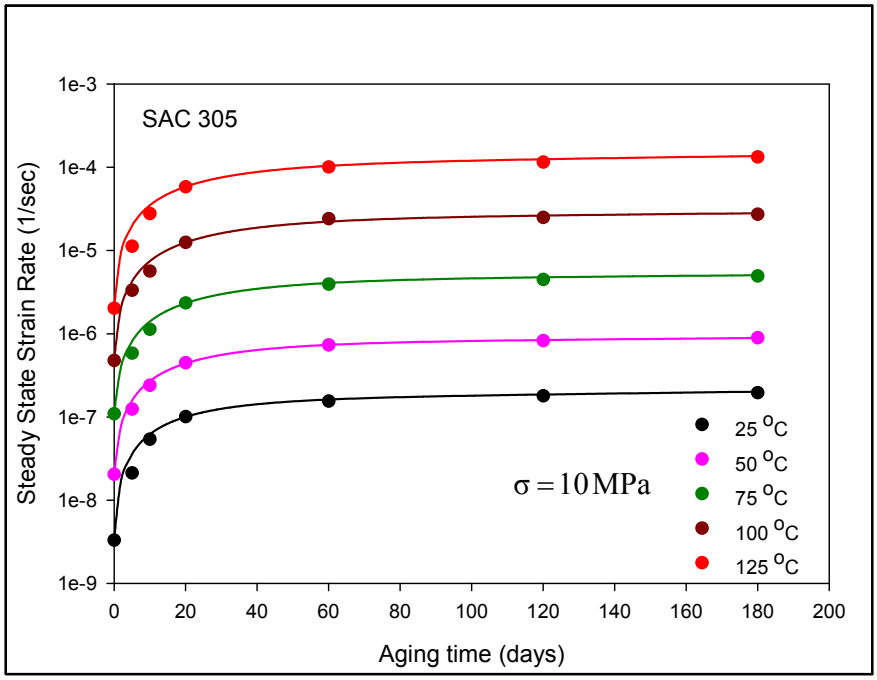

Figure 3.31 Effects of Aging on the Secondary Creep Rate

3.8 Summary and Discussion

Tensile stress-strain tests were performed for a wide range of temperatures, strain rates, and aging conditions. Also, creep tests were performed for a wide range of temperatures, stress levels, aging conditions. A unique specimen preparation procedure was developed in this study to fabricate micro-scale uniaxial tensile specimens. All solder specimens were formed in glass tubes with rectangular cross-section by using a vacuum suction system. The tubes were then cooled by sending through an SMT reflow to re-melt the solder in the tubes and subject them to any desired temperature profile to match those experienced by actual solder joints. Typical uniaxial samples with nominal dimensions of 80 × 3 × 0.5 mm were utilized.

In this study, uniaxial tensile and creep tests were performed by using a tension-torsion micro tester. Experimental data from the tensile tests were fitted by a four parameter hyperbolic tangent model and the creep data were fitted by using the Burger's model. The effects of aging on the stress-strain behavior were investigated using the SAC305 solder specimens that were aged for various durations (0-360 days) at 100 ^{o}C. As expected, dramatic degradations in the tensile test properties (elastic modulus, UTS and yield stress) were observed from the tensile test results. During first 20 days of aging, the material properties degrade dramatically, and for longer aging times, they degraded linearly with a small slope. Aging also had significant effects on the creep test results. For the SAC305 specimens that were aged for various durations (0-180 days), aging significantly increased the steady state creep strain rate or secondary creep rate. Similar to the tensile test results, the increase in secondary creep rate was dramatic during first 20 days of aging, and then it increased slowly and linearly for longer aging times.

CHAPTER 4

MODIFIED ANAND VISCOPLASTIC CONSTITUTIVE MODEL INCLUDING AGING EFFECTS

4.1 Introduction

As mentioned in Chapter 2, the Anand viscoplastic constitutive model is the most widely used material model in the finite element analysis of solder materials. This model unifies the creep and plasticity of solder by making use of a stress equation, a flow equation, and an evolution equation. It has nine parameters which are typically determined from uniaxial stress-strain tests at several strain rates and temperatures using a multistep parameter determination procedure.

In this chapter, the effects of aging on the Anand model parameters of solder will be investigated. The theoretical equations for the uniaxial stress-strain response (constant strain rate) and for the creep response of solder have been derived from the Anand viscoplastic model. Procedures for extracting the Anand model constants from experimental stress-strain and creep data have also been established. The two developed methods were then applied to determine the Anand constants for SAC305 lead free solder using the two completely different sets of experimental test data presented in the previous chapter. The first set of Anand parameters were extracted from uniaxial stress strain data measured over a wide range of strain rates ($\dot{\varepsilon}$ = 0.001, 0.0001, and 0.00001 1/sec), testing temperatures (T = 25, 50, 75, 100, and 125 ^{o}C), and aging conditions (0-12 months at 100^{o}C). The second set of Anand parameters were calculated from creep test data

measured at several stress levels (σ = 6-15 MPa), testing temperatures (T = 25, 50, 75, 100, and 125 ^{o}C), and aging conditions (0-6 months at 100 C). The two sets of Anand model constants derived from the stress-strain and creep data were then compared, and the accuracy (goodness of fit) of the Anand model using the extracted material constants was evaluated by comparing the responses calculated from the Anand model with the measured stress-strain and creep data. The evolutions of the Anand model parameters with aging time were then determined. Empirical equations for the variation of seven parameters with aging time were developed to modify the Anand viscoplastic constitutive model to include the aging effects.

4.2 Anand Viscoplastic Constitutive Model

Anand, et al. [105, 106] proposed a popular set of viscoplastic constitutive equations for rate-dependent deformation of metals at high temperatures (e.g. in excess of a homologous temperature of $0.5T_m$). Although it was originally aimed at hot working of high strength aluminum and other structural metals, the so-called Anand model has been adopted successfully to represent isotropic materials such as microelectronic solders (SnPb and lead free) with small elastic deformations and large viscoplastic deformations.

4.2.1 Primary Equations of Anand Viscoplastic Constitutive Model

The Anand model uses a scalar internal variable s to represent the isotropic resistance to plastic flow offered by the internal state of the material. It unifies the creep and rate-independent plastic behavior of the solder by making use of a stress equation, a flow equation, and an evolution equation. The model needs no explicit yield condition and no loading/unloading criterion.

For the one-dimensional case (uniaxial loading), the stress equation is given by

$$\sigma = cs;\ c < 1 \tag{4.1}$$

where s is the internal valuable and c is a function of strain rate and temperature expressed as

$$c = c(\dot{\varepsilon}_p, T) = \frac{1}{\xi}\sinh^{-1}\left\{\left[\frac{\dot{\varepsilon}_p}{A}e^{\left(\frac{Q}{RT}\right)}\right]^m\right\} \tag{4.2}$$

and where $\dot{\varepsilon}_p$ is the inelastic (plastic) strain rate, T is the absolute temperature, ξ is the multiplier of stress, A is the pre-exponential factor, Q is the activation energy, R is the universal gas constant, and m is the strain rate sensitivity. Substituting Eq. (4.2) into Eq. (4.1), the stress equation can be expressed as:

$$\sigma = \frac{s}{\xi}\sinh^{-1}\left\{\left[\frac{\dot{\varepsilon}_p}{A}e^{\left(\frac{Q}{RT}\right)}\right]^m\right\} \tag{4.3}$$

Rearranging Eq. (4.3) and solving for the strain rate yields the flow equation of the Anand model:

$$\dot{\varepsilon}_p = A\,e^{-\left(\frac{Q}{RT}\right)}\left[\sinh\left(\xi\frac{\sigma}{s}\right)\right]^{\frac{1}{m}} \tag{4.4}$$

The differential form of the evolution equation for the internal variable s is assumed to be of the form

$$\begin{aligned} \dot{s} &= h(\sigma, s, T)\dot{\varepsilon}_p \\ \dot{s} &= \left[h_o\left(1-\frac{s}{s^*}\right)^a \operatorname{sign}\left(1-\frac{s}{s^*}\right)\right]\dot{\varepsilon}_p;\quad a > 1 \end{aligned} \tag{4.5}$$

where, the term $h(\sigma, s, T)$ is associated with the dynamic hardening and recovery processes. Parameter h_o is the hardening constant, a is the strain rate sensitivity of the hardening process, and the term s* is expressed as

$$s^* = \hat{s}\left[\frac{\dot{\varepsilon}_p}{A}e^{\left(\frac{Q}{RT}\right)}\right]^n \tag{4.6}$$

where $\hat{s}$ is a coefficient and n is the strain rate sensitivity of the saturation value of the deformation resistance. Equation (4.5) can be integrated to yield the final version of the evolution equation for the internal variable s:

$$s = \hat{s}\left[\frac{\dot{\varepsilon}_p}{A}e^{\left(\frac{Q}{RT}\right)}\right]^n - \left[\left(\hat{s}\left[\frac{\dot{\varepsilon}_p}{A}e^{\left(\frac{Q}{RT}\right)}\right]^n - s_o\right)^{(1-a)} + (a-1)\left\{(h_o)\left(\hat{s}\left[\frac{\dot{\varepsilon}_p}{A}e^{\left(\frac{Q}{RT}\right)}\right]^n\right)^{-a}\right\}\varepsilon_p\right]^{\frac{1}{1-a}} \tag{4.7}$$

or

$$s = s(\dot{\varepsilon}_p, \varepsilon_p) \tag{4.8}$$

The final equations in the Anand model (1D) are the stress equation in Eq. (4.3), the flow equation in Eq. (4.4), and the integrated evolution equation in Eq. (4.7). These expressions include 9 material parameters (constants): A, ξ, Q/R, m in Eqs. (4.3, 4.4); and constants h_o, a, s_o, $\hat{s}$, and n in Eq. (4.7).

4.2.2 Theoretical Formulation for Uniaxial Stress-Strain Response

The post yield uniaxial stress-strain relations predicted by the Anand model are obtained by substituting the expression for internal variable 's' from eq. (4.7) into the stress equation in eq. (4.3). This calculation results in:

$$\sigma = \frac{1}{\xi}\sinh^{-1}\left\{\left[\frac{\dot{\varepsilon}_p}{A}e^{\left(\frac{Q}{RT}\right)}\right]^m\right\}\left(\hat{s}\left[\frac{\dot{\varepsilon}_p}{A}e^{\left(\frac{Q}{RT}\right)}\right]^n - \left[\left(\hat{s}\left[\frac{\dot{\varepsilon}_p}{A}e^{\left(\frac{Q}{RT}\right)}\right]^n - s_o\right)^{(1-a)} + (a-1)\left\{(h_o)\left(\hat{s}\left[\frac{\dot{\varepsilon}_p}{A}e^{\left(\frac{Q}{RT}\right)}\right]^n\right)^{-a}\right\}\varepsilon_p\right]^{\frac{1}{1-a}}\right)$$

$$\sigma = \sigma(\dot{\varepsilon}_p, \varepsilon_p) \tag{4.9}$$

For a uniaxial tensile test performed at fixed (constant) strain rate $\dot{\varepsilon}_p$ and constant temperature T, this expression represents highly nonlinear stress-strain behavior (power law type function) after yielding:

$$\sigma = \sigma(\varepsilon_p) \tag{4.10}$$

Anand model predictions for the yield stress (σ_Y) and the Ultimate Tensile Strength (UTS = maximum/saturation stress) can be obtained by considering limiting cases of eq. (4.9). The UTS is given by the limit as ε_p goes to ∞:

$$\text{UTS} = \sigma\big|_{\varepsilon_p \to \infty} = \frac{\hat{s}}{\xi}\left[\frac{\dot{\varepsilon}_p}{A}e^{\left(\frac{Q}{RT}\right)}\right]^n \sinh^{-1}\left\{\left[\frac{\dot{\varepsilon}_p}{A}e^{\left(\frac{Q}{RT}\right)}\right]^m\right\} \equiv \sigma^* \tag{4.11}$$

while the yield stress is given by the limit as ε_p goes to 0:

$$\sigma_Y = \sigma\big|_{\varepsilon_p \to 0} = c s_0 = \frac{1}{\xi}\sinh^{-1}\left\{\left[\frac{\dot{\varepsilon}_p}{A}e^{\left(\frac{Q}{RT}\right)}\right]^m\right\} \; s_0 = c s_0 \equiv \sigma_0 \tag{4.12}$$

Using the saturation stress (σ^* = UTS) relation in eq. (4.11), the post yield stress-strain response (power law) in eq. (4.9) can be rewritten as:

$$\sigma = \sigma^* - \left[\left(\sigma^* - c s_0\right)^{(1-a)} + (a-1)\left\{(ch_0)\left(\sigma^*\right)^{-a}\right\}\varepsilon_p\right]^{1/(1-a)} \tag{4.13}$$

4.2.3 Determination Procedure of the Model Parameters from the Stress-Strain Data

As discussed above, the nine parameters of the Anand model are A, ξ, Q/R, m, h_o, a, s_o, $\hat{s}$, and n. One method to obtain the values of these parameters for a specific material is to perform a series of stress-strain tests over a wide range of temperatures and strain rates [105, 106]. From the measured data, the value of the saturation stress (σ^* = UTS) can be obtained for several strain rates and temperatures. In addition, the stress-strain (σ, ε) data for each temperature and strain rate can be recast as stress vs. plastic strain data (σ, ε_p) by using

$$\varepsilon_p = \varepsilon - \frac{\sigma}{E} \tag{4.14}$$

where E is the initial elastic modulus of the material at the specific temperature and strain rate being considered. The Anand model parameters can be obtained by following procedure

1. Determine the values of the parameters $\hat{s}$, ξ, A, Q/R, n and m by non-linear regression (least squares) fitting of eq. (4.11) to the saturation stress vs. strain rate and temperature data.
2. Determine the values of parameters s_o, h_o, and a by non-linear regression (least squares) fitting of eq. (4.13) to the stress vs. plastic strain data at several strain rates and temperatures.

4.2.4 Theoretical Formulation for Creep Response

Substitution of the evolution expression from eq. (4.13) into the flow equation in eq. (4.4) leads to an expression relating the strain rate to the strain, applied stress, and temperature:

$$\dot{\varepsilon}_p = A\, e^{-\left(\frac{Q}{RT}\right)}\left[\sinh\left\{\xi\sigma\left(\hat{s}\left[\frac{\dot{\varepsilon}_p}{A}e^{\left(\frac{Q}{RT}\right)}\right]^n - \left(\left(\hat{s}\left[\frac{\dot{\varepsilon}_p}{A}e^{\left(\frac{Q}{RT}\right)}\right]^n - s_0\right)^{(1-a)} + (a-1)\left\{(h_0)\left(\hat{s}\left[\frac{\dot{\varepsilon}_p}{A}e^{\left(\frac{Q}{RT}\right)}\right]^n\right)^{-a}\right\}\varepsilon_p\right)^{\frac{1}{1-a}}\right)^{-1}\right\}\right]^{\frac{1}{m}} \tag{4.15}$$

For a creep test at constant temperature, σ and T are constants and eq. (4.15) represents a highly nonlinear ordinary differential equation for the creep response. This differential equation contains all nine parameters of the Anand model and must be solved to find the creep strain vs. time relationship for a given applied stress and temperature:

$$\varepsilon_p = \varepsilon_p(t) \tag{4.16}$$

Although the analytical solution of eq. (4.15) is not known, the equation can be solved numerically, and a Matlab code has been developed in this work to find the numerical solution for a particular temperature and applied stress level. The coding of the Anand model into ANSYS has also been used to verify the accuracy of our Matlab numerical solutions.

The differential equation in eq. (4.15) for the creep response can be recast as:

$$\varepsilon_p = f\left(\dot{\varepsilon}_p\right)$$

$$\varepsilon_p = \frac{1}{c_3\left(A^{-a}\dot{\varepsilon}_p\right)^n}\left[\left\{c_2\left(A^{-1}\dot{\varepsilon}_p\right)^n - \frac{\xi\sigma}{\sinh^{-1}\left(c_1 A^{-1}\dot{\varepsilon}_p\right)^m}\right\}^{1-a} - \left\{c_2\left(A^{-1}\dot{\varepsilon}_p\right)^n - s_o\right\}^{1-a}\right] \tag{4.17}$$

where

$$c_1 = e^{\left(\frac{Q}{RT}\right)}$$
$$c_2 = \hat{s}\left\{ e^{\left(\frac{Q}{RT}\right)} \right\}^n \tag{4.18}$$
$$c_3 = (a-1)\, h_0\, (c_2)^{-a}$$

4.2.5 Determination Procedure of the Model Parameters from the Creep Data

The nine parameters in the Anand model parameters can be determined solely from creep test data at different temperatures and stress levels by using equation (4.17). The solution procedure steps include:

1. Measure creep strain vs. time data for various applied stress levels and temperatures.
2. Fit the ε vs. t data for each set of testing conditions with an empirical model (e.g. Burger's model in eq. (3.6)).
3. Differentiate the empirical model (ε vs. t) to obtain an expression for the transient strain rate ($\dot{\varepsilon}$ vs. t) at each applied stress level and temperature
4. Express the strain as a function of strain rate, stress level, and temperature.
5. Determine the values of the model parameters by performing a nonlinear least squares regression fit of eq. (4.17) to the strain vs. strain rate and stress level data.

For example, using the procedure discussed above, the nine Anand model parameters for SAC305 lead free solder can be determined from the non-aged creep data in Figure 3.23. In order to apply the developed method to determine the Anand constants from creep data, plots of strain vs. strain rate must be generated for each testing temperature and stress level. For example, Figure 4.1 shows the ε vs. $\dot{\varepsilon}$ curves for non-

aged SAC305 solder subjected to a stress level of 10 MPa and temperatures of T = 25, 50, 75, 100, and 125 ^{o}C that were extracted from Figure 3.23. A non-linear least square regression method must then be used to fit Eq. (4.17) to these curves and extract the Anand constants from the experimental data.

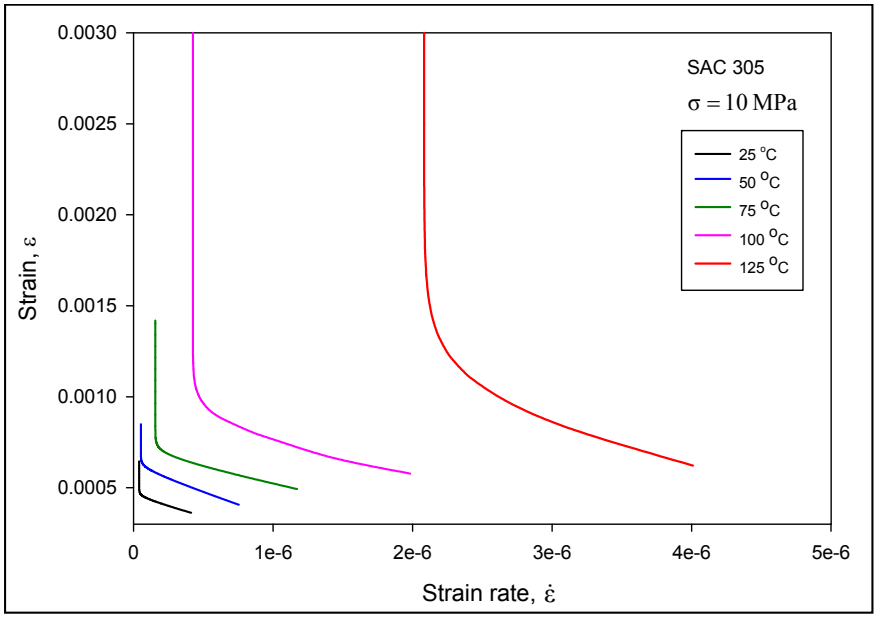

Figure 4.1 Example Strain vs. Strain Rate Plots for SAC305 Solder (σ = 10 MPa)

4.3 Determination of Anand Constants from the Stress-Strain Data (No Aging)

Using the 2-step procedure discussed above, the nine Anand model parameters for SAC305 lead free solder (non-aged) have been determined from the UTS (saturation stress) data in Figure 3.21, and the stress vs. plastic strain data extracted from the stress-strain curves in Figure 3.10. These procedures required least-squares nonlinear regression fitting, and in all cases the value of the correlation coefficient (r^2) was 0.85 or higher. The extracted Anand parameters are listed in Table 4.1.

Constant Number	Anand Constant	Units	SAC305 (Stress-Strain)	SAC305 (Creep)
1	s_0	MPa	21.00	16.33
2	Q/R	1/K	9320	9096
3	A	sec^{-1}	3501	3518
4	ξ	Dimensionless	4.0	4
5	m	Dimensionless	0.25	0.188
6	h_o	MPa	180,000	160000
7	$\hat{S}$	MPa	30.2	24.64
8	n	Dimensionless	0.01	0.015
9	a	Dimensionless	1.78	1.79

Table 4.1 Table of Anand Model Parameters Determined forSAC305 from Stress-Strain and Creep Data (No Aging)

4.3.1 Correlation of the Anand Model Predictions and Experimental Results for the Stress-Strain Curves (No Aging)

Once the Anand constants were determined, it is possible to use the constitutive model to predict the stress-strain curve at each particular temperature and strain rate used in the experimental testing. The Anand model stress-strain curves could then be correlated with the experimental stress-strain curves to evaluate the goodness of fit of the constitutive model to the test data. For each temperature and strain rate, the Anand model stress vs. plastic strain response can be determined from the measured stress-strain data and by using the following equation

$$\varepsilon = \varepsilon_e + \varepsilon_p \qquad \varepsilon_e = \frac{\sigma}{E} \tag{4.19}$$

where E is the initial elastic modulus at the particular temperature, strain rate, and aging conditions, and ε is the total strain, ε_e is the elastic strain, and E is the initial elastic

modulus. Figure 4.2 illustrates the correlation between the Anand model predictions (no aging) for the stress-strain curves and the experimental data from Figure 3.10 for the 5 temperatures and 3 strain rates considered. In all cases, good correlations were obtained indicating that the extracted Anand model parameters provide good fits to the experimentally characterized response. Correlations of the Anand model predictions with experimental results for other aging condition are shown in Appendix A.4.

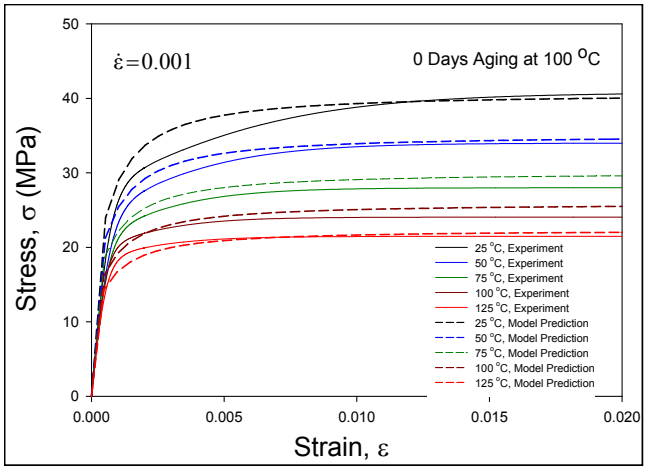

(a) $\dot{\varepsilon} = 0.001$

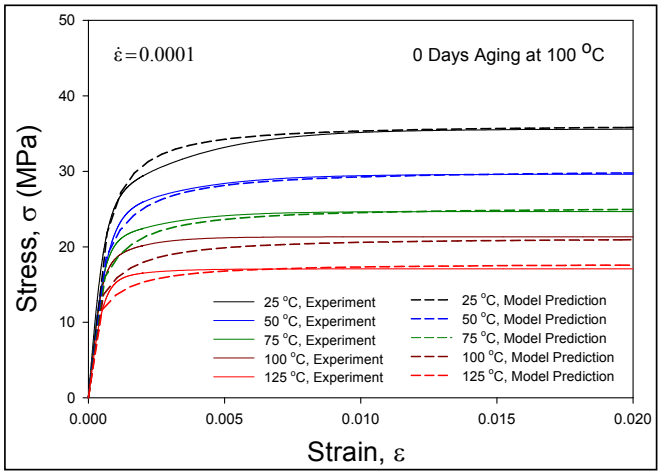

(b) $\dot{\varepsilon} = 0.0001$

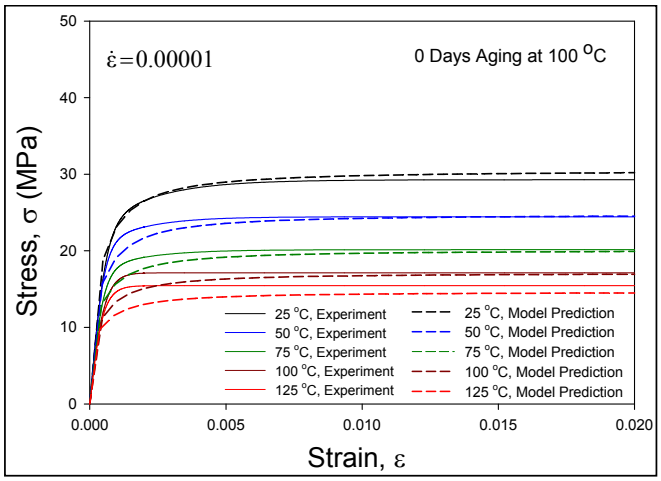

(c) $\dot{\varepsilon} = 0.00001$

Figure 4.2 Correlation of the Anand Model Predictions with Experimental Stress-Strain Data for No Aging

4.4 Determination of Anand Constants from Creep Curves (No Aging)

Using the 5-step procedure discussed above, the nine Anand model parameters for SAC305 lead free solder have been determined from the no aging creep data in Figure 3.23. In order to apply the developed method to determine the Anand constants from creep data, plots of strain vs. strain rate were generated for each testing temperature and stress level as shown in Figure 4.1. A non-linear least squares regression method was then used to extract the Anand constants from the experimental data. The value of the correlation coefficient (r^2) in the fitting result has been obtained as 0.85 or higher. The extracted Anand parameters are listed in Table 4.1.

4.4.1 Correlation of the Anand Model Predictions and Experimental Results for the Creep Curves (No Aging)

Once the Anand constants were determined from the creep data, it is possible to use the constitutive model to predict the creep curve at a particular temperature and stress level by solving Eq. (4.15) numerically. The Anand model predicted creep curves were

then correlated with the experimental creep curves to evaluate the goodness of fit of the constitutive model to the test data. Figure 4.3 illustrates the correlation between the Anand model predictions for the creep curves (no aging) and the experimental data from Figure 3.23 for the 5 temperatures and 3 stress levels considered. In all cases, good correlation was obtained indicating that the extracted Anand model parameters provide a good fit to the experimentally characterized response. Also, it has been found that the nine Anand model constants determined from two methods (stress-strain and creep testing) are very close in numerical value (see Table 4.1).

4.5 Effects of Aging on the Anand Model Parameters (Using Stress-Strain Data)

The Anand model parameters for aged SAC305 lead free solder material have been determined for each aging time from the temperature and strain rate dependent stress-strain data in Figures 3.11-3.18. The curves in each Figure were first processed to extract saturation stress (UTS) vs. strain rate and temperature data for each aging time, as well as stress vs. plastic strain data at several strain rates and temperatures for each aging time. From the extracted data from each Figure, the nine Anand parameters were calculated for each aging time using Eqs. (4.11, 4.13) and the nonlinear regression analysis procedure discussed above. The results of these computations are listed in Table 4.2.

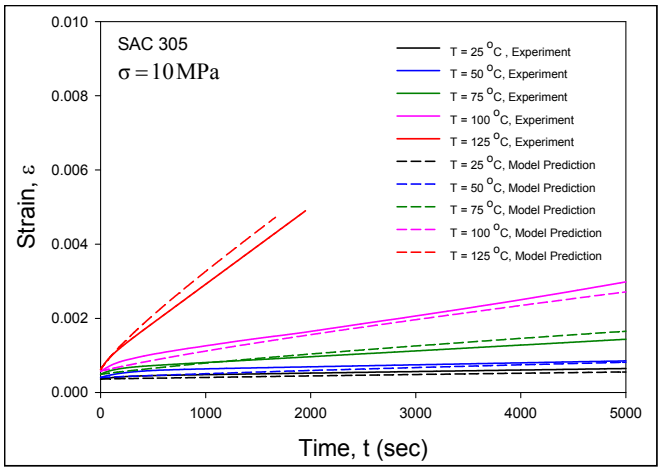

(a) σ = 10 MPa

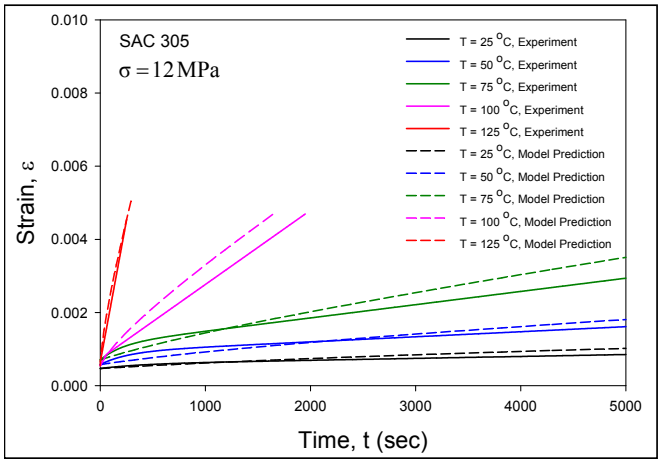

(b) σ = 12 MPa

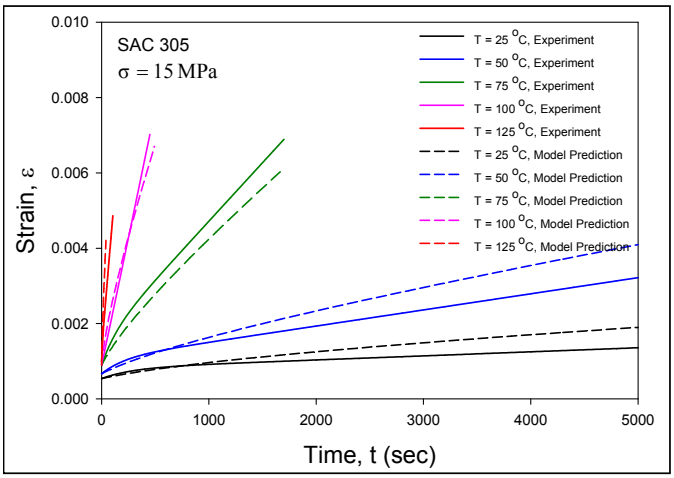

(c) σ = 15 MPa

Figure 4.3 Correlation of the Anand Model Predictions with Experimental Creep Curves for SAC305 (No Aging)

Par. No.	Anand Par.	Units	0 Days Aging	1 Days Aging	5 Days Aging	20 Days Aging	60 Days Aging	120 Days Aging	180 Days Aging	270 Days Aging	360 Days Aging
1	s_0	MPa	21.0	16.65	13.5	8.0	6.0	5.9	5.8	5.7	5.4
2	Q/R	K	9320	9320	9320	9320	9320	9320	9320	9320	9320
3	A	sec^{-1}	3501	3776	3960	4065	4095	4105	4110	4175	4210
4	ξ	-	4	4	4	4	4	4	4	4	4
5	m	-	0.25	0.226	0.21	0.19	0.18	0.18	0.18	0.18	0.18
6	h_o	MPa	180000	151000	135050	103218	89682	80825	77540	76130	73708
7	$\hat{S}$	MPa	30.2	27.7	26.0	22.8	22.3	22.0	21.9	21.7	21.4
8	n	-	0.0100	0.0058	0.0030	0.0015	0.0011	0.0010	0.0098	0.001	0.001
9	a	-	1.78	1.91	1.98	2.01	2.03	2.04	2.05	2.05	2.06

Table 4.2 Anand Model Parameters for SAC305 Solder for Various Aging Times (0-12 Months at 100 C)

The effects of aging on the Anand model parameters for SAC305 tabulated in Table 4.1 can be better visualized by plotting the extracted model parameters vs. aging time. Such graphs are presented in Figure 4.4 for parameters s_o, Q/R, A, ξ, m, h_o, $\hat{s}$, n, and a. The discrete parameter values in these Figures illustrate smooth variations with aging, and empirical mathematical models with linear and nonlinear terms have been able to accurately represent the variations of all of the Anand parameters with aging time. Parameters Q/R and ξ were found to be constant, and thus independent of aging. This is logical since Q is the activation energy of the SAC solder, which should be constant independent of aging. The other 7 parameters (s_o, A, m, h_o, $\hat{s}$, n, and a) all exhibit rapid changes during the first 20 days of aging, and then slow variations for aging times between 20 and 360 days. This is similar to the variations of the material properties with aging. The slow variations for longer aging times were found to be approximately linear with the aging time. The mathematical expressions for the aging time dependent empirical models used in Figure 4.4 are tabulated in Table 4.3. In all cases, the models

included constant and linear terms with aging time, along with a nonlinear functional term.

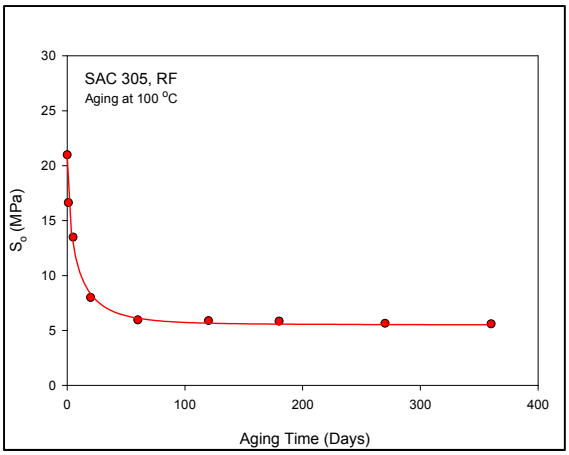

(a) Variation of s_o with Aging Time

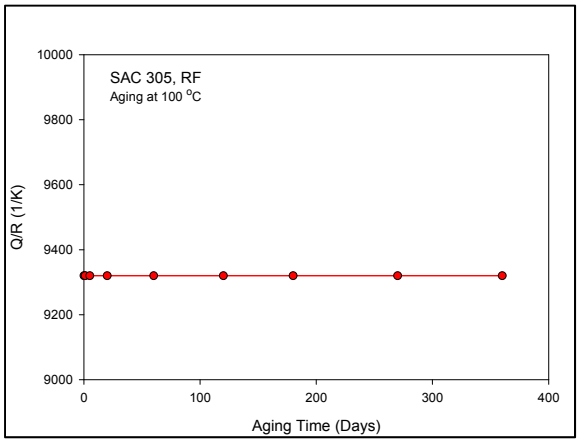

(b) Variation of Q/R with Aging Time

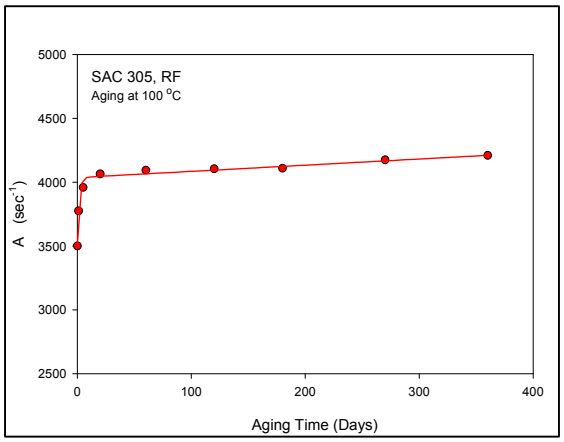

(c) Variation of A with Aging Time

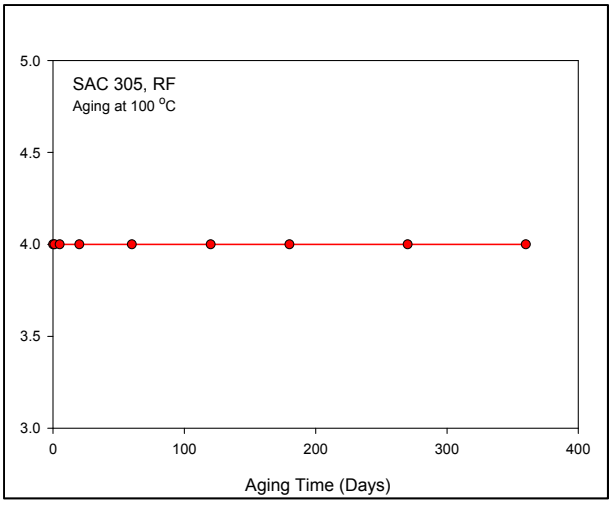

(d) Variation of ξ With Aging Time

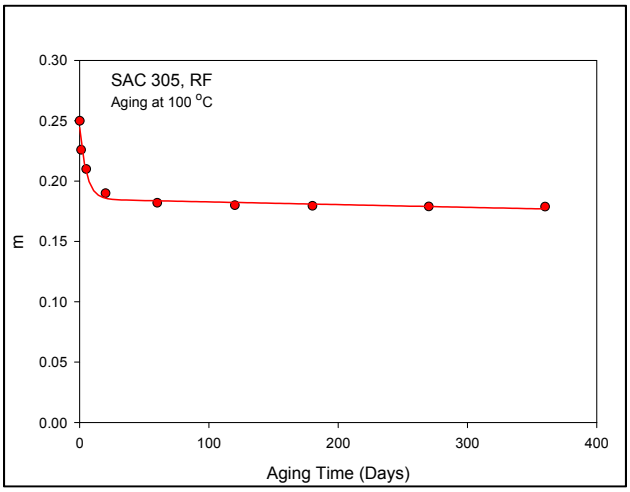

(e) Variation of m with Aging Time

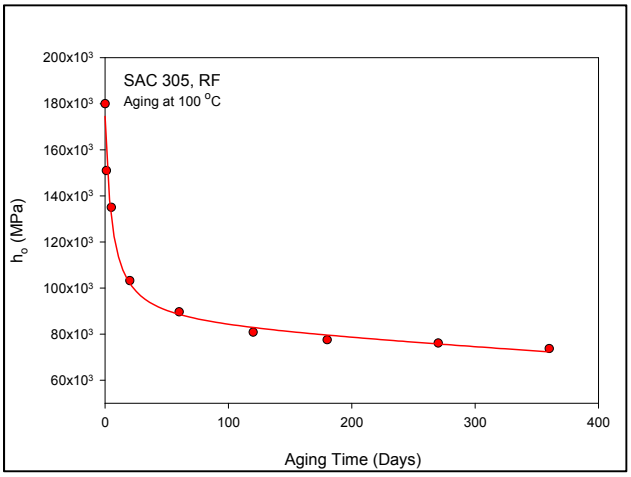

(f) Variation of h_o with Aging Time

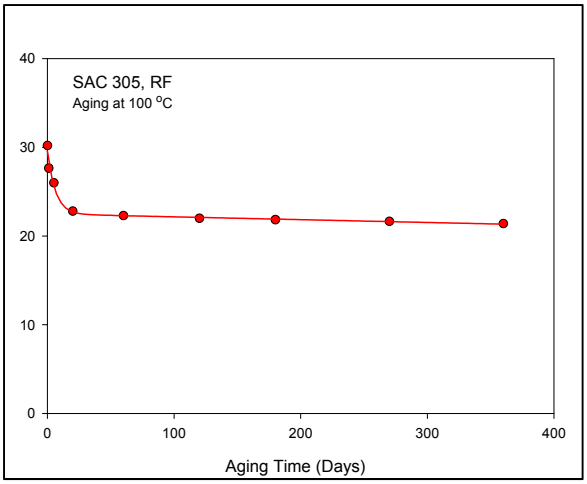

(g) Variation of $\hat{s}$ with Aging Time

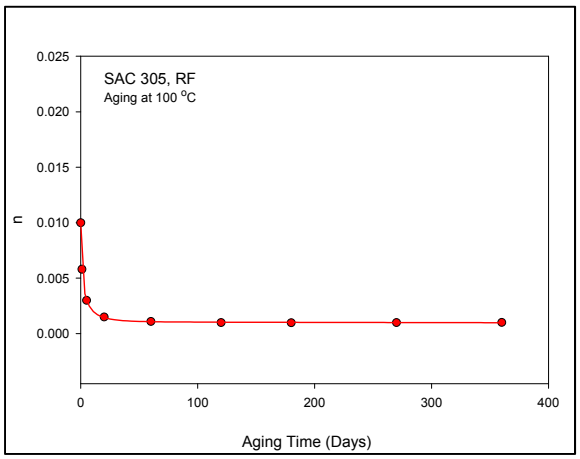

(h) Variation of n with Aging Time

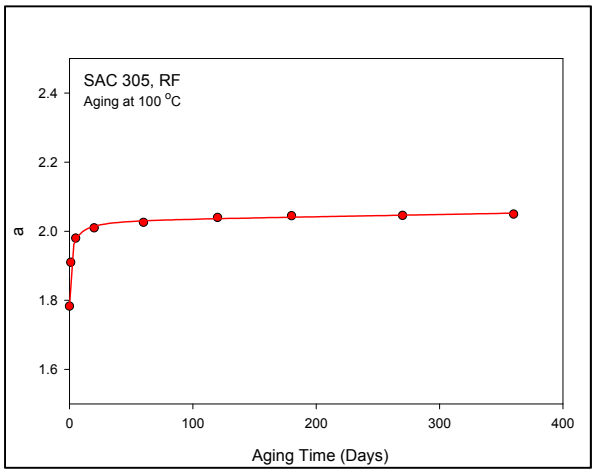

(i) Variation of a with Aging Time

Figure 4.4 Variation of the Anand Model Parameters of SAC305 Solder with Aging Time

Anand Constant	Form of Empirical Fitting Equation
S_o, m, n, a	$\text{Parameter} = C_o + C_1 t + C_2 e^{-C_3 t^{C_4}}$
A, $\hat{s}$	$\text{Parameter} = C_0 + C_1 t + C_2 (1 - e^{-C_3 t})$
h_o	$\text{Parameter} = C_0 + C_1 t + \frac{C_2}{C_3 + e^t}$
Q/R, ξ	$\text{Parameter} = C_o$

Table 4.3 Empirical Models for Variation of the Anand Model Parameters with Aging Time

4.6 Effect of Aging on the Anand Model Parameters (Using Creep Data)

The Anand model parameters for SAC305 lead free solder material have been also determined for each aging time from the temperature and stress level dependent creep data in Figures 3.23-3.28. The curves in each Figure were first processed to extract strain vs. strain rate and stress level data for each aging time (up to 6 months of aging). From the extracted data from each Figure, the nine Anand parameters were calculated for each aging time using Eq. (4.17) and the nonlinear regression analysis procedure discussed in section 4.2.5. The results of these computations are tabulated in Table 4.4.

Plots of extracted model parameters vs. aging time for the parameters found using creep data are shown in Figure 4.5. Comparisons between the Anand parameter variations determined by stress-strain and creep data are also illustrated in this figure (up to 6 months of aging). As was found when using stress-strain data, the Anand parameter values found with creep tests also illustrate smooth variations with aging, and empirical mathematical models with linear and nonlinear terms (see Figure 4.3) have been able to accurately represent the observed variations with aging time. Parameters Q/R and ξ were

again found to be constant, and thus independent of aging. The other 7 parameters (s_o, A, m, h_o, $\hat{s}$, n, and a) all exhibit rapid changes during the first 20 days of aging, and then slow variations for aging times between 20 and 180 days. This is similar to the variations of the material properties with aging.

Constant Number	Anand Constant	Units	SAC 305 0 Day Aging	SAC 305 5 Days Aging	SAC 305 10 Days Aging	SAC 305 20 Days Aging	SAC 305 60 Days Aging	SAC 305 120 Days Aging	SAC 305 180 Days Aging
1	s_0	MPa	16.33	9.95	7.67	6.37	6.1	5.4	5.1
2	Q/R	1/K	9096	9096	9096	9096	9096	9096	9096
3	A	sec^{-1}	3518	3934	4041	4145	4225	4259	4287
4	ξ	Dimensionless	4	4	4	4	4	4	4
5	m	Dimensionless	0.188	0.153	0.143	0.136	0.138	0.136	0.134
6	h_o	MPa	160000	137150	124410	122170	121875	120575	119940
7	$\hat{S}$	MPa	24.64	23.30	22.88	22.41	22.01	21.80	210.5
8	n	Dimensionless	0.015	0.0075	0.004	0.0028	0.0025	0.002	0.0019
9	a	Dimensionless	1.79	2.13	2.21	2.25	2.30	2.33	2.35

Table 4.4 Anand Model Parameters for SAC305 Solder for Various Aging Times (0-6 Months at 100 C)

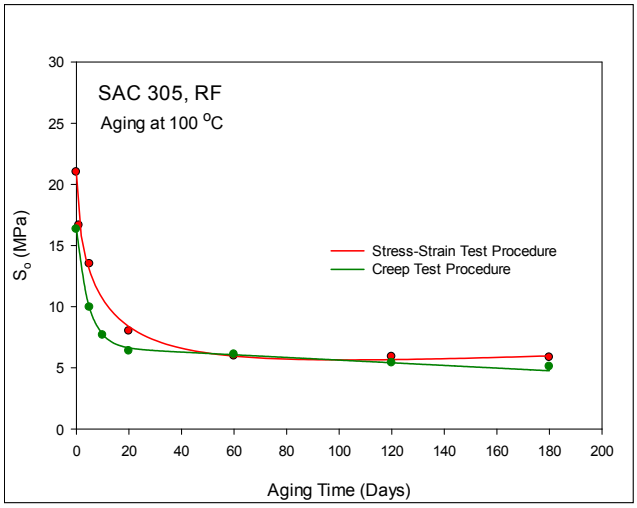

(a) Variation of s_o with Aging Time

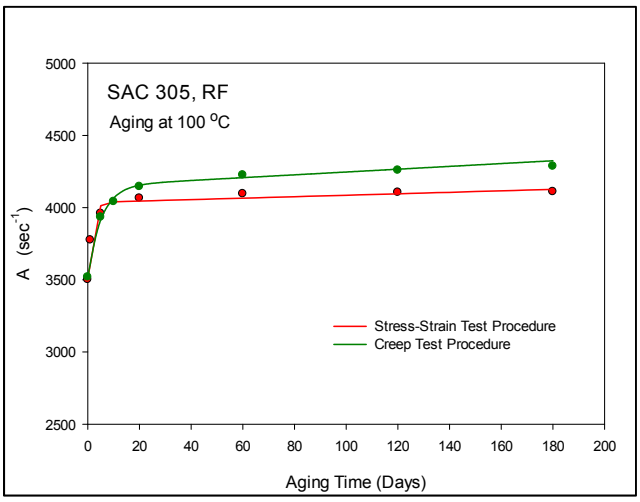

(b) Variation of A with Aging Time

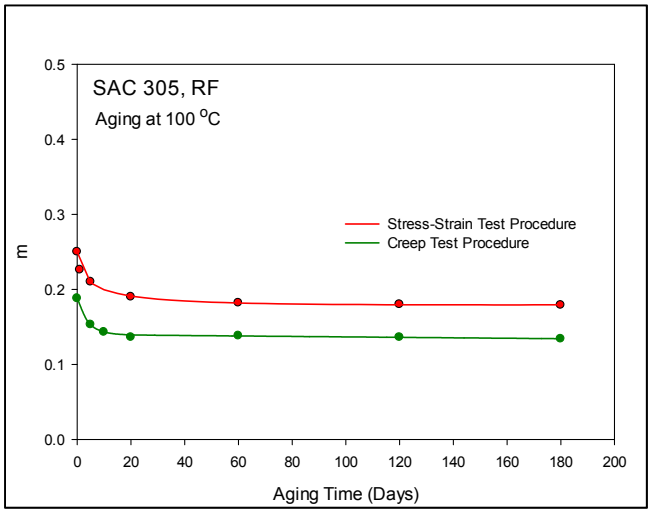

(c) Variation of m with Aging Time

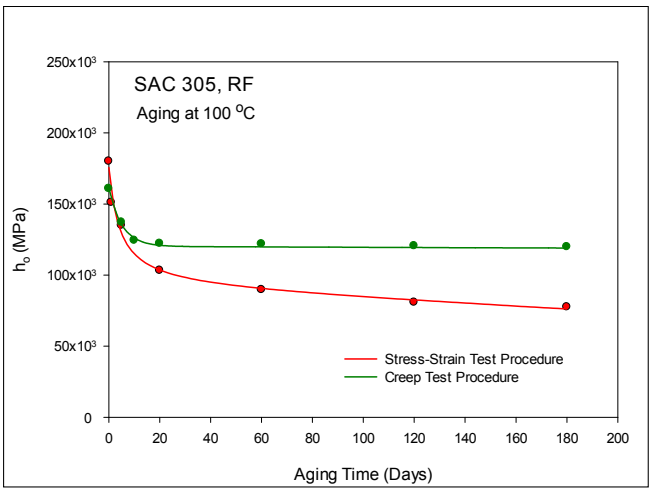

(d) Variation of h_o with Aging Time

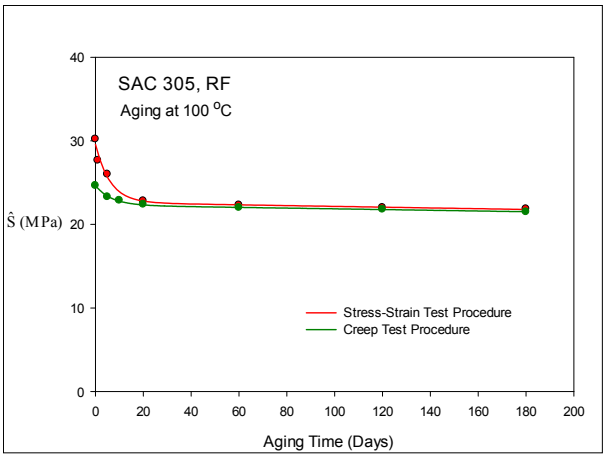

(e) Variation of $\hat{s}$ with Aging Time

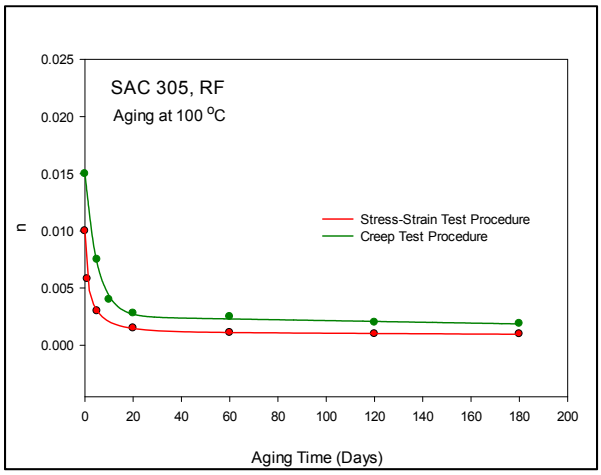

(f) Variation of n with Aging Time

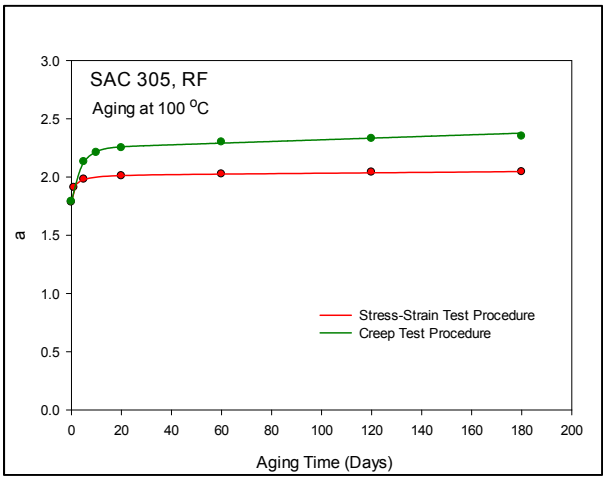

(g) Variation of a with Aging Time

Figure 4.5 Comparison of Anand Model Parameters Obtained from Stress-Strain and Creep Data

When comparing the results in Figure 4.5 for the parameters from the stress-strain test method with those from the creep test method, it appears that for some parameters (for example, h_o and a), the differences between the obtained values from the two methods become significant at longer aging times. The variations in the stress-strain response due to changes in value of a specific Anand parameter can be shown by plotting the stress-strain curve for different values of that one parameter and while keeping the other parameters fixed. Figure 4.6 shows such sensitivity plots for the parameters h_o and a. From results in Figure 4.5, it was observed that there was about 30% deviation of the parameter h_o between the creep test result and the stress-strain test result for 6 months of aging. Similarly, for parameter 'a', the analogous deviation was about was about 13%. Looking at Figure 4.6, it is observed that for 30% variation of h_o or 13% variation of 'a', the resulting stress-strain curves do not change dramatically. This supports the claim that the differences between the values of h_o and 'a' that were obtained from the two different testing methods (stress-strain and creep) are acceptable.

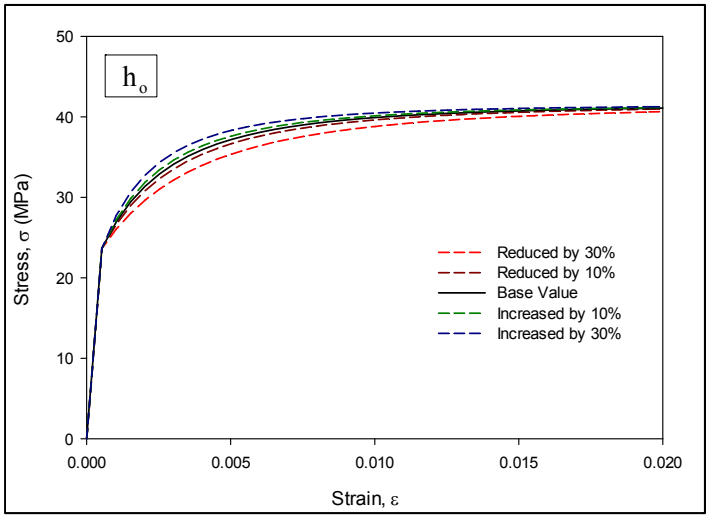

(a) Parameter h_o

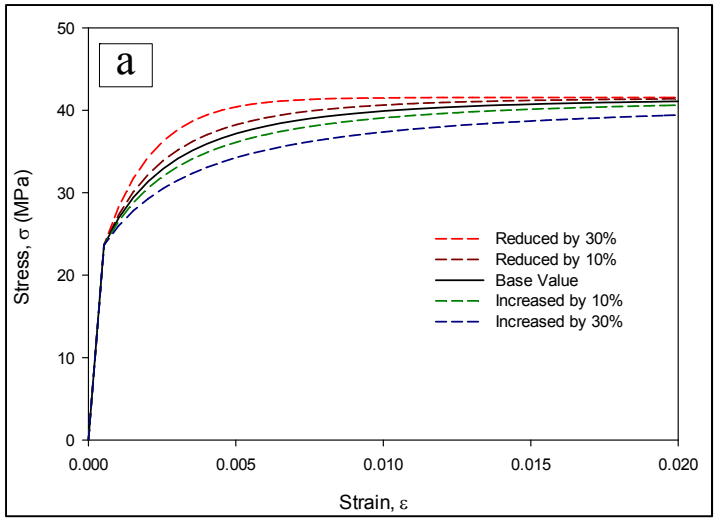

(b) Parameter a

Figure 4.6 Effects of Changing Parameters h_o and a on the Stress-Strain Curves

4.7 Estimated Anand Parameters for Other Aging Temperatures

The determination of the 100 C aging results in Figure 3.11 required 150 tensile tests (10 tests at 5 temperatures and 3 strain rates) for each aging time. Thus, 150 x 9 = 1350 tests were performed to complete Table 4.2. Extending this procedure to aging temperatures other than 100 C would necessitate performing a similar set of stress-strain experiments (multiple temperatures and strain rates) for the each additional aging temperature of interest. Obviously, this would be an extremely time consuming exercise. This procedure was shortened in this work, and an extrapolation technique was developed to estimate the variation of the Anand parameters at other aging temperatures including 25, 50, 75 and 125 ^{o}C. The estimation procedure is based on making the engineering assumption that the Anand parameters vary with aging time in a similar manner at all aging temperatures.

Empirical models were first used to fit the variation of the Anand parameters with aging time at 100 C. The same functional forms were then assumed to be valid at other

aging temperatures, and a more limited set of testing data were used to determine the constants in the empirical models and scale them (extrapolate) to the other aging temperatures. In particular, the variation of the parameters at four other aging temperatures (T = 25, 50, 75 and 125 C) was established using stress-strain data measured at room temperature (25 C) and one strain rate (0.001 sec^{-1}). Such data were available in our prior work [46, 64] at the four other aging temperatures. The results of this extrapolation procedure are shown in Figure 4.7, where the estimated variation for seven of the Anand parameters s_o, A, m, h_o, $\hat{s}$, n, and a, with aging time are plotted for the 5 different aging temperatures (T = 25, 50, 75, 100, 125 C). The brown curve in each plot (100 C aging) represents an empirical model fit to tabulated values in Table 4.2. The other curves in each plot were generated by the extrapolation procedure discussed above, which relied on the assumption of the same empirical variation for the parameter with aging time, and the use of limited stress-strain data to establish the constants in the scaled empirical model. The values of Q/R and ξ were found to be independent of aging time for 100 C aging. Thus, they were assumed to be independent of both aging temperature and aging time using the proposed estimation procedure.

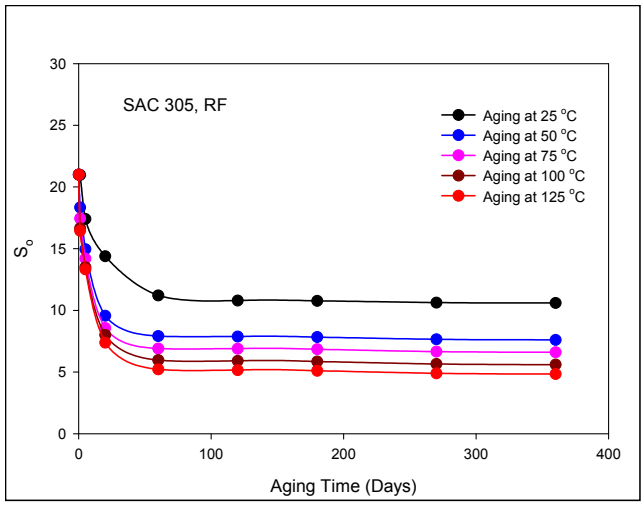

(a) Variation of s_o with Aging Time

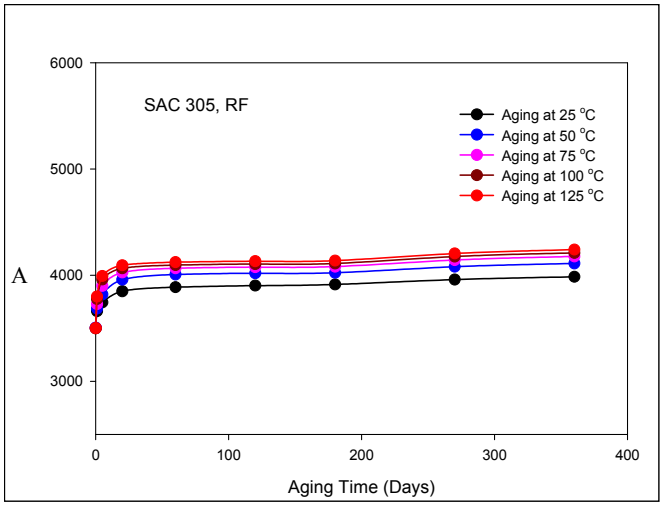

(b) Variation of A with Aging Time

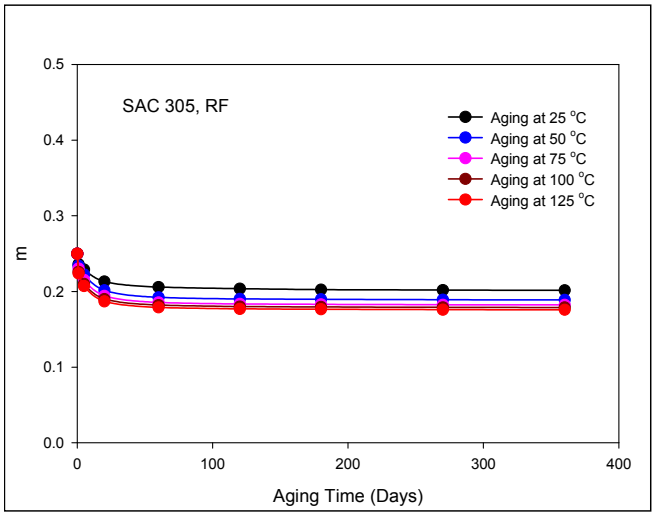

(c) Variation of m with Aging Time

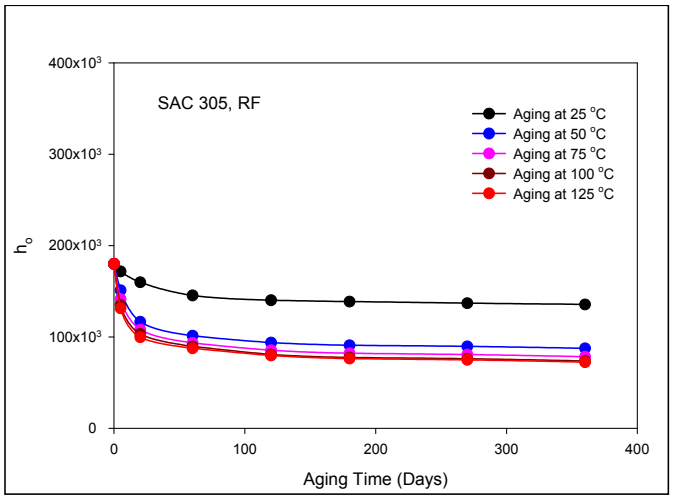

(d) Variation of h_o with Aging Time

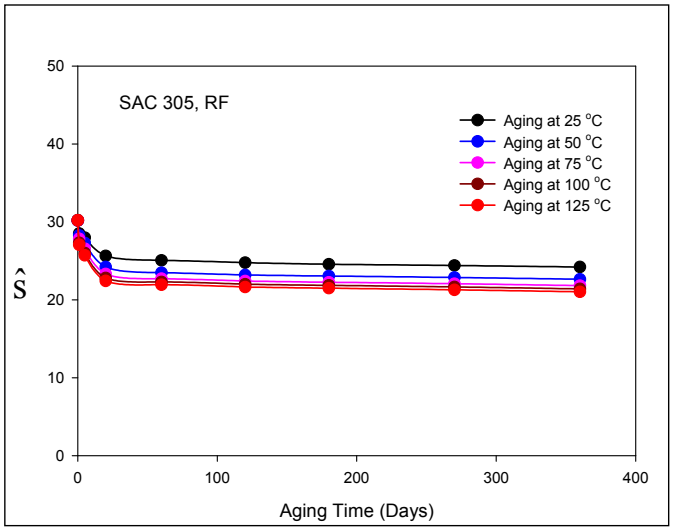

(e) Variation of $\hat{s}$ with Aging Time

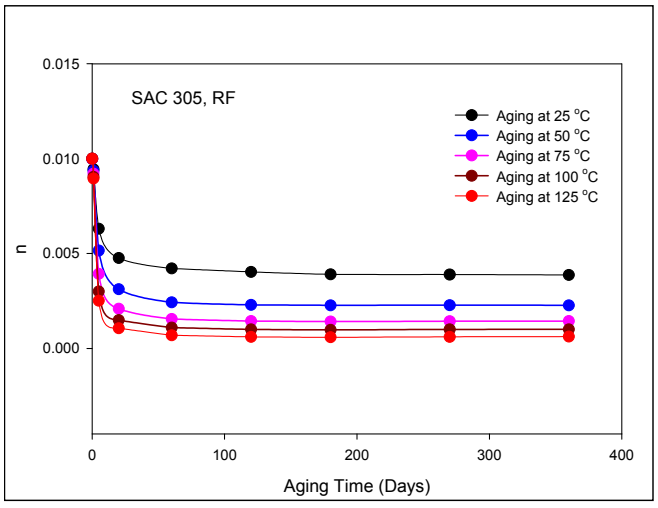

(f) Variation of n with Aging Time

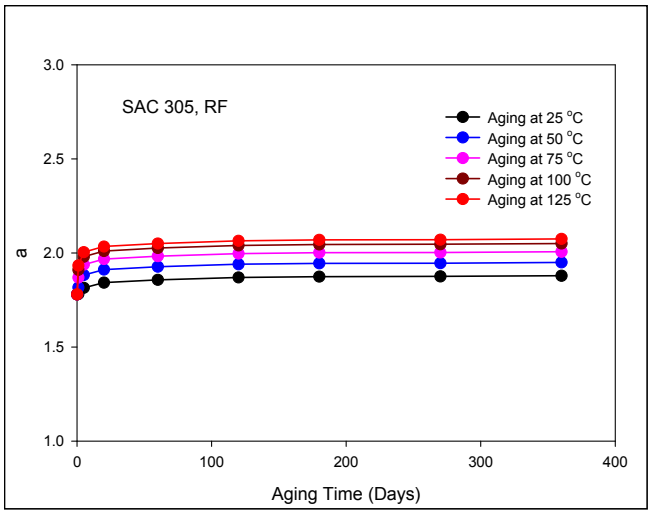

(g) Variation of a with Aging Time

Figure 4.7 Variation of the Anand Model Parameters of SAC305 Solder with Aging Time and Aging Temperature

From the plots in Figure 4.7, it is seen that 7 of the Anand model parameters (s_o, A, m, h_o, $\hat{s}$, n, a) exhibit rapid changes during the first 20 days of aging, and then slow variations for aging times between 20 and 360 days. The slow changes for longer aging times were found to be approximately linear with the aging time. Also, it is possible to generate a three-dimensional empirical aging model for the variation of each Anand parameter with aging time and aging temperature as illustrated in Figure 4.9a for Anand parameters. In this case, the mathematical expression used to fit the aging data was

$$m = C_1 + C_2 tT + C_3(1 - e^{-C_4 t})T \tag{4.20}$$

where t is the aging time and T is the aging temperature. Similar models have been established for the other parameters also as shown in Figure 4.9. As can be seen from equation (4.20), the models include constant and linear terms with aging time and aging temperature, along with a nonlinear functional term.

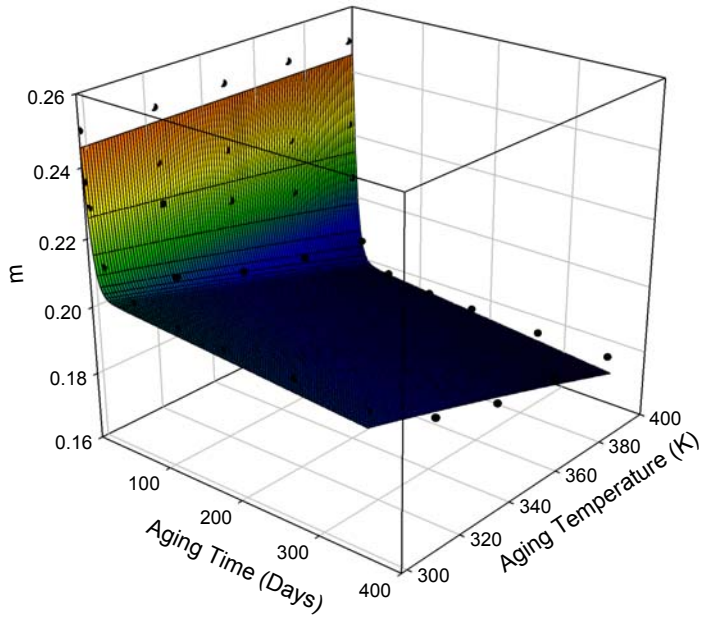

(a) Parameter m

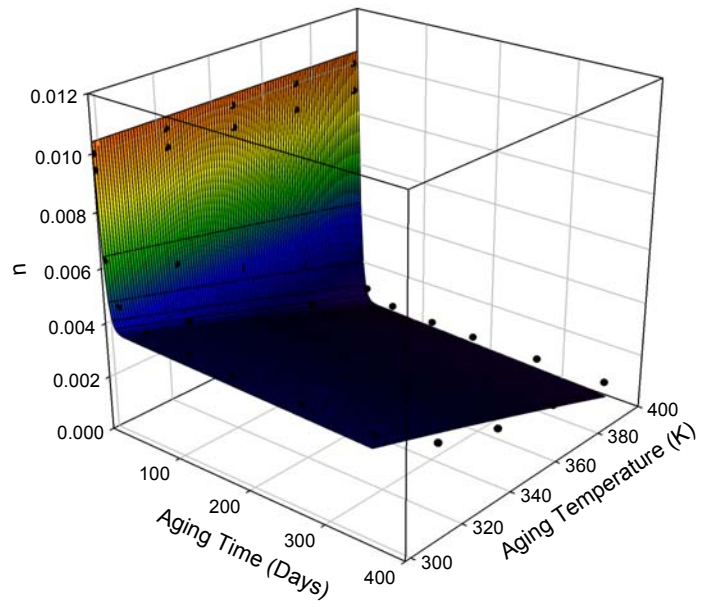

(b) Parameter n

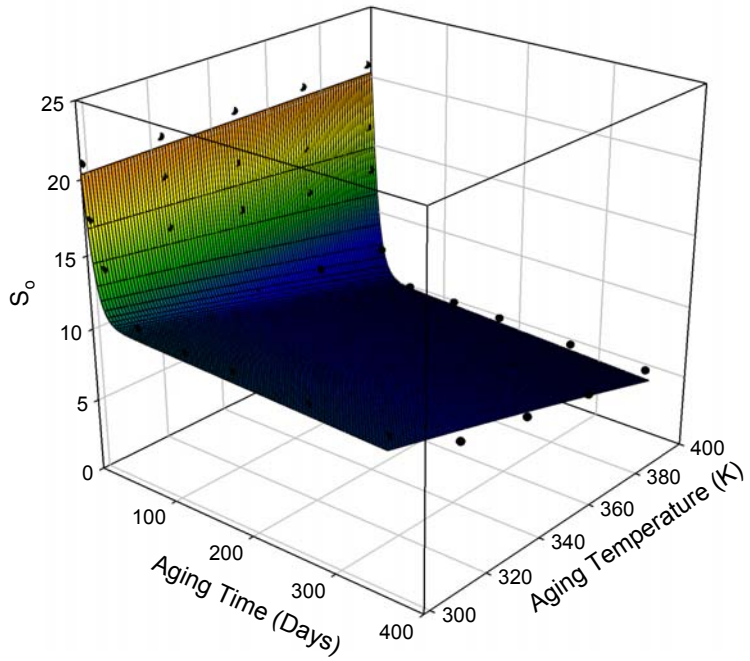

(c) Parameter s_o

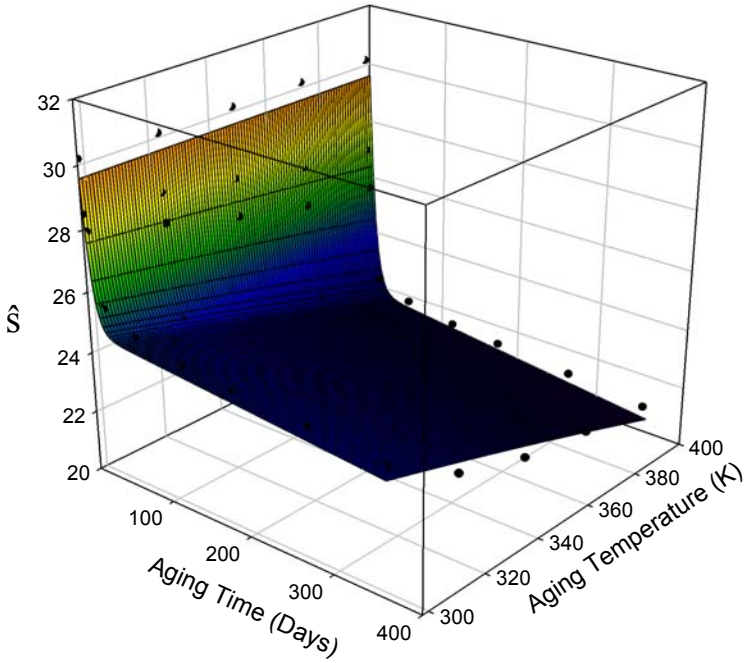

(d) Parameter $\hat{s}$

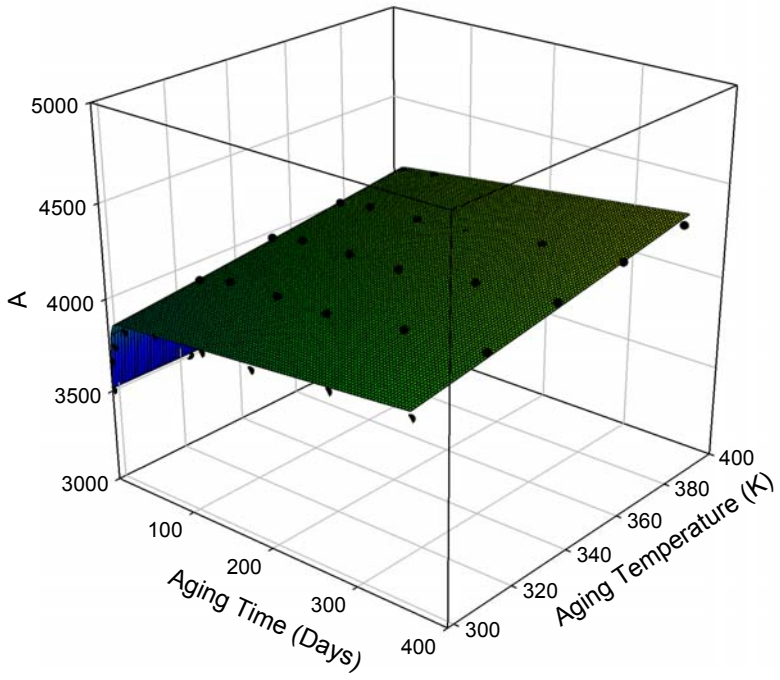

(e) Parameter A

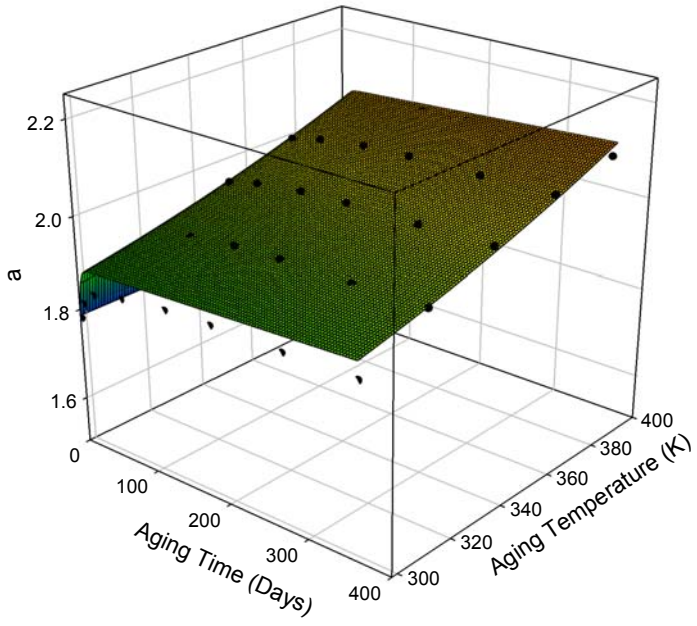

(f) Parameter a

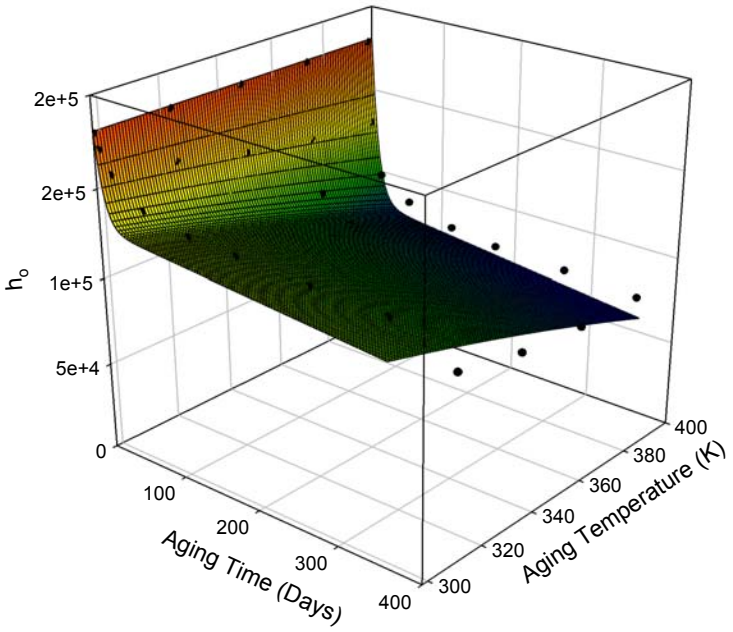

(g) Parameter h_o

Figure 4.8 Variation of the Anand Parameters of SAC305 Solder with Aging Time and Aging Temperature

4.8 Summary and Discussion

In this Chapter, the theoretical equations for the uniaxial stress-strain response (constant strain rate) and for the creep response of solder have been derived from the Anand viscoplastic model. Procedures for extracting the Anand model constants from experimental stress-strain and creep data were also established. The two developed methods were then applied to find the Anand constants for SAC305 lead free solder using the two completely different sets of experimental test data. The first set of Anand parameters were extracted from uniaxial stress strain data measured over a wide range of strain rates ($\dot{\varepsilon}$ = 0.001, 0.0001, and 0.00001 1/sec) and temperatures (T = 25, 50, 75, 100, and 125 ^{o}C), and for different durations of aging (0-12 months at 100 C). The second set

of Anand parameters were calculated from creep test data measured at several stress levels (σ = 6-15 MPa and temperatures (T = 25, 50, 75, 100, and 125 ^{o}C), and for different durations of aging (0-6 months at 100 C). The two sets of Anand model parameters derived from the stress-strain and creep data were compared, and the accuracy (goodness of fit) of the Anand model using the extracted material constants was evaluated by comparing the responses predicted from the Anand model with the measured stress-strain and creep data. The evolution of the model parameters with aging was then determined. Empirical equations for the variation of seven parameters with aging time (2 other parameters were unchanged with aging) were developed to modify the Anand viscoplastic constitutive model to include the aging effects.

Determination of Anand parameters for aging temperatures other than 100 ^{o}C would necessitate performing a similar set of stress-strain experiments (multiple temperatures and strain rates) for the each additional aging temperature of interest. Obviously, this would be an extremely time consuming exercise. This procedure was shortened in this work, and an extrapolation technique was developed to estimate the variation of the Anand parameters at other aging temperatures including 25, 50, 75 and 125 ^{o}C. The estimation procedure is based on making the engineering assumption that the Anand parameters vary with aging time in a similar manner at all aging temperatures. Empirical models were used to fit the variation of the Anand parameters with aging time at 100 C. The same functional forms were then assumed to be valid at other aging temperatures, and a more limited set of testing data were used to determine the constants in the empirical models and scale them (extrapolate) to the other aging temperatures.

CHAPTER 5

AGING EFFECTS ON RELIABILITY MODEL PARAMETERS

5.1 Introduction

Traditional finite element based predictions for solder joint reliability during thermal cycling accelerated life testing are based on solder constitutive equations (e.g. creep laws or Anand viscoplastic model) and failure models (e.g. Coffin-Manson or energy dissipation per cycle models) that do not evolve with material aging. Due to the strong influence of aging on the thermal cycling reliability of lead free solder assemblies, it is critical that aging effects be included in any reliability prediction methodology. This includes incorporation of the thermal history of the lead free solder joints such as thermal preconditioning (aging) before thermal cycling, as well as the gradual aging of the solders that occur during the thermal cycling process. Since the traditional finite element based reliability prediction methodologies discussed in Chapter 1 are based on solder constitutive equations and failure models that do not evolve with material aging, there will be significant errors in the calculations with lead free SAC alloys that illustrate dramatic aging phenomena.

In this chapter, new aging aware failure criteria has been developed based on fatigue data for lead free solder uniaxial specimens that were aged at elevated temperature for various durations prior to mechanical cycling. Using the measured fatigue data, mathematical expressions were developed for the evolution of the solder

fatigue failure criterion constants with aging, both for Coffin-Manson (strain-based) and Morrow-Darveaux (dissipated energy based) type fatigue criteria. Similar to the findings for mechanical/constitutive behavior, results show that the failure data and associated fatigue models for solder joints are affected significantly by isothermal aging prior to cycling.

5.2 Aging Effects on Solder Mechanical Fatigue Data

In a parallel investigation, Mustafa, et al. [41] measured the cyclic stress-strain behavior of lead free solders using uniaxial specimens similar to Figure 3.4, but with a shorter 10 mm gage length to avoid buckling when in the compression portion of the cycle. They also extended their work to examine long term mechanical cycling to fatigue failure. Figure 5.1 illustrates the typical evolution of the cyclic stress-strain hysteresis loop that occurs during a fatigue test. In this plot, hysteresis loops are shown for every 100 loading cycles. During the cycling, the peak stress of each loop drops continuously due to damage accumulation. In their study, failure of the specimen was defined to have occurred when there is a 50% reduction of the peak stress.

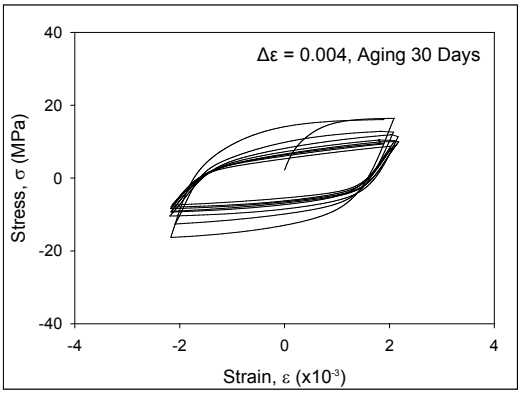

Figure 5.1 Hysteresis Loop Evolution During Fatigue Testing of SAC305 Solder [41]

In their investigation, according to the procedure discussed above, fatigue testing of SAC305 lead free solder specimens was performed for a wide range of applied strain levels and three different aging conditions prior to testing (aging at T = 125 C for 0, 30, 120 days). Figure 5.2 contains the measured fatigue data (plastic strain range vs. number of cycles to failure). Each data point represents an average of several fatigue tests at a particular strain level, and the error bars at each data point indicates the standard deviations. For each aging condition, the data varies linearly on the log-log plot, suggesting that the results can be well modeled by a Coffin-Manson [42] type low cycle fatigue law:

$$\begin{aligned} N_f^m \Delta\varepsilon_p &= C \\ \log(\Delta\varepsilon_p) &= [\log C] - m\log(N_f) \end{aligned} \tag{5.1}$$

From Figure 5.2, it is seen that fatigue life drops significantly with aging, especially during the first 30 days. Also, the value of m appears to be independent of prior aging.

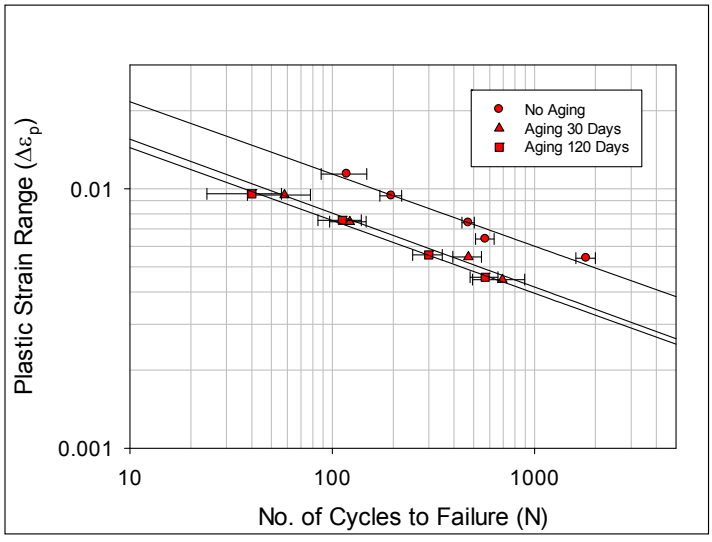

Figure 5.2 Fatigue Data for SAC305 Solder (Strain Range vs. Cycles to Failure)

The data in Figure 5.2 can be recast as energy dissipation per cycle (ΔW) versus cycles to failure as shown in Figure 5.3. For each fatigue experiment, the strain energy density was calculated from the area of the first cycle hysteresis loop. For each aging condition, the data again varies linearly on the log-log plot, suggesting that the results can be well modeled by a Morrow [134] type low cycle fatigue law

$$\begin{aligned} N_f^m \Delta W &= C \\ \log(\Delta W) &= [\log C] - m \log(N_f) \end{aligned} \tag{5.2}$$

Similar to the strain-based criterion, the value of m appears to be independent of prior aging.

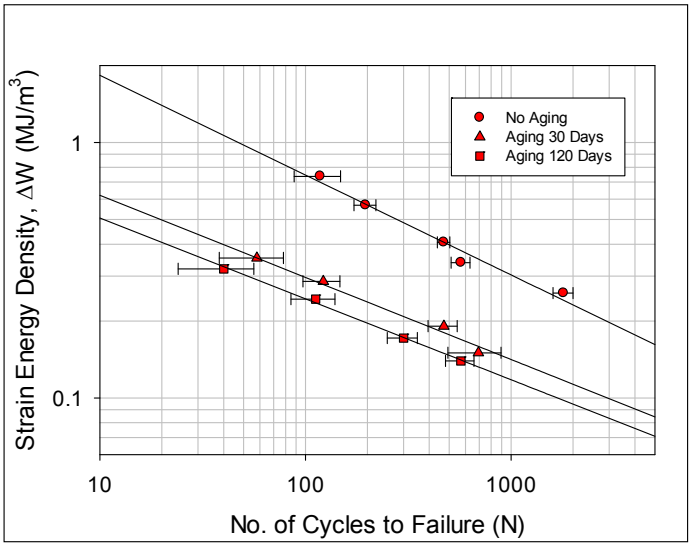

Figure 5.3 Fatigue Data for SAC305 Solder (Energy Dissipation vs. Cycles to Failure)

5.3 Determination of Life Prediction Model Parameters from the Fatigue Data

Darveaux [132] has presented energy dissipation based models for life prediction in solder joints subjected to cyclic loading. The approach consists of separate power law type relations for estimating crack initiation and crack growth rate in solder joints:

$$N_i = K_1 (\Delta W)^{K_2} \tag{5.3}$$

$$\frac{da}{dN} = K_3 (\Delta W)^{K4} \tag{5.4}$$

where N_i is the number cycles to crack initiation, da/dN is the crack growth rate (assumed constant) occurring after crack initiation, ΔW is the energy dissipation per cycle in the solder sample (e.g. critical solder ball), and K_1, K_2, K_3, and K_4 are fitting constants. Once the crack location and path are known in the solder joint, the number of cycles to failure can be estimated using:

$$N_f = N_i + \frac{a_c}{\left[\frac{da}{dN}\right]} \tag{5.5}$$

where N_f is the number of cycles to failure, a_c is the length of the fully developed crack at failure/fracture, and N_i and da/dN are calculated from ΔW using Eqs. (5.3-5.4).

5.3.1 Determination of Life Prediction Model Parameters K_1 and K_2

Since the stress state is essentially constant in a uniaxial specimen subjected to cyclic loading, the number of cycles to failure in a mechanical fatigue test is essentially the same as N_i in Eq. (5.3). Thus, parameters K_1, K_2 in the crack initiation expression can be found by using the fatigue data presented earlier. For example, Figure 5.4 shows the non-linear least squares regression fitting of Eq. (5.3) to the fatigue data in Figure 5.3

for the case of no aging prior to cycling. The calculated fitting constants of K_1 = 37.97 (Cycles/MPa^{K2}) and K_2 = -2.8 are similar to other values present in the literature. The evolution of the values of K_1 and K_2 with aging can be found by fitting Eq. (5.3) to the data in Figure 5.3 for other aging conditions. These results are tabulated in Table 5.1, and plots of the variation of K_1 and K_2 with aging time are shown on Figures 5.5 and 5.6, respectively. The fatigue data in reference [41] were available for up to 4 months aging at 125 C. The fitting curves in Figures 5.5-5.6 were used to estimate the variation of the model parameters with aging for longer aging times and all aging temperatures. This approach will be conservative for aging temperatures less than 125 C.

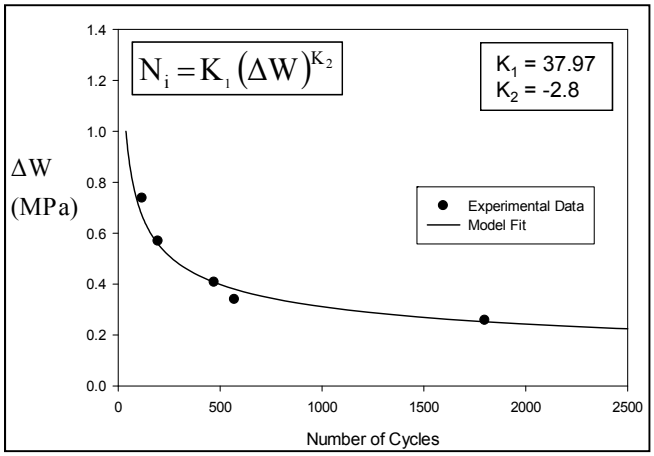

Figure 5.4 Variation of Energy Accumulated per Cycle with Number of Cycles, and Fitting Curve

Aging Time (Days)	K_1 (Cycles/MPa^{K_2})	K_2
0	37.97	-2.80
30	3.047	-2.90
120	1.413	-3.05
180	1.413	-3.13
360	1.413	-3.16

Table 5.1 Variation of Reliability Model Constants with Aging Time at 125 C

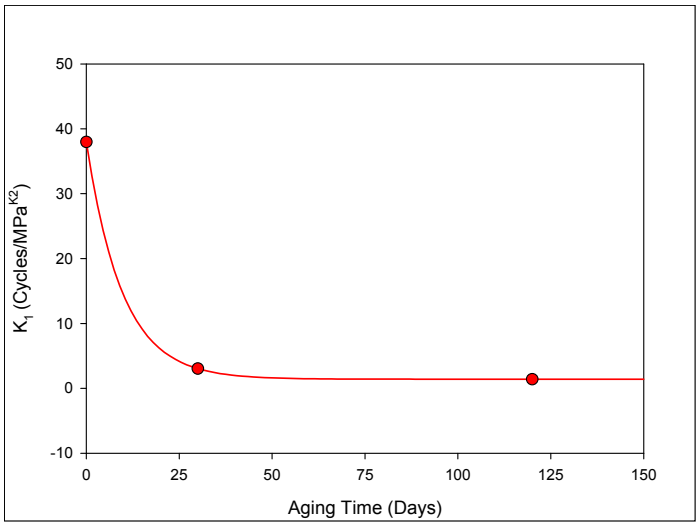

Figure 5.5 Variation of K_1 with Aging at 125 C

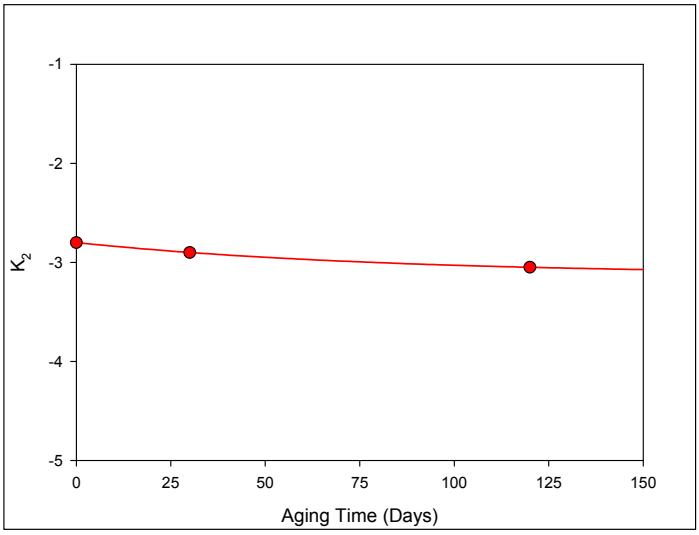

Figure 5.6 Variation of K_2 with Aging at 125 ^{o}C

5.3.2 Determination of Life Prediction Model Parameters K_3 and K_4

Calculation of parameters K_3 and K_4 in Eq. (5.4) requires crack propagation data from assemblies with a similar component form factor (PBGA) and solder alloy (SAC305). Such data were not available for the components in question. However, it is possible to estimate the values for these parameters using Weibull failure data and the assumption of a constant crack propagation rate.

The effects of aging on the degradation of the thermal cycling reliability of lead free BGA assemblies is being explored through experimental life testing by Zhang, et al. [80]. In their study, PBGA daisy chain test assemblies are being subjected to up to 2 years of aging (25, 55, 85, and 125 C), followed by thermal cycling from -40 to 125 C or -40 to 85 C to failure. The test vehicle (see Figure 5.7) includes four sizes of BGA components. The testing includes components with SAC305, SAC105, and 63Sn-37Pb solder balls. The test matrix also includes several test board surface finishes including Im-Ag, Im-Sn, HASL Sn-Pb, and ENEPIG.

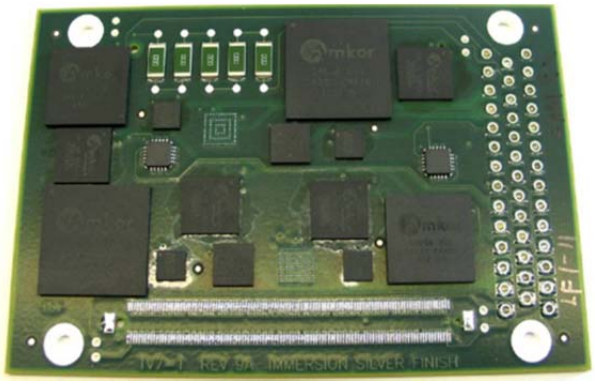

Figure 5.7 Assembled BGA Reliability Test Vehicle [80]

Results for aging up to 12 months prior to thermal cycling are available in reference [80]. For all component sizes and lead free solder alloys, the solder joint thermal cycling reliabilities of the BGA components were severely reduced by prior aging. For example, Weibull failure rate plots are shown in Figure 5.8 for 19 mm BGA components with SAC305 solder balls for (a) 6 months aging and (b) 12 months aging prior to thermal cycling. These results are for Im-Ag PCB surface finish and thermal cycling from -40 to 125 C. Clear degradations in life were observed to occur for aged components relative to non-aged components, and the amount of degradation was

exacerbated with higher aging temperatures. Using the 63.2% Weibull characteristic life (η) as a failure metric, the reliability was observed to decrease by 37% (6 months aging) and 53% (12 months aging) for the 19 mm BGA components subjected to aging at 125 C prior to thermal cycling. Figure 5.9 contains a plot illustrating the decreases in characteristic life experienced by the 19 mm BGA components (SAC305) when exposed to various aging conditions prior to thermal cycling. The effects of aging for the components with Sn-Pb solder balls were much less than those exhibited by the components with SAC lead free solder balls [80].

Rearranging eq. (5.5) yields

$$\frac{da}{dN} = \frac{a_c}{\left[N_f - N_i\right]} \tag{5.6}$$

This expression can be used to estimate the crack growth rates for various aging conditions by using the following assumptions: $N_f = \eta$ = Weibull Characteristic Life from Figure 5.8, a_c = 0.46 mm is the crack length for an assumed crack path across the top of the solder ball, and N_i is the cycles to crack initiation calculated using Eq. (5.3) with the K_1 and K_2 values from the curves in Figures 5.5-5.6, and ΔW from the finite element calculations (details are given in Chapter 6, see Figure 6.23). With this approach, the crack growth rates tabulated in Table 5.2 were found. As expected, the crack growth rate increases with the severity of the aging conditions prior to thermal cycling. Although it is interestingly observed that crack growth rate is higher for no aging condition with compare to other aging conditions, similar results were found by analyzing the failure data of PBGA assemblies from other investigators [135]. The crack propagation rate vs. ΔW plot for different prior aging conditions is shown in Figure 5.10. These data were fit

with the crack propagation model in Eq. (5.4) to yield the dependence of parameters K_3 and K_4 with aging conditions as tabulated in Table 5.3.

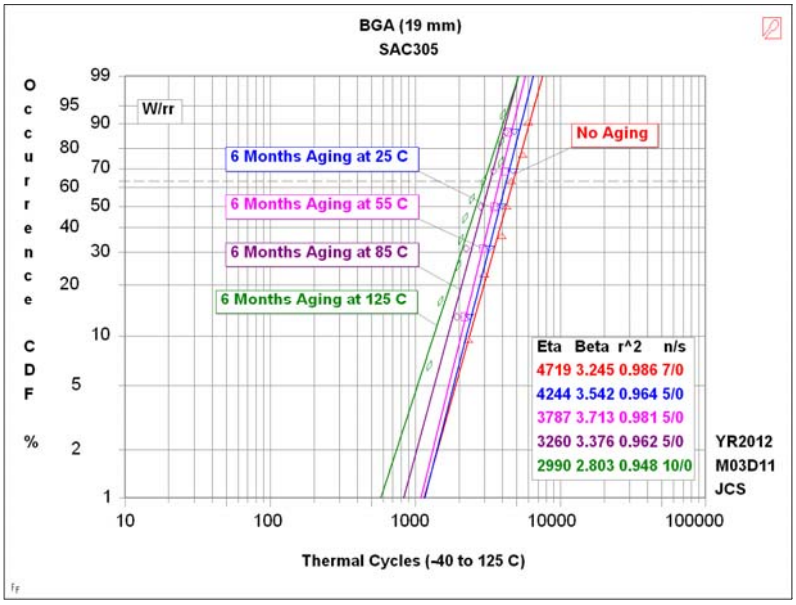

(a) Thermal Cycling Life for 6 Months Prior Aging

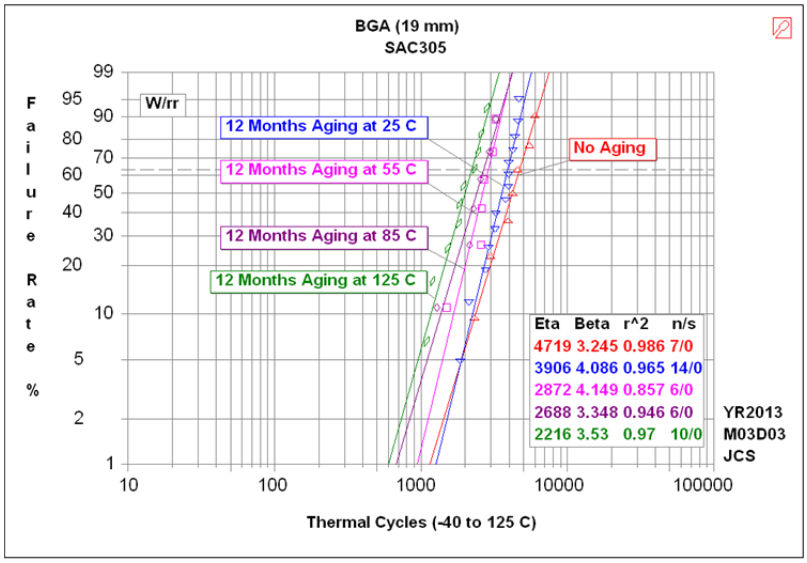

(b) Thermal Cycling Life for 12 Months Prior Aging

Figure 5.8 Life Reduction in SAC305 BGA Assemblies Subjected to Aging Prior to Thermal Cycling [80]

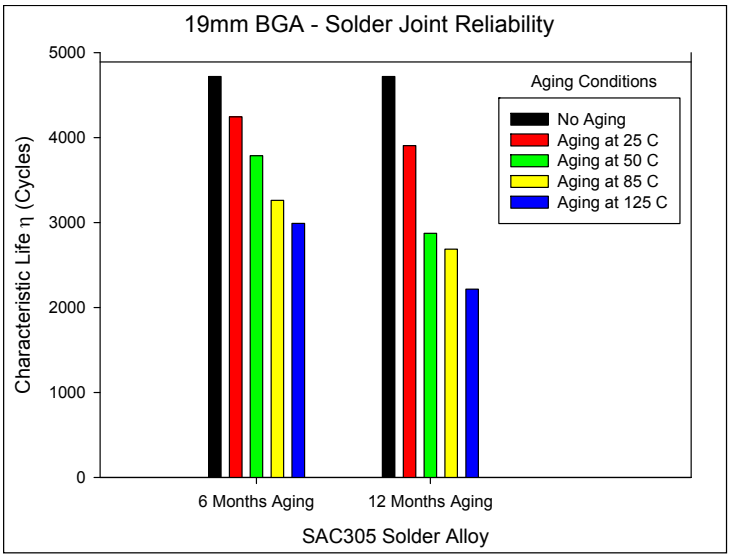

Figure 5.9 Effects of Aging on Characteristic Life
(19 mm BGA, Im-Ag Surface Finish)

Aging Time	Aging Temperatures (° C)	$\frac{da}{dN}$ (mm/Cycle)
No Aging	-	1.94E-07
6 Months	25	1.11E-07
	55	1.24E-07
	85	1.44E-07
	125	1.56E-07
12 Months	25	1.20E-07
	55	1.64E-07
	85	1.75E-07
	125	2.11E-07

Table 5.2 Crack Propagation Rates vs. Aging Conditions

The black curve in Figure 5.10 is the fitted curve through only one point (no aging data). This fit was obtained by assuming the value of K_4 and calculating the corresponding value of K_3 using equation Eq. (5.4). The determination of the constants

K_3 and K_4 for the aged packages involved the procedure of solving the Eq. (5.4) for two unknowns (K_3 and K_4). Since each aging temperature had two data points in Figure 5.10 (6 months and 12 months), it was possible to extract the two unknowns by solving the two equations with two unknowns.

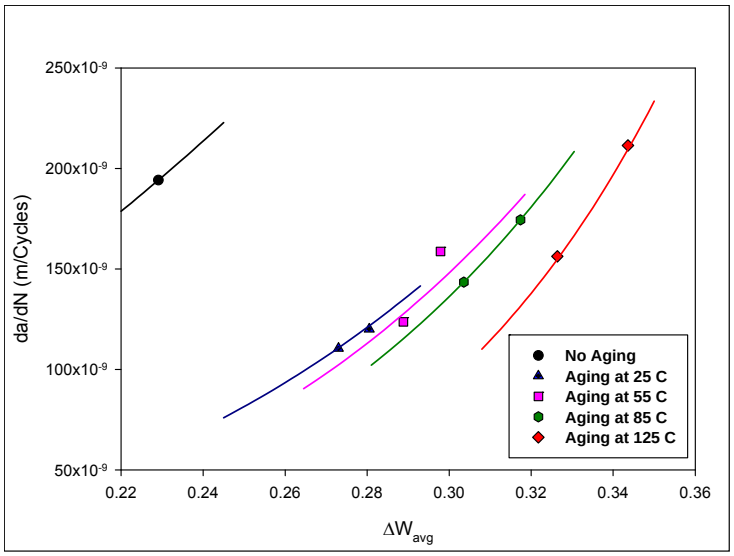

Figure 5.10 Crack Propagation Rates for Different Prior Aging Conditions and the Fits to Determine K_3 and K_4

Aging Temperature (°C)	K_3 (m/Cycles-MPa^{K_4})	K_4
No Aging	3.99×10^{-6}	2.05
25	5.96×10^{-6}	3.07
55	1.65×10^{-5}	3.92
85	2.71×10^{-5}	4.39
125	1.14×10^{-4}	5.89

Table 5.3 Variation of the Crack Propagation Rate Model Constants with Aging Time

5.4 Summary and Discussion

In this chapter, new aging aware failure criteria has been developed based on fatigue data for lead free solder uniaxial specimens that were aged at elevated temperature for various durations prior to mechanical cycling. Using measured SAC305 fatigue data for different aging conditions, the evolution of reliability model parameters K_1 and K_2 with aging were determined. Empirical models for these parameters were developed, and similar to the findings for mechanical/constitutive behavior, the values of these two parameters were affected significantly with aging.

The other two reliability model parameters, K_3 and K_4 were determined from the crack growth experimental data for a 19 mm PBGA assembly. Failure data were available for this package at aging temperatures of 25, 55, 85, and 125 ^{o}C, and for no aging, 6 months, and 12 months aging prior to thermal cycling. The evolution of parameters K_3 and K_4 with aging were determined from these experimental data, and the results showed that aging has significant effects on the model parameters.

Traditional finite element based predictions for solder joint reliability during thermal cycling accelerated life testing are based on solder constitutive equations and failure models that do not evolve with material aging. Due to the strong influence of aging on the thermal cycling reliability of lead free solder assemblies, it is critical that aging effects be included in any reliability prediction methodology. The reliability model parameters K_1, K_2, K_3 and K_4 that were determined in this chapter will be used in next chapter to estimate the life of SAC solder balls in PBGA components that were subjected to thermal cycling between -40 to 125 ^{o}C with various aging conditions prior to thermal cycling.

CHAPTER 6

THERMAL CYCLING RELIABILITY PREDICTIONS FOR LEAD FREE SOLDER JOINTS IN PBGA ASSEMBLIES SUBJECTED TO PRIOR AGING

6.1 Introduction

It has been demonstrated in this study (Chapter 3) and also in other studies [44], [46] that isothermal aging leads to large reductions (up to 50%) in several key material properties for lead free solders including stiffness (modulus), yield stress, ultimate strength, and strain to failure. In addition, even more dramatic evolution has been observed in the creep response of aged solders, where up to 10,000X increases have been observed in the steady state (secondary) creep strain rate (creep compliance). Such degradations in the stiffness, strength, and creep compliance of the solder material are expected to be universally detrimental to reliability of solder joints in electronic assemblies. Traditional finite element based predictions for solder joint reliability during thermal cycling accelerated life testing are based on solder constitutive equations (e.g. Anand viscoplastic model) and failure models (e.g. energy dissipation per cycle models) that do not evolve with material aging. Thus, there will be significant errors in the calculations with lead free SAC alloys that illustrate dramatic aging phenomena. In this study, a new reliability prediction procedure was developed that utilizes constitutive relations and failure criteria that incorporate aging effects, and then the new approach was validated through correlation with thermal cycling accelerated life testing experimental data.

In this Chapter, the developed Anand constitutive equations for solder with aging effects have been implemented within the finite element code ANSYS. Finite element simulations were then performed to model the solder joint deformations in two different PBGA components attached to FR-4 printed circuit boards that were subjected to thermal cycling. Calculations have been made for non-aged PBGA assemblies, as well as for assemblies that had been aged before being subjected to thermal cycling.

Two different studies have been performed. In the first investigation, a 3D slice finite element mesh (half model) was analyzed for a 676 I/O PBGA component. This configuration was subjected to thermal cycling from 0 to 100 C (8 minute ramps and 10 minute dwells). The plastic energy dissipation with time was calculated and the energy dissipation per cycle was determined. Finally, the evolution of the plastic energy dissipation per cycle (ΔW) with aging was also calculated.

In the second study, a three-dimensional finite element analysis (FEA) of the 19 mm PBGA component with SAC305 interconnects discussed in Chapter 5 was performed to calculate the stress/strain histories in the solder joints during thermal cycling accelerated life testing. Simulation of thermal cycling from -40 to 125 C was performed, and several sets of aging conditions (aging temperature and time) prior to thermal cycling were considered. For each case, the plastic energy dissipation per cycle in the critical solder ball was calculated. These values were then combined with the aging aware fatigue criterion to make life predictions for the components with different aging conditions. As discussed in Chapter 5, the energy based criteria proposed by Darveaux [132] was used for predicting crack initiation and crack growth in the aged solder joints using the energy dissipation values calculated from the finite element analysis.

6.2 Finite Element Modeling of PBGA Assemblies

Three dimensional nonlinear finite element modeling of the two PBGA packages with pitches of 1.34 mm and 0.8 mm was done to simulate the thermal cycling of the components between 0 to 100 C (for the case of PBGA 676) and -40 to 125 C (for the case of 19 mm PBGA). The first model (PBGA 676) was used to investigate the effects of aging on the plastic energy dissipation per cycle (ΔW) in solder joints. The results were not correlated since the experimental reliability data were not available for this package. The second model (19 mm PBGA) was also used to study the effects of aging on the plastic energy dissipation per cycle (ΔW) in solder joints. Experimental reliability data for this package was available for thermal cycling between -40 to 125 C and for different aging conditions (6 months and 12 months aging at 25, 55, 85 and 125 C) prior to thermal cycling [80]. The finite element results were correlated with the experimental reliability data for this package.

6.2.1 Slice 3D Modeling of PBGA 676

Figure 6.1 illustrates the developed a 3D slice finite element mesh (half model) for the 676 I/O PBGA component examined in the first study. For the specified loading, this configuration was subjected to thermal cycling from 0 to 100 C as shown in Figure 6.2 (8 minute ramps and 10 minute dwells). The solder balls were taken to be SAC305 lead free alloy, and the Anand model with aging dependent material parameters was utilized as the solder constitutive model. The other materials in the assembly (FR4 PCB, silicon chip, BT laminate, die attach material, solder mask, epoxy overmold) were modeled as linear elastic. Table 6.1 shows the utilized material properties.

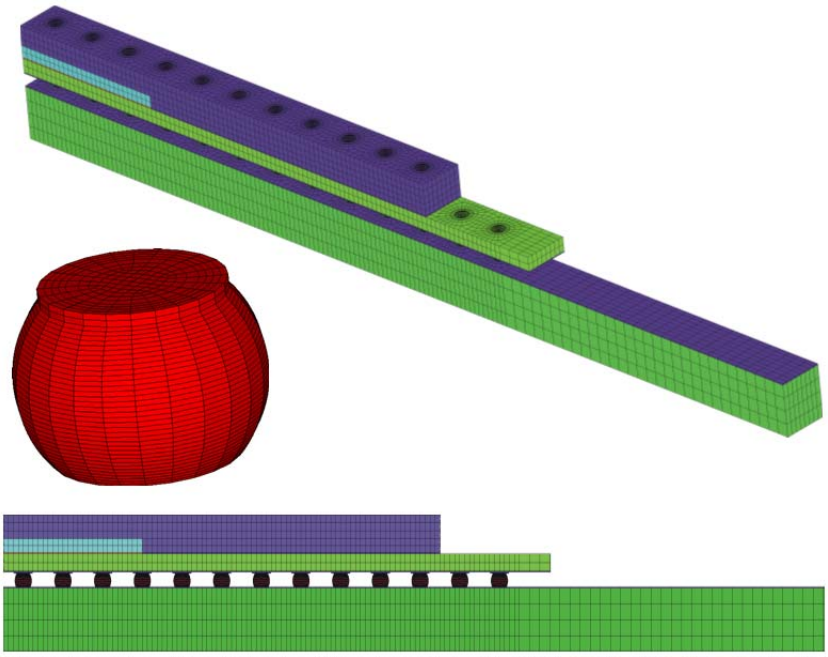

Figure 6.1 3D Slide Finite Element Model of 676 PBGA

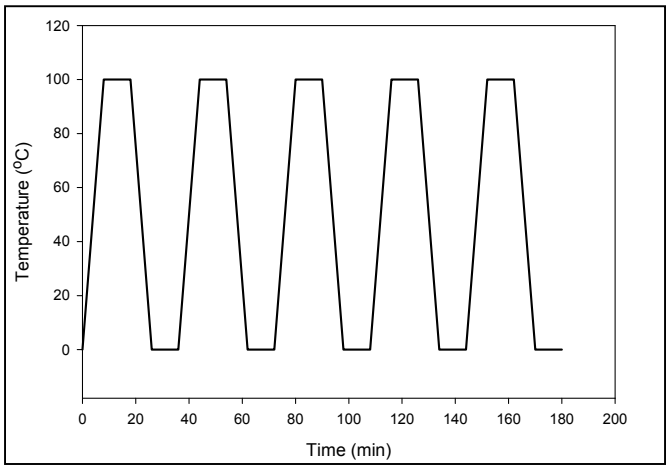

Figure 6.2 Thermal Cycle (0 to 100 C, 10 Minute Dwells)

The solder balls were modeled in ANSYS with VISCO107 structural elements with 8 nodes. This element is designed to solve both isochoric (volume preserving) rate-independent and rate-dependent large strain plasticity problems. For the other materials in the model, SOLID45 structural solid elements have been used, which are 8 node

elements with plasticity, creep, large deflection and large strain capabilities. Iterative solution procedures have been used due to the nonlinear material and kinematic properties of the model. Typical solution run times were about 1 hour per thermal cycle using a workstation with quad core processor and 16 GB of memory.

Material	Elastic Modulus (GPa)	Poisson's Ratio	CTE (ppm/C)
PCB	Ex = 16.90 Ey = 7.44 Ez = 16.90	PRxy = 0.39 PRyz = 0.39 PRxz = 0.11	CTEx = 14.5 CTEy = 67.2 CTEz = 14.5
Solder Mask	3.1	0.3	16.3
Copper	128	0.34	17
Solder	SAC305 Anand Model (Temperature Dependent)		
BT Laminate	Ex = 17.90 Ey = 7.84 Ez = 17.90	PRxy = 0.39 PRyz = 0.39 PRxz = 0.11	CTEx = 12.4 CTEy = 57 CTEz = 12.4
Die Attach	6.76	0.35	52
Die	169	0.28	2.54
Mold Compound	23.52	0.3	15

Table 6.1 Material Properties Used in the FEA Analysis (676 PBGA)

6.2.2 Quarter Modeling of 19 mm PBGA

In the second study, a three-dimensional finite element analysis (FEA) of the 19 mm PBGA component with SAC305 interconnects discussed above has been performed to calculate the stress/strain histories in the solder joints during thermal cycling accelerated life testing. The effects of prior aging have been included by using the modified Anand constitutive model developed in Chapter 4 that includes aging effects. Temperature dependent stress-strain behavior was included for the remaining packaging materials. Simulation for thermal cycling between -40 to 125 C has been performed considering several sets of aging conditions (aging temperature and time) prior to thermal

cycling. For each case, the plastic energy dissipation per cycle in the critical solder ball has been calculated. These values were then combined with an aging aware fatigue criterion to make life predictions for the components with different aging conditions. The energy based criteria proposed by Darveaux [132] have been used for predicting crack initiation and crack growth rate in the aged solder joints using the energy dissipation values calculated from the finite element analysis.

FEA analysis of 19 mm PBGA (288 solder interconnects, 0.8 mm pitch) has been used to calculate the accumulated strain energy dissipation per cycle in the solder joints as a result of thermal cycling between -40 to 125 ^{o}C. The PBGA component has a 19 x 19 mm form factor that includes a 12 x 12 x 0.28 mm silicon die. The mold compound and BT substrate both have planar dimensions of 19 x 19 mm, with thicknesses of 0.8 mm and 0.52 mm, respectively. The solder ball shapes were determined from cross-sectioning actual test assemblies (Figure 6.3).

Figure 6.4 shows the developed quarter symmetry model of the PBGA package that was developed and solved using ANSYS finite element software. The original ball height was 0.45 mm, while the final reflowed dimensions included a height of 0.40 mm (10% collapse) and a width/diameter of 0.60 mm. The PCB below the component had dimensions of 27.75 x 27.75 x 1.55 mm. The entire model utilized a structured finite element mesh with 642,880 elements and 697,242 nodes.

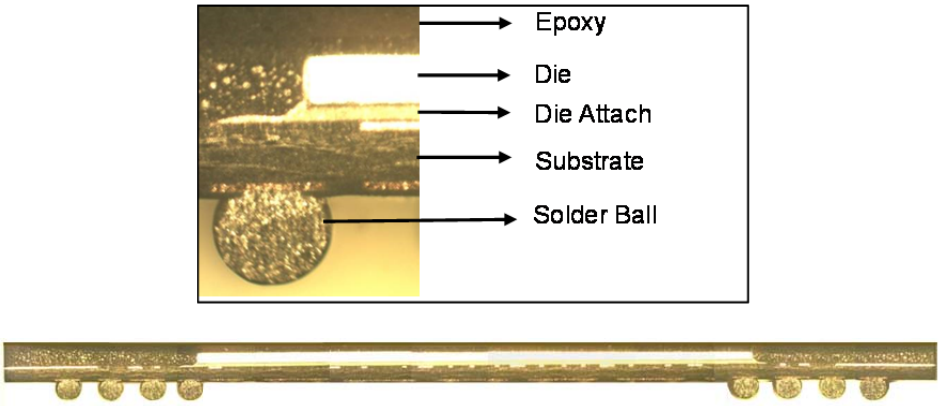

Figure 6.3 Cross Section of the 19 mm PBGA Component

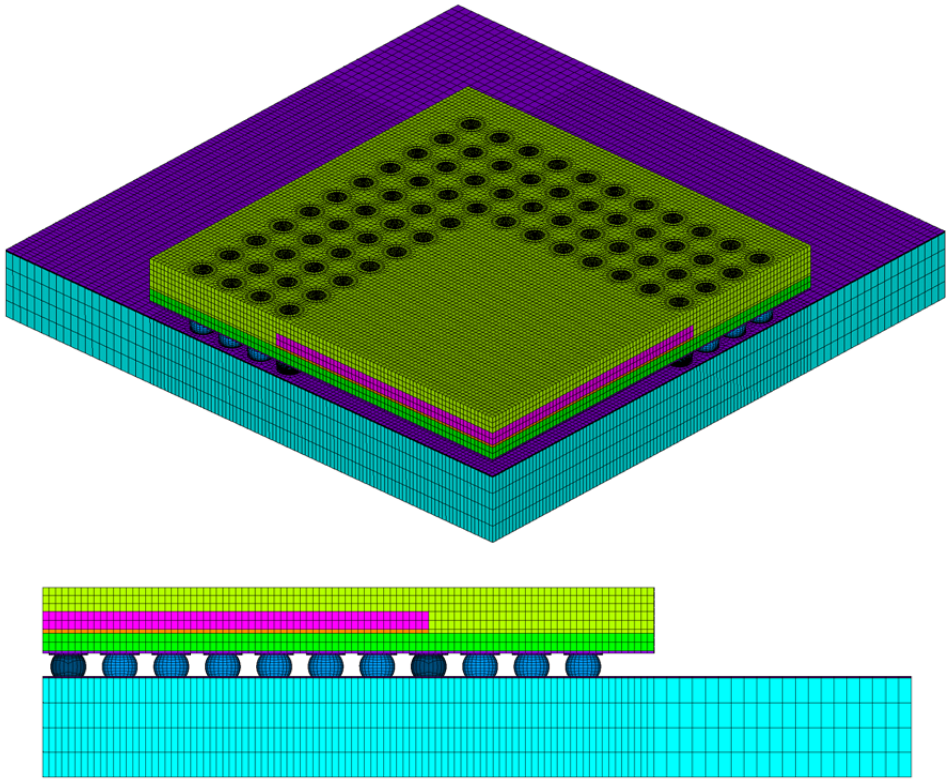

Figure 6.4 Finite Element Mesh (Quarter Symmetry)

The quarter model consisted of a perimeter array of 72 solder balls. The BT substrate and PCB bond pads and solder mask layers were included in the model. As shown in Figure 6.5, two different mesh densities were used for the solder balls. The

solder balls at the two possible critical locations along the diagonal (die shadow and package corner, see Figure 6.6) in terms of the energy dissipation have been meshed with very fine elements. For all other balls, a comparatively coarser mesh has been used to provide a balance between the accuracy and efficiency of the computation.

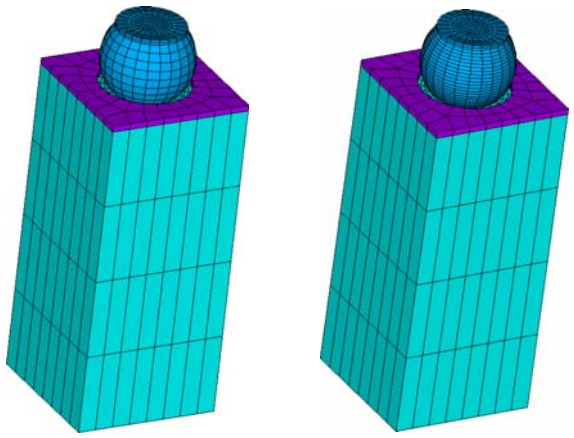

Figure 6.5 Solder Balls with Coarse and Fine Mesh Densities

The solder balls were modeled in ANSYS with VISCO107 structural elements with 8 nodes. This element is designed to solve both isochoric (volume preserving) rate-independent and rate-dependent large strain plasticity problems. For the other materials in the model, SOLID45 structural solid elements have been used, which are 8 node elements with plasticity, creep, large deflection and large strain capabilities. Iterative solution procedures have been used due to the nonlinear material and kinematic properties of the model. Typical solution run times were about 2 hours per thermal cycle using a workstation with quad core processor and 16 GB of memory.

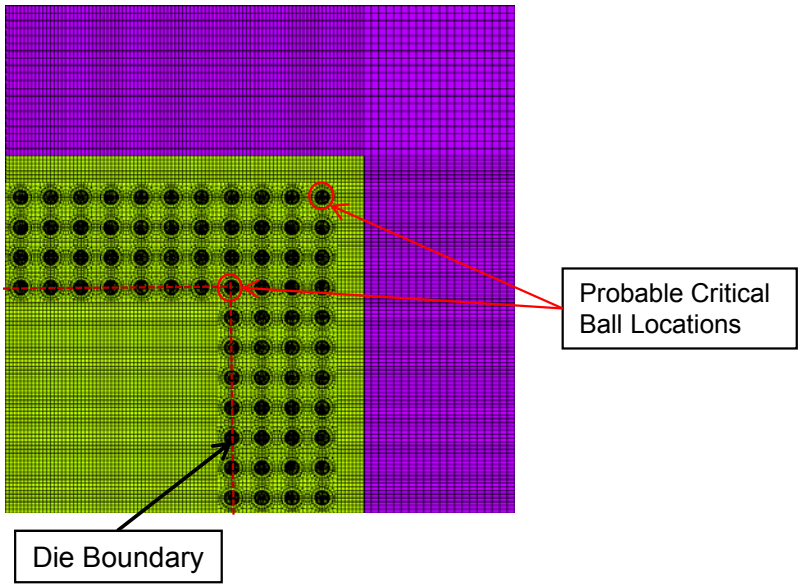

Figure 6.6 Top View Showing the Die Boundary and Probable Critical Solder Ball Locations

6.2.3 Material Behavior for 19 mm PBGA Model

The modified Anand model including aging effects developed in Chapter 4 was used to model the solder material behavior in the finite element calculations. Specific aging conditions (aging temperature and aging time) prior to thermal cycling were used to calculate the 9 Anand model parameter to use for the respective prior aging simulation. Figure 4.8 showed the variation of the Anand constants for various aging temperatures (25-125 ^{o}C) and time (0-360 days). For conditions not included on these curves, a linear interpolation between values was used to estimate the Anand parameters.

The other materials in the model were modeled as either temperature dependent elastic materials (BT substrate, PCB, copper pads, silicon die, die attachment adhesive, solder mask), or as temperature dependent elastic-plastic materials (mold compound). Room temperature material constants for the various materials are listed in Table 6.2.

The nonlinear stress-strain curves of the molding compound were characterized by extracting small tensile samples (19 x 2 x 0.4 mm) from unmounted PBGA components. The uniaxial specimens were prepared by separating the mold compound layer from the component by first polishing from the ball side of the PBGA until the die was exposed, and then by removing the silicon through a dry plasma etching process. Using the extracted specimens, stress-strain tests at temperatures of T = 25, 50, 75, 100 and 125 ^{o}C and a strain rate of 0.0001 sec^{-1} were performed using the MT-200 tension/torsion thermo-mechanical test system shown in Figure 3.6. Figure 6.7 shows the measured temperature dependent stress-strain curves. It is observed that the glass transition temperature of this material lies within the range: 100 C > T_g > 125 C.

Material	Elastic Modulus (GPa)	Poisson's Ratio	CTE (ppm/C)
PCB	Ex = 16.90 Ey = 7.44 Ez = 16.90	PRxy = 0.39 PRyz = 0.39 PRxz = 0.11	CTEx = 14.5 CTEy = 67.2 CTEz = 14.5
Solder Mask	3.1	0.3	16.3
Copper Pad	128	0.34	17
Die Attachment Adhesive	1.5	0.35	65 ($T<T_g$) 200 ($T>T_g$) T_g = 60 ^{o}C
Silicon Die	169	0.28	2.54

Table 6.2 Room Temperature Material Properties

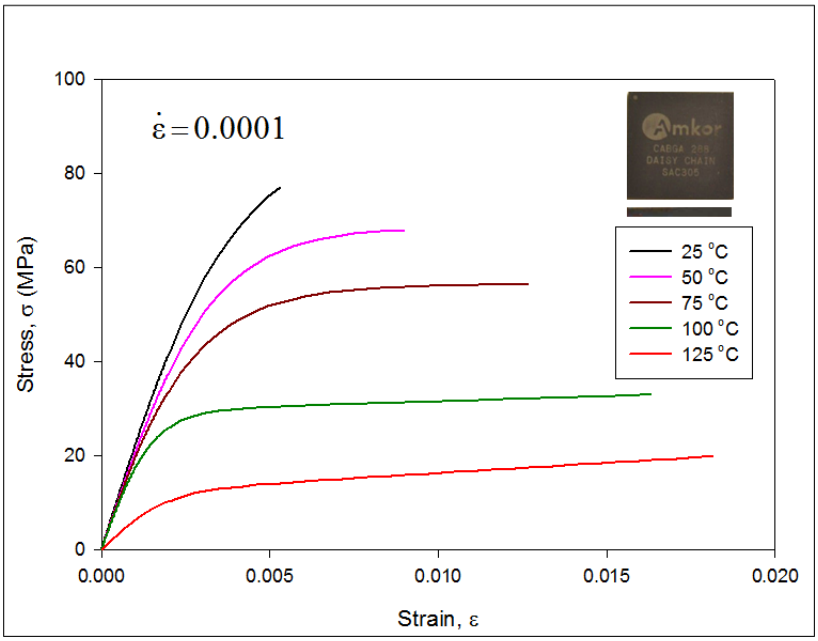

Figure 6.7 Molding Compound Stress-Strain Curves

The stress-strain properties of the BT substrate have also been characterized using tensile specimens extracted from actual PBGA components. In this case, the PBGA components have been polished from the epoxy (top) side of the part until the die was exposed. The silicon was then removed using the dry plasma etching process, and the remaining mold compound was polished away. This left only the BT laminate with attached solder balls. A second phase of polishing was then done to remove the solder balls and leave only the BT substrate, which could then be cut up into thin 19 x 2 x 0.15 mm tensile specimens. Figure 6.8 contains the measured stress-strain curves found at T = 25, 50, 75, 100 and 125 ^{o}C, and at a strain rate of 0.0001 sec^{-1}. The curves were found to be quite linear and elastic, and the elastic modulus was found to depend linearly with temperature.

Boundary Conditions and Thermal Loading

The quarter model shown in Figure 6.4 has been appropriately constrained along the axes of symmetry, so that for a node in a symmetry plane, the displacement component perpendicular to the symmetry plane was required to be zero. In addition, all three displacements were set to zero for the center node at the bottom surface of the PCB to prevent any rigid body motions.

The entire assembly was subjected to a time dependent temperature distribution to reflect the -40 to +125 C thermal cycling performed in the life testing experiments. The ramp rate for this thermal cycling profile was 16.5 ^{o}C/min, and the high and low temperature dwell times were each 20 minutes. The stress-free temperature of the package has been assumed to be T = 220 ^{o}C, which is the solidification temperature of the lead free solder joints. The applied thermal loading including the cool down after solder joint reflow and the first several thermal cycles is shown in Figure 6.9.

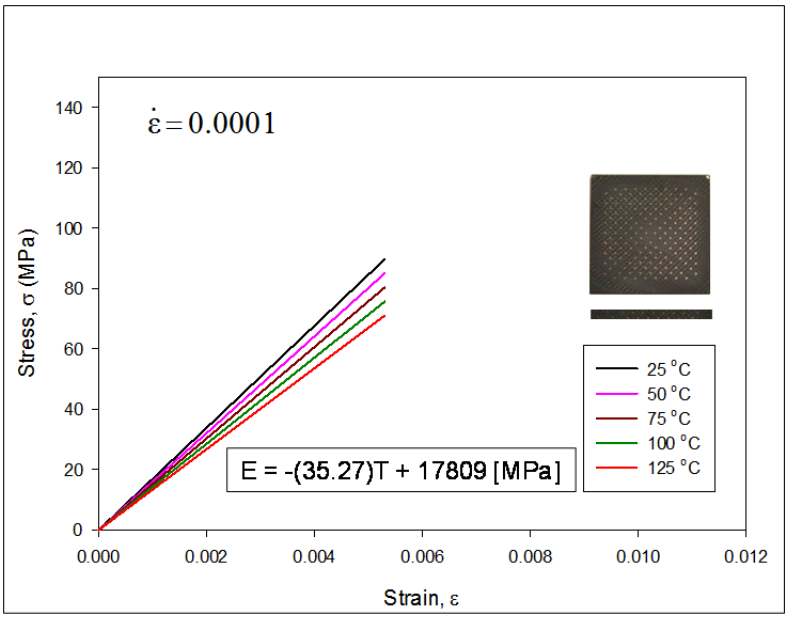

Figure 6.8 BT Substrate Stress-Strain Curves

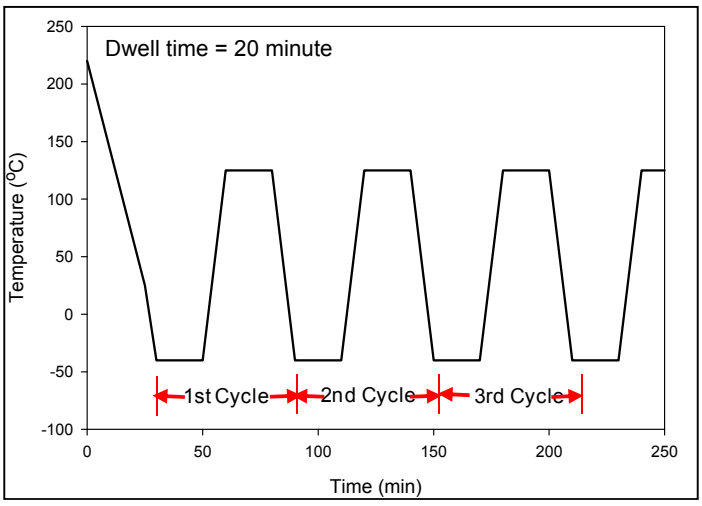

Figure 6.9 Applied Thermal Loading

Before discussing the two FEA models (slice model for PBGA 676 and quarter model for 19 mm PBGA), the procedure for calculating the plastic energy dissipation per cycle (ΔW) in solder joints is illustrated in next section for a quarter model of the 19 mm PBGA assembly.

6.2.4 Procedure for Calculating the Plastic Energy Dissipation per Cycle in Solder Joints

Using the temperature profile in Figure 6.9, the 19 mm PBGA model (Figure 6.4) was simulated for three thermal cycles between temperatures of -40 to 125 C. The plastic energy dissipation per cycle in the solder balls were calculated by six the different volume averaging methods shown in Figure 6.10. From the results of FEA simulation and considering different methods of calculating ΔW, two balls were identified as critical solder balls (see Figure 6.11).

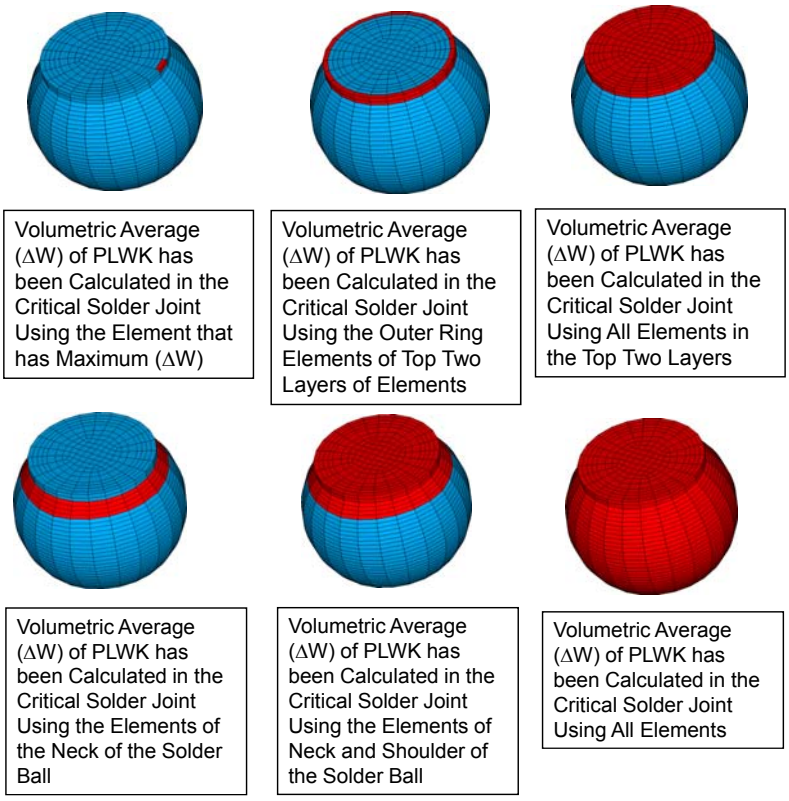

Figure 6.10 Different ΔW Calculation Methods (Volume Averaging)

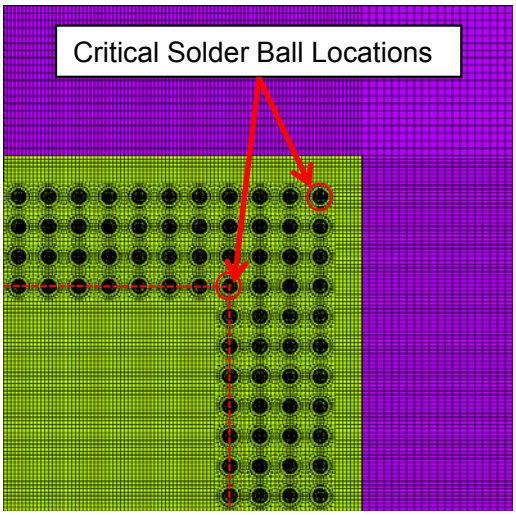

Figure 6.11 Location of the Critical balls from FEA Results

During the thermal cycling, there is plastic energy dissipation in the solder due to the hysteresis as discussed in Chapter 5. This plastic energy dissipation is accumulated during the thermal cycling. The gradual accumulation of plastic energy dissipation has been calculated for one of the critical solder joints (die shadow solder ball) at various times during the thermal cycling. Figure 6.12 shows when the calculations were made and the associated plastic work (PLWK) contours are shown in Figure 6.13. It can be seen that the plastic work gradually accumulates in the critical solder ball. Also it is observed that the plastic energy is mostly dissipated at the top of the solder joints in the so-called neck and shoulder regions. Furthermore, the maximum plastic energy dissipation occurs along the outer ring of the neck elements, and is illustrated by the red colors in the contour plots. Figure 6.14 shows a plot of the variation of the maximum plastic energy dissipation with time during the first three thermal cycles for this solder ball.

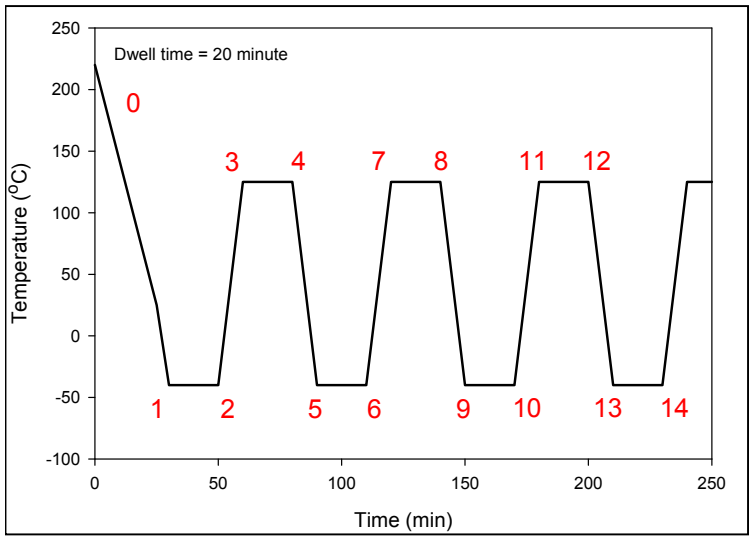

Figure 6.12 Thermal Cycling Temperature Profile (Numbers Marked at Calculation Points for the PLWK Contours)

The plastic work done per cycle (ΔW) was also calculated for the same solder joint at the end of each thermal cycle, and graphical contours are shown in Figure 6.15. These results illustrates that ΔW also has its largest values along the outer ring of the neck elements. Furthermore, these contours show that ΔW is nearly constant and does not change noticeably from cycle to cycle. In fact, the value of ΔW converges quickly and stabilizes during the first few cycles in a thermal cycling exposure. Table 6.3 shows the convergence of maximum value of ΔW during the three thermal cycles.

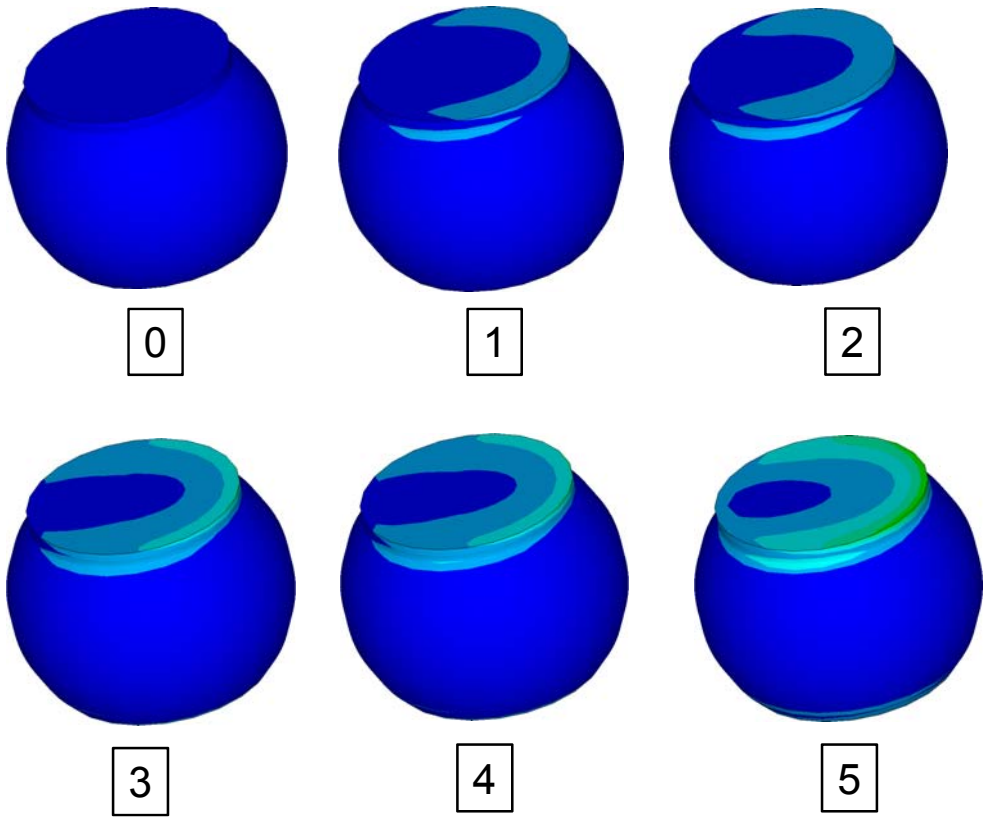

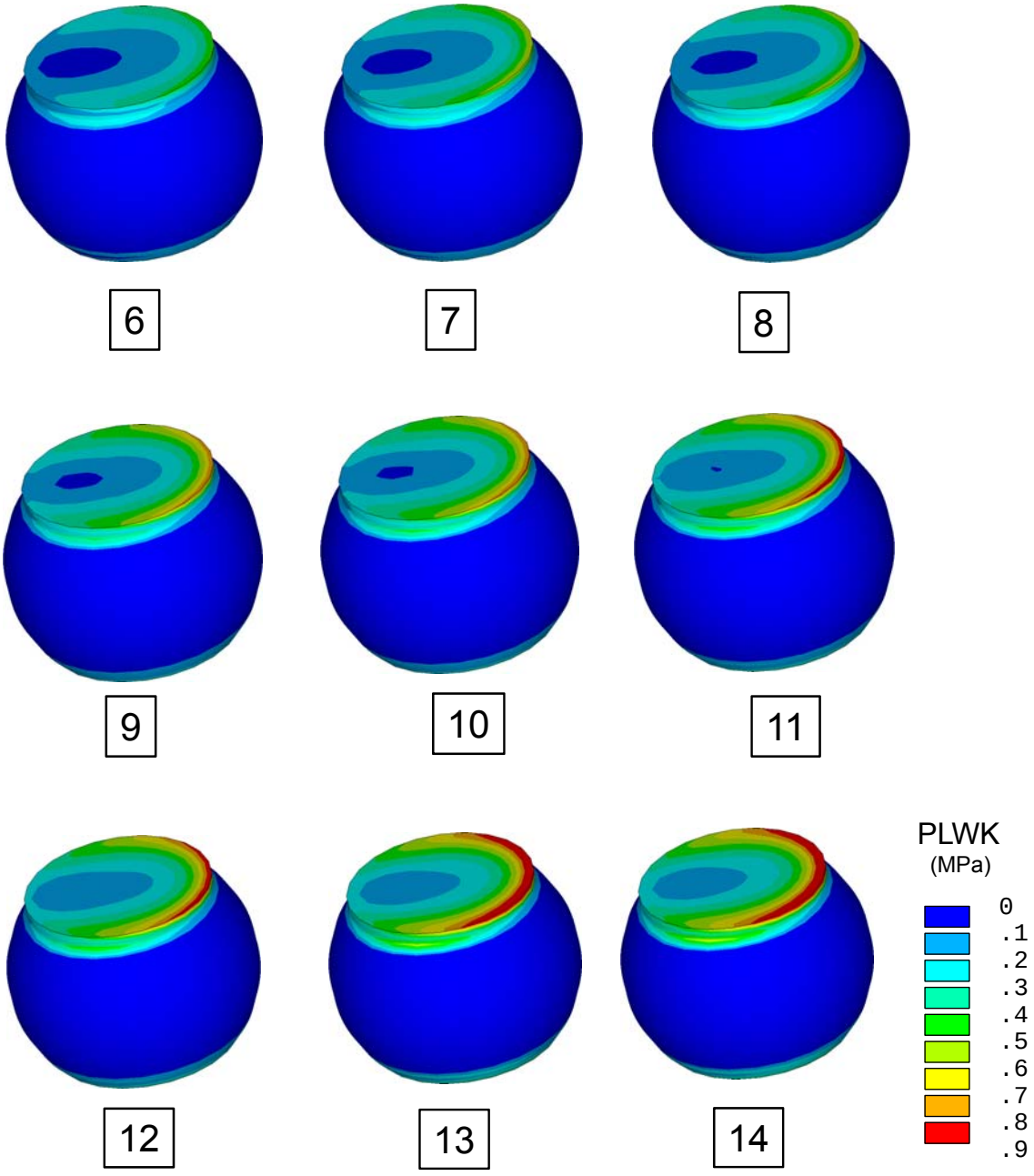

Figure 6.13 PLWK Contours at the Times Mentioned in Figure 6.12

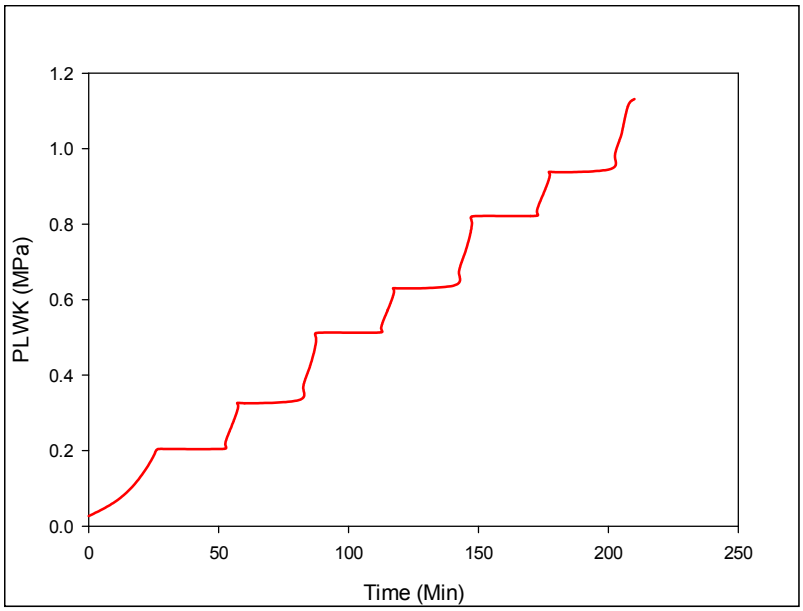

Figure 6.14 Variation of PLWK with Time

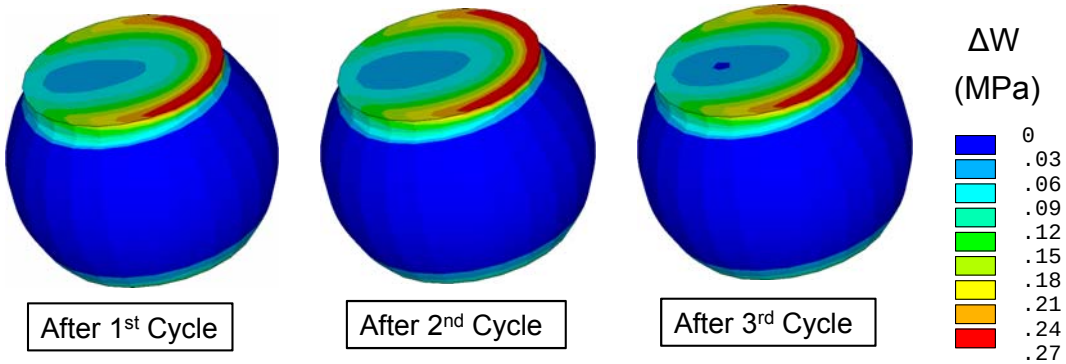

Figure 6.15 ΔW Contours for Different Cycles

Cycle No.	ΔW (MPa)
1	0.306631
2	0.308909
3	0.309667

Table 6.3 Convergence of the Maximum Value of ΔW During the First Few Cycles

6.2.5 Results for Slice 3D Modeling of PBGA 676

The analysis of the solder stresses, strains, and deformations during thermal cycling was performed assuming different durations of aging at 100 C prior to the beginning of thermal cycling. To match the material characterization tests presented earlier in Chapter 4, the aging conditions were taken to be 1, 5, 20, 60, 120, and 180 days at 100 C prior to the initiation of cycling. For the different aging times, finite element simulations of the thermal cycling were performed using the various sets of Anand parameters given in Table 4.2. The initial configuration of the assembly before cycling was assumed to be the "stress free" state of the assembly.

The critical solder ball in this PBGA configuration was the fourth from the center (under the die shadow). The volume averaged inelastic energy dissipation ΔW =PLWK (plastic work) accumulated per cycle was taken to be the metric for damage accumulation and failure of solder joints. This quantity was calculated for the two rows of elements in the neck region at the top of the critical solder ball. Figure 6.16 shows the calculated PLWK accumulation as a function of time for the first 3 thermal cycles for the various aging conditions considered prior to cycling. As expected, it was found that longer aging times prior to cycling resulted in additional energy dissipation (and thus more damage accumulation) in the solder joints. After a few cycles, the amount of energy dissipated per cycle becomes constant (steady state), and Figure 6.17 shows the dependence of the steady state ΔW accumulated per cycle with the duration of aging prior to the beginning of cycling. For the most extreme aging conditions (6 months at 100 C), a 25% increase occurred in the energy dissipated per cycle, suggesting an acceleration of damage accumulation and a reduction in the final fatigue life of the solder joint.

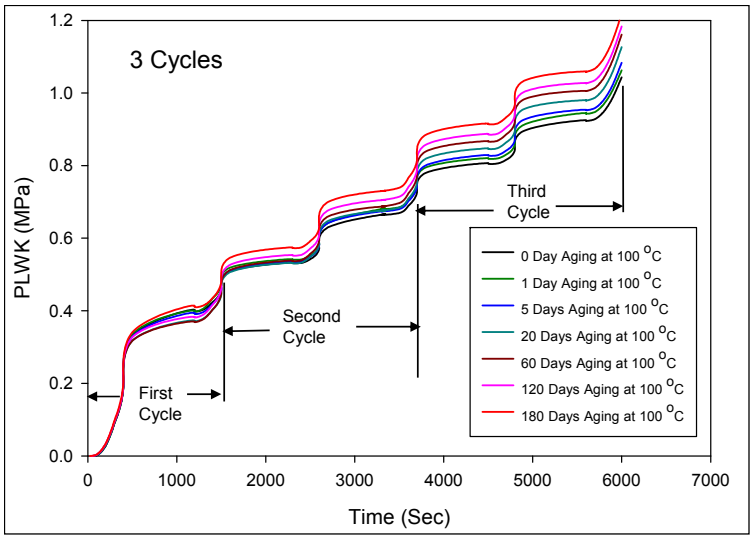

Figure 6.16 Energy Dissipation During Thermal Cycling for Different Durations of Aging Prior to Cycling

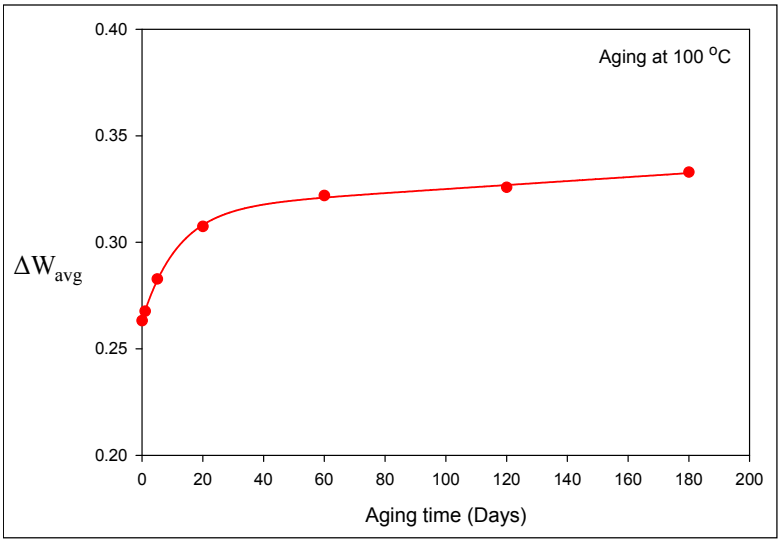

Figure 6.17 Energy Dissipation per Cycle for Different Durations of Aging Prior to Cycling

The calculations and discussion above are based on the assumption that the aging of the assemblies occurs as thermal preconditioning before thermal cycling. Aging also occurs gradually during the thermal cycling process due to the exposure of the assemblies to the high temperature dwell in each thermal cycle. The case of gradual in-situ aging of

the PBGA assembly during thermal cycling was also analyzed. In this case, no aging was assumed to have occurred prior to thermal cycling. The aging state of the assembly (and thus the Anand model constants) were allowed to evolve during the cycling due to the exposures at the high temperature dwells. Figure 6.18 illustrates the calculated evolution of the energy dissipation per cycle as a function of the number of thermal cycles. The ΔW and damage accumulation increases as cycling progresses due to use of the modified Anand model with aging effects. This again suggests an acceleration of damage accumulation and a reduction in the final fatigue life of the solder joint. When using the standard Anand model with constant material parameters, the energy dissipation per cycle remains constant during the entire cycling exposure.

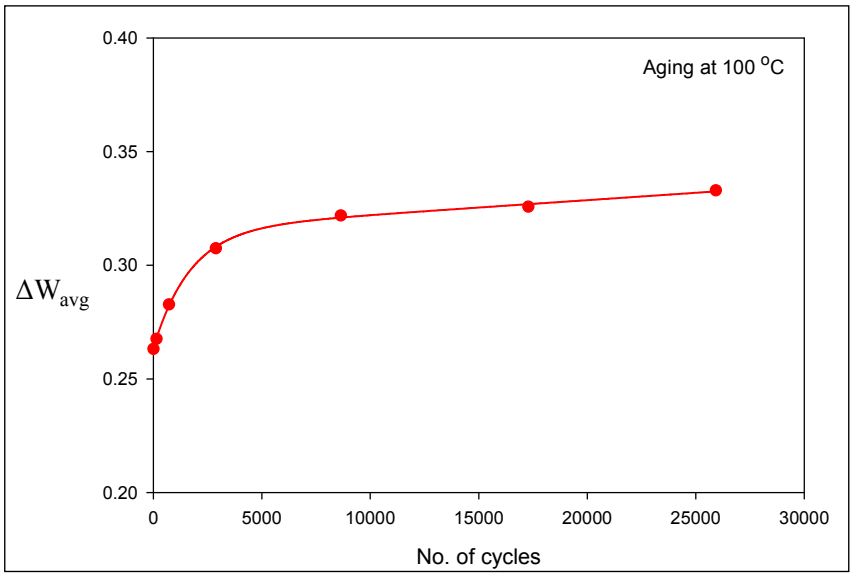

Figure 6.18 Evolution of the Energy Dissipation per Cycle During Thermal Cycling Due to Insitu Aging

6.2.6 Effect of Cycle Dwell Time on the Plastic Energy Dissipation

As was mentioned in Chapter 1, the thermal cycling dwell time significantly effects the reliability of lead free solder joints. Experimental observations have shown that an increase in the thermal cycling dwell time has adverse effects on the life of solder joints. In this study, the effects of dwell time on the damage accumulation in the critical solder joints were evaluated by using three different dwell times in the thermal cycling finite element simulations. The modeled dwell times were 10, 20, and 30 minutes as shown in Figure 6.19. In all three cases, the time for ramp up and ramp down were unchanged. The Anand parameters in the SAC305 solder joints were allowed to evolve due to insitu aging as in the simulations in the previous section.

Figure 6.20 shows the calculated variation of the plastic energy dissipated per cycle (ΔW) for the three different dwell times. The bottom blue curve in this graph represents the simulation results for a 10 minute dwell time. The pink curve and the red curve are for the 20 and 30 minute dwell times, respectively. These results show that the plastic energy dissipation increases as the dwell time is increased, which is in agreement with the findings of other researchers. However, these results were for same ramp rates of (10 minutes/100 ^{o}C). If the ramp rates were different, the results would be different too.

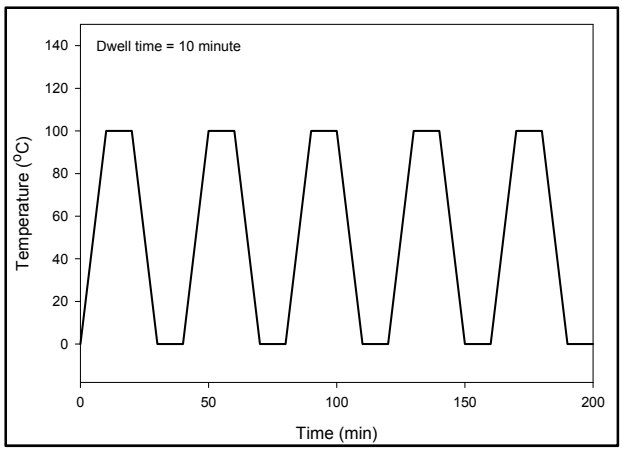

(a) Dwell Time 10 Minutes

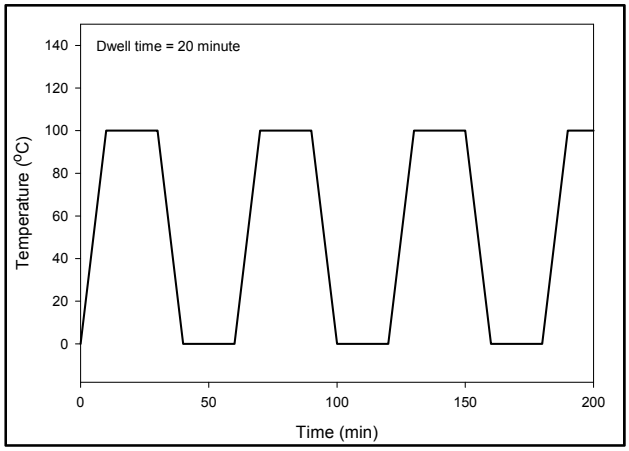

(b) Dwell Time 20 Minutes

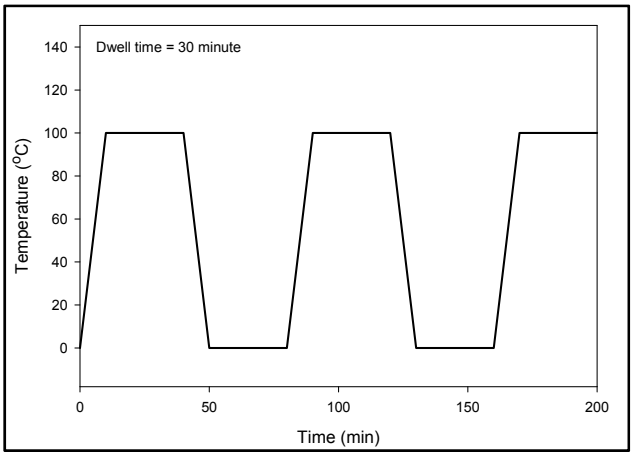

(c) Dwell Time 30 Minutes

Figure 6.19 Temperature Profile with Different Dwell Times

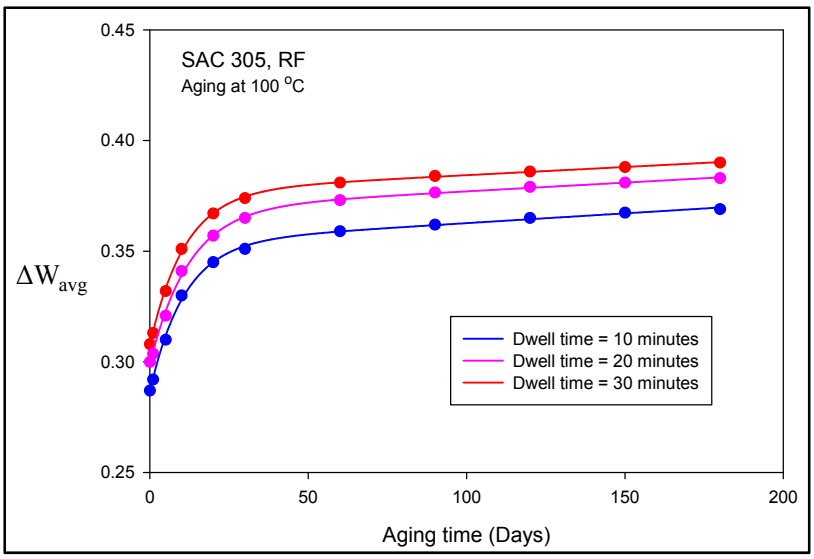

Figure 6.20 Variation of ΔW with Aging Time for Different Dwell Times

6.2.7 Results for 19 mm PBGA Quarter Model

The finite element simulations for the 19 mm PBGA have been performed for 9 different values of solder material properties. The baseline case is for the situation of no thermal aging before thermal cycling. In this case, the no aging (0 days aging) values of the Anand material parameters in Figure 4.8 were utilized. The other 8 analyzed configurations were for assembly aging prior to thermal cycling. Mimicking the experimental results shown in Figure 5.8, the aging conditions included aging temperatures of T = 25, 55, 85 and 125 °C, and aging times of 6 and 12 months. In these cases, the appropriate Anand parameters for the simulations were extracted from Figures 4.8 (linear interpolation between the graph curves were used for the T = 55 and T = 85 aging temperatures).

For all analyses, the critical solder ball in this PBGA assembly was found to be the diagonal ball located near the corner of the die (die shadow). The volume averaged inelastic energy dissipation ΔW = PLWK (plastic work) accumulated per cycle was often

taken to be the metric for damage accumulation and failure of solder joints. This quantity was calculated in the critical solder ball for all nine cases of prior aging. Following Che, et al. [136], the outer ring of elements in the top two rows were used to calculate ΔW for the third thermal cycle. This method of calculating the accumulation of plastic work results in a more conservative (higher) value when compared to other traditional methods, such as using all elements in the ball or all elements in the top few layers of the ball.

The calculated accumulated inelastic energy dissipation values for the various aging conditions prior to thermal cycling are shown in Figure 6.21. As expected, it was found that longer aging times prior to cycling resulted in additional inelastic energy dissipation (and thus more damage accumulation) in the solder joints. Similarly, higher aging temperatures resulted in higher energy dissipations. The curves connecting the single run calculations were generated by performing additional finite element analyses with aging times other than 6 and 12 months. For the most extreme aging conditions (12 months at 125 C), a 50% increase occurred in the energy dissipated per cycle (comparing with the no aging result). This suggests a large acceleration of damage accumulation and a reduction in the final fatigue life of the solder joint.

6.2.8 Prediction of Solder Joint Life in 19 mm PBGA Aged Assemblies

The thermal cycling life of the 19 mm PBGA assemblies was also predicted for various aging conditions prior to cycling. The calculation procedure makes use of: (1) plastic energy dissipation per cycle values calculated with the finite element analyses that incorporate the modified Anand model with aging dependent parameters and (2) solder failure models with aging dependent parameters. The number of cycles to crack initiation

for a particular aging condition was first calculated using eq. (5.3) with the appropriate ΔW value from Figure 6.21 and the appropriate K_1 and K_2 values from Figures 5.5-5.6. The crack growth rate for the same aging condition was then calculated using eq. (5.4) with the appropriate ΔW value from Figure 6.21 and the appropriate K_3 and K_4 values from Table 5.3. Finally, the calculated values of N_i and da/dN were substituted into eq. (5.5) with $a_c = 0.46$ mm to determine the predicted number of cycles to failure.

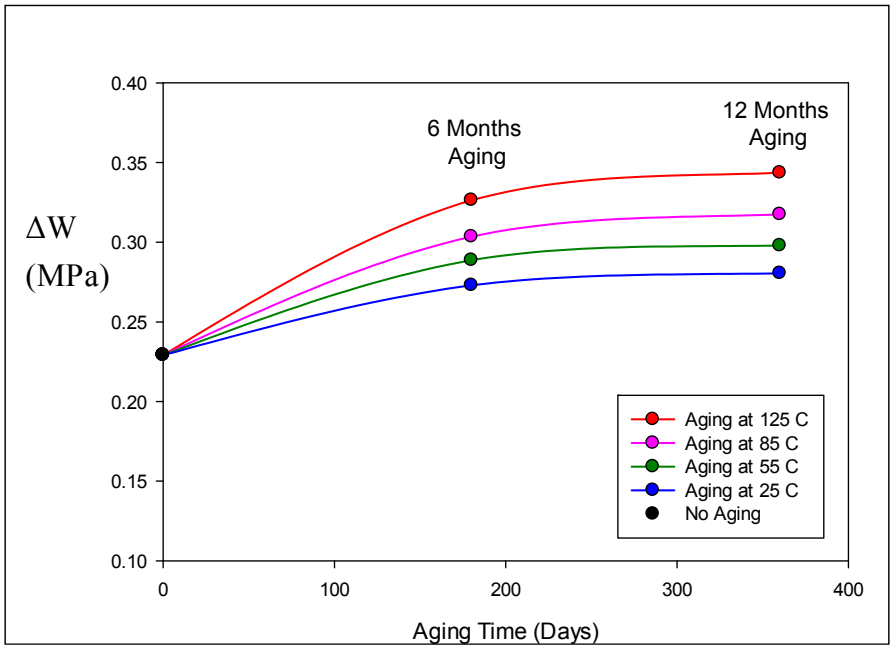

Figure 6.21 Variation of Calculated Energy Accumulation per Cycle with Aging Time and Aging Temperature

Using the procedure described above, the thermal cycling life of the 19 mm PBGA components has been calculated for prior aging at T = 25, 55, 85 and 125 ^{o}C and various aging times from 0-12 months. The results are plotted in Figure 6.23. Each curve is a life prediction trace for a particular aging temperature. The square data points in the figure are the measured characteristic life values from the Weibull plots in Figure

5.8. It is observed that there is very good agreement between the aging aware reliability predictions and the Weibull data. In particular, the numerical values are correlated in Table 6.4, and the percentage differences are all less than 15%.

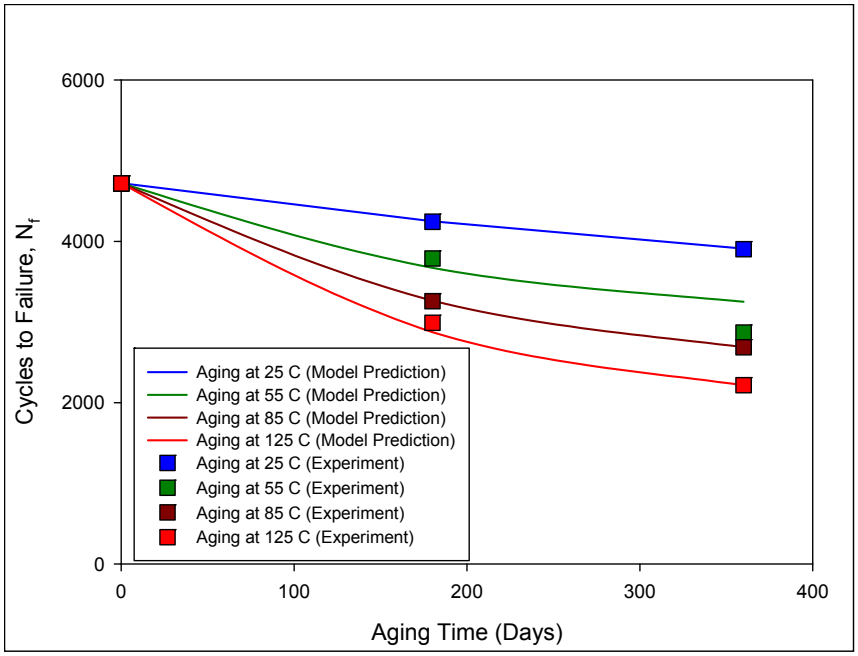

Figure 6.22 Model Life Predictions and Weibull Failure Data for Various Aging Conditions

Aging Time (Days)	Aging Temperature (°C)	Model Prediction (Cycles)	Experimental Results (Cycles)	Difference (%)
0	-	4722	4719	0.06
180	25	4249	4244	0.12
	55	3672	3787	3.04
	85	3265	3260	0.15
	125	2875	2990	3.85
360	25	3910	3906	0.10
	55	3253	2872	13.3
	85	2689	2688	0.03
	125	2216	2216	0

Table 6.4 Correlation of Model Predictions with the Experimental Results

The predicted degradations in thermal cycling life with aging for the 19 mm BGA components with SAC305 solder balls can also be visualized by generating theoretical Weibull failure rate plots as shown in Figure 6.24. The predicted thermal cycling fatigue life from Figure 6.23 has been used for the characteristics life η for each set of aging conditions, while the Weibull slope β has been taken to be the average Weibull slope from all of the experimental failure rate data shown in Figure 5.8. Clear degradations in life have been predicted to occur for aged components relative to non-aged components, and the amount of degradation was exacerbated with higher aging temperatures and longer aging times. The plots in Figure 6.24 can be directly compared to the experimental Weibull plots in Figure 5.8.

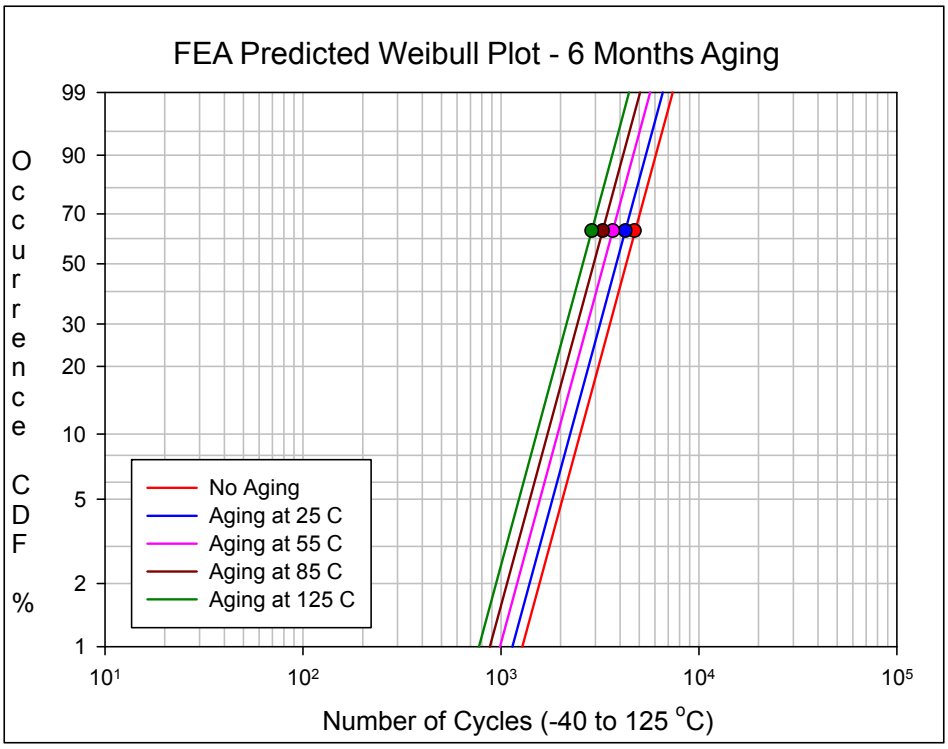

(a) Thermal Cycling Life for 6 Months Prior Aging

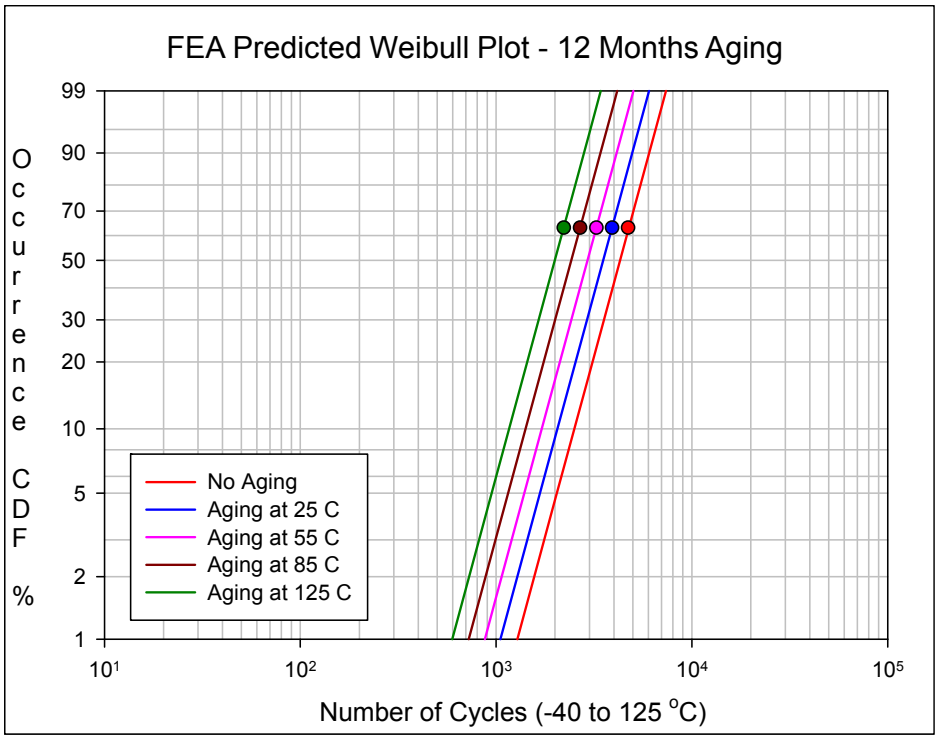

(b) Thermal Cycling Life for 12 Months Prior Aging

Figure 6.23 Predicted Life Reduction in BGA Assemblies Subjected to Aging Prior to Thermal Cycling

6.3 Summary and Discussion

It was demonstrated in Chapters 2, 3, and 4 that isothermal aging leads to large reductions (up to 50%) in several key material properties for lead free solders including stiffness (modulus), yield stress, ultimate strength, and strain to failure. In addition, even more dramatic evolution has been observed in the creep response of aged solders. Traditional finite element based predictions for solder joint reliability during thermal cycling accelerated life testing are based on solder constitutive equations (e.g. Anand viscoplastic model) and failure models (e.g. energy dissipation per cycle models) that do not evolve with material aging. Thus, there will be significant errors in the calculations with lead free SAC alloys that illustrate dramatic aging phenomena. In this study, a new

reliability prediction procedure was developed that utilizes constitutive relations and failure criteria that incorporate aging effects, and then the new approach was validated through correlation with thermal cycling accelerated life testing experimental data.

In this chapter, the developed Anand constitutive equations for solder with aging effects were implemented into the finite element code ANSYS and then the finite element simulations have been performed to model the solder joint deformations of two different PBGA components attached to FR-4 printed circuit boards that were subjected to thermal cycling. Calculations were made for non-aged PBGA assemblies, as well as for assemblies that had been aged under various conditions before being subjected to thermal cycling.

In the first study, a 3D slice finite element mesh (half model) was analyzed for a 676 I/O PBGA component. For the specified loading, this configuration was subjected to thermal cycling from 0 to 100 C (8 minute ramps and 10 minute dwells). The plastic energy dissipation with time was calculated and the energy dissipation per cycle was also determined. As expected, the plastic energy dissipation per cycle (ΔW) increased with increasing aging temperature and aging time. For this package, a 30% increase in ΔW was found for 6 months prior aging at 100 ^{o}C.

In the second study, a three-dimensional finite element analysis of the 19 mm PBGA component with SAC305 interconnects discussed in Chapter 5 was performed to calculate the stress/strain histories in the solder joints during thermal cycling accelerated life testing. Simulation of thermal cycling between -40 to 125 C was performed, and several sets of aging conditions (aging temperature and time) prior to thermal cycling were considered. For each case, the plastic energy dissipation per cycle in the critical

solder ball was calculated. These values were then combined with the aging aware fatigue criterion to perform life predictions for the components with various aging conditions. The energy based criteria proposed by Darveaux [132] was used for predicting crack initiation and crack growth in the aged solder joints using the energy dissipation values calculated from the finite element analysis. Good correlation was found between the predicted results and experimental findings for the reliability of the component.

CHAPTER 7

FINITE ELEMENT ANALYSIS OF CBGA MICROPROCESSOR ASSEMBLIES

7.1 Introduction

Microprocessor packaging in modern workstations and servers often consists of one or more large flip chip die that are mounted to a high performance ceramic chip carrier. The final assembly configuration features a complex stack up of flip chip area array solder interconnects, underfill, ceramic substrate, lid, heat sink, thermal interface materials, second level CBGA solder joints, organic PCB, etc., so that a very complicated set of loads is transmitted to the microprocessor chip, solder interconnects and other parts of the assembly. Several trends in the evolution of this packaging architecture have exacerbated die stress levels including the transition to larger die, high CTE ceramic substrates, lead free solder joints, higher levels of power generation, and larger heat sinks with increased clamping forces. Die stress effects are of concern due to several reasons including degradation of silicon device performance (mobility/speed), damage that can occur to the copper/low-k top level interconnect layers, and potential mechanical failure of the silicon in extreme cases.

In this chapter, finite element simulation results for CBGA microprocessor assemblies will be discussed. The Anand constitutive model was used for solder interconnects in the simulation of assembly processes and the revised Anand model with aging effects was included in the study of effects of aging on solder and die stresses.

Firstly, the finite element analysis of assembly induced die stresses (using Anand model for solder) in the LGA assembly will be discussed. Then the simulation of thermal cycling between 0 to 100 ^{o}C and the analysis of power cycling will be shown and the variation of die stresses with temperature as well as number of cycle will be discussed. As the next step, simulation for assembly of second level BGA solder ball, PCB attachment and underfill dispensing was done. As a further study, analysis for heat sink clamping was done to investigate its effect on the die stresses. A second phase thermal cycling and power cycling simulations for the CBGA assembly were done to determine the stress variation with temperature and number of cycle. In the simulation procedure, a novel sequential modeling approach has been utilized to predict the build-up of compressive normal stresses and shear stresses in the die. The utilized method incorporates precise thermal histories of the packaging process, element creation, and nonlinear temperature and time dependent material properties. With suitable detail in the models, good correlation has been obtained with silicon die stress sensor data measured by Roberts, et al. [136-139] in a parallel study.

7.2 Finite Element Simulation of CLGA Assembly

A cross-sectional schematic of a fully assembled Ceramic Land Grid Array (CLGA) test specimen is shown in Figure 7.1, and photographs of actual samples after various steps in the manufacturing process are illustrated in Figure 7.2. The utilized high CTE ceramic substrates had in-plane dimensions of 51 x 51 mm, and a thickness of 2 mm. In some previous studies [140, 141] it was found that die stress states after solder joint reflow were universally small (e.g. 0-2 MPa). Thus it was chosen to neglect these stresses for most of the assemblies and measure the initial “zero stress” resistance values

after the die were reflowed to the substrate. This had the advantage of avoiding the complicated and tedious die probing procedure. However, for the large die and lead free solder bumps considered in this simulation, the die stresses induced by the solder reflow process were not negligible (see results in later sections).

Simulations were sequentially done for silicon die that were solder reflowed to the ceramic substrates, and then subsequently underfilled and cured. Finally, simulation for a metallic lid (AlSiC) attachment was done to complete the ceramic LGA component. After every packaging step (solder reflow, underfill dispense and cure, lid attachment and adhesive cure), die calculated die stresses were recorded in the result file, so that the die stresses induced by each assembly operation could be evaluated.

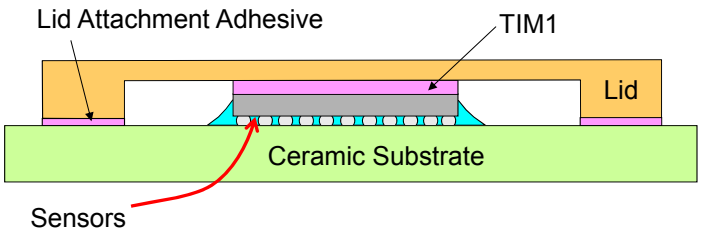

Figure 7.1 Schematic Diagram of CLGA Assembly

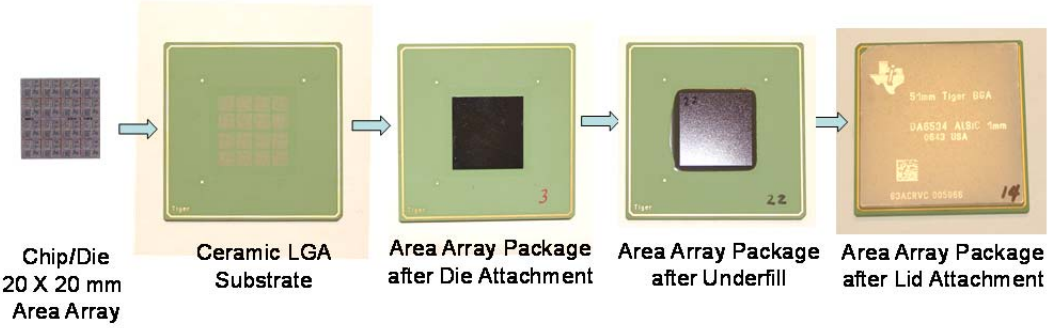

Figure 7.2 Assembly Process of the Flip Chip Packaging

7.2.1 Stresses Due to Solder Joint Reflow

The model for solder joint reflow consists of high CTE ceramic substrate, small scale solder bumps and the die. Since the objective of this work is to predict the stress distribution on the die surface, a highly refined mesh was used in the die, solders bumps, and an area of the substrate coinciding with the die. In this section, primarily the predictions for the in-plane normal stresses σ'_{11} and σ'_{22} will be discussed. These stress components were both highly compressive across the die surface, and were the largest in magnitude of all of the 6 stress components.

Using traditional methods, even a quarter model of the 3600 solder bump package proved to be very computing intensive. The solution to this issue was the use of the Multipoint Constraint (MPC) technique. In this method, it is possible to tie together two regions with dissimilar mesh densities by generating constraint equations that connect the selected nodes of one region to the selected elements of the other region. To further streamline the model, higher order elements were used in selected regions where there were large stress gradients. Figure 7.3 shows how Multipoint Constraints were defined in different layers of the model.

The stress-strain relations for the various materials in the microprocessor packaging geometry were characterized via mechanical testing or taken from vendor data sheets. The mechanical behaviors of the silicon chip, ceramic substrate, and AlSiC lid were all modeled as elastic with temperature dependent properties. For example, Figure 7.4 shows the tensile test results of the ceramic substrate between -40 ^{o}C and 220 ^{o}C. The flip chip underfill and TIM1 layer were both modeled as temperature-dependent elastic-plastic materials. For example, Figure 7.5 illustrates the measured stress-strain

curves for the underfill encapsulant. Finally, the SAC solder used in for the flip chip bumps was modeled using the viscoplastic Anand model. The 9 material constants in the model were found using temperature and strain rate dependent stress-strain data as discussed in earlier chapters. Table 7.1 contains a tabulation of the Anand material constants (ANSYS notation).

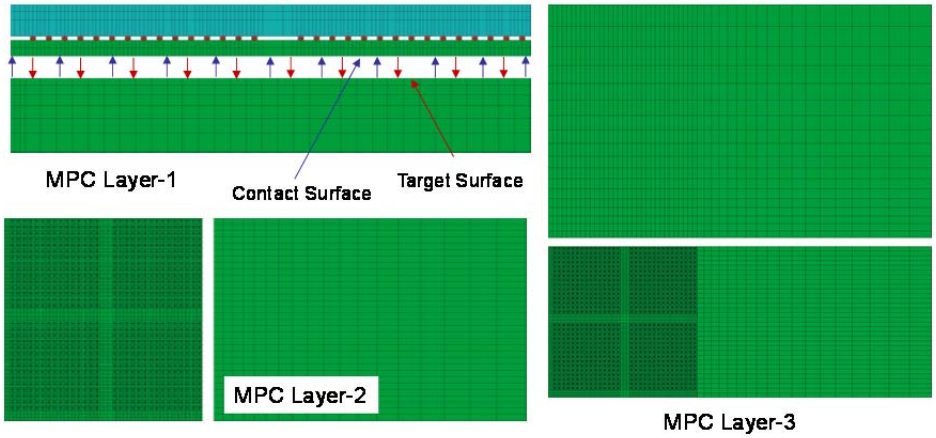

Figure 7.3 Multipoint Constraint Technique

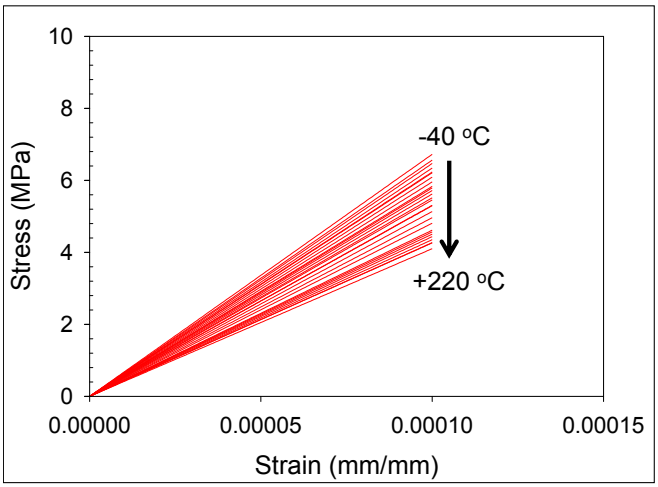

Figure 7.4 Stress-Strain Curves of the Ceramic Substrate

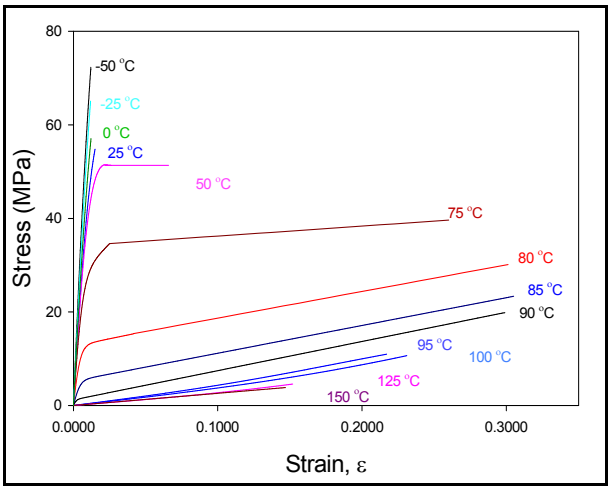

Figure 7.5 Underfill Stress-Strain Curves

Constant Number	Anand Constant	Units	SAC405 (CAVE)
1	s_0	MPa	24.1
2	Q/R	1/K	9350
3	A	sec^{-1}	4000
4	ξ	Dimensionless	4.0
5	m	Dimensionless	0.2
6	h_o	MPa	25000
7	$\hat{s}$	MPa	36.0
8	n	Dimensionless	0.01
9	a	Dimensionless	1.4

Table 7.1 Anand Constants for Modeling of SAC Solder

Due to the small size and ductile nature of the flip chip solder bumps, it is a common practice to start modeling the packaging process from the underfill curing step, and to assume that there were no initial stresses present after solder joint reflow. However, our experimental results shown above have demonstrated that the die stresses induced by the solder reflow process are not negligible for the large die and area array lead free solder bumps in this work. Thus, it was also necessary to model the die attachment step in the assembly process.

In the packaging process, chips are reflowed to the ceramic substrates, and then subsequently underfilled and cured. Finally, a metallic lid (AlSiC) is attached to complete the ceramic LGA component. Since the stress buildup in the microprocessor die depends on the packaging history, the same sequence has been maintained in the modeling process to correlate with the conditions of the experiments.

Solder joint reflow is the first step of the assembly process, and it is also called the die attachment step. Figure 7.6 shows the quarter symmetry finite element mesh used for simulating solder joint reflow, and Figure 7.7 illustrates how the layout of solder bumps in the actual package has been maintained in the modeling. The mesh includes the silicon die, solder balls, and ceramic substrate. Figure 7.7 also shows the horizontal and vertical streets with no solder balls that run through the center of the quarter section of the die.

In the analysis, a uniform initial temperature of 217 ^{o}C was assumed across the entire structure (melting temperature of the SAC solder used on the solder bumps). In the actual assembly process, packages are cooled from the solder solidification temperature to the room temperature. To simulate the stresses due to the die attachment, a uniform temperature load of 25 ^{o}C was applied to all nodes of the model. Due to the geometric and material nonlinearities in the model, the total temperature load is applied in a number of load steps to insure convergence.

Figure 7.8 shows the gradual buildup of the compression in the die for the horizontal in-plane normal stress σ'_{11} as the temperature is reduced from 217 ^{o}C to 25 ^{o}C. The maximum value of the horizontal normal stress was predicted to be -67 MPa at the center of the die. Figure 7.9 illustrates the distribution of the horizontal normal stress

across the entire surface of the die. The in-plane normal stress decreases from its maximum value of -67 MPa at the die center to zero at the left and right free edge of the die. The stress distribution also reveals local stress concentrations near the solder bumps, and this phenomenon is seen across the entire die surface. Similar results were found for the vertical in-plane normal stress σ'_{22} as shown in Figure 7.10. The maximum value was also -67 MPa at the die center. Thus, there is a predicted state of biaxial compression at the center of the die. The stress distribution for σ'_{22} was similar to σ'_{11}, except rotated by 90^{o}.

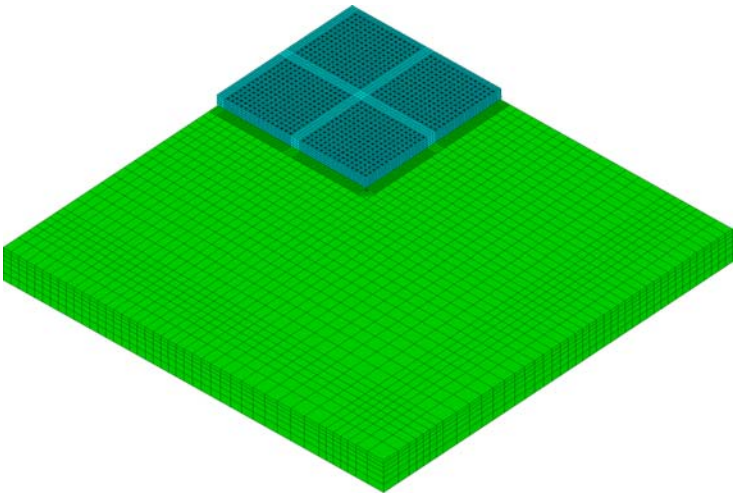

Figure 7.6 Quarter Symmetry Mesh for Solder Reflow Model

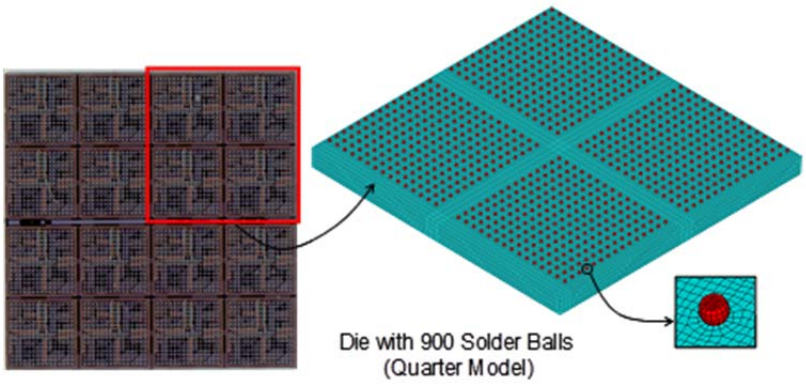

Figure 7.7 Layout of Solder Bumps

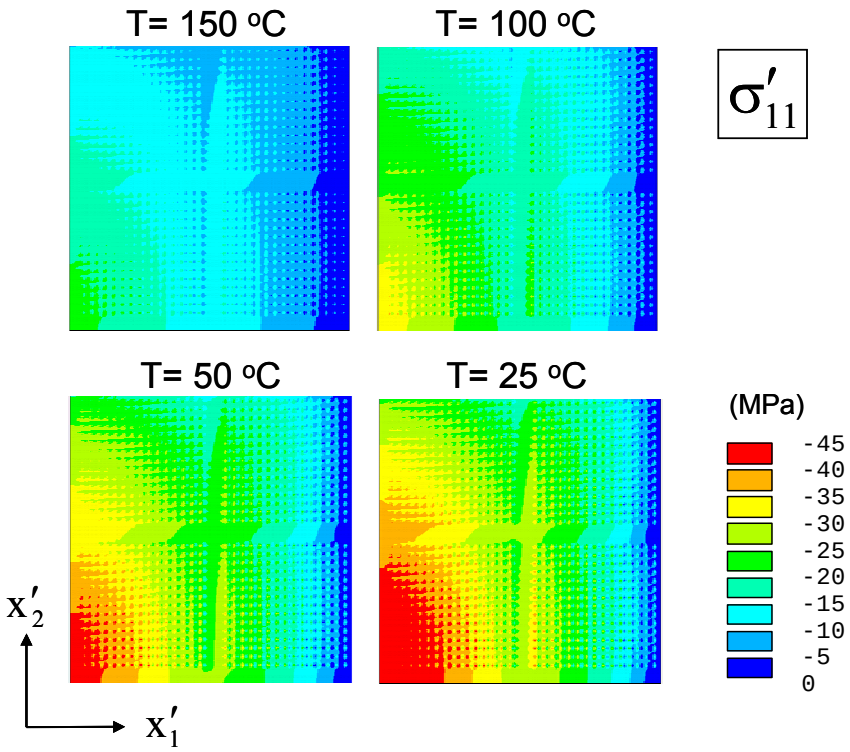

Figure 7.8 Die Stress Buildup During Cool Down after Solder Joint Reflow

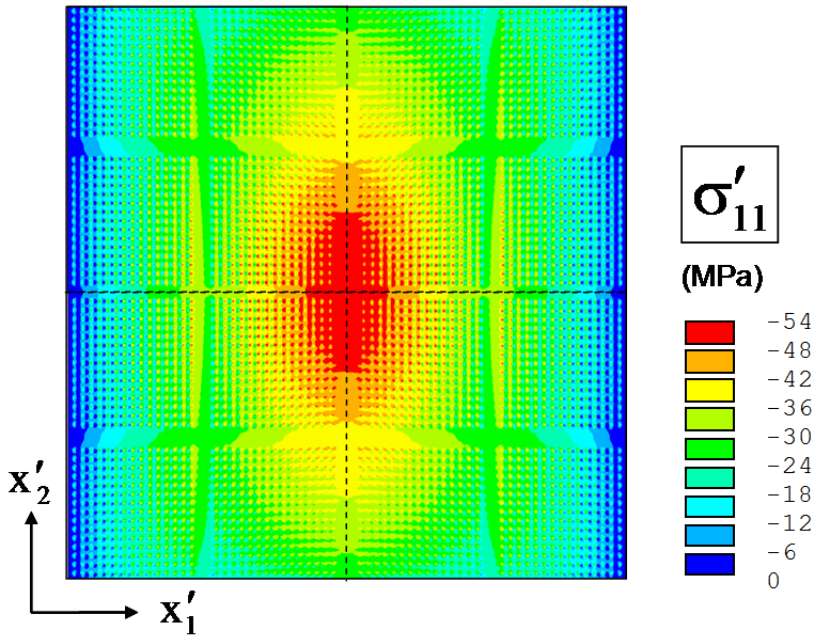

Figure 7.9 In-Plane Horizontal Normal Stress Distribution after Die Attachment Process

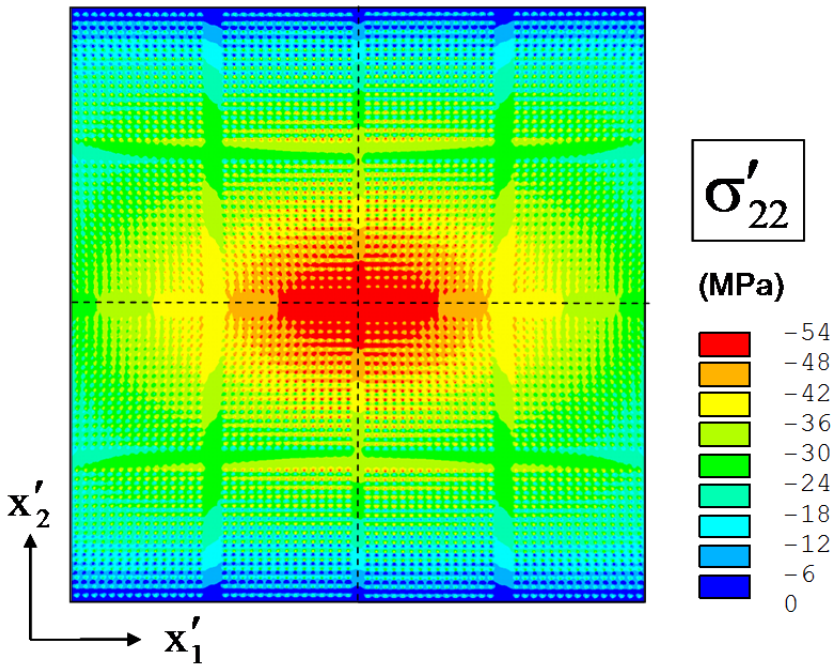

Figure 7.10 In-Plane Vertical Normal Stress Distribution after Die Attachment Process

7.2.2 Underfill Curing Process

Modeling of additional packaging processes was done using a sequential approach. To model underfill dispense and cure, the final configuration (including the initial stress distribution) from the solder joint reflow model above was taken as the starting point. An increase in temperature from 25 ^{o}C to 150 ^{o}C was applied, and then the underfill material was "added" to the model by adding elements. The temperature was then reduced to room temperature to simulate the underfill curing process. The mesh for the underfill cure modeling is shown in Figure 7.11.

The predicted distribution of the in-plane horizontal normal stress σ'_{11} on die surface after the underfill curing process is shown in Figure 7.12. The maximum compressive stress value was again found to occur at the die center. Relative to the solder reflow stresses, the value at the die center was seen to nearly triple to about -190

MPa, which correlates well with the experimental results discussed subsequently. The stress gradually decreases towards the edge of the die. The presence of an underfill fillet precludes the edge of the die from being a free surface. Thus, the horizontal normal stresses do not become zero at the left and right edges. At the corner of the die, the normal stress is -60 MPa, which is the minimum value across the die surface. It is also observed that the local stress concentrations near the solder balls were very small compared to those observed after solder joint reflow. Analogous results for σ'_{22} are shown in Figure 7.13. Again, the stress distribution for σ'_{22} was similar to σ'_{11}, except rotated by 90^{o}.

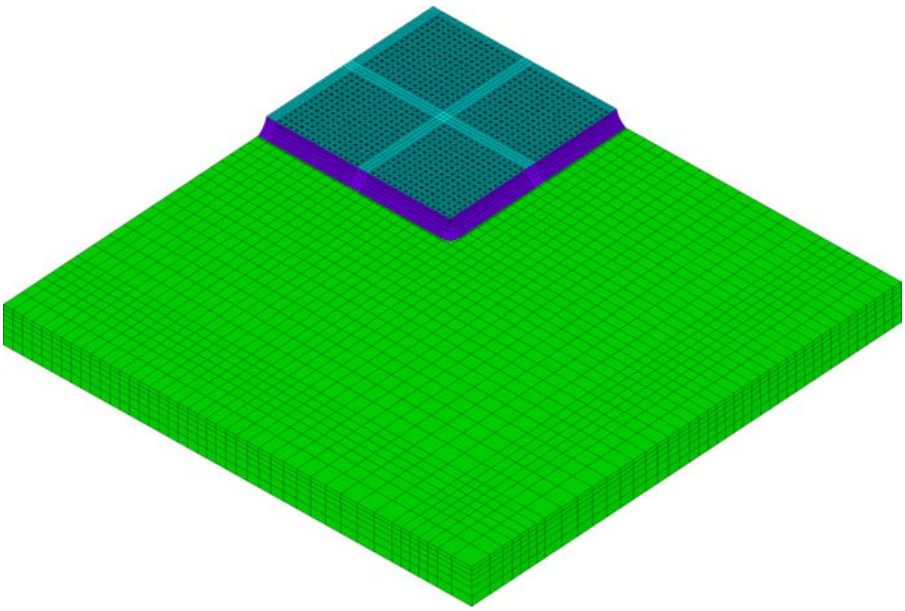

Figure 7.11 Quarter Symmetry Mesh for Underfill Cure Model

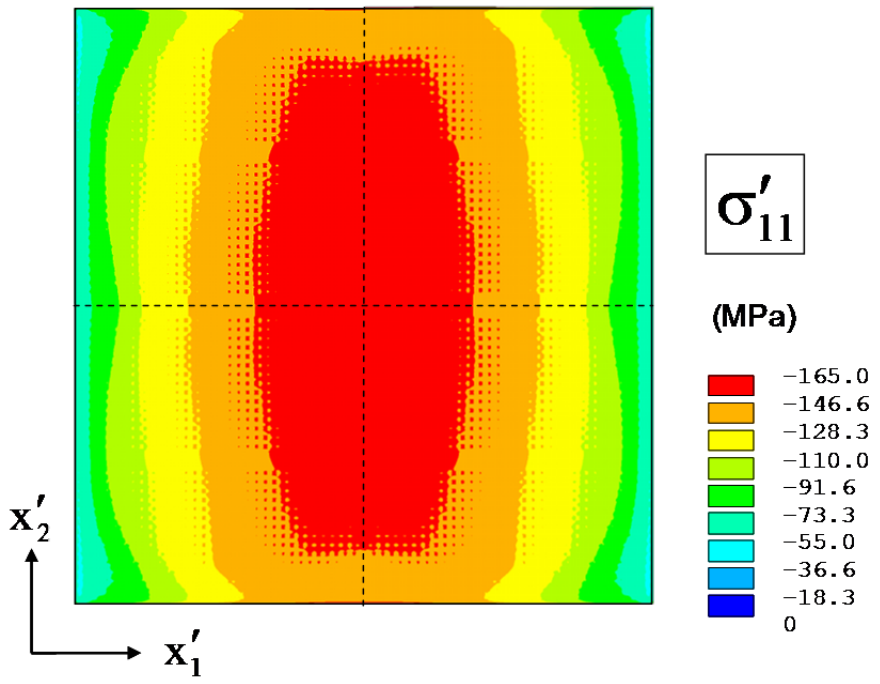

Figure 7.12 In-Plane Horizontal Normal Stress Distribution after Underfill Curing Process

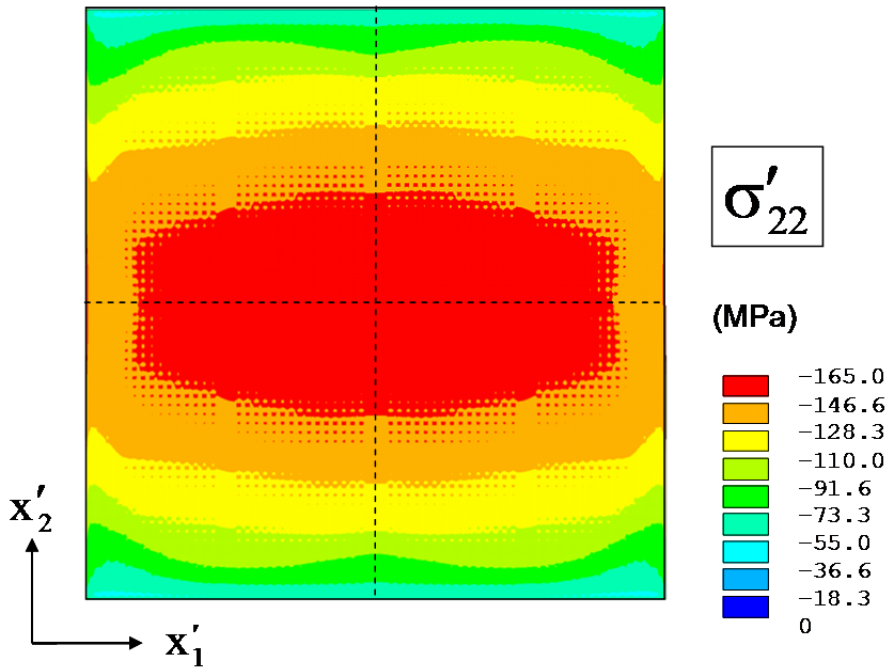

Figure 7.13 In-Plane Vertical Normal Stress Distribution after Underfill Curing Process

7.2.3 Lid Attachment Process

The lid attachment process is the last assembly step of the CLGA components. Continuing the sequential modeling of the manufacturing process, the final configuration (including the initial stress distribution) from the underfill dispenses and cure model above was taken as the starting point. An increase in temperature from 25 ^{o}C to 150 ^{o}C was applied, and then the elements for the TIM1 layer and lid were added to finite element model. Finally, the temperature was reduced to room temperature to simulate the TIM1 curing process. The mesh for the lid attachment modeling is shown in Figure 7.14. In order to know the precise configuration of the TIM layer, a micro-focus x-ray system and microscopy cross-sectioning were used (Figure 7.15).

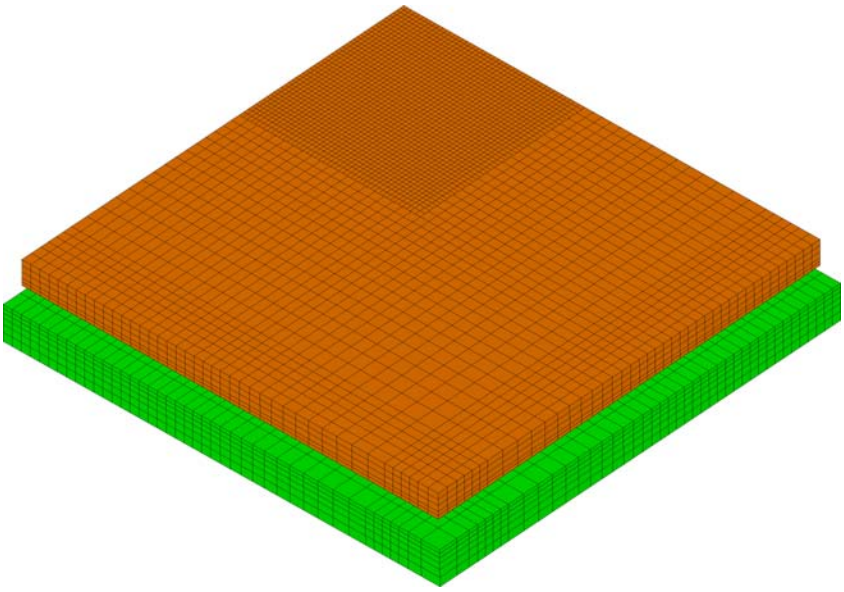

Figure 7.14 Quarter Symmetry Mesh for Lid Attachment Model

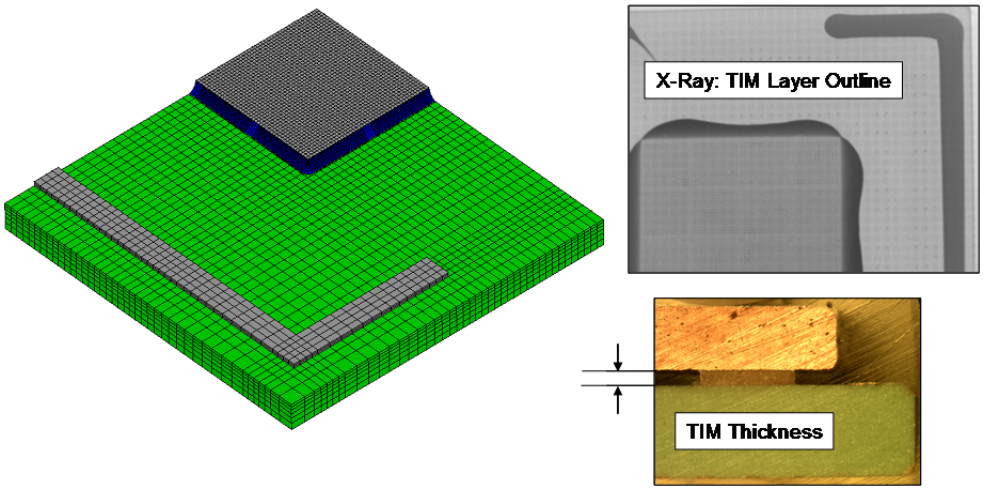

Figure 7.15 TIM Layer for Lid Attachment Model

The predicted distribution of the in-plane horizontal normal stress σ'_{11} on die surface after the lid attachment and TIM1 curing process is shown in Figure 7.16. The maximum compressive stress value was again found to occur at the die center. Relative to the stresses after underfill curing, the value at the die center was seen to increase about 10% to -205 MPa, which correlates well with the experimental results discussed subsequently. Analogous results for σ'_{22} are shown in Figure 7.17. Again, the stress distribution for σ'_{22} was similar to σ'_{11}, except rotated by 90^{o}. The entire die surface continues to be in a state of in-plane biaxial compression.

7.2.4 Correlation with Experimental Measurements

Correlations of the finite element predictions and experimental stress test chip measurements by Roberts, et al [136-138] for the horizontal normal stress σ'_{11} are shown in Figures 7.18-7.20 for the solder reflow, underfill dispense and cure, and lid attachment assembly steps, respectively. The colored contours are the finite element results from Figures 7.9, 7.12, and 7.16. Small colored squares have been added at the sensor rosette

locations, with the fill color of each square indicating the average experimental stress value at that rosette site. Correlation is excellent at most locations. The maximum compressive stresses occur at the die center in each plot. For die attachment, the maximum compressive stress predicted by finite element model (Figure 7.9) was -67 MPa, whereas the experimental measurement was -75 MPa at the rosette site closest to the die center. After underfill curing, the maximum compressive stress predicted by finite element model (Figure 7.12) was -190 MPa, while the experimental measurement was -188 MPa at the rosette site closest to the die center. Finally, after lid attachment, the maximum compressive stress predicted by finite element model (Figure 7.16) was -206 MPa, while the experimental measurement was -210 MPa.

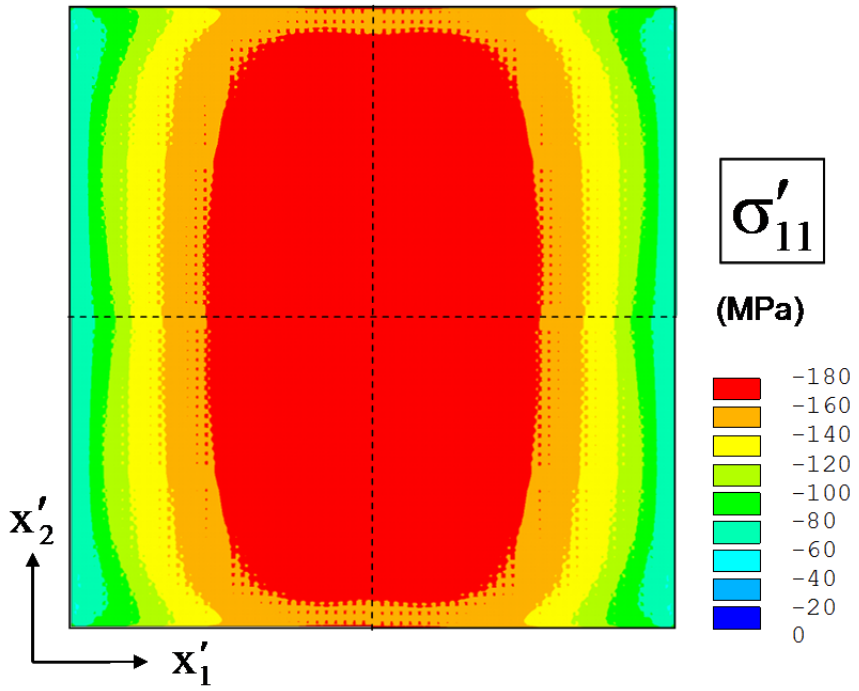

Figure 7.16 In-Plane Horizontal Normal Stress Distribution after Lid Attachment and TIM1 Curing Process

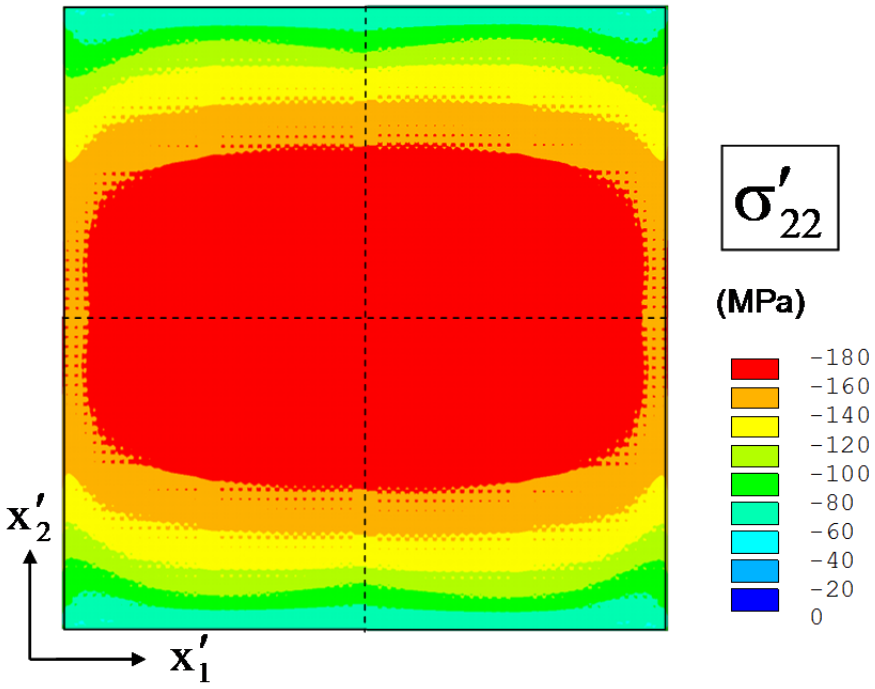

Figure 7.17 In-Plane Vertical Normal Stress Distribution after Lid Attachment and TIM1 Curing Process

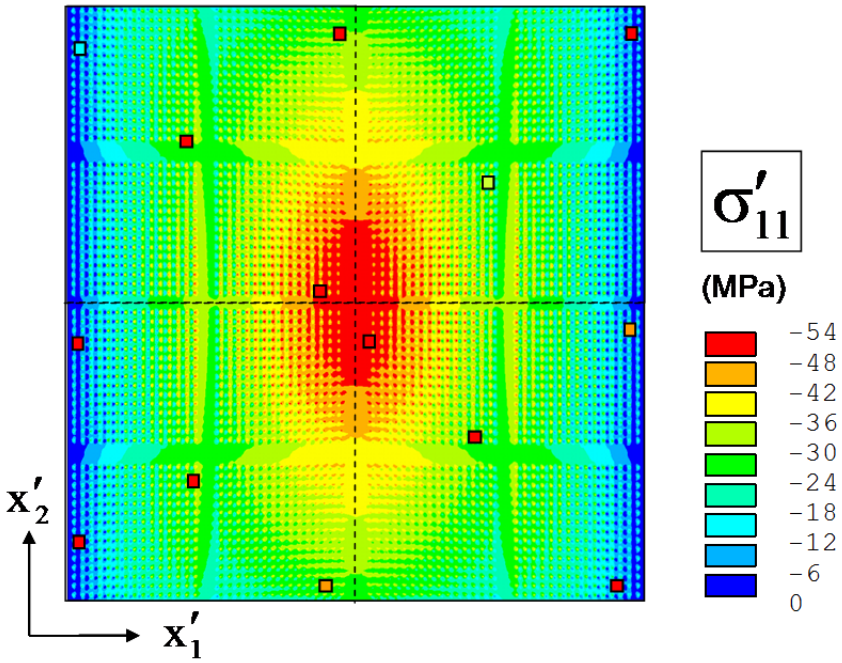

Figure 7.18 Correlation of Finite Element Predictions with Stress Sensor Data [Solder Joint Reflow]

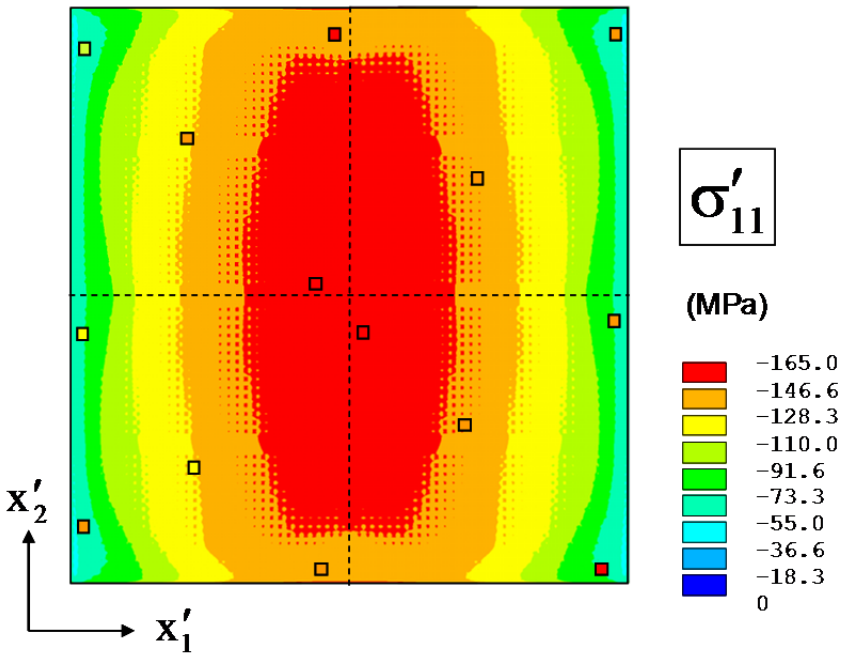

Figure 7.19 Correlation of Finite Element Predictions with Stress Sensor Data [After Underfill Cure]

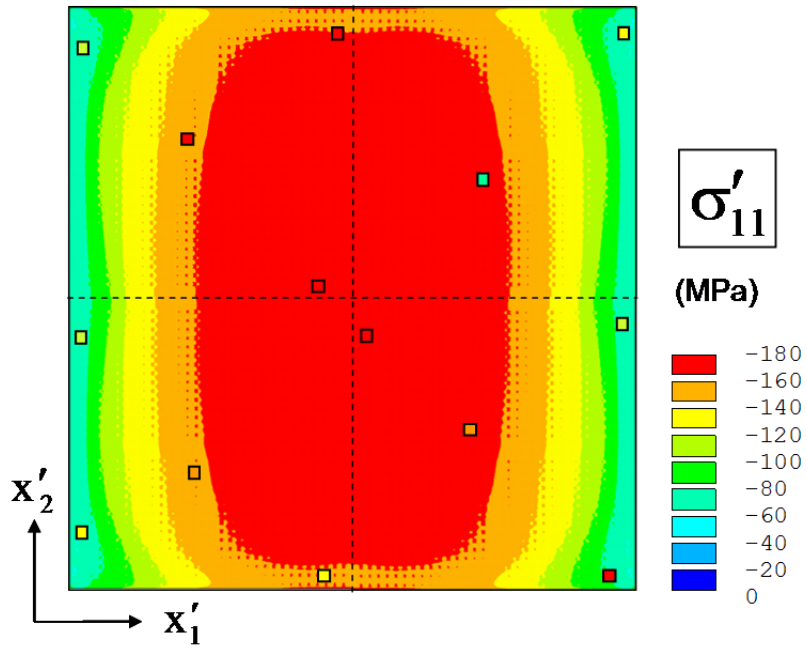

Figure 7.20 Correlation of Finite Element Predictions with Stress Sensor Data [After Lid Attachment]

7.3 Temperature Dependent Stresses

In a parallel experimental study, the wire bonded LGA test assemblies were subjected to varying temperature using an environmental chamber. The samples were initially at room temperature (20 ^{o}C). They were then subsequently raised to 100 ^{o}C, followed by a temperature decrease to T = 0 ^{o}C, and finally brought back to room temperature. A finite element model was developed to correlate with the slow, quasi-static temperature change experiments on the LGA component. As discussed above, the model began with the fully assembled at the LGA configuration, including residual stresses induced by the assembly processes. The FEA model was then subjected to the similar thermal profile and the predicted stresses were extracted at the end of each 20 minute period of constant temperature. Example stress contours for different temperatures are shown in Figure 7.21.

Figure 7.22 shows the predicted variation of the horizontal normal stress at the die center with temperature. The experimental values for one of the components were included for comparison purposes. Both sets of results indicate a linear response with temperature. The magnitudes of the predicted and measured stresses are very similar, especially in the range of 20 to 60 ^{o}C. Figure 7.23 details analogous comparisons for the in-plane shear stress at the corner of the die. Both the experimental and FEA results show a non-linear response with temperature change, especially at elevated temperatures. Both results also show hysteresis in the stress response. The finite element calculations have shown that there are large inelastic deformations of the underfill material in this region.

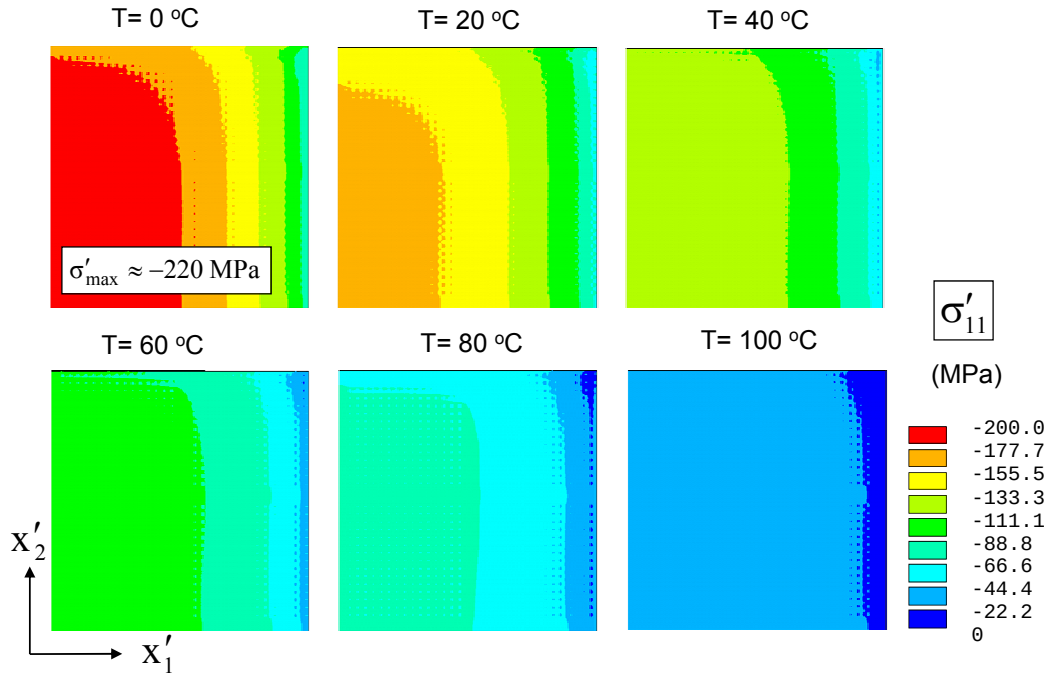

Figure 7.21 FEA Variation of the Horizontal In-Plane Normal Stress Distribution with Temperature

It is also noted that the predicted and experimental stress values in Figures 7.22-7.23 are significantly different, especially at the high and low temperature extremes. This is likely due to the fact that the experimental result is from a single sample package, and that inclusion of additional sample data and averaging of the results will enhance correlation. In addition, the finite element model itself is an idealization of the geometry of the packages and cannot fully account for all manufacturing deviations among all samples. For these reasons, it may be more prudent to compare stress changes when the experimental results are for a single package (i.e. the additional stress induced by a process, condition, or loading), rather than to compare absolute stresses.

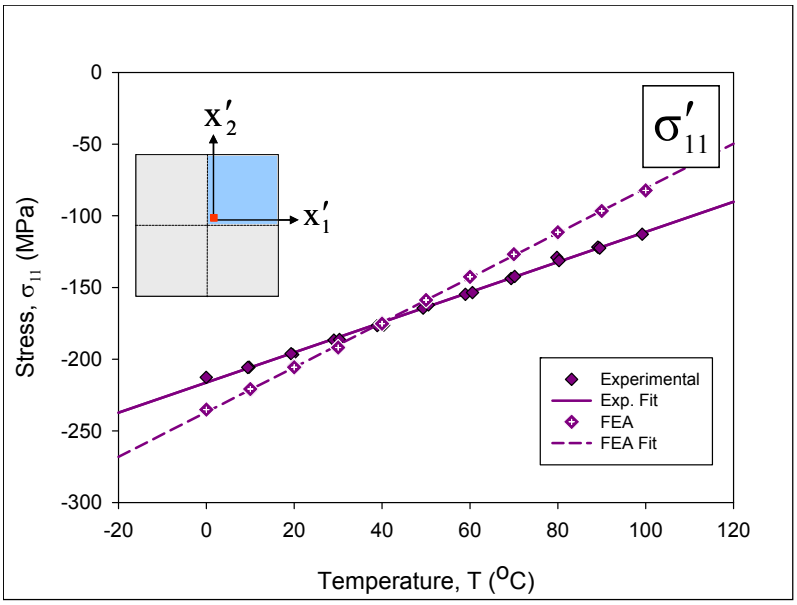

Figure 7.22 FEA Variation of the Horizontal In-Plane Normal Stress with Temperature [Die Center]

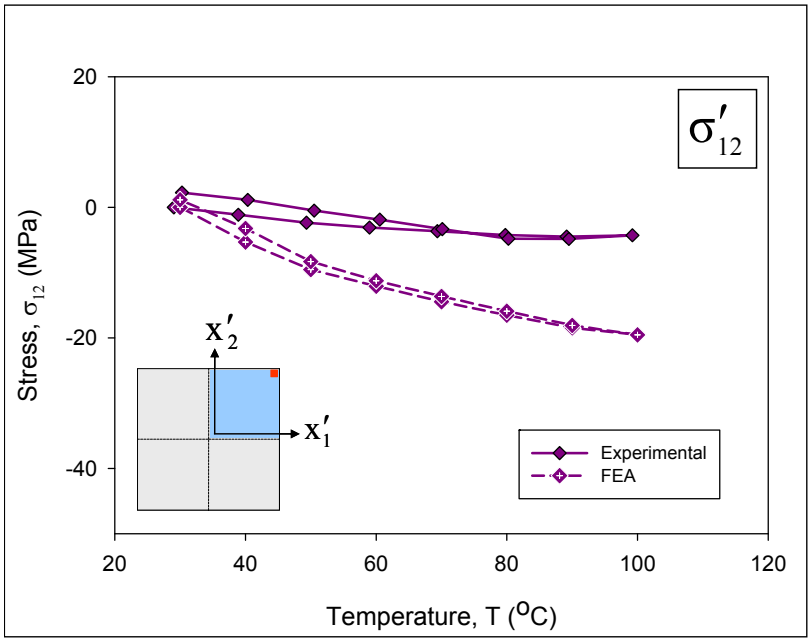

Figure 7.23 FEA Variation of the In-Plane Shear Stress with Temperature [Die Corner]

Figure 7.24 shows the predicted variation of the horizontal normal stress change at the die corner with temperature, along with the analogous experimental values from one of the packages. In this case, the initial loading shows a seemingly linear response through most of the temperature range, becoming slightly non-linear at the upper region of the range. Both results also show hysteresis, again indicating inelastic behavior of the underfill material in the corner of the die with just one slow thermal cycle. Figure 7.25 shows the contours of plastic equivalent stress (EPPLEQV) in the underfill layer which is adjacent to the device side of the die.

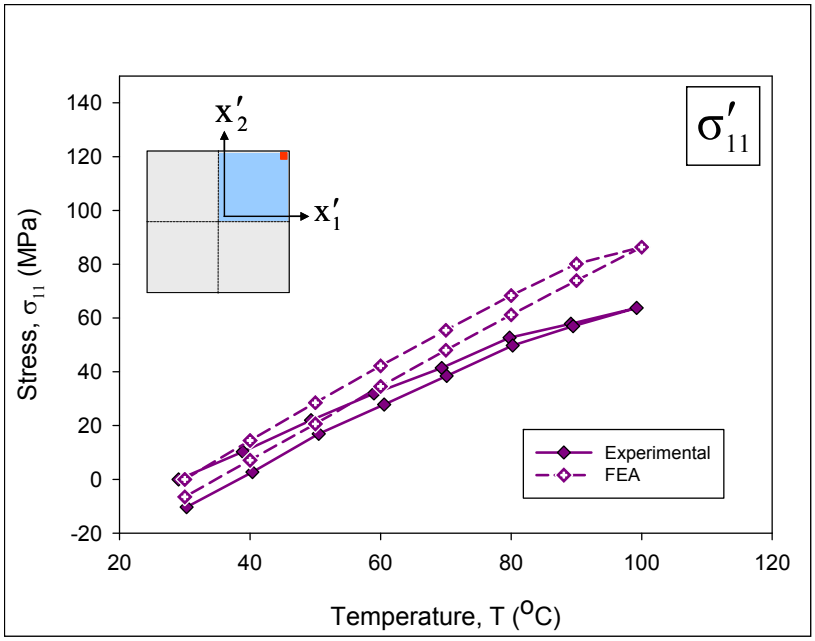

Figure 7.24 FEA Variation of the Horizontal In-Plane Normal Stress Change with Temperature [Die Corner]

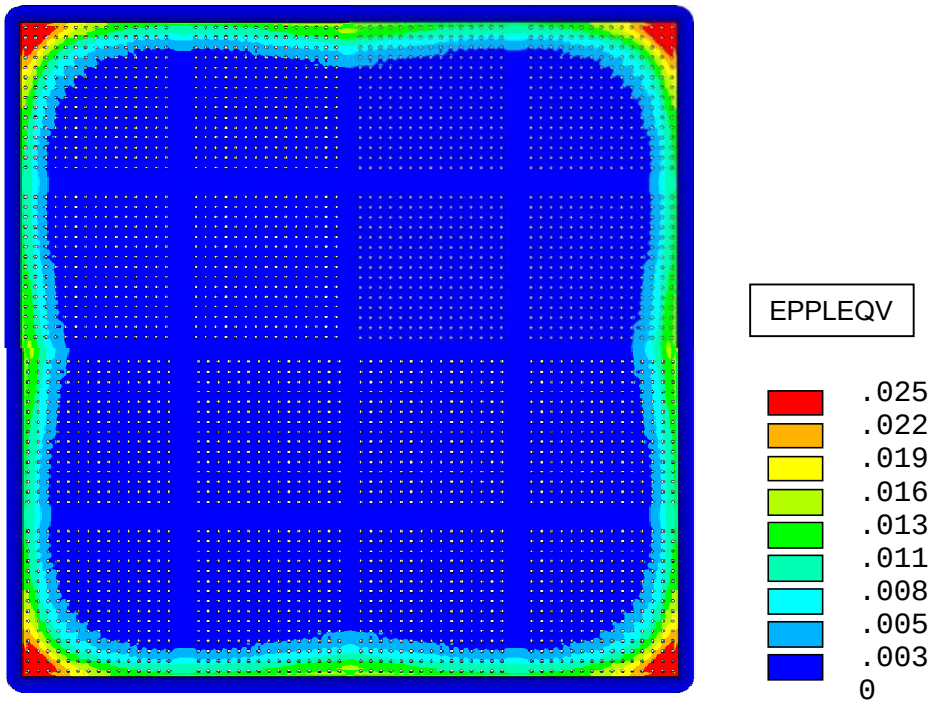

Figure 7.25 Plastic Equivalent Stress in Underfill Layer

7.4 Thermal Cycling Simulations

Finite element simulations of Accelerated Life Testing (ALT) were also performed for the LGA model. Accelerated Life Testing (ALT) is normally performed using thermal cycling, where the test assemblies are subjected to rapid changes in temperature over a much shorter period of time than the expected field exposure of the parts. The range of temperature is also often much greater than the true application environment. The thermal cycling was between 0 and 100 ^{o}C using 60 minute per cycle profile shown in Figure 7.26. The goal is to then use the ALT results to predict/estimate the reliability. This process also allows the determination of various characteristics of the packaging architecture during its life cycle, i.e. critical locations, failure modes, stress levels, etc.

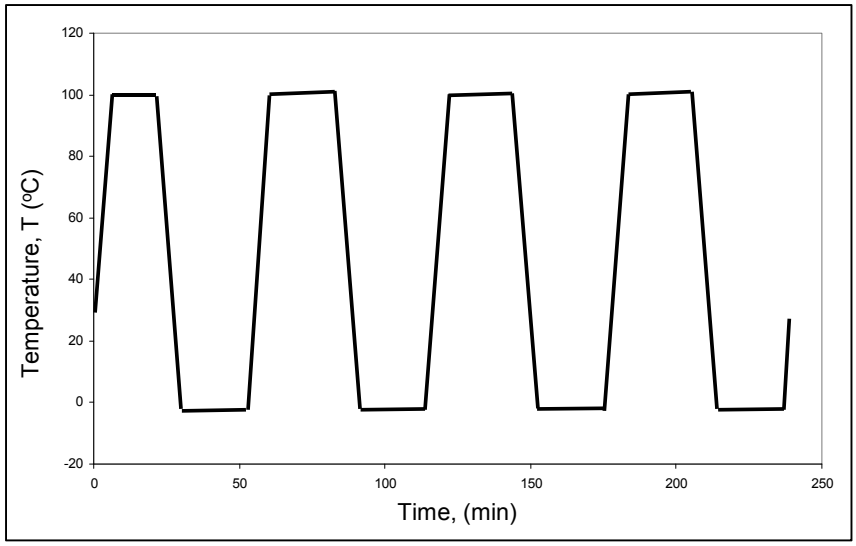

Figure 7.26 Temperature Profile for the Thermal Cycling Simulation of the CLGA Assembly

Thermal cycling simulation starts sequentially with the configuration and results of previous quarter model for lid attachment. FEA prediction of the normal stress at the die center is shown in Figure 7.27 for the initial cycles and the numerical prediction of the variation of the normal stress at the die corner during the initial cycles is shown in Figure 7.28. Also, Figures 7.29-7.30 shows the prediction of shear stresses at the die corner. The modeling results in Figures 7.27-7.30 correlated well with the experimental results [139] for several reasons. First, the shift or jump in the stress values during the initial cycles of the test was evident in both cases. Secondly, both results also showed that the stress levels equilibrate after the first few cycles, and the values from both graphs were very similar.

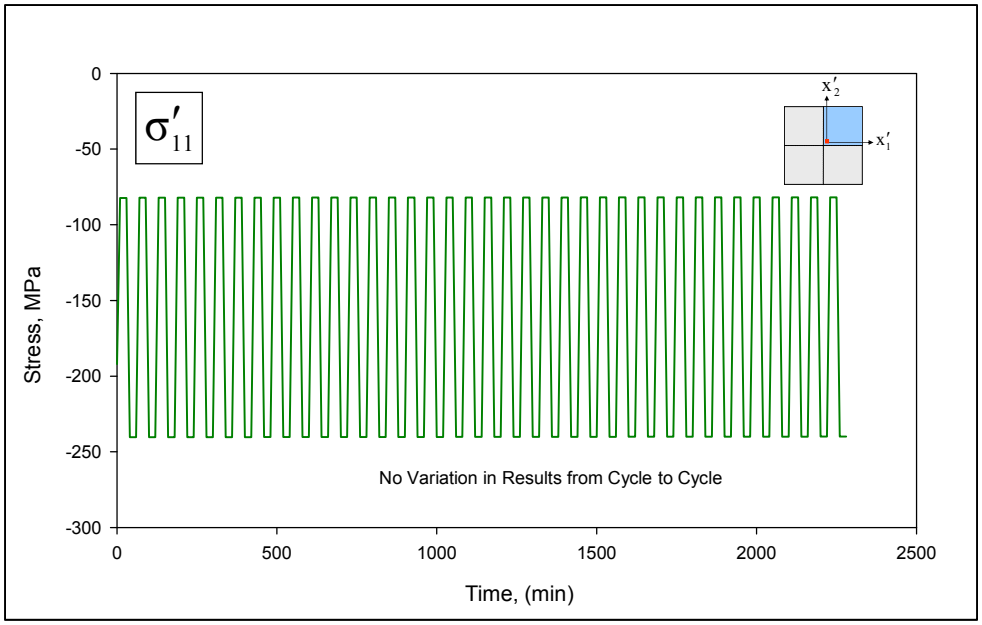

Figure 7.27 Horizontal Normal Stress at the Center of the Die During the First Few Cycles

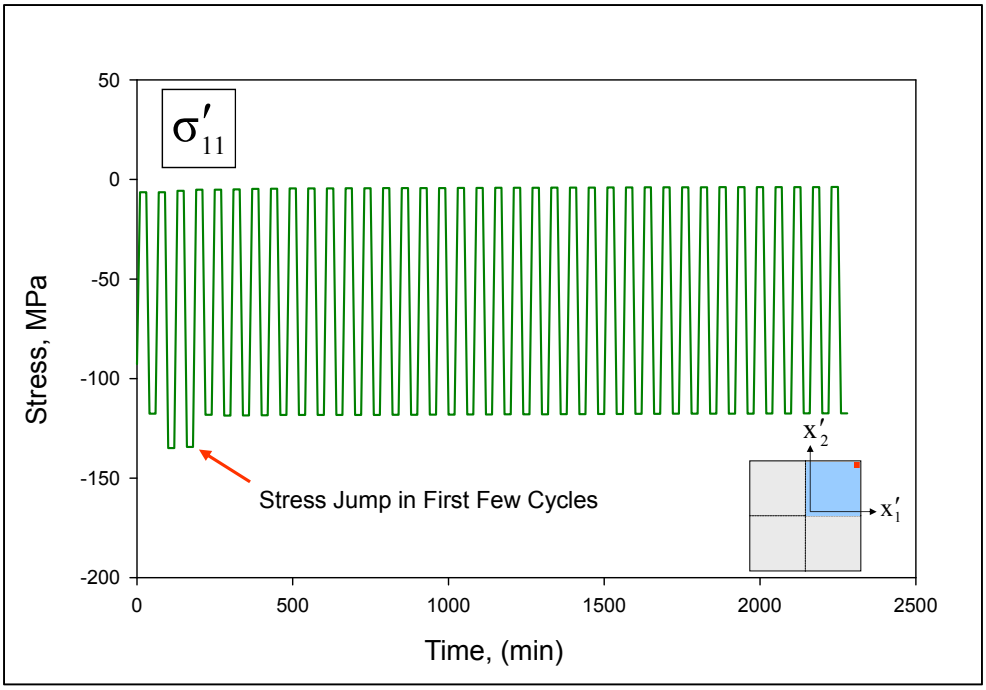

Figure 7.28 Horizontal Normal Stress at the Corner of the Die During the First Few Cycles

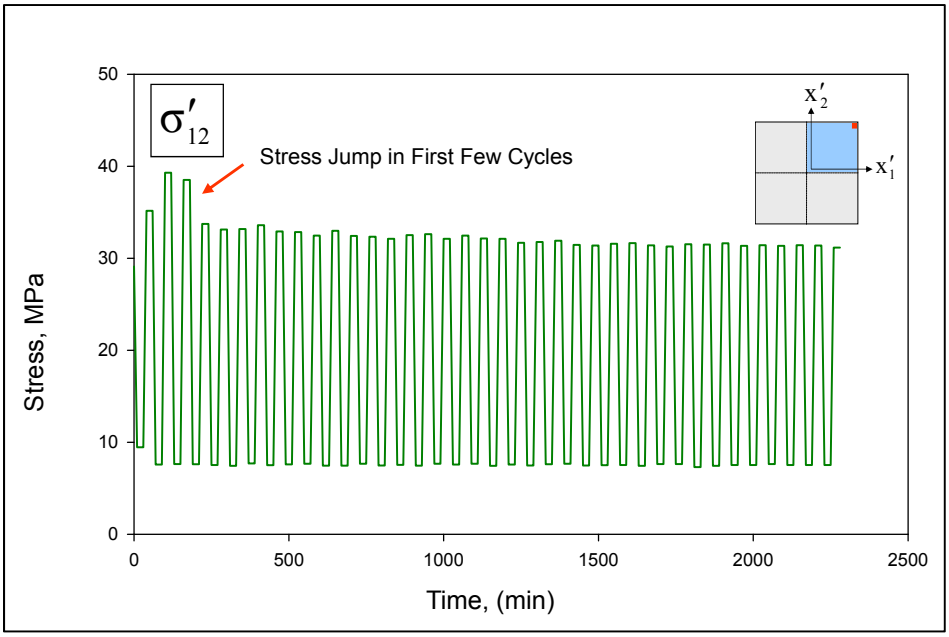

Figure 7.29 In-Plane Shear Stress at the Corner of the Die During the First Few Cycles

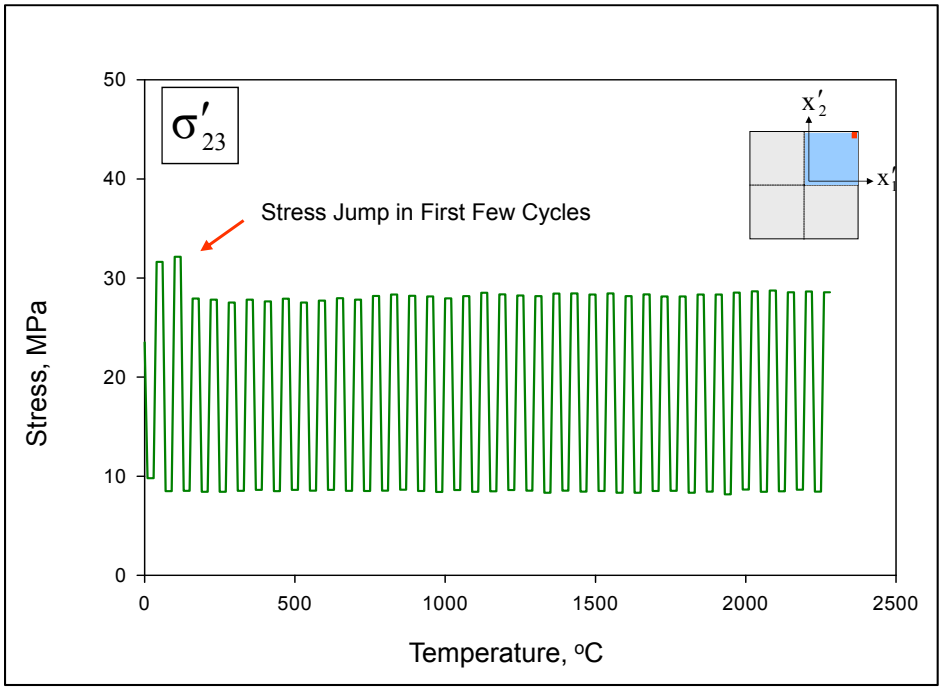

Figure 7.30 Out-of-Plane Shear Stress at the Corner of the Die During the First Few Cycles

Finite element simulations have also been performed for long term cycling from 0 to 100 C using the LGA model discussed above. The maximum (0 ^{o}C) and minimum (100 ^{o}C) normal stresses during cycling are shown in Figure 7.31 for the die center and in Figures 7.32 for the corner of the die. The maximum and minimum values of the in-plane and out-of-plane shear stress (die corner) during cycling are shown in Figure 7.33-7.34. The modeling results verify what was seen in the experimental data [139], namely that the majority of changes in the die stresses will occur early in the cycling process. Similarly, the FEA predicted stress levels were also constant for several thousand cycles.

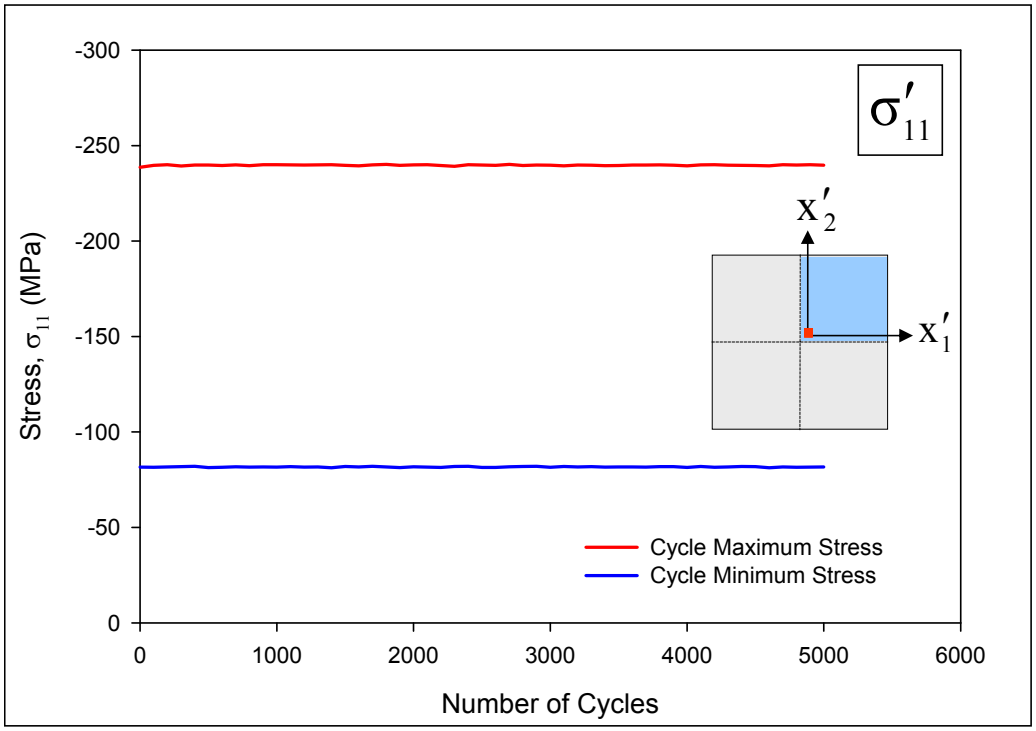

Figure 7.31 Horizontal Normal Stress at the Center of the Die During Long Term Thermal Cycling

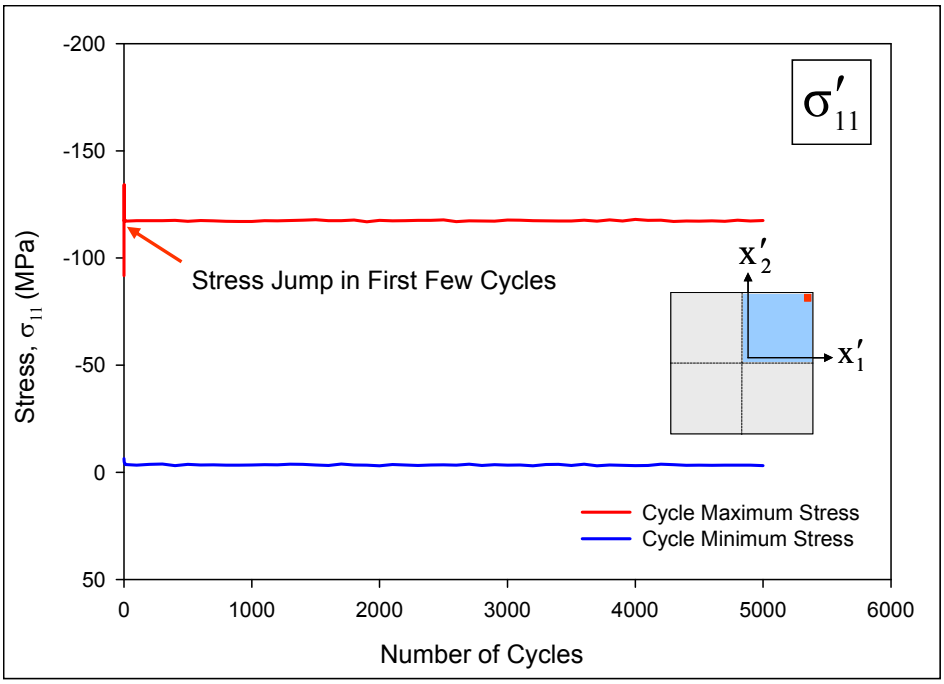

Figure 7.32 Horizontal Normal Stress at the Corner of the Die During Long Term Thermal Cycling

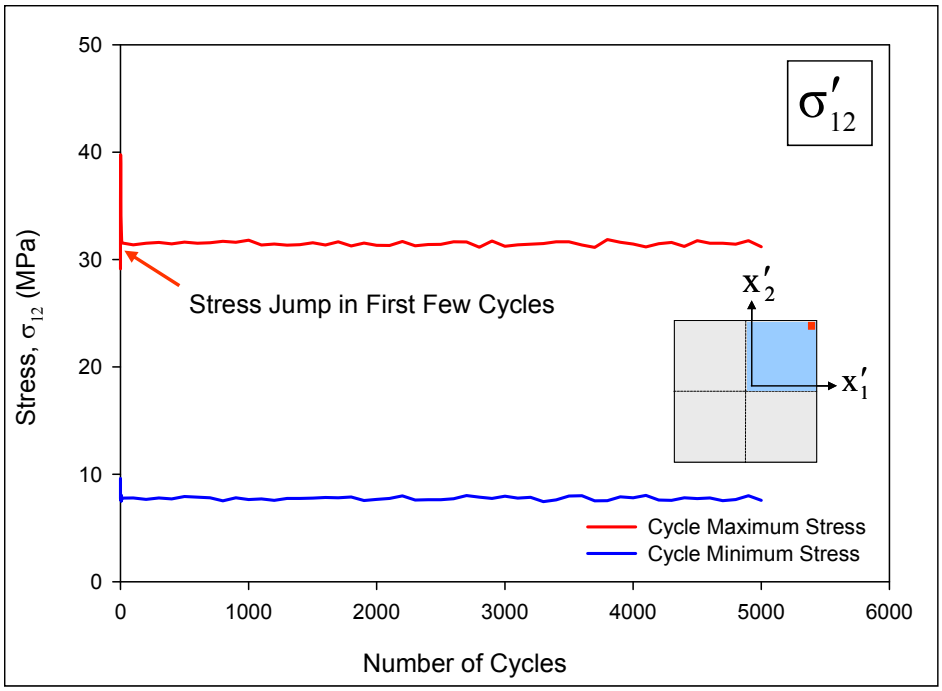

Figure 7.33 In-Plane Shear Stress at the Center of the Die During Long Term Thermal Cycling

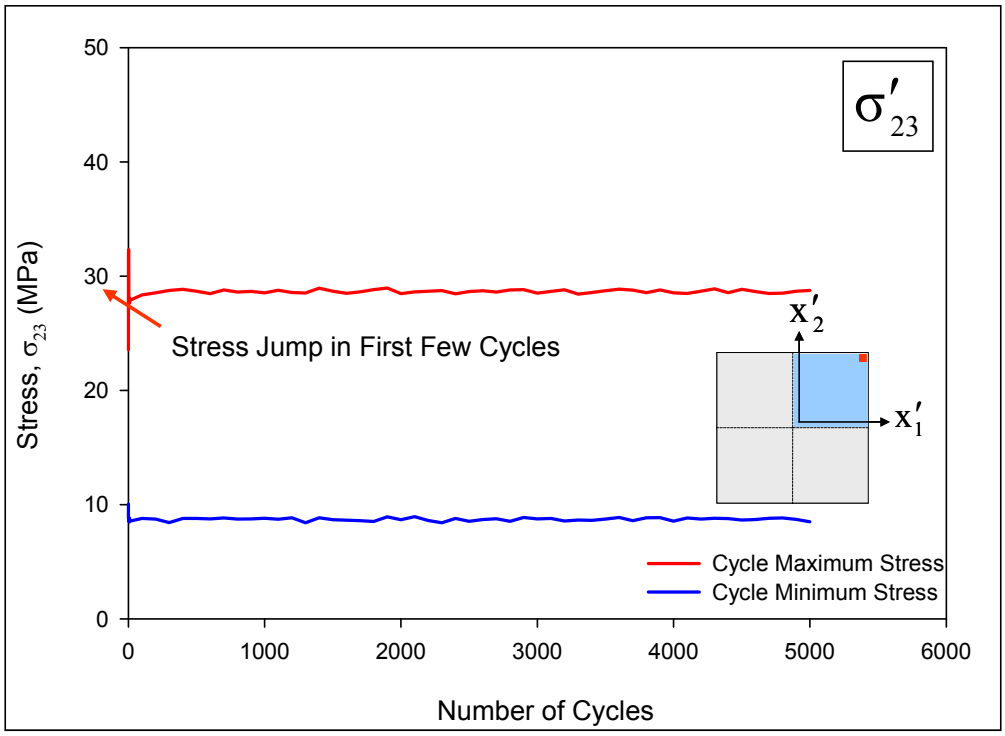

Figure 7.34 Out-of-Plane Shear stress at the Center of the Die During Long Term Thermal Cycling

7.5 Power Cycling Simulation

The tests chips featured an on-chip buried heater layer that could be excited to dissipate power. The area of the buried layer (Figure 7.35) was the same as the chip itself, allowing for uniform heating of the entire die. It was observed that steady state conditions were reached within 1000 sec for all power levels. Finite element modeling (transient heat transfer) was used to predict the on-chip temperature distributions. The LGA mesh shown in Figure 7.14 was again utilized, along with the thermal boundary conditions shown in Figure 7.36. Figure 7.37 shows the predicted transient die temperature variations for a power dissipation level of 2 Watts. Thermal properties of the materials that were used in the simulation are listed in Table 7.2. The temperature distribution obtained from the thermal analysis was used as the boundary condition for

the structural analysis to calculate the stress distribution on the die surface. Figure 7.38 shows the transient normal stress variation at the die center. Both the temperature and stress came to steady state within the 2000 sec for the 2 Watts power level. The predicted steady state temperatures correlated well with experimental measurements, while the time constant of the experimental process is slightly lower than that found using the FEA model.

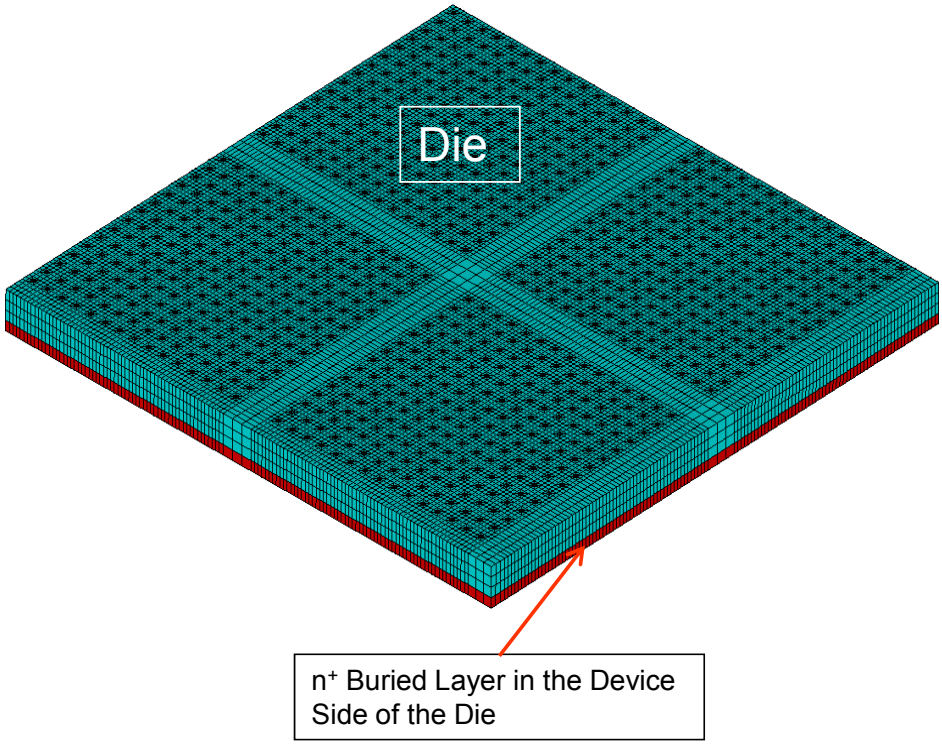

Figure 7.35 n+ Buried Layer in the Die

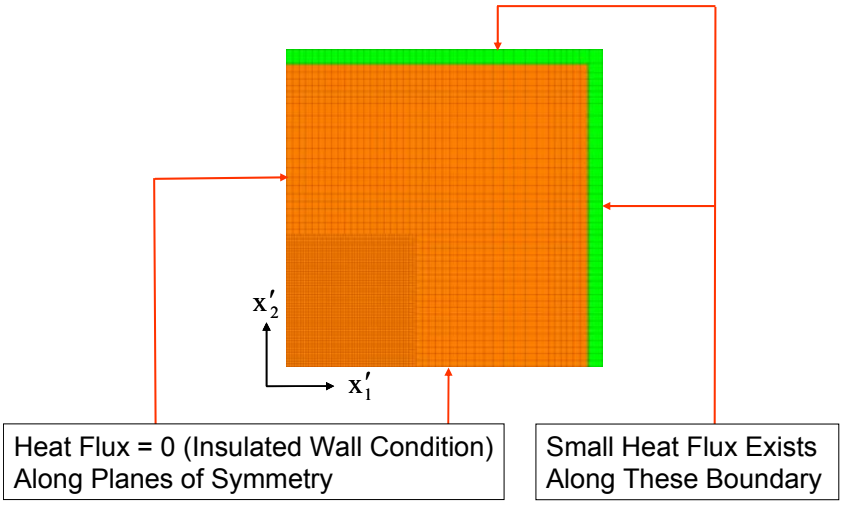

(a) Top View

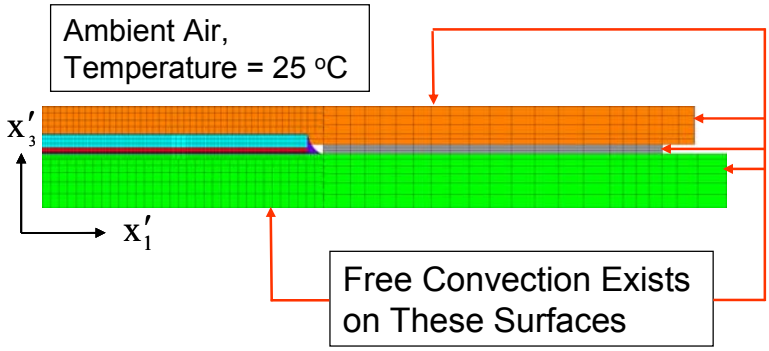

(b) Side View

Figure 7.36 Boundary Conditions for Transient Thermal Analysis for Power Dissipation Simulations

Material	Thermal Conductivity (W/mK)	Specific Heat (J/kg-K)	Density (kg/m^3)
Silicon	130	700	2330
Solder	32.3	180	9250
Underfill	0.4	1883	1149
Ceramic	25.1	920	3400
TIM	6.4	2000	4410
Copper	400	390	8940

Table 7.2 Material Properties Used for Transient Thermal Analysis

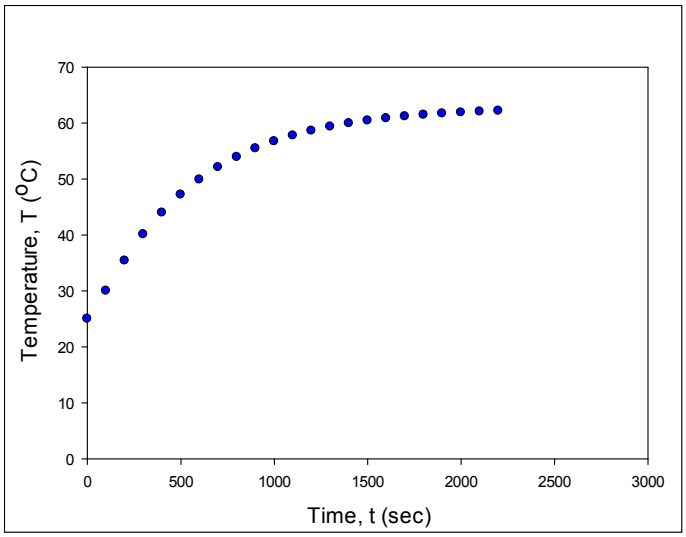

Figure 7.37 Transient Die Surface Temperatures for On-Chip Power Dissipation

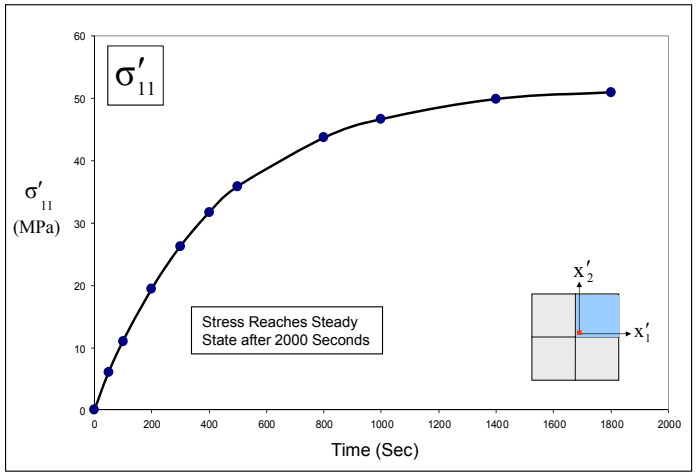

Figure 7.38 Transient Die Normal Stress at the Die Center for On-Chip Power Dissipation

Power cycling simulations were then performed for the LGA model by exciting the buried layer on the flip chip test die in a cyclical manner. The chosen transient power dissipation is shown in Figure 7.39. A square wave cycle was utilized, with a peak excitation of 2 Watts, and a cycle length of 20 minutes (10 minutes at full excitation and ten minutes of no excitation). A plot of the predicted die temperature versus time is shown in Figure 7.40. Good correlations with experimental results were observed for the

transient temperature response [139]. Similar to the power dissipation simulation, the temperature distribution in the package due to power cycling was used as the boundary conditions for a structural analysis, which was done to calculate the stress distribution in the die surface. Figure 7.41 shows the variation of normal stress at the die center. It is evident that the peak stress increases gradually during first few cycles and then stabilizes.

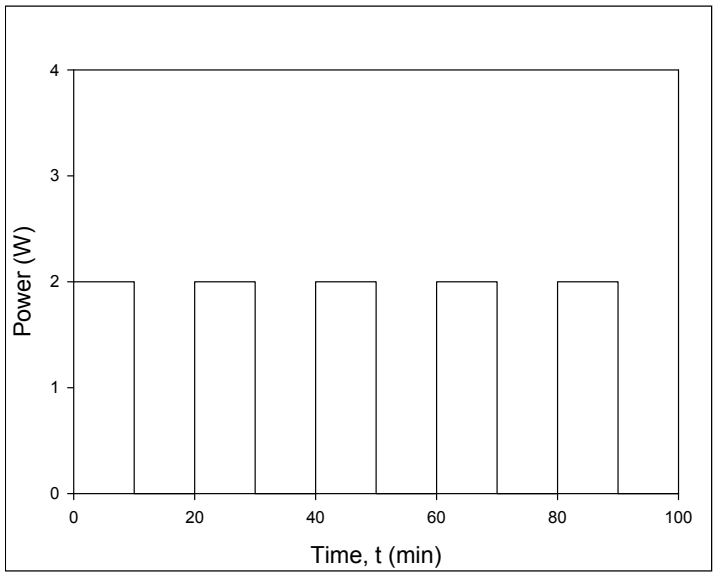

Figure 7.39 Square Wave Power Cycle

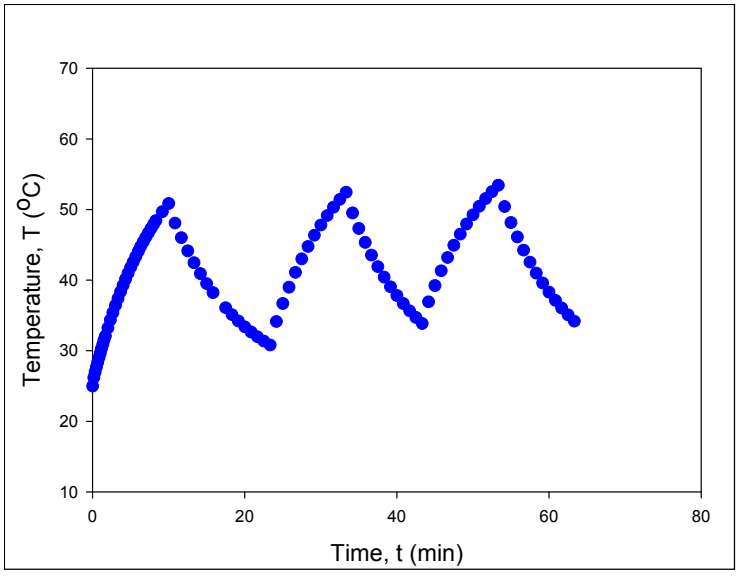

Figure 7.40 Transient Die Surface Temperature Variation for Power Cycling (LGA)

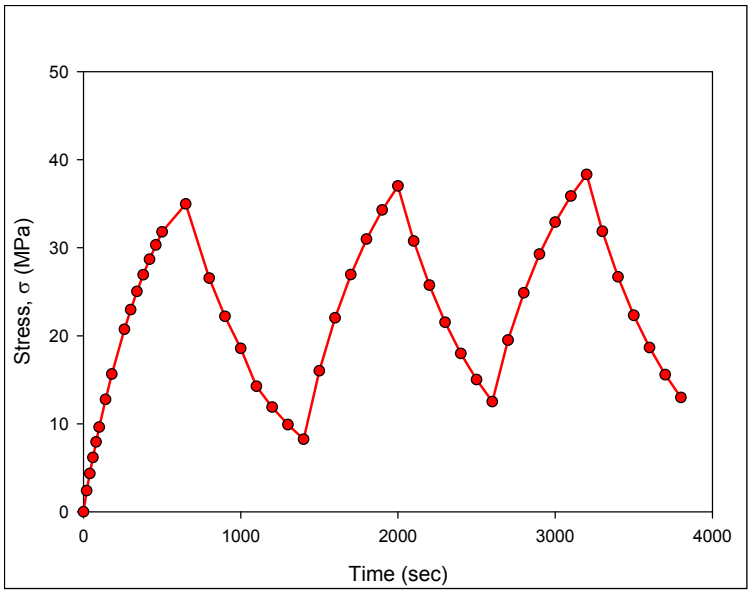

Figure 7.41 Transient Die Stress Variation at the Center of the Die for Power Cycling (LGA)

7.6 Effects of Isothermal Aging on the Die Stresses

All the stress results that are shown in the preceding sections were for a non aged assembly. In those calculations, the Anand constants for no aging condition from the Table 7.1 were used for SAC405 solder bumps. Effects of aging on the die stress distributions were also investigated or the CLGA assembly. The evolutions of Anand parameters with aging were experimentally determined for SAC305 solder and a 100 ^{o}C aging temperature in Chapter 4. In this section, we have used those parameters for the flip chip solder balls in the CLGA assembly to investigate aging effects. In particular, the Anand parameters in Table 4.2 were used for different durations of aging. The simulation was sequentially started from the configuration and results after lid attachment assembly at room temperature, and then the temperature was raised to 100 ^{o}C for aging. Figures 7.42 and 7.43 show the in-plane normal stress distributions after the lid attachment when the assembly was cooled to room temperature. These results differ slightly from those in

Figures 7.16 and 7.17 because SAC305 has been used for the solder material rather than SAC405. For the SAC305 flip chip solder balls, the maximum value for the stress σ'_{11} was -200 MPa at the center of the die.

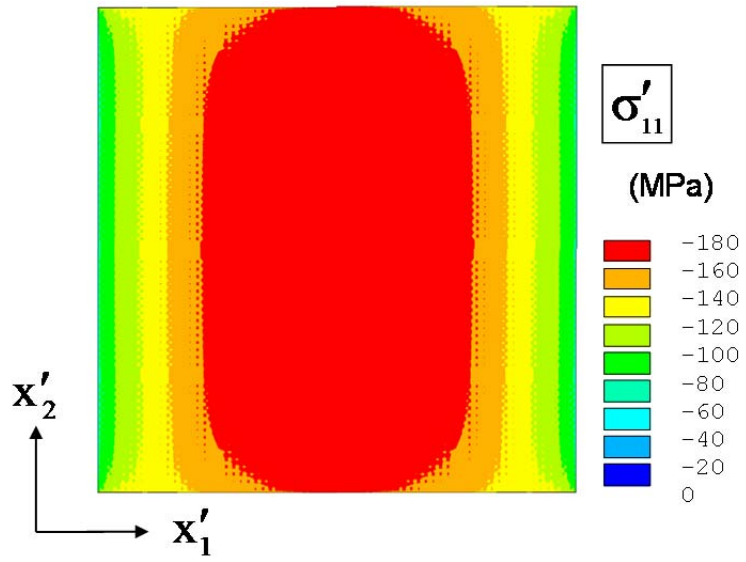

Figure 7.42 In-plane Normal Stress Distribution after Lid Attachment and TIM1 Curing Process (SAC305 Solder)

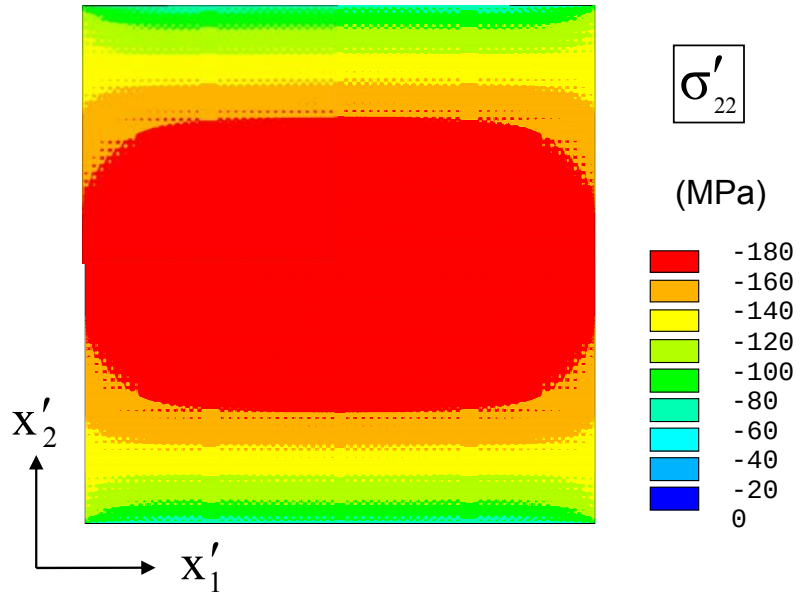

Figure 7.43 In-plane Normal Stress Distribution after Lid Attachment and TIM1 Curing Process (SAC305 Solder)

Starting with the results after lid attachment assembly, the temperature was raised to 100 ^{o}C and held constant for up to 180 days of aging. The Anand parameters of the solder were changed with aging time using the empirical formulas given in Table 4.3. Also, the underfill was considered to be a viscoelastic material for this simulation with the Prony series constants given in Table 7.3. The die stress distributions were recorded as a function of time during the aging simulation. For example, Figure 7.44 shows the effects of aging on the die normal stress distribution σ'_{11} for up to 180 days of aging (quarter model results). The top left contour plot gives the results for no aging, and the maximum stress for this case was -76 MPa at the center of the die. As the aging progressed, the maximum stress slowly decreased to about -70 MPa. The bottom right contour plot shows the results for 180 of days aging. The shifts in the contour map with time are due to a combination of a) aging of time solder material and b) stress relaxation of the underfill material. It was observed that about an 8% stress reduction occurred after 180 days of aging as illustrated in Figure 7.45.

Constants for Shear Response	Constants for Volumetric Response	Constants for Shift Functions
α_1 = 0.1366 τ_1 = 3556.6000 α_2 = 0.2300 τ_2 = 30006.0000 α_3 = 0.3111 τ_3 = 0.3009 × 10^6 α_4 = 0.0934 τ_4 = 3.01 × 10^6	α_1 = 9.0746 × 10^{-10} τ_1 = -86.8690 α_2 = 0.5313 τ_2 = 0.8663 α_3 = 0.2403 τ_3 = 94.8260 α_4 = 0.0845 τ_4 = 999.9400 α_5 = 0.0726 τ_5 = 10000.0000	T_{ref} = 88.9860 C_1 = -16.1830 C_2 = -469.2900

Table 7.3 Viscoplastic Properties Used for Underfill Material [142]

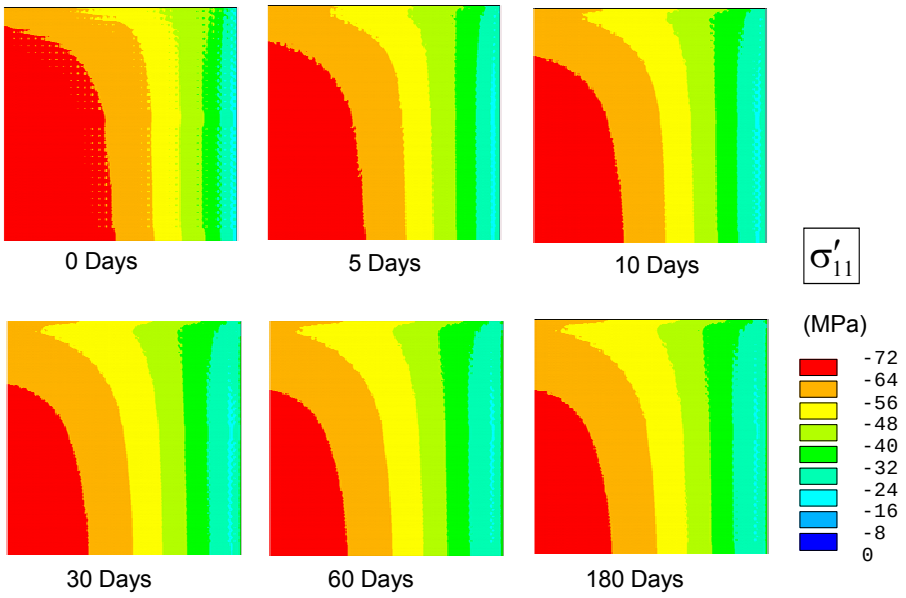

Figure 7.44 Die Stress Variation with Aging at 100 °C (Quarter Model)

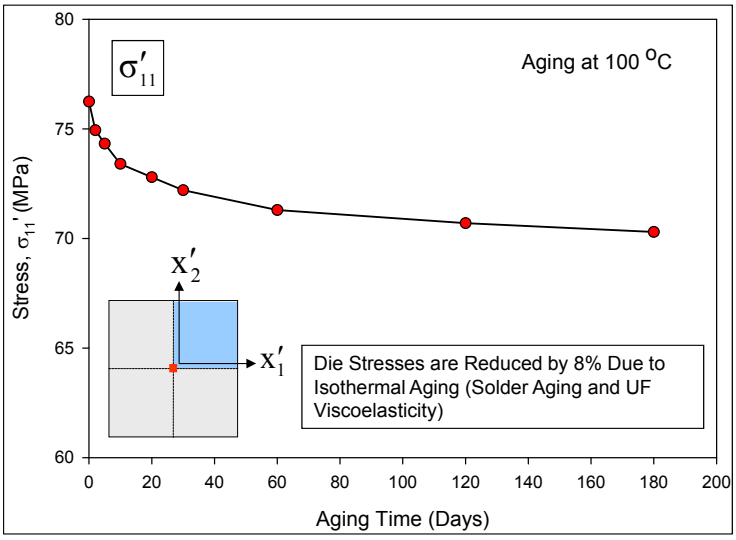

Figure 7.45 Die Stress Variation at the Die Center with Aging at 100 °C

As both the solder aging and underfill viscoelasticity contributed in the 6 MPa (8%) stress reduction, another calculation was performed to determine how much of this reduction was due to solder aging. In the second simulation, the solder was modeled with the Anand constitutive model with aging, while the underfill was modeled without any

viscoelasticity (elastic-plastic). In this simulation, it was observed that the maximum value of the die stress σ'_{11} was reduced by only 2 MPa for 6 months aging at 100 ^{o}C (see Figure 7.46). Thus, effects in the flip chip solder balls cause only very small changes in the die stress distributions. However, the stresses in the solder bumps were significantly reduced due to aging. Figure 7.47 shows the shear stress σ'_{13} distribution in the critical solder ball (corner solder ball) of the assembly. A maximum stress of 4 MPa was found for no aging. After 6 months aging at 100 C, this stress was reduced by 60% to 1.5 MPa as shown in Figure 7.48.

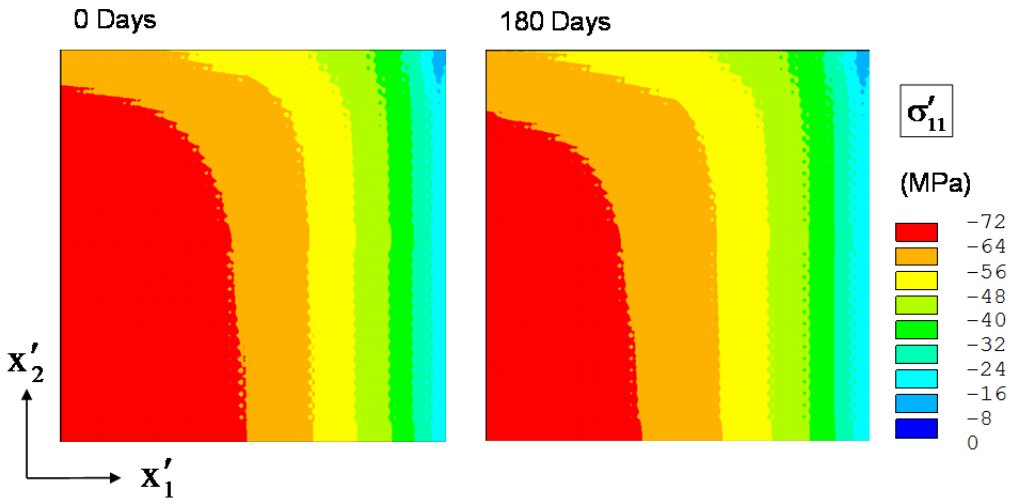

Figure 7.46 Die Stress Variation Due to Only Solder Aging Effects

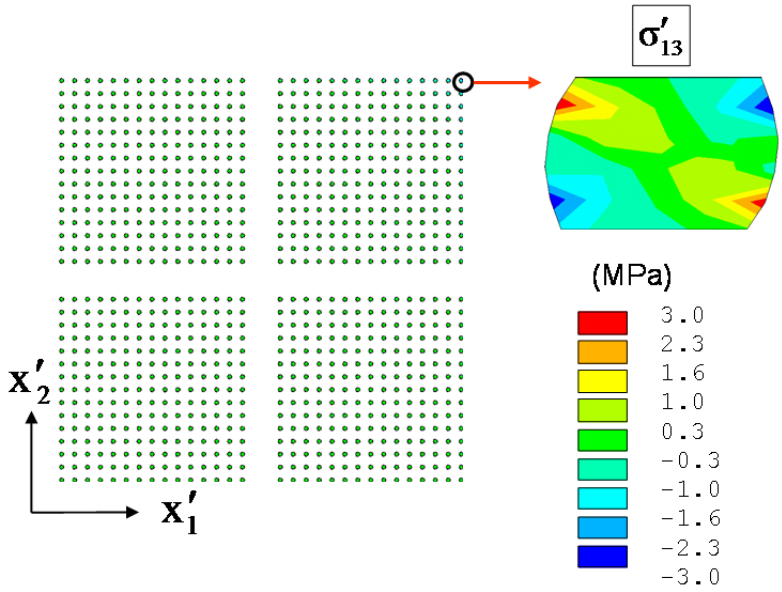

Figure 7.47 Stresses in the Critical Solder Ball (No Aging)

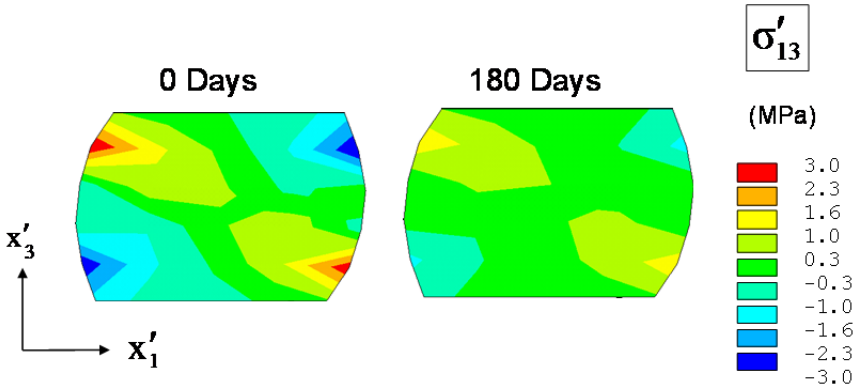

Figure 7.48 Stresses in the Critical Solder Ball (with Aging)

A third aging simulation was performed using constant Anand parameters for the solder (no aging model) and viscoplastic behavior of the underfill. In this case, about a 4 MPa (5%) die stress reduction was observed after 180 days of aging as shown in Figure 7.49. Also, Figure 7.50 shows the corresponding reduction in the Von Mises stress in the underfill layer of the assembly after the aging exposure due to the viscoelastic effects in the underfill.

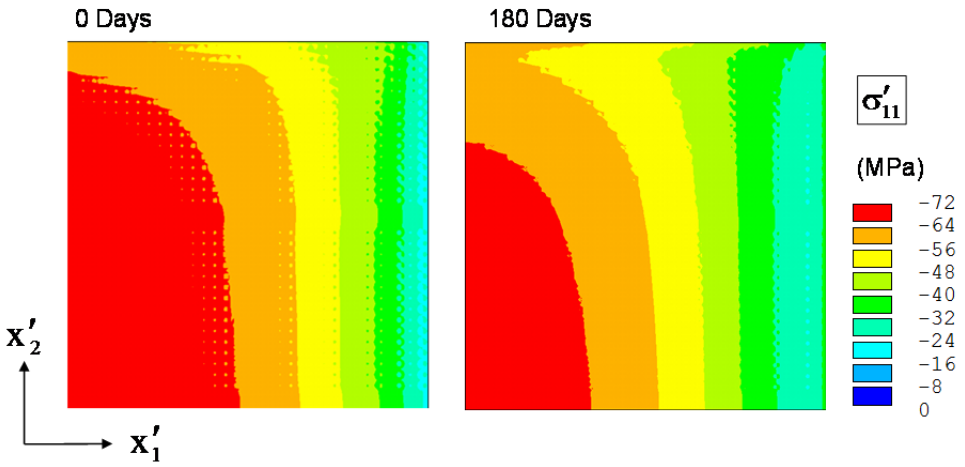

Figure 7.49 Die Stress Variation Due to Underfill Viscoelasticity

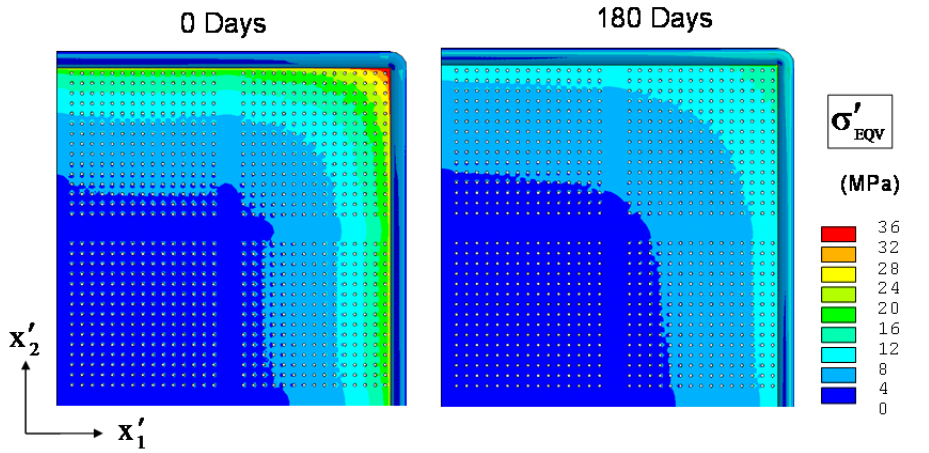

Figure 7.50 Stress Reduction in the Underfill Layer (Due to Underfill Viscoelasticity)

7.7 Prediction of the Thermal Cycling Reliability of the Critical Solder Ball

The calculation of the life of the critical solder joint under the thermal cycling loading can be performed by calculating the plastic energy dissipation in the critical solder bump by finite element analysis and then using the reliability model equations (Eqs. 5.3-5.5). For these calculations, the thermal cycling was assumed to be from 0 to 100 ^{o}C, and the temperature profile in Figure 7.26 was used. The plastic energy dissipated per cycle (ΔW) was calculated for the first 8 cycles.

Figure 7.51 shows the distribution of plastic work in the solder layer (quarter model results) at the end of 8th cycle. The maximum plastic work occurred at the corner solder ball (illustrated by the magnified view). As discussed in the previous chapter, there are various methods of calculating the volume averaged plastic energy dissipation per cycle. Figure 7.52 shows the variation of the volume averaged PLWK in the critical solder ball as a function of time. The volume averaging has been performed by 2 different ways including the use of the neck element layers and the use of elements in the neck outer ring. The magnitude of PLWK calculated using the outer ring elements was higher at all times. Thus, this approach was used in the reliability calculations since it is more conservative. Figure 7.53 shows the variation of volume averaged plastic work (outer ring) for the first 8 cycles, and the plastic work per cycle values extracted from this curve are tabulated in Table 7.4. It is observed that the value of ΔW converged during the first few cycles. Using the reliability model constants K_1, K_2, K_3, K_4 in Tables 5.1 and 5.3 for no aging, calculated number of cycles for crack initiation was 262 and the crack growth rate was 0.96 μm/ cycle for this assembly.

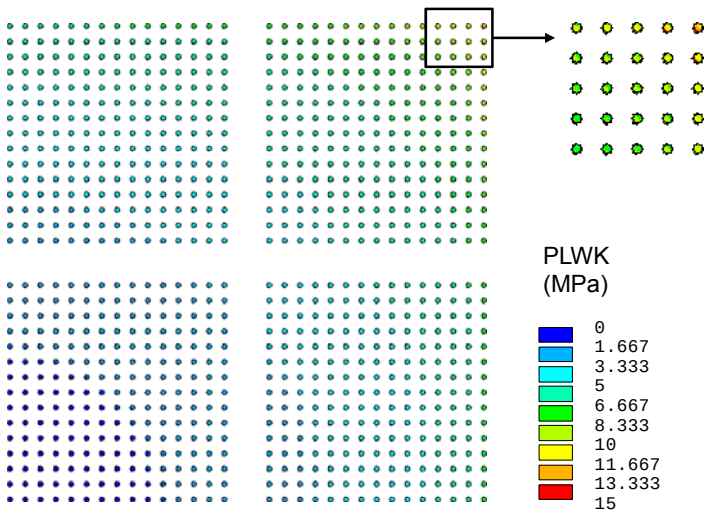

Figure 7.51 Plastic Energy Dissipation in the Flip Chip Solder Bumps after the 8th Cycle

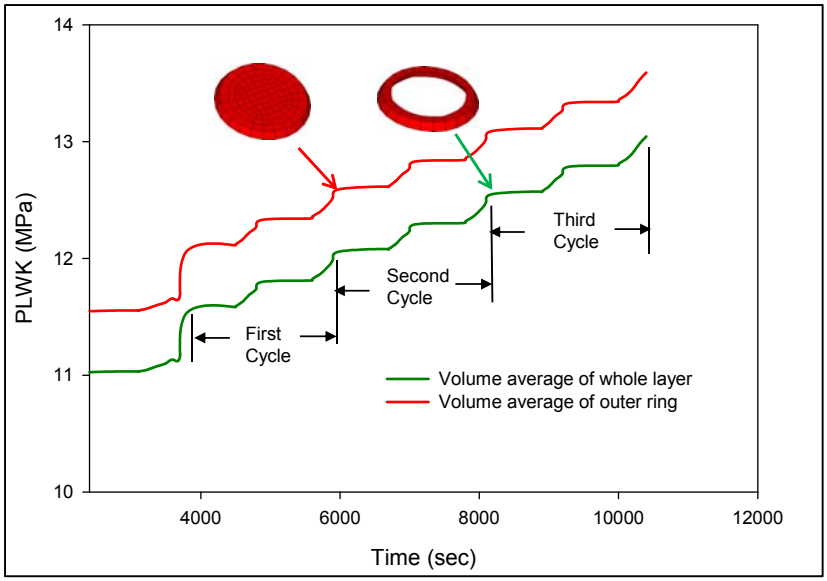

Figure 7.52 Variation of the Volume Averaged PLWK with Time in the Critical Solder Bump using Different Averaging Methods

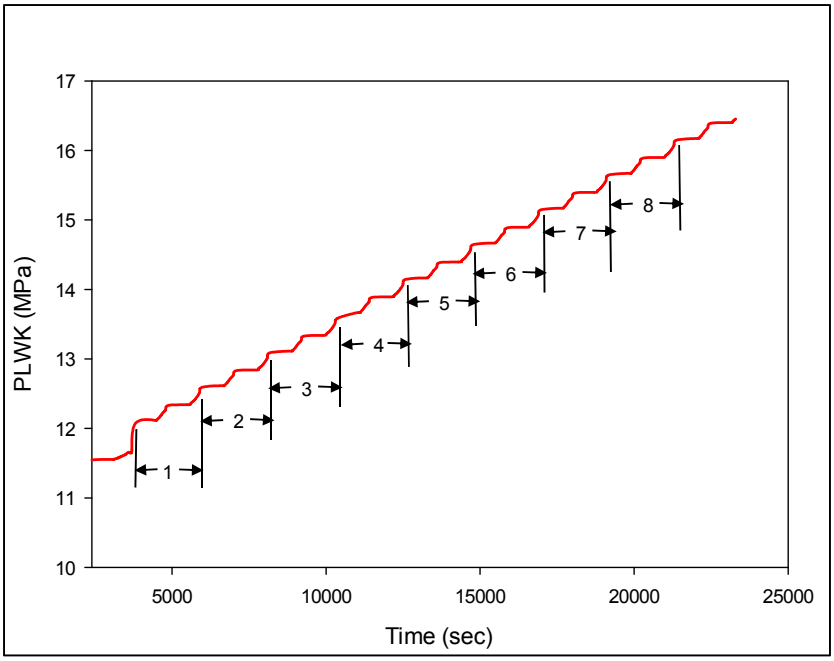

Figure 7.53 Variation of the Volume Averaged PLWK with Time in the Critical Solder Bump for the First 8 Thermal Cycles

No. of Cycles	ΔW
1	0.52898
2	0.49867
3	0.49947
4	0.50581
5	0.50097
6	0.50121
7	0.50140
8	0.50151

Table 7.4 Convergence of Volume Averaged ΔW with Number of Thermal Cycles

7.8 Stresses Due to CBGA Assembly

After carrying out the stress analysis for the LGA assembly processes, temperature dependent stresses, and stresses due to thermal and power cycling, the next analysis step was considered as the stresses due to CBGA assembly, and subsequent thermal exposures and other loadings. Figure 7.54 shows the schematic diagram of a typical CBGA assembly with heat sink clamping fixture. Second level BGA solder balls, second level underfill, and the PCB are attached to the previous LGA package to yield the CBGA structure. Figure 7.55 shows the finite element mesh for the quarter model of the CBGA assembly. In these simulations, the second level solder balls were assumed to be SAC305 lead free solder.

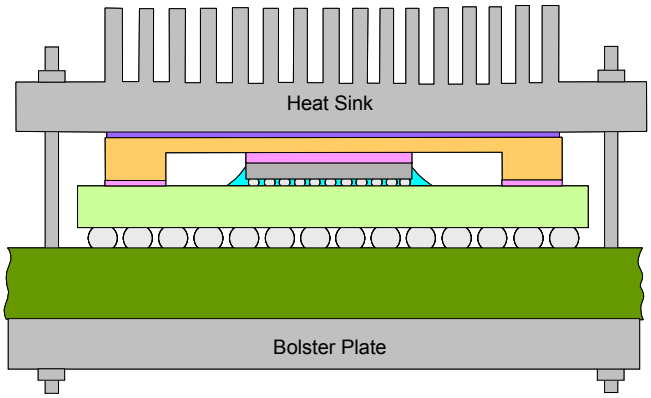

Figure 7.54 CBGA Heat Sink Clamping Geometry

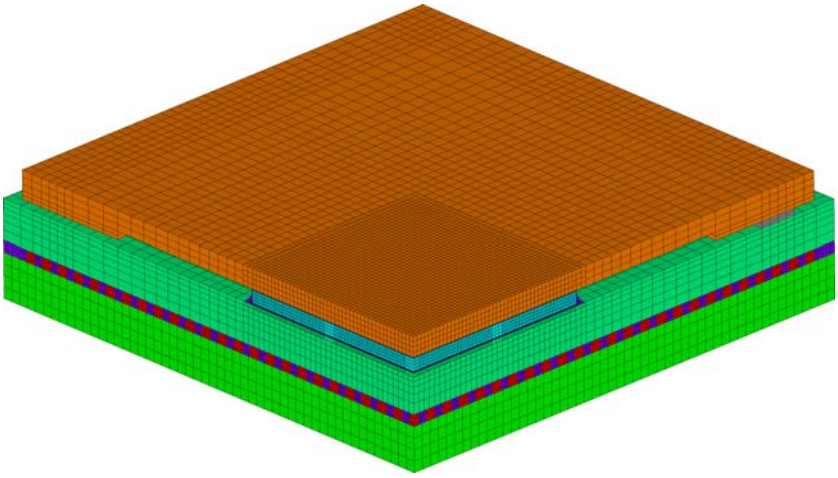

Figure 7.55 Quarter Symmetry Finite Element Mesh for the CBGA Assembly

The finite element predictions of the distribution of the horizontal normal stress σ'_{11} on the device side of the full die are shown in Figure 7.56. In this Figure, the stress distribution after CBGA assembly has been compared with the stress distribution that was obtained after the LGA assembly. The maximum stress after CBGA assembly was found to be about -225 MPa at the center of the die whereas for the LGA assembly it was about -210 MPa. Also the region of high stress in the center of the die was larger for the CBGA assembly relative to that for the LGA assembly.

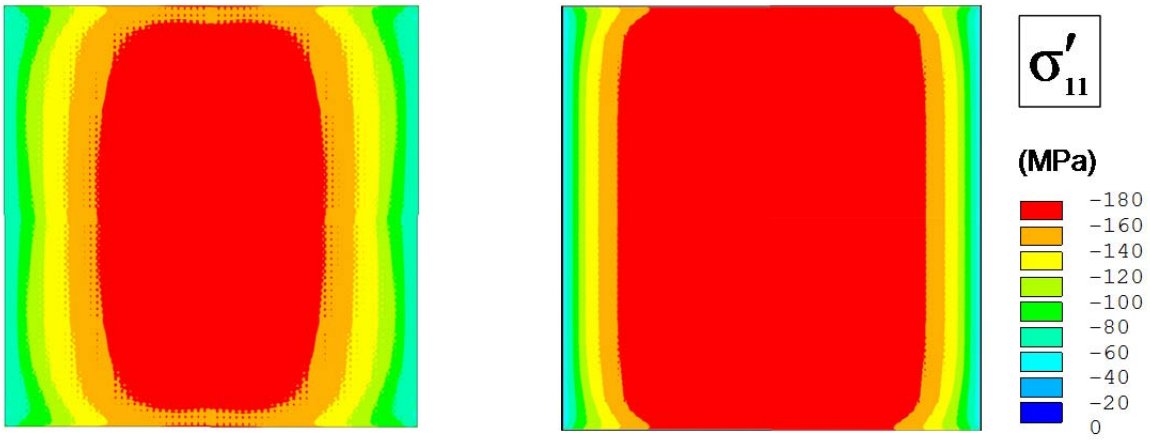

Figure 7.56 Stresses after Lid Attachment (Left) and after CBGA Assembly (Right)

7.9 Temperature Dependent Stresses (CBGA)

Similar to the temperature dependence study in section 7.3 for the LGA assembly, the stress response for temperature variations between 0 and 100 ^{o}C was also calculated for the CBGA assembly. Started with the stress results at room temperature (25 C), the temperature was slowly reduced to 0 ^{o}C, and then it was increased to 100 ^{o}C, with 20 ^{o}C increments. Finally, the temperature was brought back to room temperature. The predicted stress variations were very similar to those found for the LGA assembly. Figure 7.57 shows the variation of the horizontal normal stress σ'_{11} at the center of the die, and Figure 7.58 shows the response of the same stress component at the corner of the die. Stress Contour maps are shown in Appendix A.5. Also, Figures 7.59-7.60 show the in-plane and out-of-plane shear stress variations with temperature change. All of these stress variations were similar in nature to the variations that were observed for the LGA assembly under temperature change.

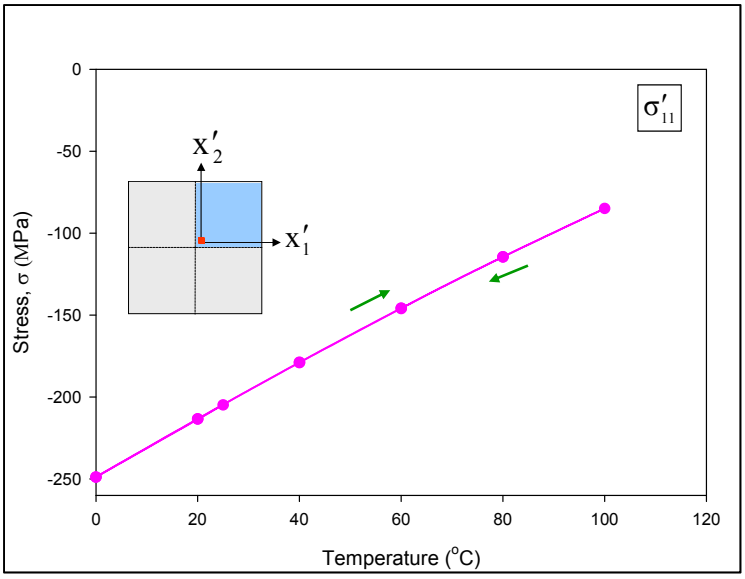

Figure 7.57 FEA Variation of Horizontal Normal Stress σ'_{11} with Temperature at the Die Center (CBGA)

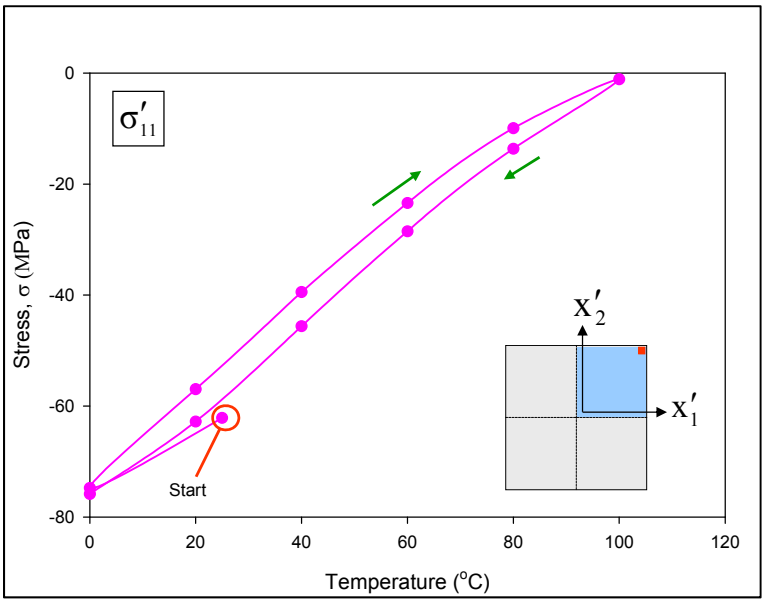

Figure 7.58 FEA Variation of Horizontal Normal Stress σ'_{11} with Temperature at the Die Corner (CBGA)

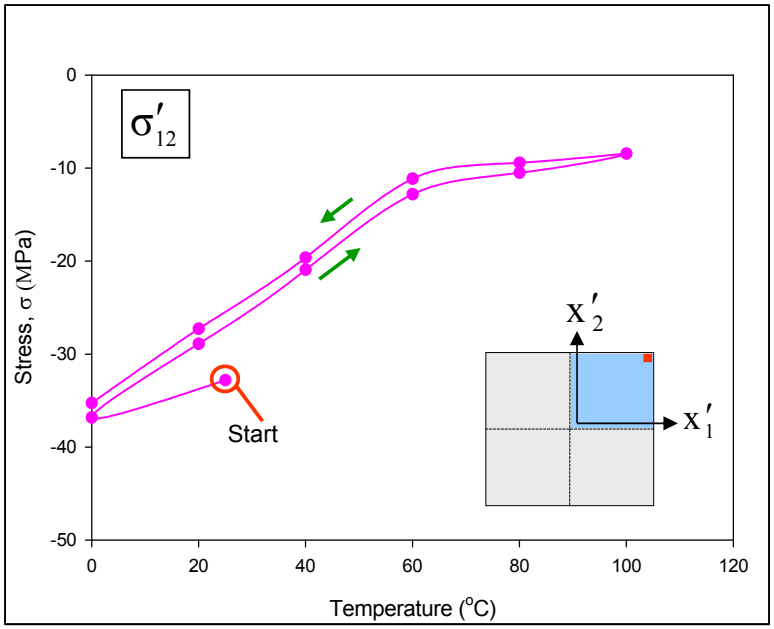

Figure 7.59 FEA Variation of In-Plane Shear Stress σ'_{12} with Temperature at the Die Corner (CBGA)

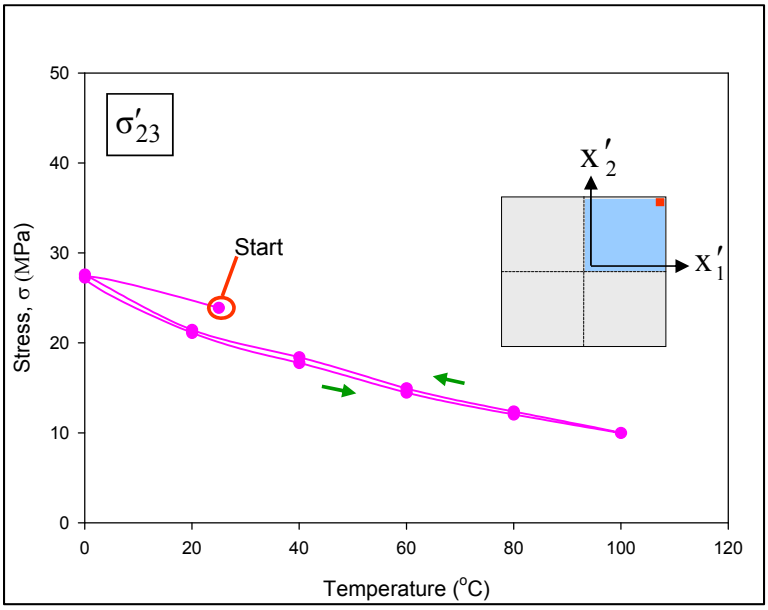

Figure 7.60 FEA Variation of Out-of-Plane Shear Stress σ'_{23} with Temperature at the Die Corner (CBGA)

7.10 Thermal Cycling Analysis (CBGA)

Thermal cycling simulations were performed for the CBGA assembly in a similar manner to the thermal cycling calculations for the LGA assembly. However, a more realistic simulation procedure was followed for the CBGA case. In actual thermal cycling experiment, the test boards with mounted components are placed in the thermal chamber where they are exposed to temperature variation (cycling) of the surrounding air. Similarly, in the simulation of the CBGA case, the model was subjected to changes in the temperature of the ambient air surrounding the CBGA assembly. The air was cycled between 0 to 100 ^{o}C and a transient heat transfer analysis was performed. Figure 7.61 shows the boundary conditions for the heat transfer analysis, and Figure 7.62 shows the simulation results for the die temperature variation. It was observed that the temperature at the center of the die closely followed the ambient temperature changes except for differences of a few degrees (about 5 ^{o}C) at the high and low temperature dwells. Figure 7.63 shows the temperature distribution in the quarter model during a high temperature dwell of the thermal cycling (point A in Figure 7.62).

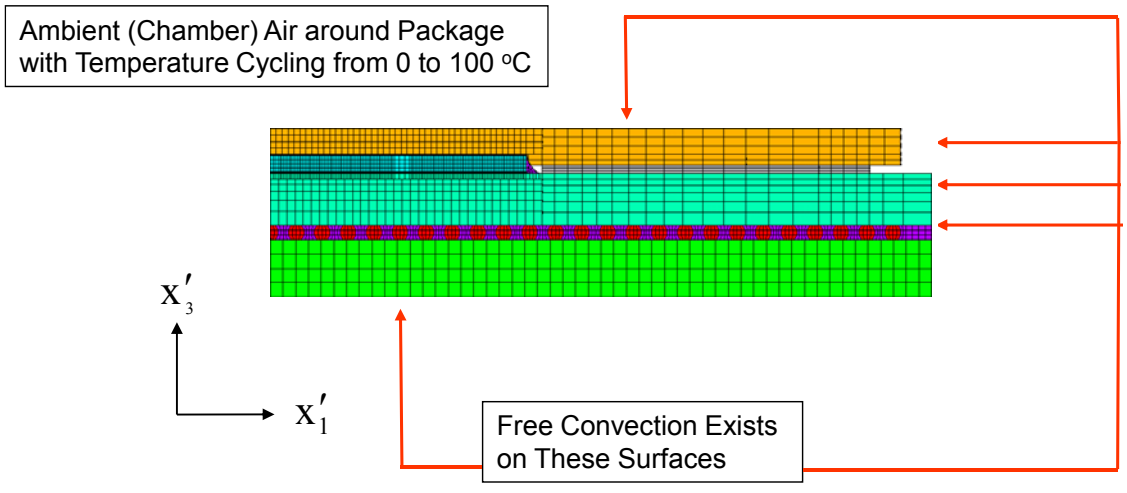

Figure 7.61 Boundary Conditions for Thermal Cycling Heat Transfer Analysis

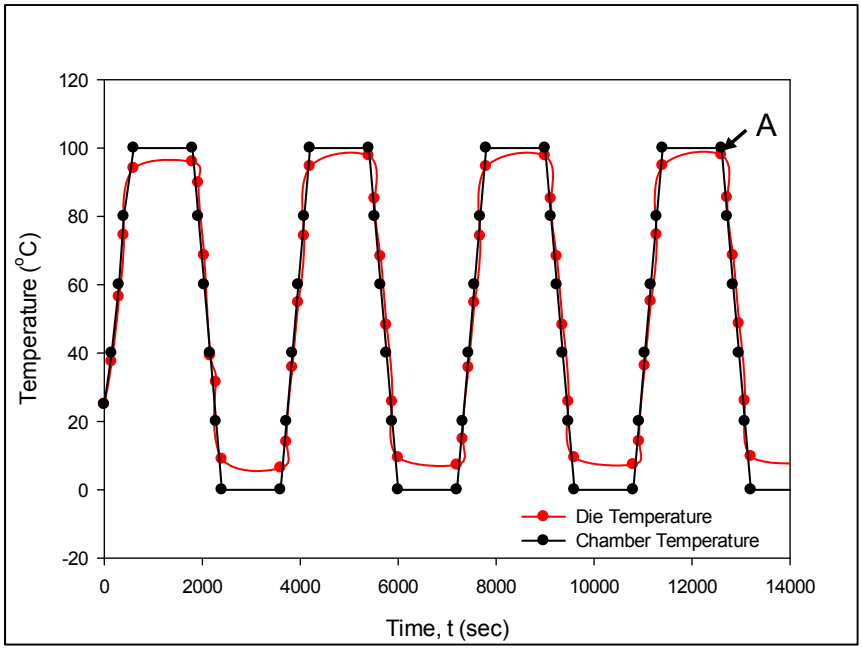

Figure 7.62 FEA Variation of the Temperature at the Die Center (CBGA)

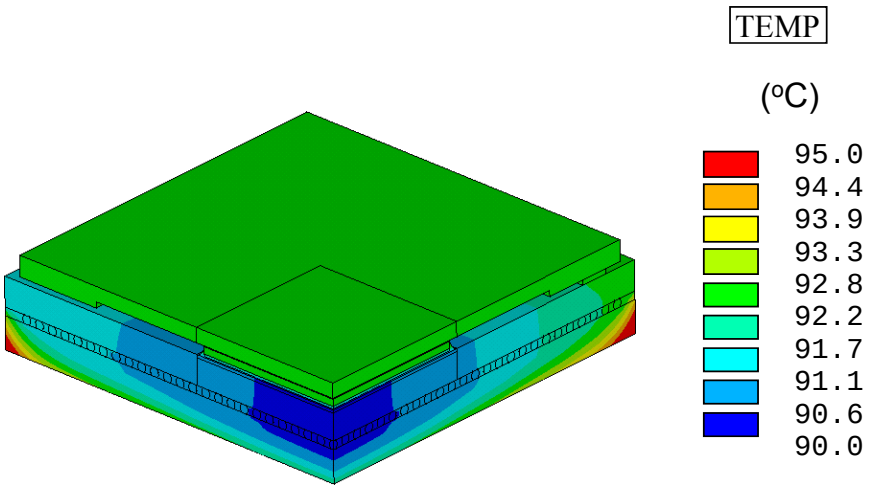

Figure 7.63 Temperature Distribution in the Package During the High Temperature Dwell at 100 C

After getting the temperature distribution as a function of time from the heat transfer analysis, they were used as boundary conditions for the stress analysis simulations under thermal cycling. The FEA stress predictions during thermal cycling are also similar to those for the LGA assembly. Figure 7.64 shows the horizontal normal

stress variation with time at the center of the die, and Figure 7.65 shows the variation of the same stress at the corner of the die. Figures 7.66 and 7.67 show the variations of in-plane and out-of-plane shear stresses at the corner of the die.

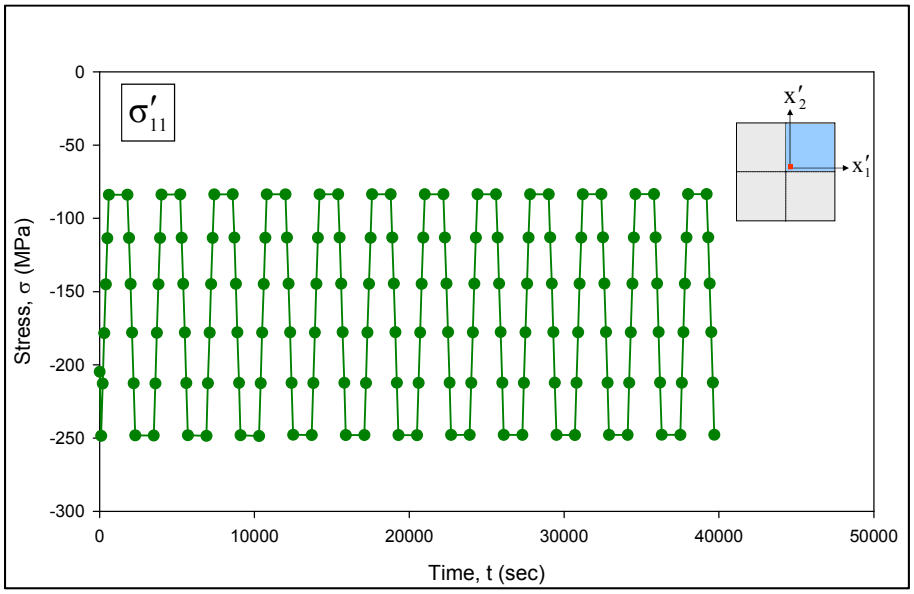

Figure 7.64 Horizontal Normal Stress at the Center of the Die During the First Few Thermal Cycles (CBGA)

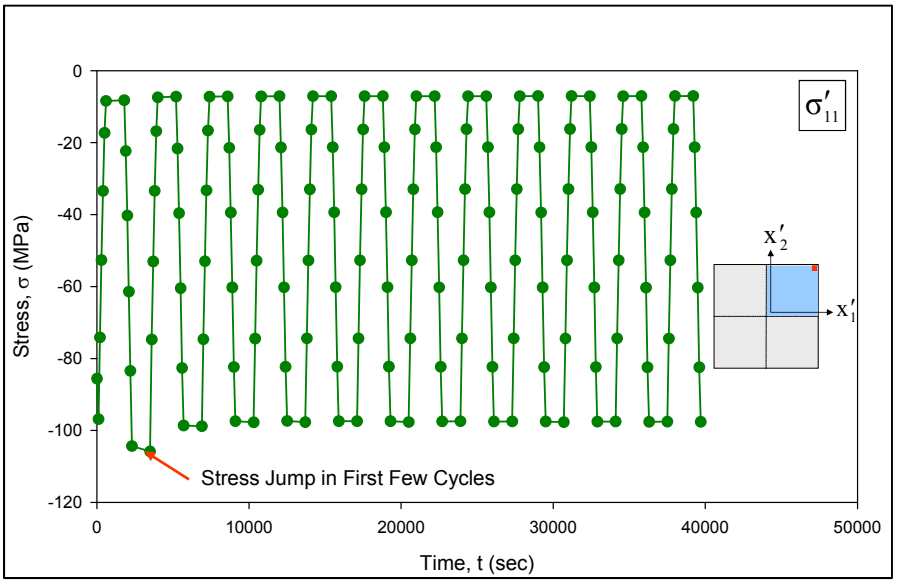

Figure 7.65 Horizontal Normal Stress at the Corner of the Die in During the First Few Thermal Cycles (CBGA)

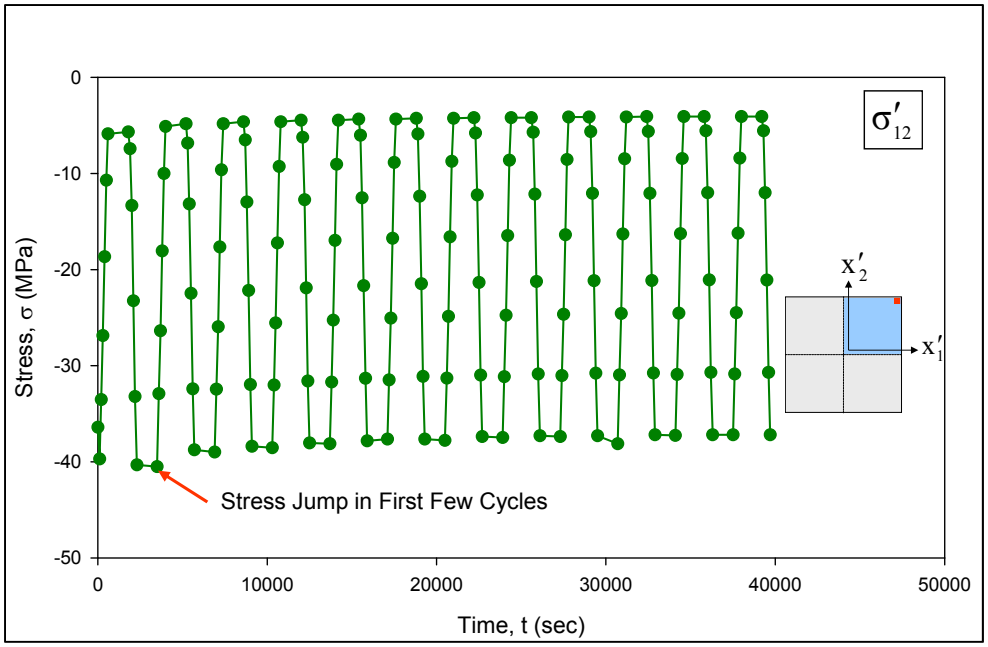

Figure 7.66 In-Plane Shear Stress at the Center of the Die During the First Few Thermal Cycles (CBGA)

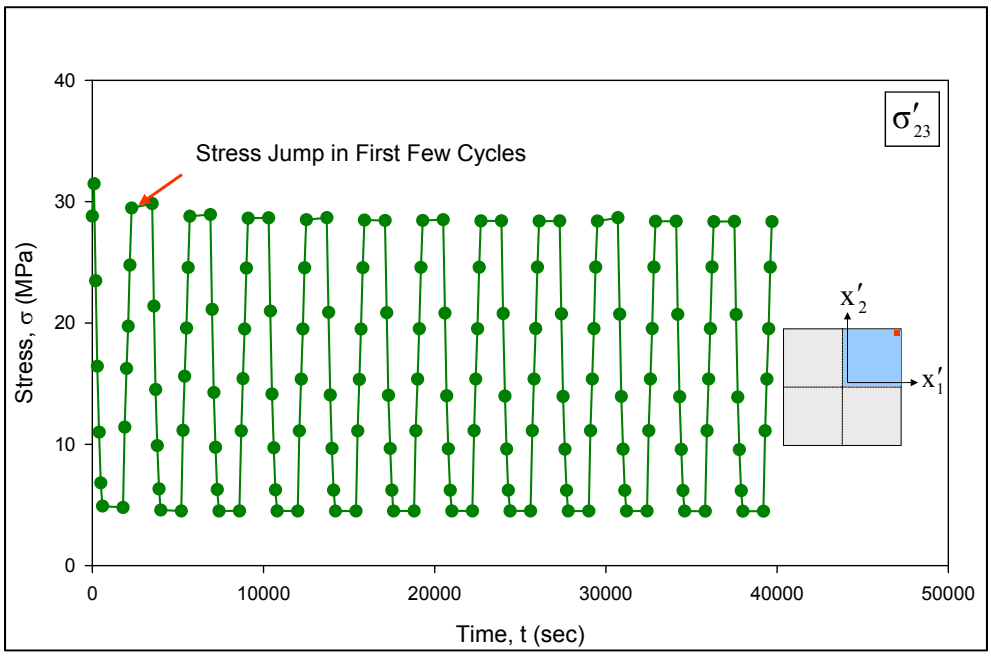

Figure 7.67 Out-of-Plane Shear Stress at the Corner of the Die During the First Few Thermal Cycles (CBGA)

7.11 Prediction of the Thermal Cycling Reliability of the Critical Solder Ball (CBGA)

The thermal cycling reliability of the critical solder ball in the CBGA assembly subjected to thermal cycling was determined by extracting the plastic work done on the solder ball and using the life prediction model from Section 5.3. Figure 7.68 shows the distribution of plastic work in the flip chip solder ball layer (quarter model). As expected, it was observed that the magnitude of plastic work was highest for the solder balls in the corner of the package. Figure 7.68 also compares the plastic work distribution for LGA and the CBGA assemblies subjected to thermal cycling. The highest plastic work was found in the CBGA assembly. Figure 7.69 shows the variation of volume averaged PLWK in the critical solder ball with time (CBGA) for the first 8 thermal cycles, and the plastic work per cycle (ΔW) values extracted from this curve are tabulated in Table 7.5. Comparing Figures 7.53 and 7.69, it is observed that the magnitude of plastic work in the critical ball of the CBGA was about 3.5 MPa higher than that for the critical ball in the LGA model. However, the plastic work accumulated per cycle (see Tables 7.4 and 7.5) are almost identical. Using the reliability model constants K_1, K_2, K_3, K_4 in Tables 5.1 and 5.3 for no aging, calculated number of cycles for crack initiation was 262 and the crack growth rate was 0.97 μm/ cycle.

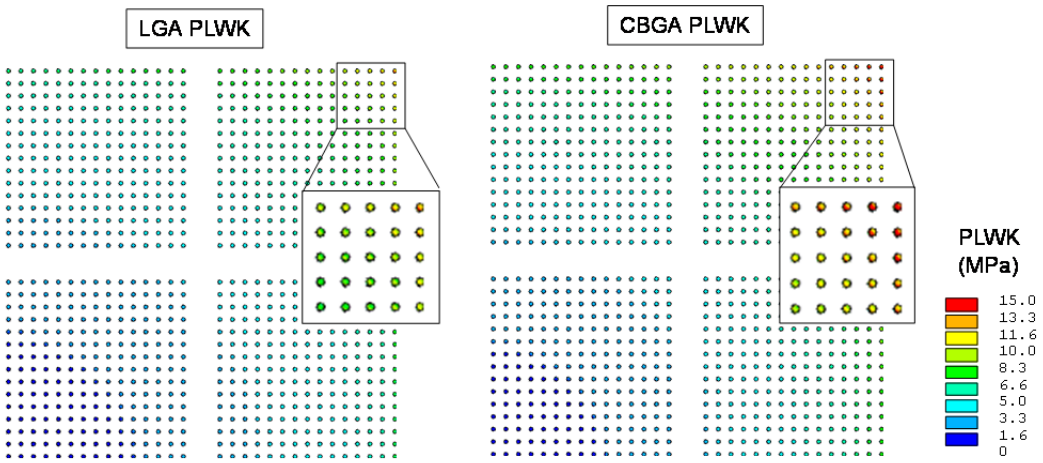

Figure 7.68 Plastic Energy Dissipation in Flip Chip Solder Bumps (LGA and CBGA)

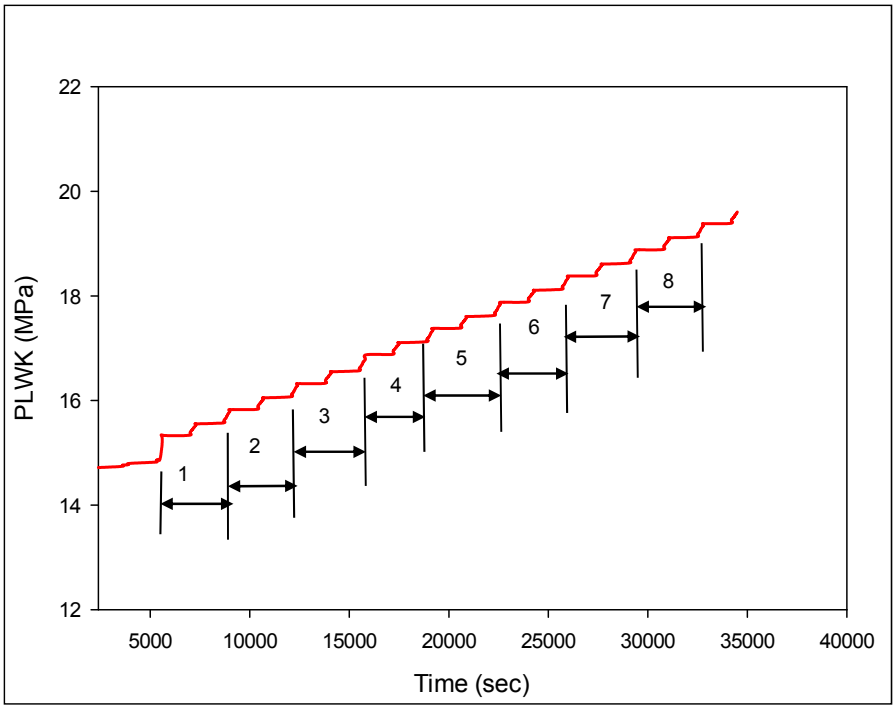

Figure 7.69 Variation of the Volume Averaged PLWK with Time in the Critical Solder Ball (CBGA) for the First 8 Thermal Cycles

No. of Cycle	ΔW
1	0.5961
2	0.4964
3	0.4980
4	0.5545
5	0.5012
6	0.5013
7	0.5016
8	0.5018

Table 7.5 Convergence of Volume Averaged ΔW with Number. of Thermal Cycles (CBGA)

7.12 Power Cycling Analysis (CBGA)

A power cycling study similar to the LGA case was also carried out for the CBGA assembly. The boundary conditions for the constant power dissipation and power cycling transient heat transfer simulations are shown in Figure 7.70. For the case of a constant power dissipation, 2 Watt power level through the n+ buried layer elements (Figure 7.35) was simulated and the temperature distribution after 2000 seconds (steady state) was calculated as shown in Figure 7.71. For power cycling, the same square wave power profile shown in Figure 7.39 was used, and the resulting die temperature variation with time is shown in Figure 7.72. This figure also shows a the comparison of the temperature variations during power cycling for the LGA and CBGA cases. It was observed that the amplitude of the temperature change due to power cycling was slightly higher in the LGA assembly than in the CBGA assembly. The temperature variations calculated in the heat transfer simulations were again used as boundary conditions for the structural analysis to calculate die stresses. Figure 7.73 shows the variation of the

horizontal normal stress σ'_{11} at the center of the die due to power cycling. Although the temperature changes were higher in the LGA assembly than in the CBGA assembly (see Figure 7.73), the stress changes were found to be approximately equal for both cases.

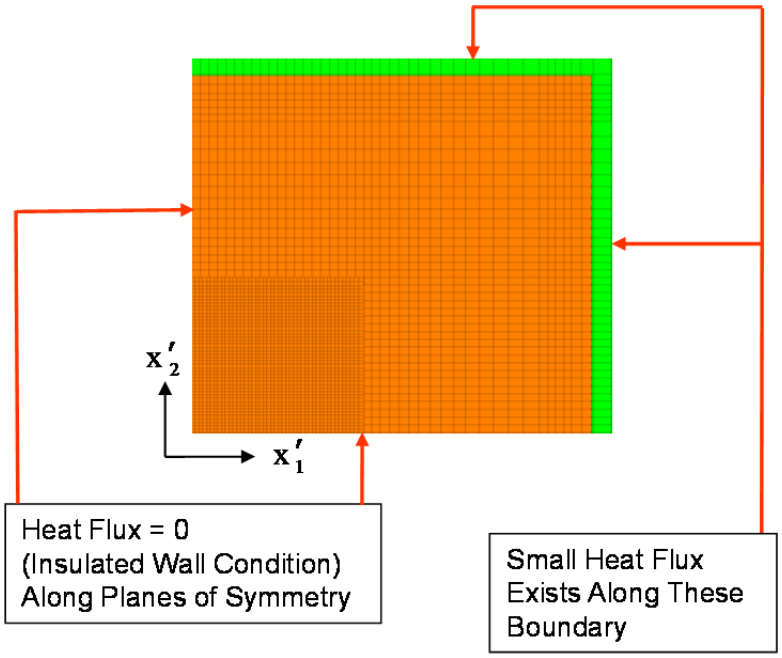

(a) Heat Flux Boundary Conditions

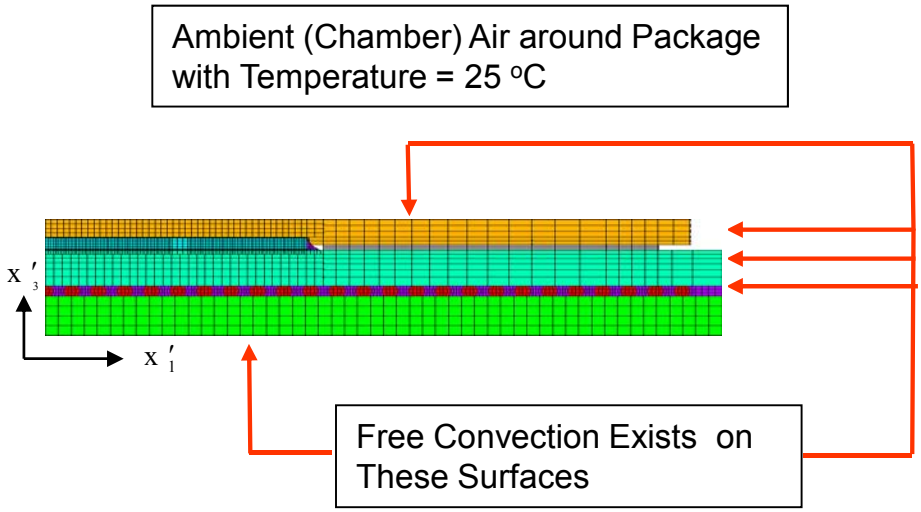

(b) Convection Boundary Conditions

Figure 7.70 Heat Transfer Boundary Conditions for Power Cycling Simulations (CBGA)

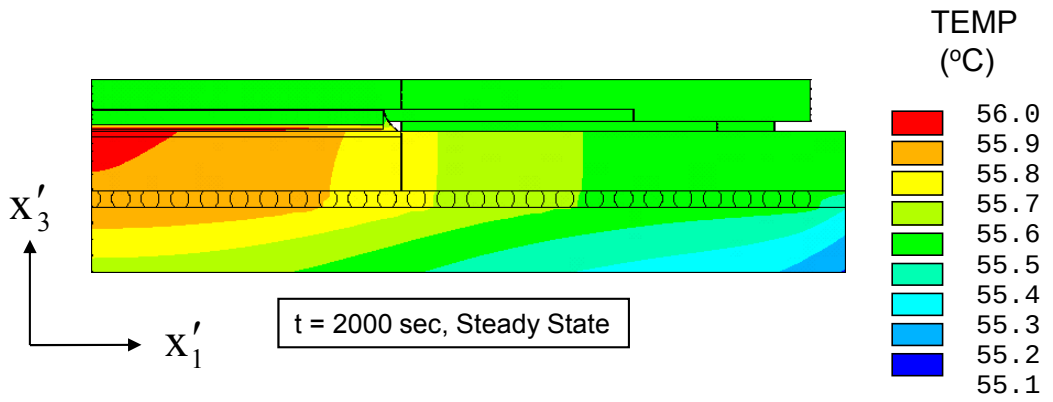

Figure 7.71 Temperature Distribution in the CBGA Package Due to a Constant Power Dissipation of 2 Watts

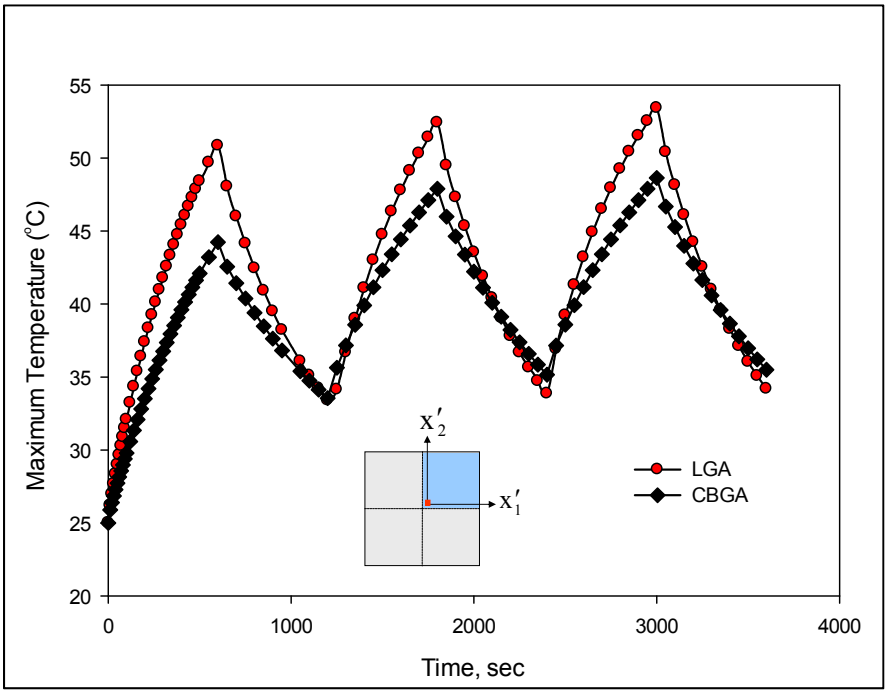

Figure 7.72 Transient Die Surface Temperature Variation for Power Cycling (LGA and CBGA)

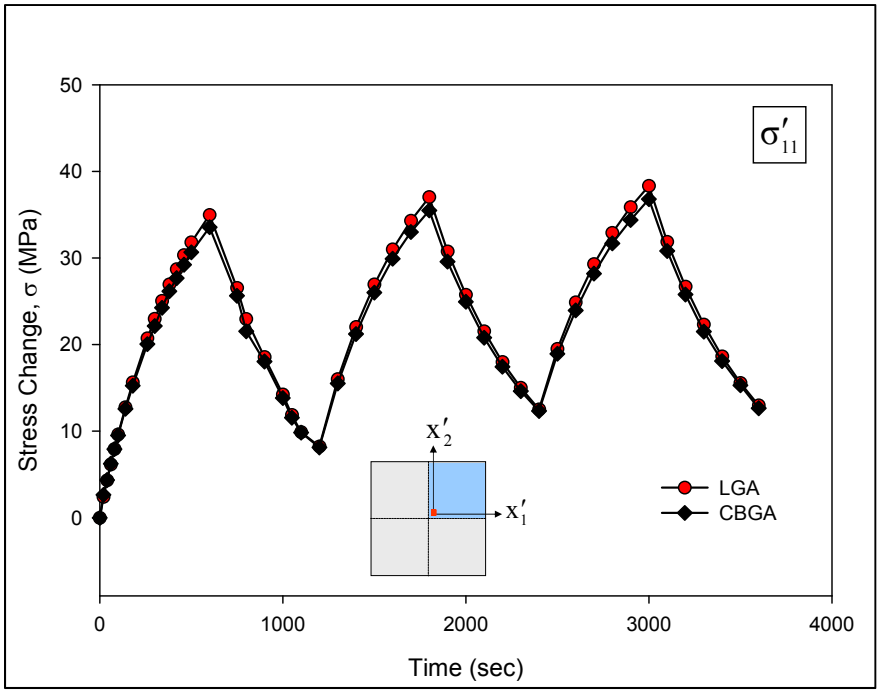

Figure 7.73 Transient Die Stress Variation at the Center of the Die for Power Cycling (LGA and CBGA)

7.13 Prediction of the Power Cycling Reliability of the Critical Solder Ball (CBGA) During Power Cycling

The reliability of the critical solder ball was also calculated for the case of power cycling. Due to the power cycling between 0 to 2 Watts, distribution of plastic work in the solder ball layer is shown in Appendix A.6. Figure 7.74 shows the variation of plastic work done with time for the first 3 power cycles, and Table 7.6 shows the calculated volume averaged plastic work done per cycle. Using the reliability model constants K_1, K_2, K_3, K_4 in Tables 5.1 and 5.3 for no aging, the calculated number of power cycles for crack initiation was 3434, and the crack growth rate was 0.21 μm/ cycle.

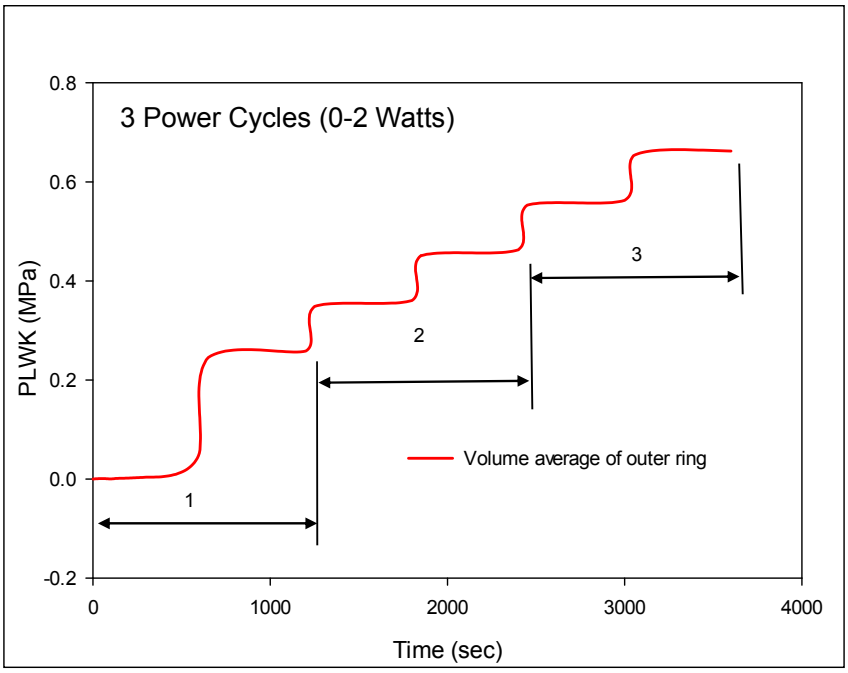

Figure 7.74 Variation of the Volume Averaged PLWK with Time in the Critical Solder Ball (CBGA) Due to Power Cycling

No. of Cycle	ΔW
1	0.2583
2	0.2044
3	0.1996

Table 7.6 Volume Averaged ΔW per Cycle in Power Cycling

7.14 Stresses Due to Heat Sink Clamping

A set of initial experiments were performed by Roberts, et al. [137] to evaluate the compressive die stresses generated due to heat sink clamping in the packaging configuration shown in Figure 7.54. Lead free solder balls were first attached to the CLGA packages discussed above to convert them into CBGA packages. The CBGAs were then assembled to PCB test boards to produce test assemblies suitable for heat sinking clamping tests.

To further study effects of heat sink clamping, finite element analysis was used to predict the stresses induced by the heat sink clamping forces. The basic mesh for the CBGA soldered to the test PCB is shown in Figure 7.55, and the boundary conditions and loading are indicated in Figure 7.75. Initially, it was assumed that the clamping fixture applied a uniform pressure onto the top of the lid. Using pressure sensitive paper, it was found that the actual distribution of clamping pressure was highly nonlinear and heavily weighted towards the center of the lid (see Figure 7.76). A comparison of the experimental measurements and finite element predictions for the stress changes at the die center are shown in Figure 7.77. Fairly good agreement was obtained.

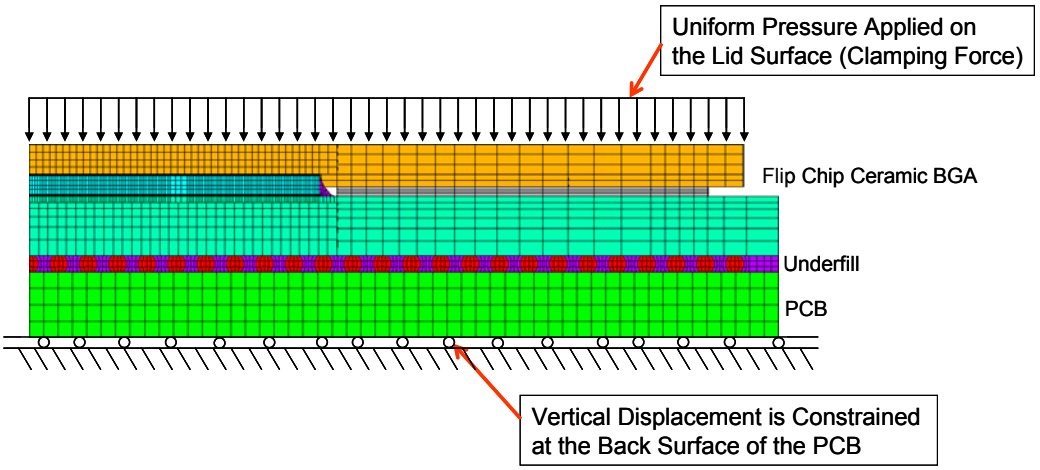

Figure 7.75 Boundary Conditions and Loading for Clamping Finite Element Model

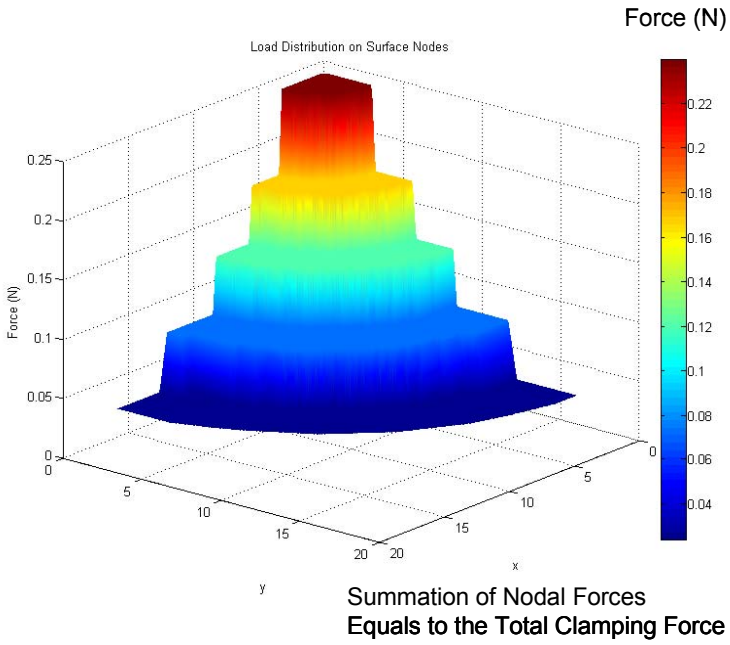

Figure 7.76 Non-Uniform Pressure Applied to the Lid of the Package During Clamping Measurements

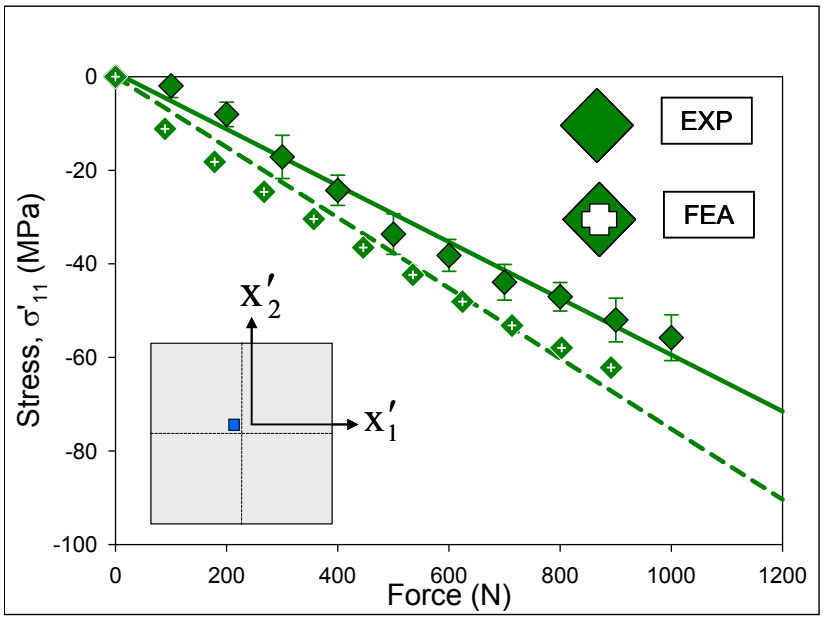

Figure 7.77 Die In-Plane Normal Stress Change at the Center of the Chip Due to Heat Sink Clamping Force

7.15 Summary and Conclusion

In this chapter, finite element simulations of the CBGA microprocessor assemblies were performed. Two different package configurations were considered for the simulations: Ceramic Land Grid Array (CLGA) and Ceramic Ball Grid Array (CBGA). The CBGA structure was assumed to be built up from the CLGA by adding the second level BGA solder balls, second level underfill, and the FR4 board to the CLGA structure. In the CLGA, the flip chip was attached to high CTE ceramic substrate, and then underfill and a lid were added to complete the assembly. For both assembly configurations, die stresses were calculated due to the assembly process (solder joint reflow, underfill cure, lid attachment, second level connection etc.), as well as due to thermal cycling, power cycling, and subsequent heat sink clamping operations. In the simulation procedure, a novel sequential modeling approach has been utilized to predict the build-up stresses, strains, and deformations in the structure. The utilized method incorporates precise thermal histories of the packaging process, element creation, and nonlinear temperature and time dependent material properties.

From the results of assembly induced die stresses, it was observed that most of the stress buildup was contributed by the underfill curing process. The solder joint reflow process resulted in about 70 MPa of compressive stress. The underfill cure and the lid attachment processes added more stress buildup to levels of -190 MPa and -210 MPa, respectively. It was also found that the compressive normal stresses were maximum at the center of the die, and the in-plane shear stresses were maximum at the corner of the die. The subsequent second level assembly (CBGA) process caused more stress buildup, with a maximum stress of about -225 MPa at the center of the die at room temperature.

Under slow temperature variation, it was found that the stress variation with temperature was linear at the center of the die and non-linear with some hysteresis at the corner of the die. It was also found that the underfill material at the corner experienced yielding, which in turn caused the non-linearity and hysteresis of the die stresses in the corner region. During thermal cycling, it was found that the peak stresses at the center of the die were nearly constant with time. However, at the corner of the die, there were some jumps during first few cycles and then the stress cycles stabilized. For constant power dissipation (2 Watts), the temperature and stresses reached steady state values after about 30 minutes. During power cycling (0-2 Watts), the temperature and stress cycles stabilized after the first few cycles.

From the thermal and power cycling results, the cycles to crack initiation and the subsequent crack propagation rates were calculated for the critical solder ball by extracting the volume averaged plastic energy dissipated per cycle and by using the reliability model equations given in Chapter 5. It was observed from the predicted results that both the LGA and CBGA configurations had the similar predicted reliability (life).

Finally, a model was developed for heat sink clamping studies. It was found that the stress response was linear with clamping force and that die compressive stresses had more buildup due to the heat sink clamping process.

CHAPTER 8

CONCLUSIONS

8.1 Literature Review

Isothermal aging has been found detrimental to the mechanical properties and the reliability of lead free solder materials. The dramatic changes in the material properties, constitutive and failure behavior of bulk solder materials as well as solder joints have been reported in the literature. However, traditional finite element based predictions for solder joint reliability during thermal cycling accelerated life testing are based on solder constitutive equations (e.g. Anand viscoplastic model) and failure models (e.g. energy dissipation per cycle model) that do not evolve with material aging. Thus, there will be significant errors in the calculations with lead free SAC alloys that illustrate dramatic aging phenomena.

Large discrepancies in measured solder mechanical properties from one study to another have been found and widely acknowledged due to the differences in the microstructures of the tested samples. This problem is exacerbated by the aging issue, as it is clear that the microstructure and material behavior of the samples change rapidly even at room temperature. For elevated temperature aging, this effect has been found to cause more dramatic change in the microstructure, material behavior and the reliability of lead free solder. Thus, the effects of aging on solder behavior must be better understood so that more accurate viscoplastic constitutive equations can be developed for SnPb and

SAC solders. Without such well-defined relationship, it is doubtful that finite element reliability predictions can ever reach their full potential.

In the current study, effects of aging on the lead free solder material have been investigated by performing stress-strain tests for a wide range of temperature, strain rate and aging conditions. Also, creep tests for wide range of temperature and stress level have been performed for specimens that were aged for different duration of time. Using the tensile test or creep data for different aging condition, the Anand viscoplastic constitutive model has been modified to include the aging effects. The modified Anand model with aging effects has been implemented in the finite element software ANSYS for accurate prediction of the thermal cycling reliability of lead free solder joints.

The discussion on life prediction or reliability models for lead free solders includes the model parameters that do not evolve with material aging. The energy based Darveaux model has four parameters (K_1, K_2, K_3 and K_4) and has been used in this study to calculate the thermal cycling reliability of solder joints. The effects of aging on these four parameters have been determined through the results of experimental investigations (fatigue tests and reliability tests). Empirical models for these parameters have been developed to include the aging effects, and by combining the finite element results with the reliability model, cycles to failure of the solder joint in a PBGA assembly have been determined for different aging conditions. Finally, good correlations have been found between the predictions of the constitutive and reliability models that include aging effects, and the experimental thermal cycling reliability data.

8.2 Specimen Preparation, Experimental and Aging Effects on Mechanical Properties of Lead Free Solders

Tensile stress-strain tests were performed for a wide range of temperatures, strain rates, and aging conditions. Also, creep tests were performed for a wide range of temperatures, stress levels, aging conditions. A unique specimen preparation procedure was developed in this study to fabricate micro-scale uniaxial tensile specimens. All solder specimens were formed in glass tubes with rectangular cross-section by using a vacuum suction system. The tubes were then cooled by sending through an SMT reflow to re-melt the solder in the tubes and subject them to any desired temperature profile to match those experienced by actual solder joints. Typical uniaxial samples with nominal dimensions of 80 × 3 × 0.5 mm were utilized.

In this study, uniaxial tensile and creep tests were performed by using a tension-torsion micro tester. Experimental data from the tensile tests were fitted by a four parameter hyperbolic tangent model and the creep data were fitted by using the Burger's model. The effects of aging on the stress-strain behavior were investigated using the SAC305 solder specimens that were aged for various durations (0-360 days) at 100 ^{o}C. As expected, dramatic degradations in the tensile test properties (elastic modulus, UTS and yield stress) were observed from the tensile test results. During first 20 days of aging, the material properties degrade dramatically, and for longer aging times, they degraded linearly with a small slope. Aging also had significant effects on the creep test results. For the SAC305 specimens that were aged for various durations (0-180 days), aging significantly increased the steady state creep strain rate or secondary creep rate. Similar

to the tensile test results, the increase in secondary creep rate was dramatic during first 20 days of aging, and then it increased slowly and linearly for longer aging times.

8.3 Effect of Aging on the Anand Model Parameters and the Modified Anand Viscoplastic Constitutive Model

The theoretical equations for the uniaxial stress-strain response (constant strain rate) and for the creep response of solder have been derived from the Anand viscoplastic model. Procedures for extracting the Anand model constants from experimental stress-strain and creep data were also established. The two developed methods were then applied to find the Anand constants for SAC305 lead free solder using the two completely different sets of experimental test data. The first set of Anand parameters were extracted from uniaxial stress strain data measured over a wide range of strain rates ($\dot{\varepsilon}$ = 0.001, 0.0001, and 0.00001 1/sec) and temperatures (T = 25, 50, 75, 100, and 125 ^{o}C), and for different durations of aging (0-12 months at 100 C). The second set of Anand parameters were calculated from creep test data measured at several stress levels (σ = 6-15 MPa and temperatures (T = 25, 50, 75, 100, and 125 ^{o}C), and for different durations of aging (0-6 months at 100 C). The two sets of Anand model parameters derived from the stress-strain and creep data were compared, and the accuracy (goodness of fit) of the Anand model using the extracted material constants was evaluated by comparing the responses predicted from the Anand model with the measured stress-strain and creep data. The evolution of the model parameters with aging was then determined. Empirical equations for the variation of seven parameters with aging time (2 other parameters were unchanged with aging) were developed to modify the Anand viscoplastic constitutive model to include the aging effects.

Determination of Anand parameters for aging temperatures other than 100 ^{o}C would necessitate performing a similar set of stress-strain experiments (multiple temperatures and strain rates) for the each additional aging temperature of interest. Obviously, this would be an extremely time consuming exercise. This procedure was shortened in this work, and an extrapolation technique was developed to estimate the variation of the Anand parameters at other aging temperatures including 25, 50, 75 and 125 ^{o}C. The estimation procedure is based on making the engineering assumption that the Anand parameters vary with aging time in a similar manner at all aging temperatures. Empirical models were used to fit the variation of the Anand parameters with aging time at 100 C. The same functional forms were then assumed to be valid at other aging temperatures, and a more limited set of testing data were used to determine the constants in the empirical models and scale them (extrapolate) to the other aging temperatures.

8.4 Effects of Aging on the Reliability Model Parameters

A new aging aware failure criteria has been developed based on fatigue data for lead free solder uniaxial specimens that were aged at elevated temperature for various durations prior to mechanical cycling. Using measured SAC305 fatigue data for different aging conditions, the evolution of reliability model parameters K_1 and K_2 with aging were determined. Empirical models for these parameters were developed, and similar to the findings for mechanical/constitutive behavior, the values of these two parameters were affected significantly with aging.

The other two reliability model parameters, K_3 and K_4 were determined from the crack growth experimental data for a 19 mm PBGA assembly. Failure data were available

for this package at aging temperatures of 25, 55, 85, and 125 ^{o}C, and for no aging, 6 months, and 12 months aging prior to thermal cycling. The evolution of parameters K_3 and K_4 with aging were determined from these experimental data, and the results showed that aging has significant effects on the model parameters.

Traditional finite element based predictions for solder joint reliability during thermal cycling accelerated life testing are based on solder constitutive equations and failure models that do not evolve with material aging. Due to the strong influence of aging on the thermal cycling reliability of lead free solder assemblies, it is critical that aging effects be included in any reliability prediction methodology. The reliability model parameters K_1, K_2 , K_3 and K_4 that were determined that have been used to estimate the life of SAC solder balls in PBGA components that were subjected to thermal cycling between -40 to 125 ^{o}C with various aging conditions prior to thermal cycling.

8.5 Thermal Cycling Reliability Prediction for Lead Free Solder Joint in PBGA Assemblies with Aging Effects

It was demonstrated in Chapters 2, 3, and 4 that isothermal aging leads to large reductions (up to 50%) in several key material properties for lead free solders including stiffness (modulus), yield stress, ultimate strength, and strain to failure. In addition, even more dramatic evolution has been observed in the creep response of aged solders. Traditional finite element based predictions for solder joint reliability during thermal cycling accelerated life testing are based on solder constitutive equations (e.g. Anand viscoplastic model) and failure models (e.g. energy dissipation per cycle models) that do not evolve with material aging. Thus, there will be significant errors in the calculations with lead free SAC alloys that illustrate dramatic aging phenomena. In this study, a new

reliability prediction procedure was developed that utilizes constitutive relations and failure criteria that incorporate aging effects, and then the new approach was validated through correlation with thermal cycling accelerated life testing experimental data.

The developed Anand constitutive equations for solder with aging effects were implemented into the finite element code ANSYS and then the finite element simulations have been performed to model the solder joint deformations of two different PBGA components attached to FR-4 printed circuit boards that were subjected to thermal cycling. Calculations were made for non-aged PBGA assemblies, as well as for assemblies that had been aged under various conditions before being subjected to thermal cycling.

In the first study, a 3D slice finite element mesh (half model) was analyzed for a 676 I/O PBGA component. For the specified loading, this configuration was subjected to thermal cycling from 0 to 100 C (8 minute ramps and 10 minute dwells). The plastic energy dissipation with time was calculated and the energy dissipation per cycle was also determined. As expected, the plastic energy dissipation per cycle (ΔW) increased with increasing aging temperature and aging time. For this package, a 30% increase in ΔW was found for 6 months prior aging at 100 ^{o}C.

In the second study, a three-dimensional finite element analysis of the 19 mm PBGA component with SAC305 interconnects discussed in Chapter 5 was performed to calculate the stress/strain histories in the solder joints during thermal cycling accelerated life testing. Simulation of thermal cycling between -40 to 125 C was performed, and several sets of aging conditions (aging temperature and time) prior to thermal cycling were considered. For each case, the plastic energy dissipation per cycle in the critical

solder ball was calculated. These values were then combined with the aging aware fatigue criterion to perform life predictions for the components with various aging conditions. The energy based criteria proposed by Darveaux [132] was used for predicting crack initiation and crack growth in the aged solder joints using the energy dissipation values calculated from the finite element analysis. Good correlation was found between the predicted results and experimental findings for the reliability of the component.

8.6 Finite Element Analysis of CBGA Assemblies Using Anand Constitutive Model

Finite element simulations of the CBGA microprocessor assemblies were performed. Two different package configurations were considered for the simulations: Ceramic Land Grid Array (CLGA) and Ceramic Ball Grid Array (CBGA). The CBGA structure was assumed to be built up from the CLGA by adding the second level BGA solder balls, second level underfill, and the FR4 board to the CLGA structure. In the CLGA, the flip chip was attached to high CTE ceramic substrate, and then underfill and a lid were added to complete the assembly. For both assembly configurations, die stresses were calculated due to the assembly process (solder joint reflow, underfill cure, lid attachment, second level connection etc.), as well as due to thermal cycling, power cycling, and subsequent heat sink clamping operations. In the simulation procedure, a novel sequential modeling approach has been utilized to predict the build-up stresses, strains, and deformations in the structure. The utilized method incorporates precise thermal histories of the packaging process, element creation, and nonlinear temperature and time dependent material properties.

From the results of assembly induced die stresses, it was observed that most of the stress buildup was contributed by the underfill curing process. The solder joint reflow process resulted in about 70 MPa of compressive stress. The underfill cure and the lid attachment processes added more stress buildup to levels of -190 MPa and -210 MPa, respectively. It was also found that the compressive normal stresses were maximum at the center of the die, and the in-plane shear stresses were maximum at the corner of the die. The subsequent second level assembly (CBGA) process caused more stress buildup, with a maximum stress of about -225 MPa at the center of the die at room temperature.

Under slow temperature variation, it was found that the stress variation with temperature was linear at the center of the die and non-linear with some hysteresis at the corner of the die. It was also found that the underfill material at the corner experienced yielding, which in turn caused the non-linearity and hysteresis of the die stresses in the corner region. During thermal cycling, it was found that the peak stresses at the center of the die were nearly constant with time. However, at the corner of the die, there were some jumps during first few cycles and then the stress cycles stabilized. For constant power dissipation (2 Watts), the temperature and stresses reached steady state values after about 30 minutes. During power cycling (0-2 Watts), the temperature and stress cycles stabilized after the first few cycles.

From the thermal and power cycling results, the cycles to crack initiation and the subsequent crack propagation rates were calculated for the critical solder ball by extracting the volume averaged plastic energy dissipated per cycle and by using the reliability model equations given in Chapter 5. It was observed from the predicted results that both the LGA and CBGA configurations had the similar predicted reliability (life).

Finally, a model was developed for heat sink clamping studies. It was found that the stress response was linear with clamping force and that die compressive stresses had more buildup due to the heat sink clamping process.

8.7 Future Work

In this study, the Anand model for lead free solder was modified to include the aging effects. Tensile and creep tests were done with SAC305 solder specimens for various aging exposure times (0-12 months at 100 C for stress-strain and 0-6 months at 100 C for creep). It implies that similar tests need to be done for other aging temperatures (25, 50, 75 and 125 C) to investigate the effects of aging temperature. Similar tests need to be done for other SAC alloys (SAC105, SAC205, and SAC405) to further investigate the effects of alloy constituents on the variation of Anand parameters with aging. After completing all of these tests, a generalized Anand viscoplastic constitutive model can be developed that will include both aging time and aging temperature effects as well as effects of alloy constituents. Future studies can also include the development of the method to get the Anand parameters for actual solder joints. Also, methods can be developed to determine Anand parameters with fewer number of tensile or creep tests.

REFERENCES

[1] P. T. Vianco, "Development of alternatives to lead-bearing solders," Proceedings of the Technical Program on Surface Mount International, San Jose, CA, 1993.

[2] J. S. Hwang, Implementing lead-free electronics, McGraw-Hill, New York, 2005.

[3] Q. Zhang, A. Dasgupta, and P. Haswell, "Creep and high-temperature isothermal fatigue of Pb-free solders, "Proceedings of InterPACK 2003, pp. 955-960, 2003.

[4] NCMS, Lead-Free Solder Project Final Report, National Center for Manufacturing Sciences, Michigan,1997.

[5] N. C. Lee, "Getting Ready for Lead-free Solders," Soldering & Surface Mount Technology, vol. 9, pp. 65-69, 1997.

[6] K. S. Kim, S. H. Huh, and K. Suganuma, "Effects of intermetallic compounds on properties of Sn–Ag–Cu lead-free soldered joints," Journal of Alloys and Compounds, vol. 352, pp. 226-236, 2003.

[7] J.-W. Yoon, S.-W. Kim, and S.-B. Jung, "IMC morphology, interfacial reaction and joint reliability of Pb-free Sn–Ag–Cu solder on electrolytic Ni BGA substrate," Journal of Alloys and Compounds, vol. 392, pp. 247-252, 2005.

[8] D. Q. Yu and L. Wang, "The growth and roughness evolution of intermetallic compounds of Sn–Ag–Cu/Cu interface during soldering reaction," Journal of Alloys and Compounds, vol. 458, pp. 542-547, 2008.

[9] C. M. L. Wu, D. Q. Yu, C. M. T. Law, and L. Wang, "Properties of lead-free solder alloys with rare earth element additions," Materials Science and Engineering: R: Reports, vol. 44, pp. 1-44, 2004.

[10] C. H. Wang and S. W. Chen, "Sn–0.7 wt.% Cu/Ni interfacial reactions at 250° C," Acta Materialia, vol. 54, pp. 247-253, 2006.

[11] D. Li, C. Liu, and P. P. Conway, "Characteristics of intermetallics and micromechanical properties during thermal ageing of Sn–Ag–Cu flip-chip solder interconnects," Materials Science and Engineering: A, vol. 391, pp. 95-103, 2005.

[12] Y. C. Chan and D. Yang, "Failure mechanisms of solder interconnects under current stressing in advanced electronic packages," Progress in Materials Science, vol. 55, pp. 428-475, 2010.

[13] M. Abtew and G. Selvaduray, "Lead-free solders in microelectronics," Materials Science and Engineering: R: Reports, vol. 27, pp. 95-141, 2000.

[14] A. Furusawa, K. Suetsugu, A. Yamaguchi, and H. Taketomo, "Thermoset Pb Free Solder Using Heat-Resistant Sn Ag Paste," National Technical Report Osaka, vol. 43, pp. 46-53, 1997.

[15] M. McCormack and S. Jin, "Improved Mechanical Properties in New, Pb-Free Solder Alloys," Journal of Electronic Materials, vol. 23, pp. 715-720, 1994.

[16] P. L. Liu and J. K. Shang, "Interfacial Embrittlement by Bismuth Segregation in Copper/Tin-Bismuth Pb-Free Solder Interconnect," Journal of Materials Research, vol. 16, pp. 1651-1659, 2001.
[17] H. Habassis, J. W. Rutter, and W. C. Winegard, "Phase Relationships In Bi–In–Sn Alloy System," Materials Science and Technology, vol. 2, pp. 985-988, 1986.
[18] J. Glazer, "Metallurgy of Low Temperature Pb-Free Solders For Electronic Assembly," International Materials Reviews, vol. 40, pp. 65-93, 1995.
[19] M. McCormack, S. Jin, G. W. Kammlott, and H. S. Chen, "New Pb Free Solder Alloy With Superior Mechanical Properties," Applied Physics Letters, vol. 63, pp. 15-17, 1993.
[20] K. Nogita, "Stabilization of Cu_6Sn_5 by Ni in Sn-0.7Cu-0.05Ni lead-free solder alloys," Intermetallics, Vol. 18(1), pp. 145-149, 2010.
[21] F. X. Che, J. E. Luan, and X. Baraton, "Effect of Silver Content and Nickel Dopant on Mechanical Properties of Sn-Ag-Based Solders," Proceedings of the 58th Electronic Components and Technology Conference, pp. 485-490, 2008.
[22] F. Guo, J. Lee, S. Choi, J. P. Lucas, T. R. Bieler, and K. N. Subramanian, "Processing And Aging Characteristics of Eutectic Sn-3.5 Ag Solder Reinforced With Mechanically Incorporated Ni Particles," Journal of Electronic Materials, vol. 30, pp. 1073-1082, 2001.
[23] Z. G. Chen, Y. W. Shi, Z. D. Xia, and Y. F. Yan, "Study on the microstructure of a novel lead-free solder alloy SnAgCu-RE and its soldered joints," Journal of electronic materials, vol. 31, pp. 1122-1128, 2002.
[24] C. M. T. Law and C. M. L. Wu, "Microstructure Evolution and Shear Strength of Sn-3.5Ag-RE Lead-free BGA Solder Balls," Proceedings of the Sixth High Density Microsystem Design and Packaging and Component Failure Analysis Conference, pp. 60-65, 2004.
[25] N.-C. Lee, "Lead-free soldering-where the world is going," Advancing Microelectronics, vol. 26, pp. 29-35, 1999.
[26] F. Gao, S. Mukherjee, Q. Cui, and Z. Gu, "Synthesis, characterization, and thermal properties of nanoscale lead-free solders on multisegmented metal nanowires," The Journal of Physical Chemistry C, vol. 113, pp. 9546-9552, 2009.
[27] A. Pirondi, "Mechanical Failure in Microelectronic Packaging," Convegno IGF XIII Cassino, vol. IGF 13, 1997.
[28] R. W. Hertzberg, R. P. Vinci, and J. L. Hertzberg, Deformation and Fracture Mechanics of Engineering Materials, 4th edition, John Wiley & Sons Inc, 1996.
[29] S. Wiese, A. Schubert, H. Walter, R. Dukek, F. Feustel, E. Meusel, and B. Michel, "Constitutive Behavior of Lead-free Solders vs. Lead-containing Solders - Experiments on Bulk Specimens and Flip-Chip Joints," Proceeding of the 51st Electronic Components and Technology Conference, pp. 890-902, 2001.
[30] R. J. McCabe and M. E. Fine, "Athermal And Thermally Activated Plastic Flow in Low Melting Temperature Solders At Small Stresses," Scripta Materialia, vol. 39, pp. 189-195, 1998.
[31] J. H. Lau, "Solder Joint Reliability of Flip Chip And Plastic Ball Grid Array Assemblies Under Thermal, Mechanical, And Vibrational Conditions," IEEE Transactions on Components, Packaging, and Manufacturing Technology, Part B: Advanced Packaging, vol. 19, pp. 728-735, 1996.

[32] K. M. Ralls, Courtney, T. H., Wulff, J., Introduction to Materials Science and Engineering, Wiley, 1976.
[33] J. Cadek, Creep in metallic materials, Elsevier Science Publisher, 1988.
[34] F. Garofalo and D. B. Butrymowicz, "Fundamentals of creep and creep-rupture in metals," Physics Today, vol. 19, p. 100, 1966.
[35] R. W. Evans and B. Wilshire, "Creep of Metals And Alloys," The Institute of Metals, 1985.
[36] M. F. Ashby, "A First Report on Deformation-Mechanism Maps," Acta Metallurgica, vol. 20, pp. 887-897, 1972.
[37] J. Weertman, "Steady - State Creep through Dislocation Climb," Journal of Applied Physics, vol. 28, pp. 362-365, 1957.
[38] R. L. Coble, "A model for boundary diffusion controlled creep in polycrystalline materials," Journal of Applied Physics, vol. 34, pp. 1679-1682, 1963.
[39] C. Herring, "Diffusional viscosity of a polycrystalline solid," Journal of Applied Physics, vol. 21, pp. 437-445, 1950.
[40] E606-92, Standard Practice for Strain-Controlled Fatigue Testing, Annual Book of ASTM Standards, vol. 3, 2004.
[41] M. Mustafa, J. C. Roberts, J. C. Suhling, P. Lall, "The Effects of Aging of the Cyclic Stress-Strain and Fatigue Behaviors of Lead Free Solders," Proceedings of InterPACK 2013, pp. 1-12, 2013.
[42] L. F. Coffin, "A Study of the Effects of Cyclic Thermal Stresses on Ductile Metal," ASME Transactions, vol. 76, 1954.
[43] H. Ma and J. C. Suhling, "A review of mechanical properties of lead-free solders for electronic packaging," Journal of Materials Science, vol. 44, pp. 1141-1158, 2009.
[44] H. Ma, J. C. Suhling, Y. Zhang, P. Lall, and M. J. Bozack, "The influence of elevated temperature aging on reliability of lead free solder joints," Proceedings of the 57th Electronic Components and Technology Conference, pp. 653-668, 2007.
[45] H. Ma, J. C. Suhling, P. Lall, and M. J. Bozack, "Reliability of the aging lead free solder joint," Proceedings of the 56th Electronic Components and Technology Conference, pp. 849-864, 2006.
[46] Y. Zhang, Z. Cai, J. C. Suhling, P. Lall, and M. J. Bozack, "The Effects of Aging Temperature on SAC Solder Joint Material Behavior and Reliability," Proceedings of the 58th Electronic Components and Technology Conference, pp. 99-112, 2008.
[47] A. S. Medvedev, "Aging of Tin-Lead Solders and Joints Soldered by Them," Metallovedenie i Obrabotka Metallov, vol. 7, pp. 16-23, 1956.
[48] B. T. Lampe, "Room temperature aging properties of some solder alloys," Welding Journal, vol. 55, pp. 330-340, 1976.
[49] J.-W. Yoon, C.-B. Lee, and S.-B. Jung, "Growth of An Intermetallic Compound Layer With Sn-3.5 Ag-5Bi On Cu And Ni-P/Cu During Aging Treatment," Journal of Electronic Materials, vol. 32, pp. 1195-1202, 2003.
[50] S. Choi, T. R. Bieler, J. P. Lucas, and K. N. Subramanian, "Characterization of The Growth of Intermetallic Interfacial Layers of Sn-Ag and Sn-Pb Eutectic

Solders and Their Composite Solders on Cu Substrate during Isothermal Long-Term Aging," Journal of Electronic Materials, Vol. 28, pp. 1209-1215, 1999.

[51] L. Xu, J. H. L. Pang, K. H. Prakash, and T. H. Low, "Isothermal And Thermal Cycling Aging on IMC Growth Rate in Lead-Free and Lead-Based Solder Interface," IEEE Transactions on Components and Packaging Technologies, vol. 28, pp. 408-414, 2005.

[52] I. E. Anderson, J. W. Walleser, J. L. Harringa, F. Laabs, and A. Kracher, "Nucleation Control and Thermal Aging Resistance of Near-Eutectic Sn-Ag-Cu-X Solder Joints by Alloy Design," Journal of Electronic Materials, vol. 38, pp. 2770-2779, 2009.

[53] T. C. Hsuan and K. L. Lin, "Effects of Aging Treatment of Mechanical Properties and Microstructure of Sn-8.5Zn-0.5Ag-0.01Al-0.1Ga Solder," Materials Science and Engineering, A, vol. 456, pp. 202-209, 2007.

[54] C. M. Chuang, T.-S. Lui, and L.-H. Chen, "Effect of Aluminum Addition on Tensile Properties of Naturally Aged Sn-9Zn Eutectic Solder," Journal of Materials Science, vol. 37, pp. 191-195, 2002.

[55] J. H. L. Pang, T. H. Low, B. S. Xiong, X. Luhua, and C. C. Neo, "Thermal cycling aging effects on Sn–Ag–Cu solder joint microstructure, IMC and strength," Thin Solid Films, vol. 462-463, pp. 370-375, 2004.

[56] R. Darveaux, "Shear Deformation of Lead Free Solder Joints," Proceedings of the 55th Electronic Components and Technology Conference, pp. 882-893, 2005.

[57] S. Wiese and K. J. Wolter, "Creep of thermally aged SnAgCu-solder joints," Microelectronics Reliability, vol. 47, pp. 223-232, 2007.

[58] I. Dutta, D. Pan, R. A. Marks, and S. G. Jadhav, "Effect of Thermo-mechanically Induced Microstructural Coarsening on the Evolution of Creep Response of SnAg-based Microelectronic Solders," Materials Science and Engineering A, vol. 410-411, pp. 48-52, 2005.

[59] Z. Cai, Y. Zhang, J. C. Suhling, P. Lall, R. W. Johnson, and M. J. Bozack, "Reduction of Lead Free Solder Aging Effects Using Doped SAC Alloys," Proceedings of the 60th Electronic Components and Technology Conference, pp.1493-1511, 2010.

[60] R. Darveaux and K. Banerji, "Fatigue Analysis of Flip Chip Assemblies Using Thermal Stress Simulations and A Coffin-Manson Relation," Proceedings of the 41st Electronic Components and Technology Conference, pp. 797–805, 1991.

[61] Y. Zhang, "The Effects of Aging on the Mechanical Behavior of Lead Free and Mixed Formulation Solder Alloys," Ph.D. Dissertation, Auburn University, 2010.

[62] Y. Ding, C. Wang, Y. Tian, and M. Li, "Influence of Ageing Treatment on Deformation Behavior of 96.5Sn3.5Ag Lead Free Solder Alloy During In Situ Tensile Tests," Journal of Alloys and Compounds, vol. 428, pp. 274–285, 2007.

[63] Q. Xiao, H. J. Bailey, and W. D. Armstrong, "Aging effects on microstructure and tensile property of Sn3. 9Ag0. 6Cu solder alloy," Journal of Electronic Packaging, vol. 126, p. 208, 2004.

[64] Y. Zhang, Z. Cai, J. C. Suhling, P. Lall, and M. J. Bozack, "The Effects of SAC Alloy Composition on Aging Resistance and Reliability," Proceedings of the 59th Electronic Components and Technology Conference, pp. 370-389, 2009.

[65] K.-S. Kim, C.-H. Yu, and J.-M. Yang, "Aging treatment characteristics of solder bump joint for high reliability optical module," Thin solid films, vol. 462, pp. 402-407, 2004.
[66] I. E. Anderson and J. L. Harringa, "Elevated temperature aging of solder joints based on Sn-Ag-Cu: effects on joint microstructure and shear strength," Journal of electronic materials, vol. 33, pp. 1485-1496, 2004.
[67] K. Mysore, D. Chan, D. Bhate, G. Subbarayan, I. Dutta, V. Gupta, J. Zhao, and D. Edwards, "Aging-Informed Behavior of Sn3.8Ag0.7Cu Solder Alloys," Proceedings of ITHERM 2008, pp. 870-875, 2008.
[68] S. Chavali, Y. Singh, P. Kumar, G. Subbarayan, I. Dutta, and D. R. Edwards, "Aging Aware Constitutive Models for SnAgCu Solder Alloys," Proceedings of the 61st Electronic Components and Technology Conference, pp.701-705, 2011.
[69] A. Bansal, T. K. Lee, K.C. Liu, and J. Xue, "Effects of Isothermal Aging and In-Situ Current Stress on The Reliability of Lead-Free Solder Joints," Proceedings of the 60th Electronic Components and Technology Conference, pp. 1529-1535, 2010.
[70] M. Mustafa, Z. Cai, J. C. Suhling, and P. Lall, "The Effects of Aging on The cyclic Stress-Strain Behavior And Hysteresis Loop Evolution of Lead Free Solders," Proceedings of the 61th Electronic Components and Technology Conference, pp. 927-939, 2011.
[71] A. R. Fix, W. Nüchter, and J. Wilde, "Microstructural changes of lead-free solder joints during long-term ageing, thermal cycling and vibration fatigue," Soldering and Surface Mount Technology, vol. 20, pp. 13-21, 2008.
[72] W. M. Chen, P. McCloskey, and S. C. O'Mathuna, "Isothermal aging effects on the microstructure and solder bump shear strength of eutectic Sn37Pb and Sn3. 5Ag solders," Microelectronics Reliability, vol. 46, pp. 896-904, 2006.
[73] S. L. Allen, M. R. Notis, R. R. Chromik, and R. P. Vinci, "Microstructural evolution in lead-free solder alloys: Part I. Cast Sn–Ag–Cu eutectic," Journal of Materials Research, vol. 19, pp. 1417-1424, 2004.
[74] Y. Miyazawa and T. Ariga, "Influences of Aging Treatment on Microstructure and Hardness of Sn-(Ag, Bi, Zn) Eutectic Solder Alloys," Materials Transactions of the Japan Institute of Metals, Vol. 42(5), pp. 776-782, 2001.
[75] R. Gagliano, "Shear Testing of Solder Joints: The Effect of Various Parameters on the Maximum Shear Stress of Eutectic Tin-Lead Solder," Advanced Materials for the 21st Century: Proceedings of the 1999 Julia R. Weertman Symposium, pp. 107-116, 1999.
[76] S. W. R. Lee, Y.-K. Tsui, X. Hunag, and E. C. C. Yan, "Effects of Room Temperature Storage Time on the Shear Strength of PBGA Solder Balls," Proceedings of the 2002 ASME International Mechanical Engineering Congress and Exposition, pp. 1-4, 2002.
[77] M. Hasnine, Mustafa, M., Suhling, J. C., Porok, M., Bozack, M., Lall, P. , "Characterization of Aging Effects in Lead Free Solder Joints using Nanoindentation," Proceedings of the 63rd Electronic Components and Technology Conference, 2013.
[78] M. Motalab, Mustafa, M., Suhling, J. C., Zhang, J., Evans, J. L., Bozack, M. J., Lall, P., "Correlation of Reliability Models Including Aging Effects with Thermal

Cycling Reliability Data," Proceedings of the 63rd Electronic Components and Technology Conference, 2013.

[79] T. Zhang, J. Evans, C. Mitchell, Z. Z. Li, E. Crandall, J. Ridenour, and F. Xie, "Reliability of lead-free BGA with SnPb solder paste for harsh environments," Proc. SMTA/CAVE Symposium on AIMS Harsh Environment Electronics, 2009.

[80] J. Zhang, Thirugnanasambandam, S., Evans, J. L., Bozack, M. J., Zhang, Y., Suhling, J. C., "Correlation of Aging Effects on the Creep rate and Reliability in Lead Free Solder Joints," SMTA Journal, vol. 25(3), pp. 19-28, 2012.

[81] T. K. Lee and H. Ma, "Aging impact on the accelerated thermal cycling performance of lead-free BGA solder joints in various stress conditions," Proceedings of the 62nd Electronic Components and Technology Conference, pp. 477-482, 2012.

[82] L. Yin, M. Meilunas, B. Arfaei, L. Wentlent, and P. Borgesen, "Effect of microstructure evolution on Pb-free solder joint reliability in thermomechanical fatigue," Proceedings of the 62nd Electronic Components and Technology Conference (ECTC), pp. 493-499, 2012.

[83] R. J. Coyle, P. P. Solan, A. J. Serafino, and S. A. Gahr, "The Influence of Room Temperature Aging on Ball Shear Strength and Microstructure of Area Array Solder Balls," Proceedings of the 50th Electronic Components and Technology Conference, pp. 160-169, 2000.

[84] T. K. Lee, H. Ma, K. C. Liu, and J. Xue, "Impact of isothermal aging on long-term reliability of fine-pitch ball grid array packages with Sn-Ag-Cu solder interconnects: Surface finish effects," Journal of Electronic Materials, vol. 39, pp. 2564-2573, 2010.

[85] A. C. Chilton, M. A. Whitmore, and W. B. Hampshire, "Fatigue Failure in a Model SMD Joint," Soldering and Surface Mount Technology, vol.1, pp. 21-24, 1989.

[86] M. Li, K. Y. Lee, D. R. Olsen, W. T. Chen, B. T. C. Tan, and S. Mhaisalkar, "Microstructure, joint strength and failure mechanisms of SnPb and Pb-free solders in BGA packages," IEEE Transactions on Electronics Packaging Manufacturing, vol. 25, pp. 185-192, 2002.

[87] J.-M. Koo and S.-B. Jung, "Effect of displacement rate on ball shear properties for Sn–37Pb and Sn–3.5 Ag BGA solder joints during isothermal aging," Microelectronics Reliability, vol. 47, pp. 2169-2178, 2007.

[88] J. R. Oliver, J. Liu, and Z. Lai, "Effect of Thermal Aging on the Shear Strength of Lead-free Solder Joints," Proceedings of the International Symposium on Advanced Packaging Materials: Processes, Properties and Interfaces, pp. 152-157, 2000.

[89] J. H. L. Pang, K. H. Tan, X. Q. Shi, and Z. P. Wang, "Microstructure and intermetallic growth effects on shear and fatigue strength of solder joints subjected to thermal cycling aging," Materials Science and Engineering: A, vol. 307, pp. 42-50, 2001.

[90] T. K. Lee, B. Zhou, and T. R. Bieler, "Impact of Isothermal Aging and Sn Grain Orientation on the Long-Term Reliability of Wafer-Level Chip-Scale Package Sn–Ag–Cu Solder Interconnects," IEEE Transactions on Components, Packaging and Manufacturing Technology, vol. 2, Issue 3, pp. 496-501, 2012.

[91] J. Smetana, R. Coyle, P. Read, R. Popowich, D. Fleming, and T. Sack, "Variations in Thermal Cycling Response of Pb-free Solder Due to Isothermal Preconditioning," Proceedings of SMTAI 2011, pp. 641-654, 2011.
[92] S. Wiese, M. Roellig, and K. J. Wolter, "Creep of Eutectic SnAgCu in Thermally Treated Solder Joints," Proceedings of the 55th Electronic Components and Technology Conference, pp. 1272-1281, vol. 2005.
[93] W. K. Jones, Y. Liu, M. A. Zampino, G. Gonzalez, and M. Shah, "Design and reliability of solders and solder interconnections," TMS Proceedings, 1997.
[94] W. K. Jones, Y. Q. Liu, M. A. Zampino, and G. L. Gonzalez, "The at-temperature mechanical properties of lead-tin based alloys," Microelectronic Interconnections and Assembly, pp. 53-58, 1998.
[95] X. Q. Shi, W. Zhou, H. L. J. Pang, Z. P. Wang, and Y. P. Wang, "Effect of temperature and strain rate on mechanical properties of 63Sn/37Pb solder alloy," Journal of Electronic Packaging, vol. 121, pp. 179-185, 1999.
[96] H. Nose, M. Sakane, Y. Tsukada, and H. Nishimura, "Temperature and strain rate effects on tensile strength and inelastic constitutive relationship of Sn-Pb solders," Journal of Electronic Packaging, vol. 125, pp. 59-66, 2003.
[97] W. J. Plumbridge and C. R. Gagg, "Effects of strain rate and temperature on the stress–strain response of solder alloys," Journal of Materials Science: Materials in Electronics, vol. 10, pp. 461-468, 1999.
[98] F. Lang, H. Tanaka, O. Munegata, T. Taguchi, and T. Narita, "The effect of strain rate and temperature on the tensile properties of Sn3.5 Ag solder," Materials Characterization, vol. 54, pp. 223-229, 2005.
[99] L. H. Dai and S.-W. R. Lee, "Characterization of strain rate-dependent behavior of 63Sn-37Pb solder alloy," Proceedings of InterPACK 2001, pp. 307-313, 2001.
[100] J. H. L. Pang, B. S. Xiong, and F. X. Che, "Modeling stress strain curves for lead-free 95.5Sn-3.8Ag-0.7Cu solder," Proceedings of the 5th EuroSimE Conference, pp. 449-453, 2004.
[101] J. G. Harper, L. A. Shepard, and J. E. Dorn, "Creep of aluminum under extremely small stresses," Acta Metallurgica, vol. 6, pp. 509-518, 1958.
[102] H. Yang, P. Deane, P. Magill, and K. L. Murty, "Creep deformation of 96.5Sn-3.5Ag solder joints in a flip-chip package," Proceedings of the 46th Electronic Components and Technology Conference, pp. 1136-1142, 1996.
[103] X. Q. Shi, Z. P. Wang, Q. J. Yang, and H. L. J. Pang, "Creep behavior and deformation mechanism map of Sn-Pb eutectic solder alloy," Journal of Engineering Materials and Technology, vol. 125, pp. 81-88, 2003.
[104] J.-P. Clech, "An Obstacle-Controlled Creep Model for Sn-Pb and Sn-based Lead-Free Solders," Proceedings of the SMTA International Conference, 2004.
[105] L. Anand, "Constitutive equations for hot-working of metals," International Journal of Plasticity, vol. 1, pp. 213-231, 1985.
[106] S. B. Brown, K. H. Kim, and L. Anand, "An internal variable constitutive model for hot working of metals," International Journal of Plasticity, vol. 5, pp. 95-130, 1989.
[107] M. Motalab, Z. Cai, J. C. Suhling, and P. Lall, "Determination of Anand constants for SAC solders using stress-strain or creep data," Proceedings of ITHERM 2012, pp. 910-922, 2012.

[108] F. X. Che, H. L. J. Pang, W. H. Zhu, W. Sun, and A. Y. S. Sun, "Modeling constitutive model effect on reliability of lead-free solder joints," Electronic Packaging Technology, pp. 1-6, 2006.
[109] M. Pei and J. Qu, "Constitutive modeling of lead-free solders," Advanced Packaging Materials: Processes, Properties and Interfaces, pp. 45-49, 2005.
[110] K. Mysore, G. Subbarayan, V. Gupta, and R. Zhang, "Constitutive and aging behavior of Sn3. 0Ag0. 5Cu solder alloy," IEEE Transactions on Electronics Packaging Manufacturing, vol. 32, pp. 221-232, 2009.
[111] X. Chen, G. Chen, and M. Sakane, "Modified Anand constitutive model for lead-free solder Sn-3.5 Ag," Proceedings of ITHERM 2004, vol. 2, pp. 447-452. 2004.
[112] M. Amagai, M. Watanabe, M. Omiya, K. Kishimoto, and T. Shibuya, "Mechanical characterization of Sn–Ag-based lead-free solders," Microelectronics Reliability, vol. 42, pp. 951-966, 2002.
[113] Y. Kim, H. Noguchi, and M. Amagai, "Vibration fatigue reliability of BGA-IC package with Pb-free solder and Pb–Sn solder," Microelectronics Reliability, vol. 46, pp. 459-466, 2006.
[114] N. Bai, X. Chen, and H. Gao, "Simulation of uniaxial tensile properties for lead-free solders with modified Anand model," Materials and Design, vol. 30, pp. 122-128, 2009.
[115] J. Wilde, K. Becker, M. Thoben, W. Blum, T. Jupitz, G. Wang, and Z. N. Cheng, "Rate dependent constitutive relations based on Anand model for 92.5 Pb5Sn2. 5Ag solder," IEEE Transactions on Advanced Packaging, vol. 23, pp. 408-414, 2000.
[116] G. Z. Wang, Z. N. Cheng, K. Becker, and J. Wilde, "Applying Anand model to represent the viscoplastic deformation behavior of solder alloys," Journal of Electronic Packaging, vol. 123, pp. 247-253, 2001.
[117] B. Rodgers, B. Flood, J. Punch, and F. Waldron, "Determination of the Anand viscoplasticity model constants for SnAgCu," Proceedings of InterPACK 2005, pp. 17-22, 2005.
[118] D. Bhate, D. Chan, G. Subbarayan, T. C. Chiu, V. Gupta, and D. R. Edwards, "Constitutive behavior of Sn3. 8Ag0. 7Cu and Sn1. 0Ag0. 5Cu alloys at creep and low strain rate regimes," IEEE Transactions on Components and Packaging Technologies, vol. 31, pp. 622-633, 2008.
[119] A. Syed, "Updated life prediction models for solder joints with removal of modeling assumptions and effect of constitutive equations," Proceedings of the 7th EuroSimE Conference, pp. 1-9, 2006.
[120] A. Schubert, R. Dudek, E. Auerswald, A. Gollbardt, B. Michel, and H. Reichl, "Fatigue life models for SnAgCu and SnPb solder joints evaluated by experiments and simulation," Proceedings of the 53rd Electronic Components and Technology Conference, pp. 603-610, 2003.
[121] Q. Zhang, A. Dasgupta, and P. Haswell, "Viscoplastic constitutive properties and energy-partitioning model of lead-free Sn3. 9Ag0. 6Cu solder alloy," Proceedings of the 53rd IEEE Electronic Components and Technology Conference, pp. 1862-1868, 2003.

[122] B. Zahn, "Solder Joint Fatigue Life Model Methodology for 63Sn37Pb and 95.5 Sn4Ag0.5Cu Materials," Proceedings of the 53rd IEEE Electronic Components and Technology Conference, pp. 83-94, 2003.
[123] W. W. Lee, L. T. Nguyen, and G. S. Selvaduray, "Solder joint fatigue models: review and applicability to chip scale packages," Microelectronics reliability, vol. 40, pp. 231-244, 2000.
[124] S. Ridout and C. Bailey, "Review of methods to predict solder joint reliability under thermo‐mechanical cycling," Fatigue & Fracture of Engineering Materials and Structures, vol. 30, pp. 400-412, 2007.
[125] C. Basaran and H. Tang, "A damage mechanics based fatigue life prediction model for solder joints," Journal of Electronic Packaging, vol. 125, pp. 120-125, 2003.
[126] G. Gustafsson, I. Guven, V. Kradinov, and E. Madenci, "Finite Element Modeling of BGA Packages for Life Prediction," Proceedings of the 50th IEEE Electronic Components and Technology Conference, pp. 1059-1063, 2000.
[127] J. H. L. Pang, T.-I. Tan, and S. K. Sitaraman, "Thermo-mechanical analysis of solder joint fatigue and creep in a flip chip on board package subjected to temperature cycling loading," Proceedings of the 48th IEEE Electronic Components and Technology Conference, pp. 878-883, 1998.
[128] D. A. Shnawah, M. F. M. Sabri, and I. A. Badruddin, "A review on thermal cycling and drop impact reliability of SAC solder joint in portable electronic products," Microelectronics reliability, vol. 52, pp. 90-99, 2012.
[129] H. Liu, J. Zhang, S. Chen, M. Du, N. Feng, and Q. Wang, "Board Level Thermal Cycle Reliability of BGA for a New Type of Pad Structure with OSP Surface Finish," 2007, Proceedings of 2007 ICEPT Conference, pp.1-3, 2007
[130] S. Y. Yu, Y.-M. Kwon, J. Kim, T. Jeong, S. Choi, and K.-W. Paik, "Studies on the Thermal Cycling Reliability of BGA System-in-Package (SiP) with an Embedded Die," IEEE Transactions on Components, Packaging and Manufacturing Technology, vol. 2, pp. 625-633, 2012.
[131] V. Vasudevan and X. Fan, "An acceleration model for lead-free (SAC) solder joint reliability under thermal cycling," Proceedings of the 58th IEEE Electronic Components and Technology Conference, pp. 139-145, 2008.
[132] R. Darveaux, "Effect of simulation methodology on solder joint crack growth correlation," Proceedings of the 50th IEEE Electronic Components and Technology Conference, pp. 1048-1058, 2000.
[133] M. Motalab, Z. Cai, J. C. Suhling, J. Zhang, J. L. Evans, M. J. Bozack, and P. Lall, "Improved predictions of lead free solder joint reliability that include aging effects," Proceedings of the 62nd IEEE Electronic Components and Technology Conference, pp. 513-531, 2012.
[134] J. Morrow, "Cyclic plastic strain energy and fatigue of metals," ASTM STP 378, American Society for Testing and Materials, pp. 45-49, 1964.
[135] F. X. Che, J. H. L. Pang, B. S. Xiong, L. Xu, and T. H. Low, "Lead Free Solder Joint Reliability Characterization for PBGA, PQPF and TSSOP Assemblies," Proceedings of the 55th IEEE Electronic Components and Technology Conference, pp. 916-921, 2005.

[136] J. Roberts, S. Hussain, M. K. Rahim, M. Motalab, J. C. Suhling, R. C. Jaeger, P. Lall, and R. Zhang, "Characterization of microprocessor chip stress distributions during component packaging and thermal cycling," Proceedings of the 60th IEEE Electronic Components and Technology Conference, pp. 1281-1295, 2010.

[137] J. C. Roberts, M. Motalab, S. Hussain, J. Suhling, R. C. Jaeger, and P. Lall, "Squeezing the Chip: The Buildup of Compressive Stress in a Microprocessor Chip by Packaging and Heat Sink Clamping," Proceedings of the 61st IEEE Electronic Components and Technology Conference, pp. 406-423, 2011.

[138] J. C. Roberts, M. Motalab, S. Hussain, J. C. Suhling, R. C. Jaeger, and P. Lall, "Characterization of Compressive Die Stresses in CBGA Microprocessor Packaging Due to Component Assembly and Heat Sink Clamping," Journal of Electronic Packaging, vol. 134, pp. 031005-1 - 031005-17 2012.

[139] J. Roberts, M. Motalab, S. Hussain, J. C. Suhling, R. C. Jaeger, and P. Lall, "Measurement of die stresses in microprocessor packaging due to thermal and power cycling," Proceedings of the 62nd IEEE Electronic Components and Technology Conference, pp. 756-770, 2012.

[140] M. K. Rahim, J. C. Suhling, D. S. Copeland, M. S. Islam, R. C. Jaeger, P. Lall, and R. W. Johnson, "Die stress characterization in flip chip on laminate assemblies," IEEE Transactions on Components and Packaging Technologies, vol. 28, pp. 415-429, 2005.

[141] M. K. Rahim, J. C. Suhling, R. C. Jaeger, and P. Lall, "Fundamentals of delamination initiation and growth in flip chip assemblies," Proceedings of the 55th IEEE Electronic Components and Technology Conference, pp. 1172-1186, 2005.

[142] N. J. Chhanda, J. C. Suhling, and P. Lall, "Implementation of a viscoelastic model for the temperature dependent material behavior of underfill encapsulants," Proceedings of ITHERM 2012, pp. 269-281, 2012.

APPENDIX

APPENDIX

A.1 Model Constants for Creep Rate Variation with Aging

Temperature (^oC)	C_0	C_1	C_2	C_3
25	1.066×10^{-7}	8.9462×10^{-10}	6.6612×10^{-8}	0.141501
50	4.216×10^{-7}	3.071×10^{-9}	2.141×10^{-7}	0.14755
75	9.102×10^{-7}	7.504×10^{-9}	7.7312×10^{-7}	0.15786
100	2.412×10^{-6}	3.8482×10^{-8}	1.8133×10^{-6}	0.3991
125	8.420×10^{-6}	1.269×10^{-7}	1.5763×10^{-5}	0.2816

Table A.1 Constants for the Steady State Creep Rate Empirical Models

A.2 Model Constants for Anand Parameter Variation with Aging (Aging Temperature = 100 ^oC)

Anand Parameters	C_0	C_1	C_2	C_3	C_4
s_o	5.60707	2.6393×10^{-4}	15.2463	0.27791	0.60957
m	0.24449	1.088×10^{-5}	7.3094×10^{-2}	0.37902	0.489407
n	0.001059	2.6393×10^{-4}	8.9445×10^{-3}	0.63934	0.53138
a	2.02935	6.4255×10^{-5}	0.24664	0.74637	0.43281
A	3511.32	525.82	0.6111	0.4837	–
$\hat{s}$	29.582	-7.0913	0.1581	-0.0032	–
h_o	82764.8	-32.9415	339495	3.70239	0.66732
ξ	4	–	–	–	–
Q/R	9320	–	–	–	–

Table A.2 Empirical Model Constants for Anand Parameter Variation with Aging at 100 C

A.3 3-D Model Constants for Anand Parameter Variation with Aging (Aging Temperature 25 – 125 ^{o}C)

Anand Parameters	C_0	C_1	C_2	C_3	C_4
s_o	20.32	-7.577×10^{-6}	-0.00156	0.1214	1.534
m	0.2454	-6.250×10^{-8}	-4.861×10^{-6}	0.17	1.59
n	0.0104	-2.947×10^{-9}	-2.351×10^{-6}	0.2515	1.395
a	2.02935	6.4255×10^{-5}	0.24664	0.74637	0.43281
A	3517	0.00134	0.03827	0.477	1.606
$\hat{s}$	29.59	-8.902×10^{-6}	-0.00051	0.1438	1.609
h_o	1.80×10^{5}	-0.1399	-0.1388	0.1112	2.255
ξ	4	–	–	–	–
Q/R	9320	–	–	–	–

Table A.3 Empirical Model Constants for Anand Parameter Variation with Aging Time and Temperature

A.4 Correlation of Predicted Stress-Strain Curves with Experimental Measurements for Different Aging Times

The correlations between the model predictions and the experimental stress-strain curves for no aging were shown in Figure 4.2. In this case, the Anand model constants from Table 4.1 for 0 days aging were utilized. The experimental curves were those shown earlier in Figure 3.10. Good correlations were obtained, with the Anand model was able to represent the stress-strain curves accurately over a wide range of temperatures and strain rates. Analogous comparisons for other durations of aging are shown in Figures A.1-A.8. In these plots, the Anand model constants from Table 4.1 for the respective days of aging were utilized, along with the experimental curves from Figures 3.11-3.18. Again, good correlations were obtained for all temperatures and strain rates.

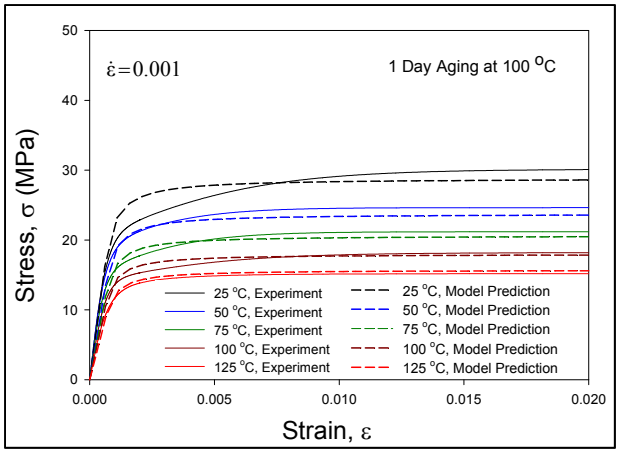

(a) $\dot{\varepsilon} = 0.001$

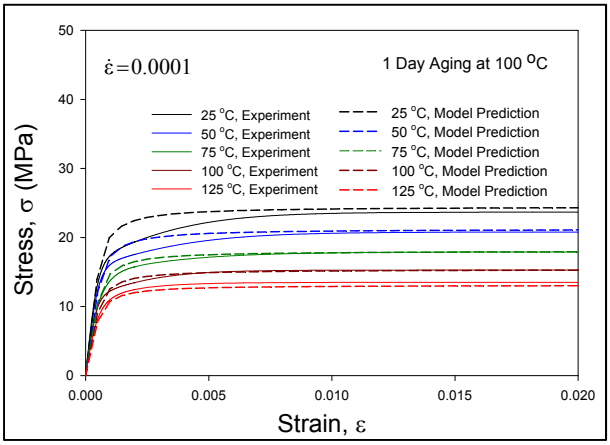

(b) $\dot{\varepsilon} = 0.0001$

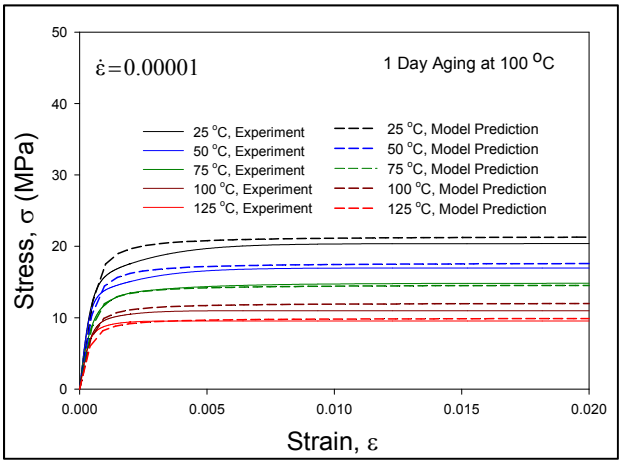

(c) $\dot{\varepsilon} = 0.00001$

Figure A.1 Correlation of the Anand Model Predictions with Experimental Stress-Strain Data for 1 Day Aging

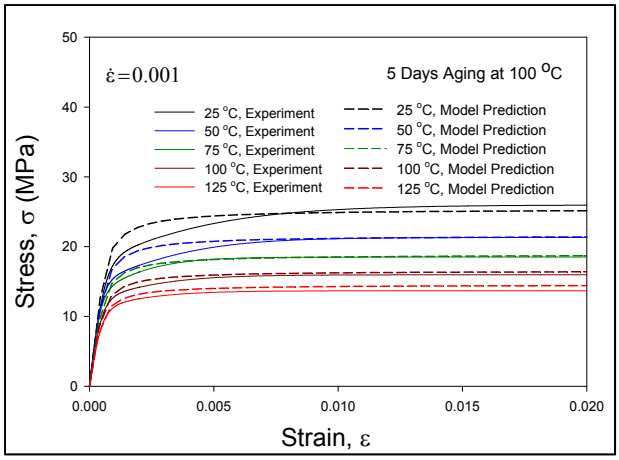

(a) $\dot{\varepsilon} = 0.001$

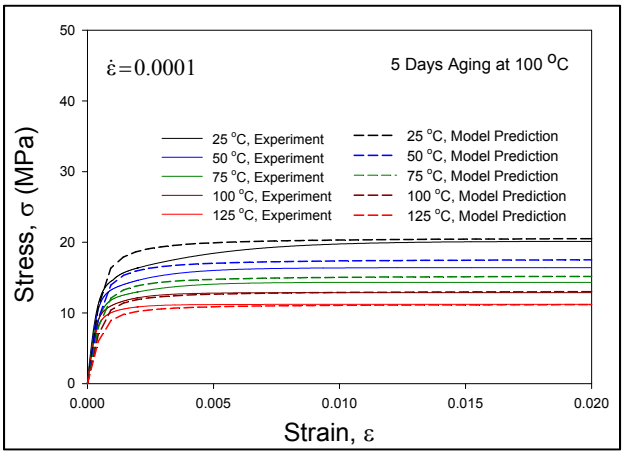

(b) $\dot{\varepsilon} = 0.0001$

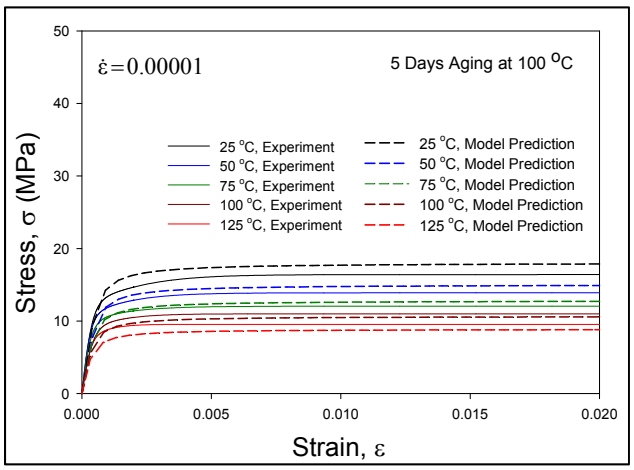

(c) $\dot{\varepsilon} = 0.00001$

Figure A.2 Correlation of the Anand Model Predictions with Experimental Stress-Strain Data for 5 Days Aging

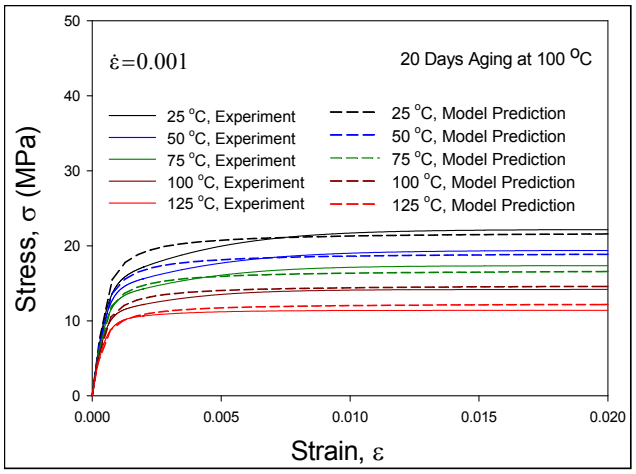

(a) $\dot{\varepsilon} = 0.001$

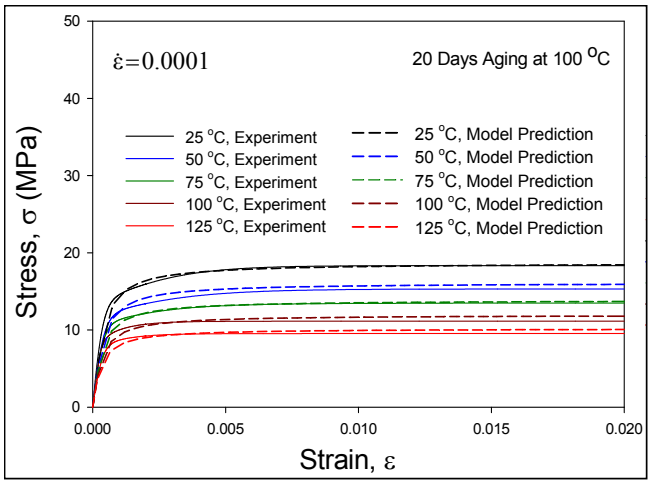

(b) $\dot{\varepsilon} = 0.0001$

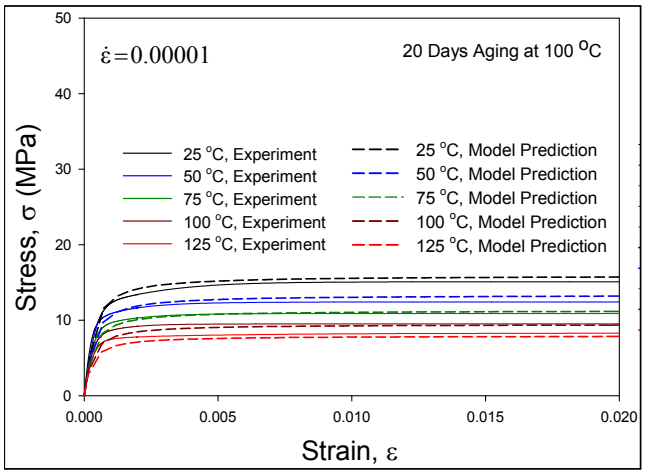

(c) $\dot{\varepsilon} = 0.00001$

Figure A.3 Correlation of the Anand Model Predictions with Experimental Stress-Strain Data for 20 Days Aging

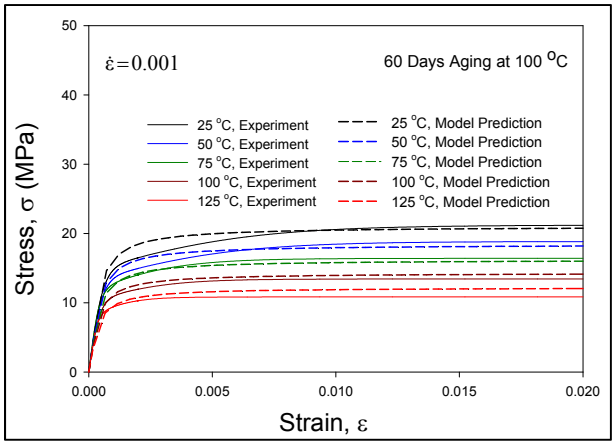

(a) $\dot{\varepsilon} = 0.001$

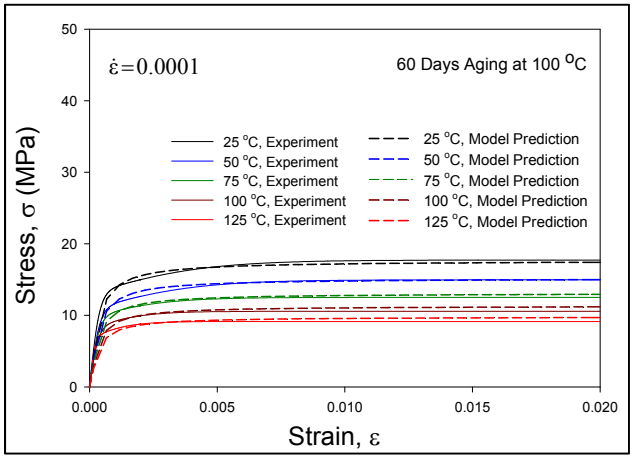

(b) $\dot{\varepsilon} = 0.0001$

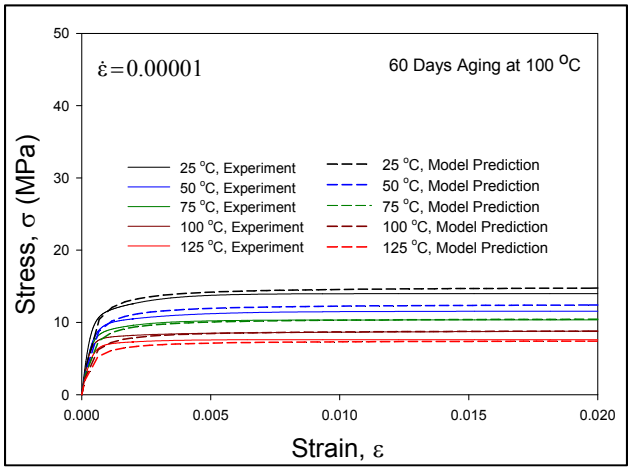

(c) $\dot{\varepsilon} = 0.00001$

Figure A.4 Correlation of the Anand Model Predictions with Experimental Stress-Strain Data for 60 Days Aging

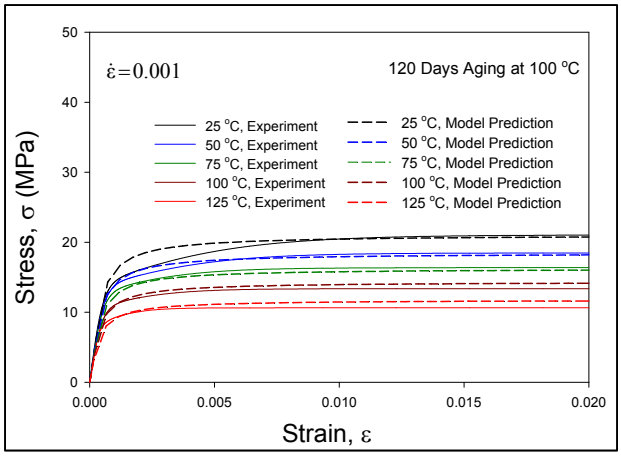

(a) $\dot{\varepsilon} = 0.001$

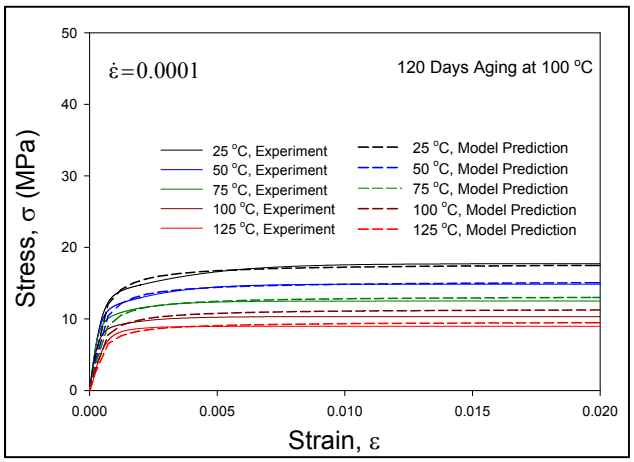

(b) $\dot{\varepsilon} = 0.0001$

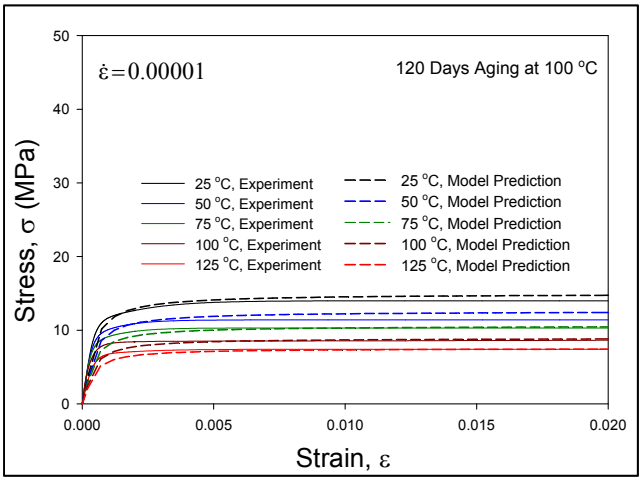

(c) $\dot{\varepsilon} = 0.00001$

Figure A.5 Correlation of the Anand Model Predictions with Experimental Stress-Strain Data for 120 Days Aging

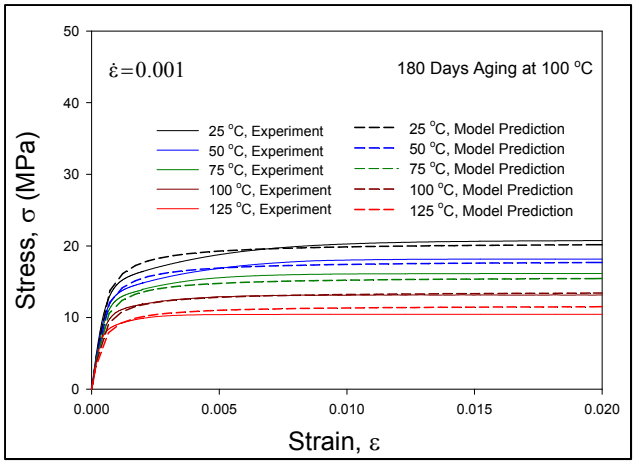

(a) $\dot{\varepsilon} = 0.001$

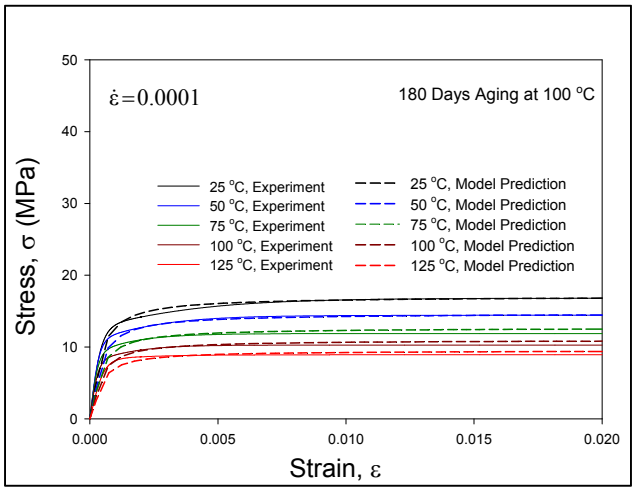

(b) $\dot{\varepsilon} = 0.0001$

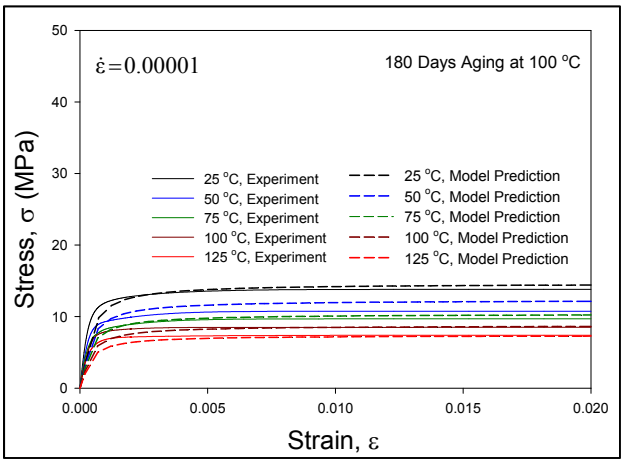

(c) $\dot{\varepsilon} = 0.00001$

Figure A.6 Correlation of the Anand Model Predictions with Experimental Stress-Strain Data for 180 Days Aging

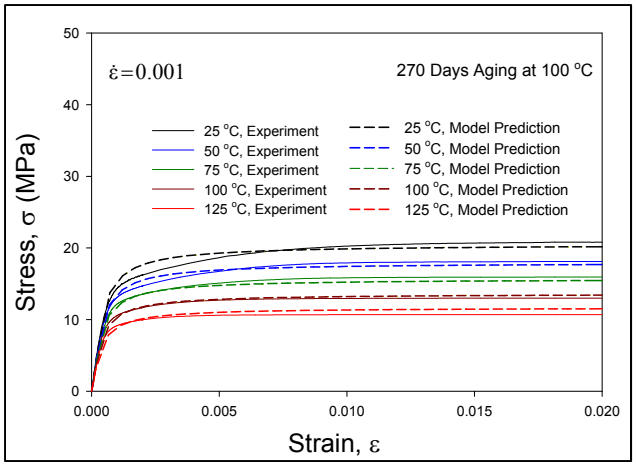

(a) $\dot{\varepsilon} = 0.001$

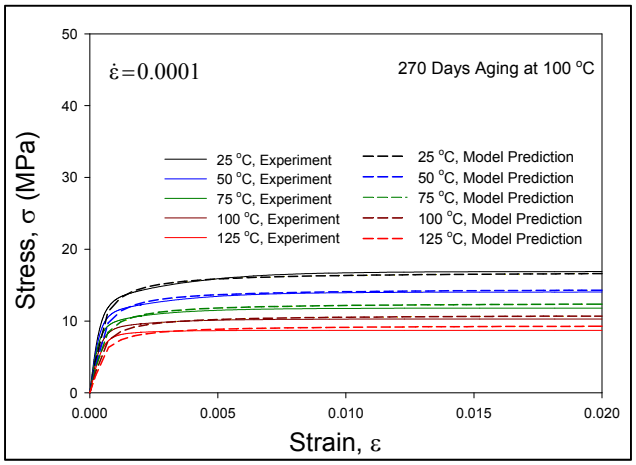

(b) $\dot{\varepsilon} = 0.0001$

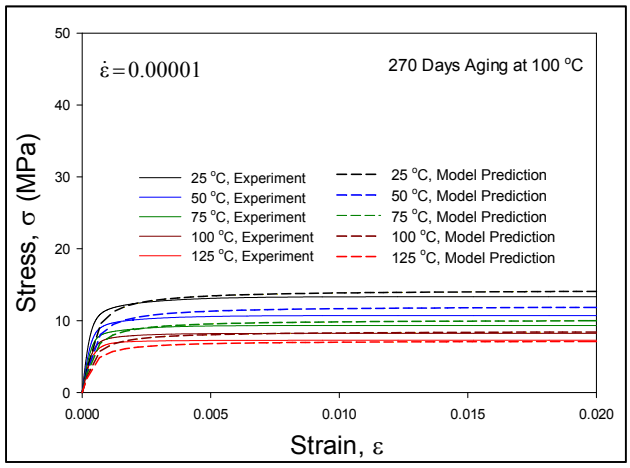

(c) $\dot{\varepsilon} = 0.00001$

Figure A.7 Correlation of the Anand Model Predictions with Experimental Stress-Strain Data for 270 Days Aging

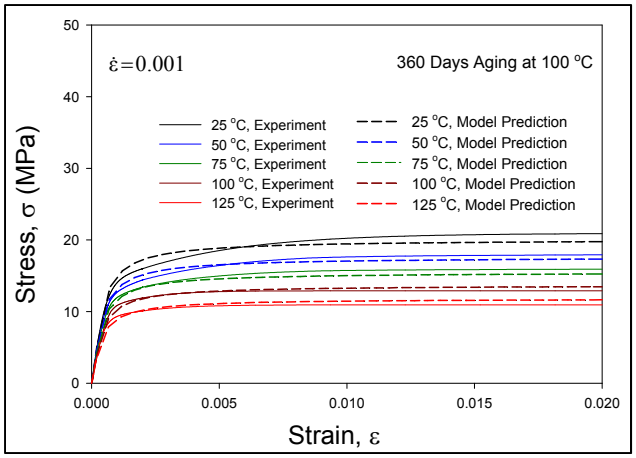

(a) $\dot{\varepsilon} = 0.001$

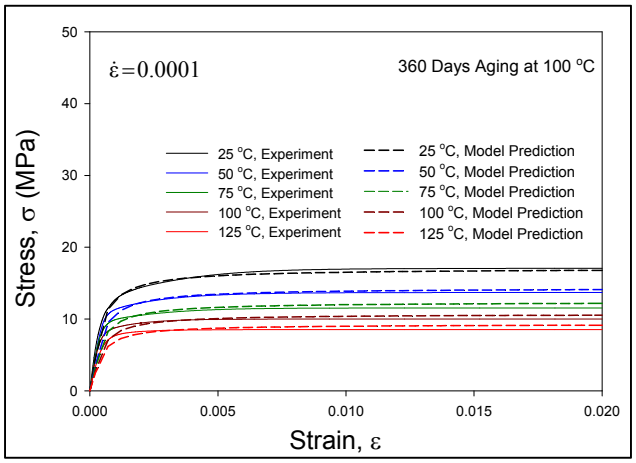

(b) $\dot{\varepsilon} = 0.0001$

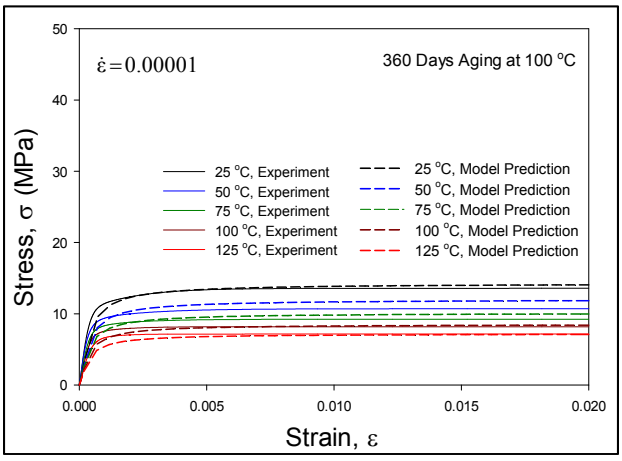

(c) $\dot{\varepsilon} = 0.00001$

Figure A.8 Correlation of the Anand Model Predictions with Experimental Stress-Strain Data for 360 Days Aging

A.5 Variation of Die Stress Distribution with Temperature in the CBGA Assembly

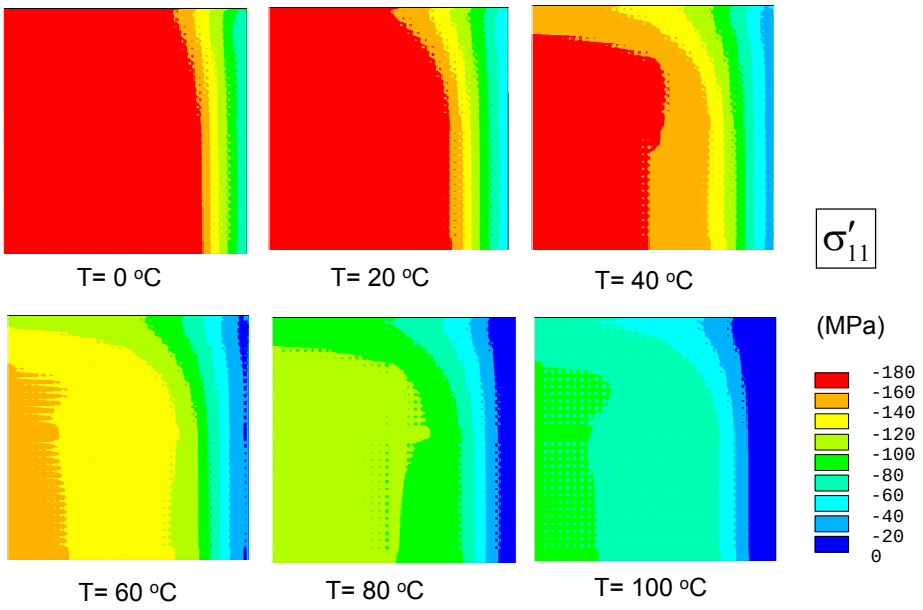

Figure A.9 Die Stress Temperature Variation in the CBGA Assembly

A.6 Plastic Work Distribution in Solder Joints (CBGA) Due to Power Cycling

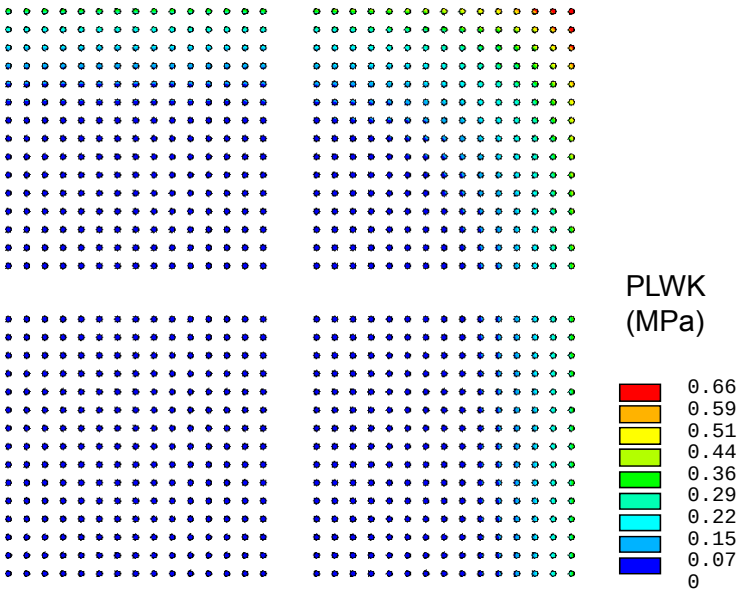

Figure A.10 Plastic Energy Dissipation in Flip Chip Solder Bumps in the CBGA Assembly